Role of structure in determining the properties of transition metal / post transition metal compounds

Thesis submitted for the degree of

Doctor of Philosophy (Science)

in

Physics (Theoretical)

by

SAGAR SARKAR

Department of Physics

University of Calcutta

2018

Dedicated to

This vast NATURE for giving me Space, Time, and Scope
to Observe, Think, and Learn;
AND
my near and dear ones

Acknowledgement

In this memorable moment of submitting my Ph.D thesis, I would like to take this opportunity to express my hearty gratitude to those generous people who have guided me, motivated me and have been still with me all through a period of five and a half years of my academic journey in the S. N. Bose National Centre For Basic Sciences where this journey has touched the summit at last. First and foremost, I would like to offer my heartiest gratitude to my supervisor, Prof. Priya Mahadevan, for her continuous supervision and guidance throughout the period of my research work and the Ph.D thesis which could not be able to see the light of the day without her sincere help. Her valuable advice and guidance, as a flame of light, will surely show me the right way in my future career and life also. I am fortunate enough to work with a nice person like her who has helped in every respect, even in my personal problems also. Now I would also like to offer thanks to Dr. Manoranjan Kumar, Dr. Sugata Mukherjee, Dr. Kalyan Mandal of the S. N. Bose Centre for their valuable suggestions and comments. I must thank the S. N. Bose Centre, as a whole, for providing me with good research facilities and a clam, cosy, peaceful environment all along. I also thank the C.S.I.R(India) for providing me with scholarship regularly for the entire period of my Ph.D programme.

After this, I would like to thank all of my group members(PMG Group); first my seniors, Srimanta da, Ashis da, Bipul da, Kapil da, Abhinav da, Ruma di, Soumya da, Basudeb, Shishir from whom I have learned a lot of valuable lessons; then about my juniors, Poonam, Joydeep, Sumanti whom I shall never forget for their suggestions and help; I would like to thank, specially, Shishir and Poonam for their constant help and support during the last year. Besides my group, there are many persons who became my good friends here and I would also like to thank them all for their nice company. In this very moment I, do, remember my seniors like Arindam da, Subhajit da, Shinde da; my batch mates, Azahar, Aslam, Subrata, Kartik, Poulami; my juniors, Arka, Kausik, Monalisa, Samiran, Subhadip, Atanu, Juriti, Ritam, Ransell for their help, well wishes and warm company. I shall never forget Supriyo for his warm inspiring company, best co-operation and specially for all those happy moments we spent together.

Now, I want to express my sincere gratitude to those people whose inspiration helped me to reach here in the S. N. Bose centre for my higher studies; firstly, all of my teachers, Mr. Anjan Mukherjee, Mr. Bhabani Nandi, Mr. Ashoke Ghosh, Mr. Bidur Pramanik during my school days; Prof. Debasis Bhattacharya during my graduation period; Prof. Tanmoy Banerjee, Prof. Abhijit Chatterjee, Prof. Pabitra Kumar Chakrabarti, Prof. Sanjoy Mukherjee of the University of Burdwan during my P.G. studies – they are all my path-makers and helped me to dream.

Next come all of my close friends, Swaraj, Ali, Bappa, Samim, Sumanjan, Subhadip, Subhrajit, Ramanuj, Deepanjan, Swagata, Debabrata and others; They all are praiseworthy for their love, and warm company. I shall, specially, thank my friend Smita for all her well wishes and cheerful words.

Last but not the least, I would like to convey my uttermost respect and gratitude to all the members of my family, especially, my father, mother, both grandmothers, Rinku and my only younger brother, Saikat, for their blessings, love and care. Saikat is not only my brother but also a best friend. He has always extended his helping hands and best cooperation where and when necessary for me. So, mere thanks are not due to him at all, he deserves more.

The aggregate of all these people's blessings, love and well wishes is the result of this Ph.D thesis which I am going to submit.

With regards,

Sagar Sarkar
S. N. Bose Centre
Kolkata, India
January, 2018

List Of Publications

1. Size of the Organic Cation Tunes the Band Gap of Colloidal Organolead Bromide Perovskite Nanocrystals
   Mona Mittal, Atanu Jana, **Sagar Sarkar** *, Priya Mahadevan, Sameer Sapra.
   J. Phys. Chem. Lett. **7**, 3270 (2016). (* First author from the theory group)

2. Driving force for martensitic transformation in $Ni_2Mn_{1+x}Sn_{1-x}$.
   Soumyadipta Pal, **Sagar Sarkar**, S. K. Pandey, Chhayabrita Maji and Priya Mahadevan.
   Phys. Rev. B **94**, 15143 (2016).

3. The driving force for charge ordering in rare earth nickelates.
   Sagar Sarkar*, Basudeb Mandal*, S. K. Pandey, Priya Mahadevan, Cesare Franchini, A. J. Millis and D. D. Sarma.
   arXiv:1701.06819v1. (*both authors have equal contributions)

4. Role of the *A*-site cation in determining the properties of hybrid perovskite $CH_3NH_3PbBr_3$.
   Sagar Sarkar and Priya Mahadevan.
   Phys. Rev. B **95**, 214118 (2017).

5. Doping a dipole into an incipient ferroelectric: Route to relaxor ferroelectrics.
   N. V. P. Chaudhary*, **Sagar Sarkar***, N. Sharma, A. K. Kundu, K. S. R. Menon, A. Das, P. Mahadevan and A. Venimadhav,
   Phys. Rev. B **96**, 024107 (2017). (*both authors have equal contributions)

6. Mechanism for Ferroelectricity in $PbTiO_3$ and comparison with $BaTiO_3$.
   Sagar Sarkar and Priya Mahadevan
   Manuscript in preparation.

7. Unravelling the charge ordered state in the rare earth nickelates.
   Sagar Sarkar and Priya Mahadevan
   Manuscript in preparation.

8. Hybrid Perovskites under pressure: Revisiting some structural chemistry concepts.
   Sagar Sarkar and Priya Mahadevan
   Manuscript in preparation.

9. Mechanisms to drive an incipient ferroelectric into a ferroelectric.
   Sagar Sarkar and Priya Mahadevan
   Manuscript in preparation.

Contents

Table of Contents **xi**

List of Figures **xx**

List of Tables **xxiii**

1 Introduction **1**

1.1 Perovskite structure and the tolerance factor 3

1.2 Transition metal in a perovskite structure 7

1.2.1 Octahedral crystal field splitting 7

1.2.2 Filling of the d orbitals under crystal field 9

1.2.3 Octahedral distortion : Jahn-Teller effect 12

1.3 Electronic structure of 3d Transition metal compounds 15

1.3.1 On-site coulomb repulsion energy **U** and Hubbard model 15

1.3.2 Charge transfer energy $\mathbf{\Delta}$ 18

1.3.3 The ZSA phase diagram 19

1.4 Properties of Rare earth Nickelates 20

1.4.1 Effect of pressure and strain 23

1.5 Octahedral tilting in Hybrid perovskites 26

1.5.1 Generalized tolerance factor 27

1.5.2 Role of Hydrogen bonding in octahedral tilting 30

1.6 Ferroelectricity due to cation displacement 34

1.6.1 Electric polarization and Dielectric response 35

1.6.2 Ferroelectricity and its origin in perovskite $BaTiO_3$ 42

1.6.3 Displacive phase transition and soft modes 46

2 Theoretical Concepts **59**

2.1 Introduction . . . 61
2.2 Formulation of Density functional theory . . . 62
2.2.1 Many body Schrödinger equation and Born-Oppenheimer Approximation . . . 62
2.2.2 Hartree-Fock(HF) Theory : A wave function based approach . . . 65
2.2.3 Density Functional Theory : From wave function to electron density 71
2.2.4 Approximations for the exchange - correlation Energy $\mathbf{E_{XC}}[\mathbf{n}(\mathbf{r})]$ . . 77
2.3 Numerical Approximations for DFT Calculations . . . 80
2.3.1 Plane Wave Basis and Energy cutoff : . . . 80
2.3.2 Performing K-Space Integrations : . . . 82
2.3.3 Frozen core approximation and Pseudopotential : . . . 83
2.3.4 Projector Augmented Wave(PAW) method : . . . 85
2.4 Introduction to Wannier Functions . . . 86

3 The driving force for charge ordering in rare earth nickelates 93
3.1 Introduction . . . 95
3.2 Methodology . . . 96
3.3 Results and Discussion . . . 98
3.4 Conclusion . . . 109

4 Role of the A-site cation in determining the properties of Hybrid Perovskite $CH_3NH_3PbBr_3$ 115
4.1 Introduction . . . 117
4.2 Methodology . . . 119
4.3 Results and Discussion . . . 120
4.3.1 How does the molecule sit inside the inorganic cage? . . . 120
4.3.2 How does the molecule interact with the inorganic cage? . . . 123
4.3.3 Implications on physical properties . . . 126
4.4 Conclusions . . . 128

5 Hybrid Perovskites under pressure: Revisiting some structural chemistry concepts 133
5.1 Introduction . . . 135
5.2 Methodology . . . 137
5.3 Results and Discussion . . . 138

5.4 Conclusions 145

6 Doping a dipole into an incipient ferroelectric: A route to stabilizing ferroelectricity 151

6.1 Introduction 153

6.2 Methodology 155

6.3 Results and Discussion 156

6.4 Conclusions 161

7 Mechanism for Ferroelectricity in $PbTiO_3$ and comparison with $BaTiO_3$. 167

7.1 Introduction 169

7.2 Methodology 170

7.3 Results and Discussion 170

7.4 Conclusions 177

8 Summary and Conclusions 183

Appendix A 1

A 1

A.1 $a^-b^-c^-$ octahedral tilt pattern 1

A.2 Finding the favored orientation of the molecule inside the cavity 1

A.3 Conformation of the molecule 3

A.4 Fitting of Tight binding and Ab-initio band structure 4

List of Figures

1.1 (a) The unit cell of an ideal cubic perovskite structure where, the B cations sits at the cube corners, anions at the edge center positions and the A cations at the body center position of the cube. (b) Octahedral coordination of the B cation surrounded by 6 anions. (c) A perovskite structure visualized as a corner shared network of BO_6 octahedras with the A cation sitting at the octahedral voids. 4

1.2 Space filling model of a perovskite structure where the atoms are considered as spheres touching each other, showing the relation between (a) the lattice parameter a and ionic radii r_B, r_X; (b) the lattice parameter a and ionic radii r_A, r_X. (c) The ideal cubic perovskite structure with B-X-B bond angles equal to 180^o. (d) Lower symmetry orthorhombic perovskite structure with octahedral tilts showing the deviation of B-X-B bond angles from 180^o. The orthorhombic unit cell is shown with the black lines. . . 4

1.3 (a) A larger atom at the A-site creates excessive internal pressure to break the octahedral connectivity leading to anion deficiency in some of the octahedral units. (b) To conserve the ionic coordination the anion deficient octahedra bends and becomes face shared with the next one. This leads to chains of face shared octahedras along a particular direction separated by the A cations. This is called a 2H perovskite structure. (c) 2H perovskite unit cell of $BaMnO_3$ viewed along the c-axis. 6

1.4 Shape and orientation of the five d orbitals belonging to (a) e_g manifold and (b) t_{2g} manifold under octahedral crystal field. Inset : octahedral crystal field splitting of the five degenerate d orbitals into lower energy t_{2g} and higher energy e_g levels. 8

1.5 (a) The filling of 5 degenerate d orbitals with four electrons according to Hund's rule maximizing total spin **S** and total angular momentum **L**. (b) Filling with a violation of Hund's rule showing double occupancy of the orbitals. (c) A high spin state following Hund's rule for a small crystal field effect. (d) A low spin state for a large crystal field splitting where Hund's rule is no longer valid. 10

1.6 (a) Splitting of the five degenerate d orbitals into t_{2g} and e_g manifold for a regular BX_6 octahedral environment shown in the inset. (b) Splitting of the energy levels within the t_{2g} and e_g manifold for an elongation of the octahedra along the z-direction. (c) Splitting of the energy levels within the t_{2g} and e_g manifold for a compression of the octahedra along the z-direction. 13

1.7 The crystal structure of $KCuF_3$ viewed along the c-axis([001] direction) with (a) out of phase rotations of distorted octahedra between layers along the c-axis; (b) a [001] layer showing the cooperative orbital ordering. Pseudocubic x or y-axis are shown by dotted lines in panel (a). 14

1.8 (a) A model for one-dimensional chain of atoms with a lattice constant a. There is a single orbital per atom that can be occupied by two electrons with opposite spins. No magnetic ordering of the electron spins are considered. (b) A non-interacting picture where electrons can hop from one site to other with a transition probability t. (c) Due to electron-electron correlation the gain from hopping(t) is compensated by the correlation energy **U** at the doubly occupied sites. 16

1.9 (a) A half filled band with band width **W** due to single electrons per site of a 1D chain of atoms. (b) The density of states corresponding to the half filled band. (c) Splitting of the half filled band into Upper and Lower Hubbard band as a result of electron-electron correlation. 17

1.10 (a) Mott-Hubbard insulator for $\mathbf{U} < \mathbf{\Delta}$ where the gap is between two d bands. (b) Charge transfer insulator for $\mathbf{U} > \mathbf{\Delta}$ where the gap is between the ligand p band and the upper Hubbard band. (c) Expected band overlap and a metallic state in the -ve $\mathbf{\Delta}$ region(upper panel) and opening of a gap due to strong $p-d$ hopping(lower panel) . . 18

1.11 (a)The ZSA phase diagram (b) Modified ZSA phase diagram showing the covalent insulating region. 20

1.12 (a) Resistivity vs. Temperature plot showing the metal to insulator transition below $\sim$ 400 K in $SmNiO_3$ thin films(10 nm)[Figure taken from Ref. [38]] (b) Metal-insulator and magnetic transitions as a function of the tolerance factor α for the rare earth nickelates[Figure taken from Ref. [1]] (c) Straightening the Ni-O-Ni bond angle (by increasing rare earth-radius) increases the orbital overlap and stabilizes the metallic state. 21

1.13 Normalized sheet resistance as a function of temperature for $NdNiO_3$ films of different thickness grown epitaxially on $NdGaO_3$ single crystal substrates (tensile lattice mismatch of 1.3%). Inset: evolution of $T_{_{MIT}}$(here $T_{_{MIT}} = T_{_{MI}}$) as a function of film thickness. Epitaxial strain stabilizes the metallic phase and depresses the metal-insulator transition; as the strain is relaxed, the bulk behaviour is progressively recovered.[Figure taken from Ref. [1]] 24

1.14 (a) A typical hybrid perovskite structure where a Methylammonium(MA) molecule is sitting at the A-site, inside the inorganic cage formed by B cation and anions. (b) A schematic representation of the structure of Methylammonium(MA)[upper panel] and Ethylammonium(EA)[lower panel] molecules. 26

1.15 (a) Structure of the Guanidinium $[C(NH_2)_3]$ molecule with the center of mass(CM) at the C atom. r_{mass} and r_{ion} are also mentioned. (b) Schematic of the model considering the anions as rigid cylinders to calculate the tolerance factors of perovskites containing complex molecular anions like $HCOO^-$. 28

1.16 (a) Total orientational disorder of the MA molecule in the cubic phase without any octahedral tilts. The Pb-I-Pb bond angles along all the three cubic directions are 180^o (b) Below 330 K (MA)PbI_3 enters tetragonal phase with octahedral rotations about the *c*-direction, leading to the in-plane(*ab*-plane) Pb-I-Pb bond angles to deviate from 180^o and the molecule is four-fold orientationally disordered around the *c*-axis. (c) Deviation of all the Pb-I-Pb bond angles from 180^o in the orthorhombic phase below 160 K and ordering of the MA molecules. 30

1.17 (a) The ground state (GS) and (b) high symmetry (HS) structures of orthorhombic (MA)PbI_3, composed of PbI_6 octahedra and MA molecules at the octahedral cavity. (c) The energy difference between the HS and the GS structures(E_{HS-GS}) as a function of the tolerance factor for the $APbI_3$ inorganic series (green circles) and (MA)PbI_3 (yellow square). The horizontal error bar in (MA)PbI_3 represent the difference in tolerance factor calculated using the sphere and cylinder methods(see section 1.5.1)[Figures are taken from Ref. [78]]. 32

1.18 (a) The charge distribution of the valence electrons around the ion cores in a covalent solid, in absence and presence of an electric field. In the presence of an electric field, they are shifted with respect to the ion cores and act as a dipole. This gives overall polarization of the material. (b) A 1D NaCl chain. Without any external field, the positions of the ions are such that the dipoles along +ve and -ve *x*-direction cancels each other. But in the presence of an external field, the ions get shifted and there is a net dipole moment per unit cell. (c) The HCl molecule possesses a dipole moment **p** due to the H^+ and Cl^- ions. In the absence of any field, the dipoles are random due to thermal agitation. An external electric field produces a torque on the dipoles and tries to align them with the field direction. (d) A dielectric material between two electrodes with an equal number of positive ions and negative ions. The negative ions can move and with the application of an electric field, they accumulate at the interface near the positive electrode. There is a charge separation with a net polarization 37

1.19 (a) A schematic representation of the frequency dependence of the real($\chi^{'}$) and imaginary($\chi^{''}$) part of dielectric susceptibility in the vicinity of the resonance frequency ω_0 (b) The temperature and frequency dependence of the relative permittivity, $\epsilon_r^{'}$, of $SrFe_{0.5}Ta_{0.5}O_3$ ceramics[Figure taken from Ref. [84]]. The logarithmic scales on each axis shall be noted. (c) The frequency dependence of the real($\epsilon_r^{'}$) and imaginary($\epsilon_r^{''}$) part of dielectric permittivity in the presence of interfacial, orientational, ionic, and electronic polarization mechanisms.[Figure taken from Ref. [85]] 41

1.20 (a) Regular TiO_6 octahedra with the Ti atom surrounded by six oxygen atoms. Possible directions of movement of the Ti atom is shown by the arrows. (b) Location of six potential well minimums along the six Ti-O bonds at a distance δ from the center of the octahedra. (c) Shape of the potential barrier with height ΔU at the center of the octahedra during movement of the Ti ion from one minima to the other. 44

1.21 Tetragonal $BaTiO_3$: (a) The tetragonal unit cell compared to the cubic unit cell (dashed). Tetragonality is along the *c*-axis. (b) Displacements of the Ti and O atoms found in tetragonal $BaTiO_3$; (c) a schematic showing dipole array in tetragonal $BaTiO_3$; (d) schematic of a typical domain structure in a crystal slice. (All distortions are greatly exaggerated)[Figures are taken from Ref. [84]]. 45

1.22 Schematic representations of ferroelectric soft mode behaviour: (a) behaviour of the phonon dispersion curves with temperature. (b) Atomic displacements. [Figures are taken from Ref. [97]] 47

1.23 A typical structural distortion due to zone center phonon softening. For (a) $T > T_c$ and (b) $T < T_c$. 48

1.24 Schematic behaviour of (a) zone boundary acoustic and optic soft modes.(b) Atomic displacements showing doubling of the unit cell and canceling induced dipole moments. [Figures are taken from Ref. [97]] 49

2.1 Total energy per atom of fcc Cu using a 10×10×10 k-points grid as a function of the cutoff energy E_{cut} 81

2.2 Total energy per atom for fcc Cu as a function of N implying a $N \times N \times N$ k-points calculation 83

2.3 Schematic diagram of the Pseudopotential $V^{PS}(r)$ and pseudo-wavefunction $\phi(r)$. The left figure shows valence wave function $\psi(r)$ and Coulomb potential $V^{Coul}(r)$. In the right figure, r_c represents the cutoff radius beyond which the wave function and the potential are not affected.(Taken from, Atomic and Electronic Structure of Solids, E. Kaxiras, Cambridge University Press [37]) 84

3.1 The spin resolved (upper and lower panel) Ni e_g and O p contributions to the density of states for (a) Ni^{2+}, (b) Ni^{4+} sites in $NdNiO_3$ considering the T-type antiferromagnetic structure and U = 4 eV on Ni. 99

3.2 A comparison of the *ab-initio* band structure and the tight binding fit for nonmagnetic $NdNiO_3$ at a $\Delta = 0.81$ eV 100

3.3 Variation in the (a) Ni-O bond lengths and (b) Magnetic moments on the Ni sites with Δ for ferromagnetic $NdNiO_3$ with U = 4 eV. 100

3.4 Variation in the (a) Ni-O bond lengths and (b) Magnetic moments on the Ni sites with Δ_{eff} for ferromagnetic $NdNiO_3$ with U = 4 eV. 101

3.5 Schematic indicating the definitions Δ and Δ_{eff} used in the text. While a positive Δ_{eff} has uniform NiO_6 octahedra, a negative Δ_{eff} leads to transfer of holes to the oxygen p bands and occurrence of a breathing distortion of the NiO_6 octahedra. 102

3.6 Δ_{eff} calculated for all the rare earth nickelates with U = 2 eV on Ni sites. 103

3.7 (a) The E′ type non-collinear antiferromagnetic ordering of the Ni moments. (b) Ni-O bond lengths and Ni-O-Ni bond angles of Ni^{2+} and Ni^{4+} along the three pseudo cubic directions for non-strained $NdNiO_3$. (c) Effective collinear type antiferromagnetic ordering of the Ni^{2+} moments in the optimized structures of both strained and non-strained $NdNiO_3$. (d) Ni-O bond lengths and Ni-O-Ni bond angles of Ni^{2+} and Ni^{4+} along the three pseudo cubic directions for strained $NdNiO_3$. 104

3.8 2 monolayer case : (a) Schematic showing the two monolayers of $NdNiO_3$ on $NdGaO_3$ substrate. (b) Ni-O bond lengths and (c) the in-plane(*ab*-plane) Ni-O-Ni bond angles after structural optimization. The magnetic moments associated with each of the Ni atoms are also mentioned. (d) Non-collinear type antiferromagnetic ordering of the Ni moments in the single NiO_2 layer. 106

3.9 3 monolayer case : (a) Schematic showing the three monolayers of $NdNiO_3$ on $NdGaO_3$ substrate. (b) Ni-O bond lengths and (c) the in-plane(*ab*-plane) Ni-O-Ni bond angles after structural optimization. The magnetic moments associated with each of the Ni atoms are also mentioned. (d) Non-collinear type antiferromagnetic ordering of the Ni moments in the single NiO_2 layer. 106

3.10 4 monolayer case : (a) Schematic showing the four monolayers of $NdNiO_3$ on $NdGaO_3$ substrate. (b) Ni-O bond lengths and (c) the in-plane(*ab*-plane) Ni-O-Ni bond angles in the two NiO_2 layers after structural optimization. The magnetic moments associated with each of the Ni atoms are also mentioned. (d) Non-collinear type antiferromagnetic ordering of the Ni moments in the two NiO_2 layers. 107

3.11 5 monolayer case : (a) Schematic showing the five monolayers of $NdNiO_3$ on $NdGaO_3$ substrate. (b) Ni-O bond lengths and (c) the in-plane(*ab*-plane) Ni-O-Ni bond angles in the two NiO_2 layers after structural optimization. The magnetic moments associated with each of the Ni atoms are also mentioned. 108

3.12 6 monolayer case : (a) Schematic showing the six monolayers of $NdNiO_3$ on $NdGaO_3$ substrate. (b) Ni-O bond lengths in the three NiO_2 layers after structural optimization. The magnetic moments associated with each of the Ni atoms are also mentioned. . . . 109

4.1 Bird's eye view in the *ac*-plane of (a)orthorhombic unit cell of $MAPbBr_3$ without any octahedral tilts, (b) experimental orthorhombic cell. (c) Top: An alternate orientation of the molecule along a body diagonal of the cavity shown by the dotted line was considered, its projection on the *ac*-plane is shown by solid line. Bottom: Orientation in the optimized structure. 121

4.2 (a)Position of the molecule at the center of the ideal cavity(upper panel) and corresponding H-Br bonds(lower panel). (b) Movement of the molecule from the center of the cage shown by dotted line(upper panel) and increased hydrogen bonding after the movement(lower panel) compared to the ideal case shown in Figure 2(a). (c) Distorted cavity due to octahedral tilts(upper panel) and corresponding hydrogen bondings(lower panel). The hydrogen atoms in the NH_3 and CH_3 group are indicated by light(green) and dark(black) circles respectively. Distance between H atoms of NH_3 and Br atoms less than 3.0 Å are shown by solid green lines. The numbers denote the corresponding distances in Angstroms. 123

4.3 (a) The tight-binding(circles) and *ab-initio*(solid line) band structure of optimized $MAPbBr_3$ for case3. (b) Schematic showing how the molecule interacts with the inorganic cage. There is stronger covalent interaction between the methyl group and Br atoms whereas it is largely electrostatic in nature between amine group and Br atoms. (c) As a result of this asymmetric interaction the molecule move towards one direction and Br atoms may also be displaced towards the molecule, giving rise to octahedral tilts. 124

4.4 (a) The spatial distribution of the Wannier functions(WFs) of the hydrogens attached to the N atom (b) The spatial distribution of the two hydrogen WFs attached to the C atom with smaller spread and (c) having the largest spread with the Wannier center(shown by black dot) moving away from the C-H bond. The matrix elements(MEs) corresponding to the interactions of these basis functions with Br are also specified. An isosurface value equal to half the maximum value was used to make these plots. 126

4.5 (a) The change in the energy as a function of the rotation(in *ac*-plane) angle of the molecule. The angle θ is shown in the inset. The optimized structure for the two minimum energy configurations where C-N axis makes an angle (b) $\sim 12^o$ (configuration A) and (c)$\sim 28^o$ (configuration B) with the (101) direction 127

5.1 (a) Band gap variation as a function of uniform volume change about the experimental volume and with a fixed angular distortion of the optimized structure. (b) Variation in the band gap as function of angular distortion with fixed unit cell volume. (c) Increased band gap due to an decreased bonding-antibonding splitting as a result of increased Pb-X bond length. (d) Decreased band gap due to an increased bandwidth as a result of decreased angular distortion. 140

5.2 Pb-Br bond lengths and Pb-Br-Pb bond angles along the three pseudocubic directions in the optimized structures of $CsPbBr_3$ for (a) 4% volume compression (b) experimental volume and (c) 4% volume expansion. 141

5.3 Band gap variation in $MAPbBr_3$. *Circle* : Band gap variation as a function of uniform volume change about the experimental volume and with a fixed angular distortion of the optimized structure. *Square* : Band gap variation as a function of uniform volume change about the experimental volume and with an allowed structural optimization. *Triangle* : Difference plot. 142

5.4 Pb-Br bond lengths and Pb-Br-Pb bond angles along the three pseudocubic directions in the optimized structures of $MAPbBr_3$ for (a) 4% volume compression (b) experimental volume and (c) 4% volume expansion. 143

5.5 (a) Position of the MA molecule inside the octahedral cavity and its translational, orientational degrees of freedom in the *ac*-plane. Pb-Br bond lengths and Pb-Br-Pb bond angles along the three pseudocubic directions in the optimized structures with optimized volume of (a) $MAPbBr_3$ and (b) $EAPbBr_3$. Insets: Conformation of the MA and EA molecules. 144

6.1 Upper panel : Tetragonal unit cell of TiO_2. (a) No ferroelectric distortion or off-centering of the Ti atom in the relaxed experimental unit cell. (b) Off-centering of the Ti atom in the relaxed unit cell with an initial ferroelectric distortion. Lower panel : Two possible doping configuration among many others where Nb, Cr replaces (c) two nearest neighbor Ti atoms in the first case, and (d) two next nearest neighbor Ti atoms in the second case. 156

6.2 The calculated up (solid line) and down (dashed line) spin projected (a) Ti d, (b) Cr d, and (c) Nb d partial density of states at 5% of doping. The Ti atom which is just above the Cr atom is the one for which the density of states is shown. The transition metal(TM)-oxygen bond lengths of the $(TM)O_6$ octahedra are shown in the insets. . . 157

6.3 The calculated up (solid line) and down (dashed line) spin projected (a) Mn d and (b) Zr d partial density of states at 2.5% of doping. The transition metal-oxygen bond lengths of the (TM)O_6 octahedra are shown in the insets. 159

6.4 (a) Ti-dopant distances for different doping cases. For Nb-Cr co-doping there is a deliberate breaking of inversion symmetry with different Cr-Ti and Nb-Ti distances along c-axis. Whereas when we dope only Mn or Zr in the system, there is no inversion symmetry breaking. However for Zr-Mn co-doping there is similar inversion symmetry breaking like Nb-Cr co-doping. (b) For 5% Zr-Mn co-doping, instead of inversion symmetry breaking no off-centering of the metal atoms in the (TM)O_6 octahedra was observed. Zr-O, Mn-O and Ti-O bond lengths are shown. (c) Schematic representation of the doped Nb-Cr pair acting as a dipole and the polarization in the nearby TiO_6 octahedra. 160

6.5 Doping of two Nb-Cr pair for 10% doping with two situations. (a) Clustering and (b) non-clustering of the two doped dipoles. For the non-clustering case, the two doped dipoles are separated by a distance of $\sim$ 6.50 Å. 161

7.1 Experimental tetragonal unit cell of $BaTiO_3$. (a) Displacement of atoms from their ideal positions (b) unequal Ti-O bond lengths due to ferroelectric distortions. 171

7.2 Total energy variation with (a) Ti displacement and (b) Apical-O displacement from their ideal position in the ideal perovskite structure. Figures plotted with the data taken from Ref. [9] 172

7.3 Hartree energy variation with (a) Ti displacement and (b) apical oxygen displacement from their ideal positions in the ideal perovskite structure. (c) Displacement of planar oxygens from their ideal face-centered positions in the experimental structure of $BaTiO_3$. The displacements are along the c-axis and away from the Ti atom. Figures plotted with the data taken from Ref. [9] 173

7.4 Experimental tetragonal unit cell of $PbTiO_3$. (a) Displacement of atoms from their ideal positions (b) unequal Ti-O bond lengths due to ferroelectric distortions. 174

7.5 Total energy variation with (a) Ti displacement and (b) Apical-O displacement from their ideal position in the ideal perovskite structure. 175

7.6 Hartree energy variation with (a) Ti displacement and (b) apical oxygen displacement from their ideal positions in the ideal perovskite structure. 175

7.7 Unit cell dimension and tetragonality of the (a) $BaTiO_3$ and (b) $PbTiO_3$ unit cell with the atoms sitting in their ideal positions. (c) Total energy variation with Ti displacement towards apical oxygen in $BaTiO_3$ with the experimental lattice parameters of $PbTiO_3$. 176

A.1 $a^-b^-c^-$ octahedral tilt pattern viewed along the b-axis when the system was relaxed with a molecular orientation along the body diagonal of the cavity as shown in the upper panel of Figure 4.1(c) of chapter 4. 1

A.2 (a) Two anionic planes corresponding to the two possible orientations of the molecule and the relevant H_N-Br distances after the molecule was relaxed are shown for orientation of the molecule towards (b) plane 1 and (c) plane 2. The hydrogen bonds less than 3Å are shown with solid green lines. 2

A.3 (a) Distance between the amine part(nitrogen atom) of the molecule and the corresponding anion plane after the molecule was relaxed with an orientation towards (a) plane 1 and (b) plane 2. 2

A.4 (a) Ferroelectric and antiferroelectric stacking of the molecular dipoles along the *b*-axis. (b) Orthogonal arrangement of the dipoles in the *ac*-plane 3

A.5 The fitting of tight-binding and ab-initio band structure for (a) case1, where the molecule is at the center of the cavity without any octahedral tilts. (b) case2, where the molecule is allowed to move for maximum hydrogen bonding. 4

List of Tables

1.1 Effective ionic radii of molecular cations(taken from Ref. [11]). Ionic radii for the inorganic ions were used from Ref. [12] 28

1.2 Tolerance factor of some important hybrid perovskite systems calculated using the generalized approach [11]). The effective ionic radii for the inorganic ions were taken from Ref. [12] 29

4.1 Quantitative analysis of the covalent interaction between hydrogen and Br atoms 125

4.2 Spread of the wannier functions of the hydrogens attached to N and C atoms in the optimized structure 125

Chapter 1

Introduction

General Intruduction

Structure and electronic properties of any material are strongly correlated. Electronic properties can be tuned by varying the parameters that can induce changes in the structure of the material [1–5]. For example, considering the well known perovskite nickelates with the general formula $RNiO_3$ where R = Lu to La, is a rare earth atom, it has been observed that changing the rare earth atom can induce changes in the electronic structure of the system. The system can behave as an insulator or metal, with a variation in the temperature at which the metal to insulator transition occurs [6–8]. This happens as a result of structural changes that occurs when one changes the rare earth atom. This suggests that we can tune the electronic properties via structural modulations, and to efficiently do that we need to understand the structure-property correlation in details. For this, we have to know the electronic structure and crystal structure of the material. Rare earth nickelates belong to the family of $3d$ transition metal compounds with a perovskite structure. In this thesis, we work with systems mainly having a perovskite structure or perovskite related structure. So, we start by giving a brief description of the perovskite structure and the common structural distortions that it can undergo.

1.1 Perovskite structure and the tolerance factor

Perovskite materials having a simple crystal structure has played an important role in understanding the microscopic interactions leading to interesting electronic properties in many compounds. Perovskite materials are materials with a crystal structure related to the mineral Calcium titanate($CaTiO_3$) with general formula ABX_3, where A and B are cations and X is an anion. For example, in case of rare earth nickelates($RNiO_3$), a rare earth atom R sits at the A-site, Ni sits at the B-site and the anion is oxygen.

If we consider the unit cell as a cube(for example in $SrTiO_3$), then as shown in Figure 1.1(a), the B cation sits at the cube corners, the anions at the edge center positions and the A cation at the body center position. The B cation has an octahedral coordination surrounded by 6 anions[see Figure 1.1(b)]. Together they form a corner sharing octahedral network with the A cations sitting at the octahedral voids coordinated by 12 anions[Figure 1.1(c)]. The BX_6 octahedra[Figure 1.1(b)] in perovskite materials act as an important and fundamental functional unit to tune material properties [9]. The B-X bond lengths(size and shape of the octahedra) and the B-X-B bond angles are the basic structural parameters that can be varied to tune the electronic properties. For an ideal cubic perovskite structure($SrTiO_3$), the B-X-B bond angles are 180^o as shown in Figure

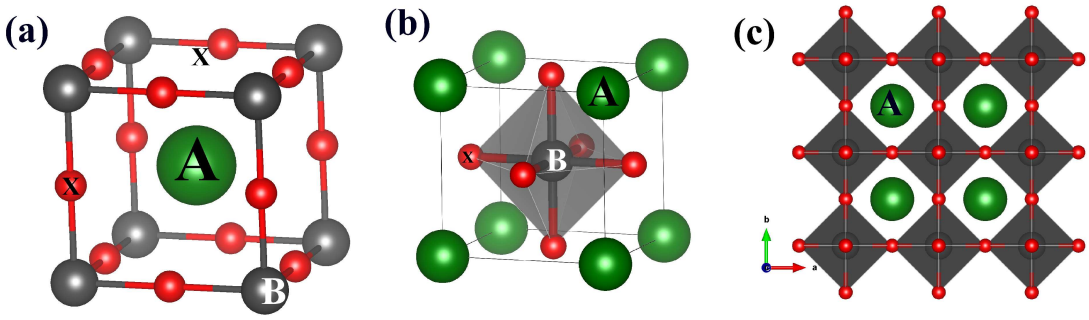

Figure 1.1: (a) The unit cell of an ideal cubic perovskite structure where, the B cations sits at the cube corners, anions at the edge center positions and the A cations at the body center position of the cube. (b) Octahedral coordination of the B cation surrounded by 6 anions. (c) A perovskite structure visualized as a corner shared network of BO_6 octahedras with the A cation sitting at the octahedral voids.

1.2(c). However, most of the perovskite materials have distorted perovskite structure with octahedral tilting and rotations, where the B-X-B bond angles deviate from 180^o leading to unit cells having lower symmetry.

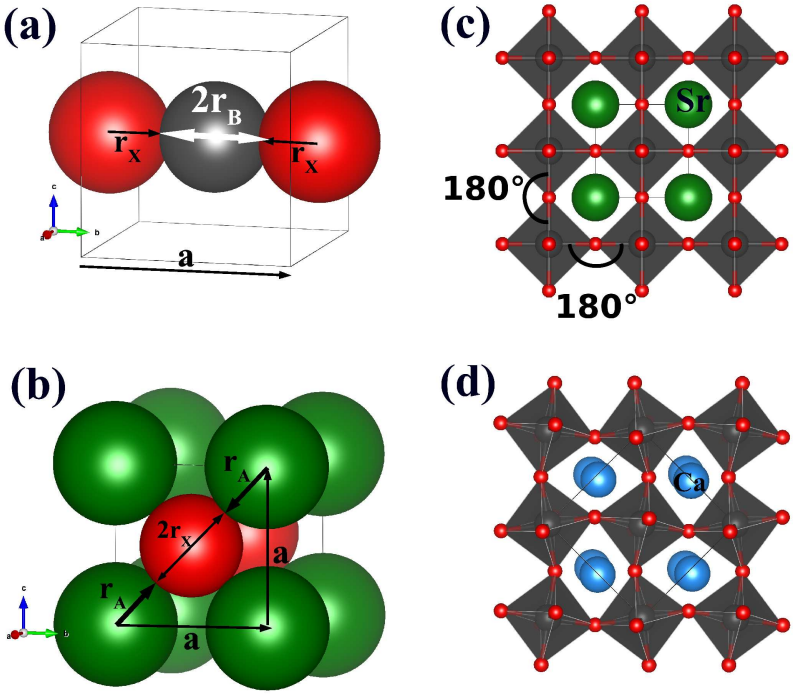

Figure 1.2: Space filling model of a perovskite structure where the atoms are considered as spheres touching each other, showing the relation between (a) the lattice parameter a and ionic radii r_B, r_X; (b) the lattice parameter a and ionic radii r_A, r_X. (c) The ideal cubic perovskite structure with B-X-B bond angles equal to 180^o. (d) Lower symmetry orthorhombic perovskite structure with octahedral tilts showing the deviation of B-X-B bond angles from 180^o. The orthorhombic unit cell is shown with the black lines.

These structural distortions have been understood in terms of an empirical factor known as the Goldschmidt tolerance factor (α) [10]. Considering the idea of dense ionic packing where the ions are considered as solid spheres touching each other [see Figs. 1.2(a) and (b)], the lattice parameter a of an ideal cubic perovskite is related to the ionic radii r_A, r_B and r_X by the equations.

$$a = \sqrt{2}(r_A + r_X) \quad (1.1)$$

$$= 2(r_B + r_X) \quad (1.2)$$

The ratio,

$$\alpha = \frac{(r_A + r_X)}{\sqrt{2}(r_B + r_X)} \quad (1.3)$$

is called the tolerance factor that gives an estimate of the propensity of octahedral rotations in perovskites. For values of α in the range 0.9 - 1.0, one usually finds cubic perovskites, whereas values of 0.80 - 0.89 due to a smaller A cation or larger B cation predominantly leads to distorted perovskites with octahedral tilting [11]. This can be understood qualitatively considering basic electrostatic interactions. For example, a smaller size of the A cation reduces the unit cell volume. This makes the B-X distances shorter, leading to an increased Coulomb repulsion between electrons on B and those on X. This increased Coulomb repulsion can be compensated by an octahedral tilting that prevents further decrease in the B-X bond lengths and results in B-X-B angles to deviate from 180°. This in turn makes the A-X distances shorter. Considering the effective ionic radii(Shannon model [12]) of Sr^{2+}, Ti^{4+} and O^{2-} to be 1.44, 0.60 and 1.42 Å, for $SrTiO_3$ having an ideal cubic structure, gives a value of $\alpha = 1.0$. But in $CaTiO_3$, Ca^{2+} having an effective ionic radii of 1.12 Å gives $\alpha = 0.88$. This leads to octahedral tilting with an orthorhombic unit cell as shown in Figure 1.2(d).

However, whether a reduction in unit cell volume would be accommodated entirely by the B-X bond compression or octahedral tilting, depends on the relative compressibilities of the BX_6 and AX_{12} units. Combined experimental and theoretical study [13] on the well-known perovskite $CaSnO_3$, shows that similar compressibilities of the SnO_6 and CaO_{12} units would result in a change of the Ca-O and Sn-O bond lengths with uniform pressure, without any angular distortions. On the other hand almost rigid SnO_6 and CaO_{12} units shall lead to angular distortions dominantly. But experimental observations suggest that a “rigid unit” approach is inappropriate, and a higher compressibility of the CaO_{12} unit

compared to SnO_6 makes the Sn-O-Sn bond angle change drastically with pressure from the very beginning, compared to the Sn-O bond length.

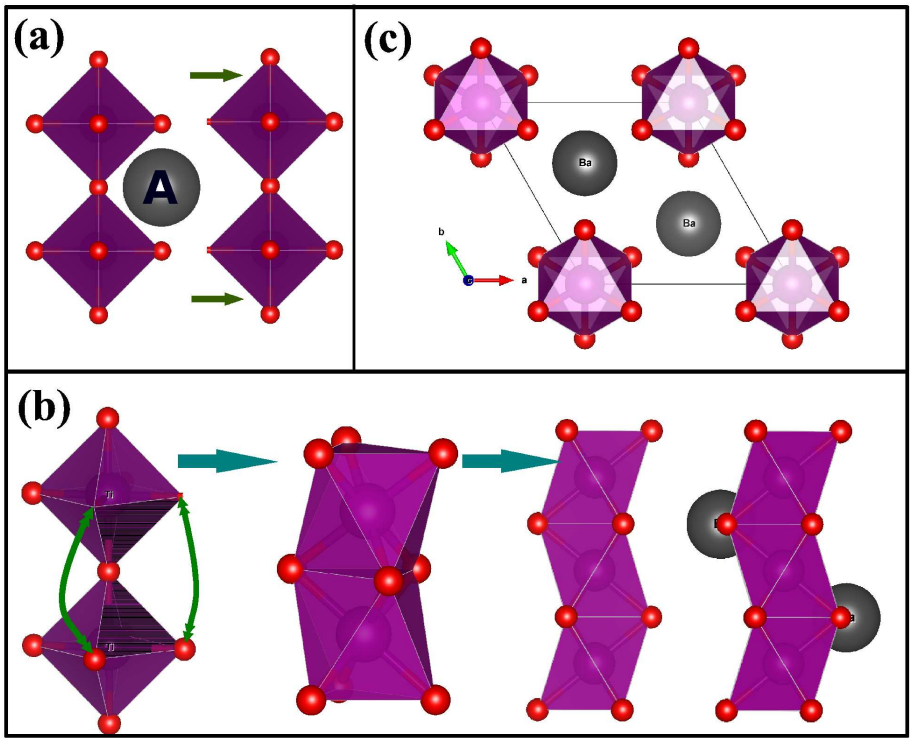

Figure 1.3: (a) A larger atom at the A-site creates excessive internal pressure to break the octahedral connectivity leading to anion deficiency in some of the octahedral units. (b) To conserve the ionic coordination the anion deficient octahedra bends and becomes face shared with the next one. This leads to chains of face shared octahedras along a particular direction separated by the A cations. This is called a 2H perovskite structure. (c) 2H perovskite unit cell of $BaMnO_3$ viewed along the c-axis.

On the other hand if $\alpha > 1$ as a result of large A or a small B cation, then low dimensional hexagonal variants of the perovskite structure forms. A larger size of the A cation can give rise to an excessive internal pressure that can break the corner shared octahedral network [see Figure 1.3(a)] leading to anion vacancies in some of the octahedra. Now to conserve the ionic coordination, octahedra with fewer anions bend and become face shared with the other one as shown in Figure 1.3(b). This leads to parallel chains of face shared octahedras separated by the A cation. This structure is called a 2H perovskite structure. For example $BaMnO_3$ is predicted to adopt a 2H perovskite structure [14] with $\alpha = 1.06$ Å [see Figure 1.3(c)].

But we must remember that all transition metal compounds are not purely ionic, so for transition metal compounds with a perovskite structure, the tolerance factor can only give a rough estimate. By transition metal compounds we mean crystalline solids where the unit cell must contain one or more transition metal atoms and one or more nonmetal elements from group $VIIA$ (O, S or Se), also called ligands. Other atoms may also be

present, for example the rare earth atom(R = Lu to La) in the rare earth nickelates. But they generally take part in structural stabilization without any direct contributions to the electronic properties. One of the important properties of transition metal elements is their possible multiple valence states. In an isolated atom the atomic shells defined by quantum number n are filled one after another. But starting from $n = 3$, the filling scheme changes [15]. After the $3s$ and $3p$ shells are occupied, $4s$ shell gets filled first before $3d$. After that the energy levels of the inner $3d$ shell starts to fill producing the $3d$ transition metal series, from Sc to Cu and then the $4p$ states are occupied. Quite similar thing happens for the $4d$ and $5d$ series. As $3d$ and $4s$ electrons lie close in energy, the s electrons together with some of the inner shell d electrons can participate in bonding. This leads to multiple valence of transition metal atoms in compounds. For example Ti can have 2+, 3+, 4+ oxidation states. This is why transition metals can act as good catalysts in a chemical reaction where it can easily give or take electrons to the reagent depending on the nature of the reaction [16]. Multiple valences leads to many possible electron configurations and as a result the bonding in transition metal compounds ranges from ionic to covalent along with a wide range of possible crystal structure. For example the compound NiO(Nickel(II) oxide) with Ni^{2+} has a rock salt structure and is strongly ionic. Whereas rare earth nickelates($RNiO_3$) with Ni^{3+} have a perovskite structure and the bonding is believed to be of mixed character [17]. When we focus on any transition metal compound where the atom is now in a crystal structure, we also need to consider the effect of the crystal structure on the transition metal atom. Now the symmetry of the atom is determined by the local symmetry of the crystal structure and renormalization of the isolated atomic energy levels takes place. In this context now let us consider the effects and properties of the perovskite structure with a transition metal atom.

1.2 Transition metal in a perovskite structure

1.2.1 Octahedral crystal field splitting

When the transition metal atom is in a crystal, we also need to consider the effect of the crystal structure on the transition metal atom. An isolated transition metal atom has a spherical symmetry and all the five d orbitals are energetically degenerate. Now, if we consider a negatively charged sphere with uniform charge distribution around a transition metal atom, the energy of the d orbitals increases due to coulomb repulsion between the electrons in the d orbitals and negative charge on the surrounding sphere. But they still remain energetically degenerate as a result of the spherical symmetry. Now

in a crystal structure, this spherical symmetry is lost and the symmetry is determined by the local symmetry of the crystal structure. For example, as shown in Figure 1.1(b), for a perovskite structure the transition metal atom is surrounded by six negatively charged anions/ligands(X) forming an octahedron. Their effect on the transition metal atom can be understood using crystal field theory, a model to understand the effect of the electric field produced by the surrounding anions on the transition metal atom. In this model, the ligands are replaced by negative point charges and the interaction between the electrons on the transition metal atom and ligand is considered to be purely electrostatic.

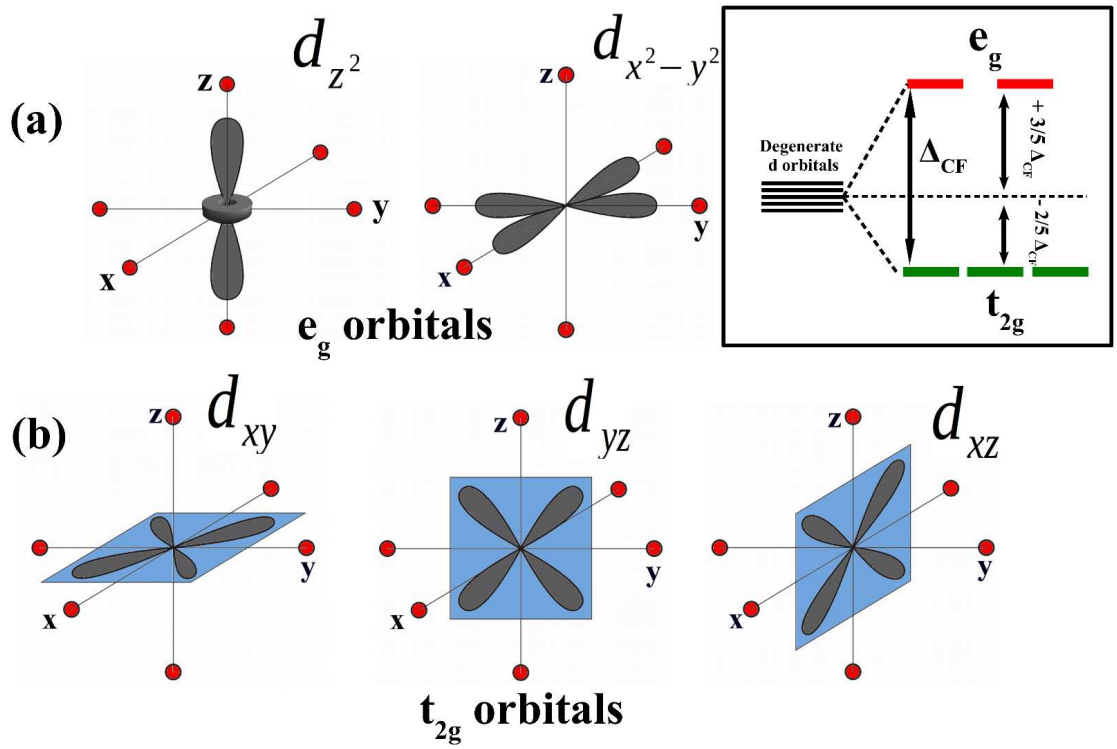

Figure 1.4: Shape and orientation of the five d orbitals belonging to (a) e_g manifold and (b) t_{2g} manifold under octahedral crystal field. Inset : octahedral crystal field splitting of the five degenerate d orbitals into lower energy t_{2g} and higher energy e_g levels.

Figure 1.4 shows a schematic representation of the charge density distribution corresponding to the five d orbitals of a transition metal atom. Considering an ideal cubic perovskite with lattice constant a, all the orbitals are surrounded by six point charges(shown as red dots representing the ligands) located at $+\frac{a}{2}\hat{i}$, $-\frac{a}{2}\hat{i}$, $+\frac{a}{2}\hat{j}$, $-\frac{a}{2}\hat{j}$, $+\frac{a}{2}\hat{k}$ and $-\frac{a}{2}\hat{k}$ respectively. From the schematic it is clear that all the d orbitals will not interact with the point charges equally. $d_{3z^2-r^2}$(later we use d_{z^2} to represent $d_{3z^2-r^2}$ for simplicity) and $d_{x^2-y^2}$ have lobes along the axis and pointed directly towards the ligands, hence experiencing strong coulomb repulsion[Figure 1.4(a)]. In contrast d_{xy}, d_{yz} and d_{xz} have their charge

densities distributed between the point charges resulting in a weaker coulomb repulsion. As a result the energy of d_{z^2} and $d_{x^2-y^2}$ becomes higher compared to d_{xy}, d_{yz} and d_{xz}. This lifts the degeneracy of the five d orbitals into two groups: Together, the two degenerate d_{z^2} and $d_{x^2-y^2}$ orbitals with higher energy are called e_g and three degenerate d_{xy}, d_{yz} and d_{xz} orbitals with lower energy are called t_{2g} orbitals respectively. Such nomenclature comes from group theory and the corresponding splitting between them(Δ_{CF}) is called the crystal field splitting [15][see inset of Figure 1.4]. If we consider the center of gravity of these levels to remain unchanged and taken as zero, then the t_{2g} states are stabilized by an energy $E_{t_{2g}} = -\frac{2}{5}\Delta_{CF}$ and the e_g states are destabilized by an energy $E_{e_g} = +\frac{3}{5}\Delta_{CF}$.

The splitting of the d levels depends on the coordination of the transition metal atom. If the coordination deviates from a regular octahedron then the splitting shall change. For example, in case of tetrahedral coordination, the e_g states become lower in energy compared to the t_{2g} states with a lower splitting energy. We are not going to discuss those in detail here, but the crystal field splitting makes the atomic descriptions invalid in any crystalline system. In the next part, we discuss how crystal field splitting affects the filling of the d orbitals compared to an isolated atom.

1.2.2 Filling of the d orbitals under crystal field

As a result of a crystal field splitting, the order of filling of the d orbitals changes compared to what we have for an isolated atom. In an isolated atom, filling of the five degenerate d orbitals follow certain rules called the Hund's rule [18]. The most important of them is the first rule which states that, for any number of electrons the filling shall be in such a way as to maximize the total spin($\mathbf{S}$) of the system. For example, if there are four electrons, then four d orbitals shall be singly occupied with parallel spin as shown Figure 1.5(a). Which four of the five d orbitals shall be occupied is specified by the second Hund's rule. The four d orbitals that maximize the total angular momentum($\mathbf{L}$) shall be occupied. This gives a total spin $|\mathbf{S}| = 2$. So, according to first Hund's rule, double occupancy of the orbitals cannot start from the beginning as shown in Figure 1.5(b) which shall give $|\mathbf{S}| = 0$. The microscopic origin of this rule is the electron-electron coulomb repulsion between two electrons in an atom. Occupying different orbitals reduces the overlap between electronic charge as the spatial extent of their wave functions are different. This reduces the Coulomb repulsion. In addition to this, two electrons on different orbitals minimizes screening effect leading to stronger attraction between the nucleus and electrons. Again as electrons are fermions, according to Pauli principle electrons with parallel spins avoid each other and

as a result Coulomb repulsion can be further reduced. This decreases the total energy of the spin system and favors parallel spin arrangement of single occupied orbitals.

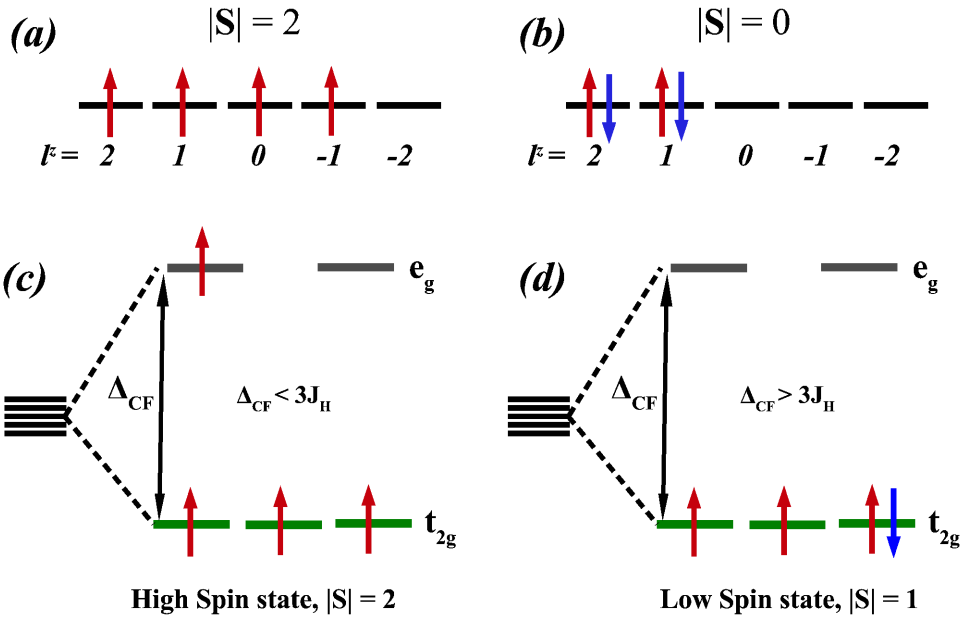

Figure 1.5: (a) The filling of 5 degenerate d orbitals with four electrons according to Hund's rule maximizing total spin **S** and total angular momentum **L**. (b) Filling with a violation of Hund's rule showing double occupancy of the orbitals. (c) A high spin state following Hund's rule for a small crystal field effect. (d) A low spin state for a large crystal field splitting where Hund's rule is no longer valid.

A quantum mechanical treatment of the electron-electron interaction within the same shell of a single atom, allow us to write the interaction energy in terms of an effective spin Hamiltonian given as [18] :

$$H_{exch} = -J_{\alpha\beta} \sum_{\alpha \neq \beta} (2\mathbf{S}_\alpha.\mathbf{S}_\beta + \frac{1}{2}) + constant \tag{1.4}$$

H_{exch} is called the exchange Hamiltonian(Please note that this is not the Heisenberg Hamiltonian that represents inter-atomic exchange). $\mathbf{S}_\alpha$ and $\mathbf{S}_\beta$ indicates the spin of the electrons in orbitals α and β respectively which can either be $+1/2$ or $-1/2$. $J_{\alpha\beta}$ is the intra-atomic Hund's exchange interaction energy between two electrons in orbitals α and β. Exchange energy is a quantum mechanical manifestation of the electron-electron Coulomb repulsion having no classical counterpart(see section 2.2 of chapter 2 for details). Within the same atom and same atomic shell, we can treat $J_{\alpha\beta}$ to be identical for any pair of orbitals and is denoted as J_H. The above Hamiltonian simply says that each pair of d electrons with parallel spins gives a contribution of $-J_H$ to the total energy of the spin system. For example, the spin arrangements shown in Figure 1.5(a) and (b) gives a

Hund's energy of $-6J_H$ and $-2J_H$ respectively, making the first configuration to dominate over the other. Typical values of J_H for transition metals are $J_H \sim 0.8$ - 0.9 eV for $3d$, $J_H \sim 0.6$ - 0.7 eV for $4d$, and $J_H \sim 0.5$ eV for $5d$ elements. This is because J_H depends on higher moments of Coulomb interactions ($F^2 + F^4$) [19], which decreases because the orbitals become more delocalized as we go from $3d$ to $4d$ to $5d$. However screening effects are larger in $4d$, $5d$ transition metal compounds and hence their values further reduces when they form compounds.

The rules for filling the isolated atomic levels change when there is crystal field splitting. For a transition metal atom in an octahedral environment, the three lowest energy t_{2g} levels are occupied first with 3 electrons having parallel spins following first Hund's rule. But for the fourth electron, there are two possibilities. It can either occupy one of the degenerate e_g levels as shown in Figure 1.5(c), or it can occupy one of the preoccupied t_{2g} level with an opposite spin as shown in Figure 1.5(d). For the first case[Figure 1.5(c)], the spin of the e_g electron becomes parallel with the spin of the 3 t_{2g} electrons. This gives a Hund's energy gain of $-3J_H$, but to occupy the higher energy e_g levels there is an energy cost of Δ_{CF}. In the second case[Figure 1.5(d)] the electron is in the t_{2g} manifold, so there is no cost of Δ_{CF} but we lose the Hund's energy gain of $-3J_H$. Now if we assume that the total electron-electron Coulomb repulsion energy between two electrons is independent of the d orbitals occupied, then there is a competition between J_H and Δ_{CF}. If the crystal field splitting is not too large and,

$$\Delta_{CF} < 3J_H \tag{1.5}$$

then the first state is favored where the total spin is maximum, $|\mathbf{S}| = 2$. This is called a high spin state. But if the crystal field splitting is large enough to satisfy the criterion,

$$\Delta_{CF} > 3J_H \tag{1.6}$$

then the fourth electron occupies one of the t_{2g} levels and the second state with $|\mathbf{S}| = 1$ is favored. Such spin states are called low spin states.

As we go from $3d$ to $4d$ to $5d$, the value of J_H decreases, whereas the crystal field, splitting(Δ_{CF}) increases due to larger spread of the $4d$ and $5d$ orbitals compared to $3d$ orbitals. So, in general for $3d$ transition metal perovskites a high spin state and for $4d$ and $5d$ compounds a low spin state shall be favored. For example, $3d$ ion $Mn^{3+}(d^4)$ is usually in the high spin state($t_{2g}^3 e_g^1$) with $|\mathbf{S}| = 2$[Figure 1.5(c)], whereas it's $4d$ counterpart $Ru^{3+}(d^4)$ is typically in the low spin state($t_{2g}^4 e_g^0$) with $|\mathbf{S}| = 1$ [15] [Figure 1.5(d)].

However, exceptions are there because the crystal field splitting directly depends on the transition metal-ligand interaction, which is controlled by the crystal structure and electronic structure of the system. For example, $Cu^{2+}(d^9)$ in perovskite $KCuF_3$ is in a low spin state($t_{2g}^6 e_g^3$) due to large Δ_{CF} as a result of larger spread of the F p states.

1.2.3 Octahedral distortion : Jahn-Teller effect

Till now we have explained the origin of octahedral rotations and effect of the octahedral crystal field on the transition metal atom/ion sitting at the B-site. In the above cases, we have considered ideal regular octahedra with six equal B-X bond lengths where the transition metal atom have a cubic symmetry. However octahedral distortions reduce the cubic symmetry further and can act as a perturbation on the t_{2g} and e_g levels. One of the most important types of octahedral distortion in perovskites is the Jahn-Teller distortion. These distortions occur due to the Jahn-Teller effect, which was first observed in nonlinear molecules. The Jahn-Teller theorem [20] essentially states that, a nonlinear molecule in an electronically degenerate state must undergo a structural distortions to remove the degeneracy and lower the energy of the system. Any localized system with a degenerate electron configuration lowers energy via such structural distortions and removes the degeneracy. Presence of a transition metal ion at the center of the octahedra with a degenerate electron configuration makes it Jahn-Teller active and the octahedra distort to remove the degeneracy. By a degenerate electron configuration, we mean that there is more than one way to fill the d orbitals. For example, $Mn^{3+}(d^4)$ in the high spin state($t_{2g}^3 e_g^1$) has a single electron in the e_g levels[Figure 1.5(c)]. This single electron can occupy either the d_{z^2} or $d_{x^2-y^2}$ giving two degenerate energy configurations $t_{2g}^3 d_{z^2}^1 d_{x^2-y^2}^0$ and $t_{2g}^3 d_{x^2-y^2}^1 d_{z^2}^0$. This makes Mn^{3+} a Jahn-Teller active ion. Other examples are $Ni^{3+}(d^7)$ in a low spin state($t_{2g}^6 e_g^1$), $Cu^{2+}(d^9)$ in a low spin state($t_{2g}^6 e_g^3$) etc. An elongation[inset of Figure 1.6(b)] or compression[inset of Figure 1.6(c)] of the regular octahedra along one of the octahedral axis further lifts the degeneracy within the t_{2g} and e_g manifold, killing the possibility of any degenerate energy configuration.

This can be qualitatively understood from the knowledge of the crystal field splitting. Considering the octahedral volume to remain constant, an elongation in the z-direction[inset of Figure 1.6(b)] increases the transition metal-ligand distance in that direction, whereas the transition metal-ligand distance along the x and y-direction decreases. This lowers the energy of the d_{z^2} orbital which has dominant electron distribution along the z-direction[see Figure 1.4(a)]. On the other hand energy of $d_{x^2-y^2}$ increases as it has charge density along the x and y-directions. A quite similar thing happens to the t_{2g}

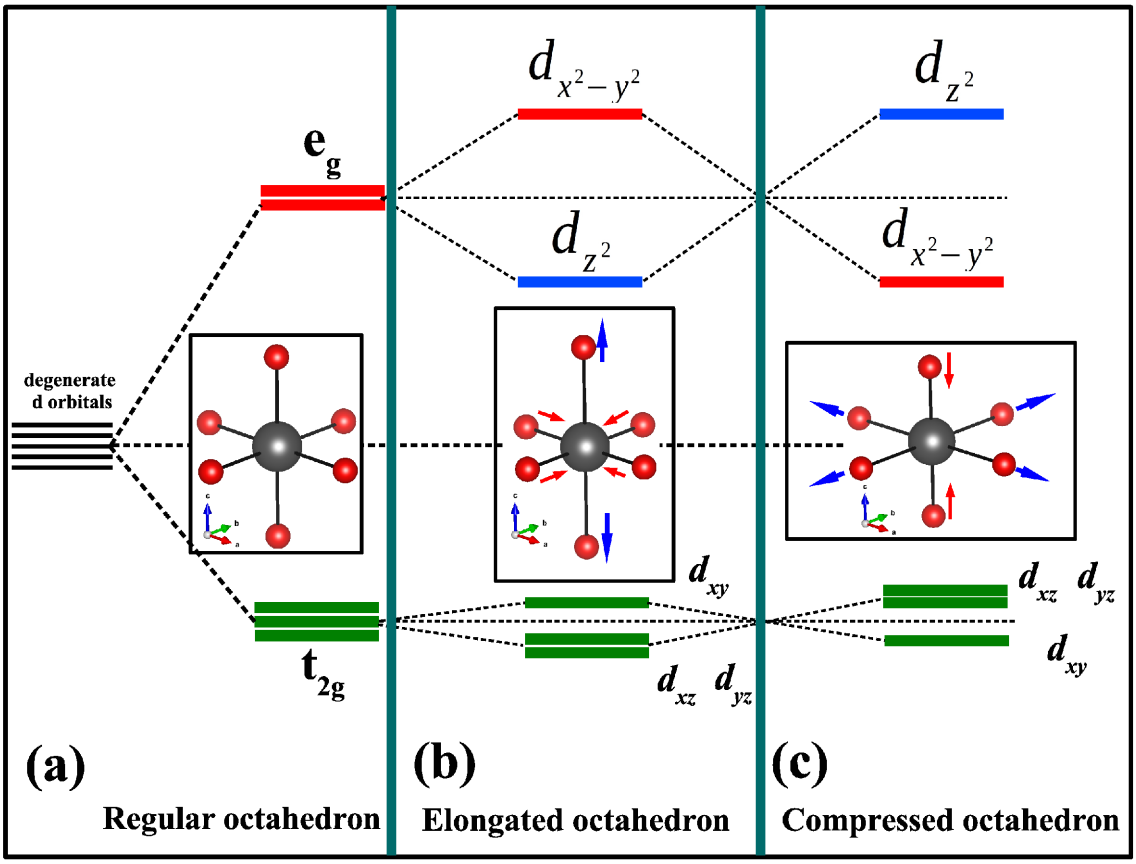

Figure 1.6: (a) Splitting of the five degenerate d orbitals into t_{2g} and e_g manifold for a regular BX_6 octahedral environment shown in the inset. (b) Splitting of the energy levels within the t_{2g} and e_g manifold for an elongation of the octahedra along the z-direction. (c) Splitting of the energy levels within the t_{2g} and e_g manifold for a compression of the octahedra along the z-direction.

states. As d_{xz} and d_{yz} have a component along the z-direction, so they are stabilized in energy. Whereas energy of the d_{xy} orbital lying entirely in the xy-plane increases. However, due to the smaller interaction of the t_{2g} orbitals with the ligands, changes in the t_{2g} manifold is rather small. For an octahedral compression in the z-direction the same arguments follow leading to an energy level splitting shown in Figure 1.6(c).

As an example, perovskite $KCuF_3$ contains a Jahn-Teller active ion Cu^{2+} with two possible electron distribution $t_{2g}^6 d_{z^2}^2 d_{x^2-y^2}^1$ and $t_{2g}^6 d_{x^2-y^2}^2 d_{z^2}^1$. Hence the CuF_6 octahedra undergoes Jahn-Teller distortion in the form of elongation along one of the pseudo cubic directions [21]. The tetragonal unit cell of $KCuF_3$ projected along the c-axis is shown in Figure 1.7(a). It consists two layers of CuF_6 octahedra along the c-axis, which are all corner shared in the ab plane and out of plane direction. The Jahn-Teller distortion results in an elongation of the octahedra either along the pseudocubic x or y-axis[shown by dotted lines in Figure 1.7(a)]. Distortion occurs in a cooperative manner such that $d_{3x^2-r^2}$ and $d_{3y^2-r^2}$

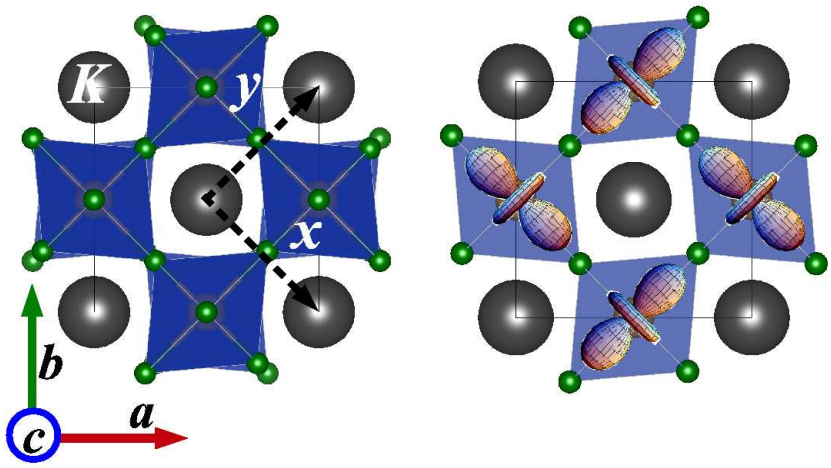

Figure 1.7: The crystal structure of $KCuF_3$ viewed along the c-axis([001] direction) with (a) out of phase rotations of distorted octahedra between layers along the c-axis; (b) a [001] layer showing the cooperative orbital ordering. Pseudocubic x or y-axis are shown by dotted lines in panel (a).

orbitals in the ab-plane are stabilized and occupied in an alternative manner [21][Figure 1.7(b)].

The Jahn-Teller effect itself is an example of the correlation between structural distortion and electronic state of the transition metal atom. At this point, we must know that an orbital degeneracy does not always lead to a Jahn-Teller distortion. The occurrence of such a distortion to remove orbital degeneracy is easy to understand considering the local electrostatic effects in an isolated octahedra. But in a crystalline environment where atomic states form bands, the fate of the Jahn-Teller distortion depends on the electronic structure of the system. For example, Jahn-Teller distortion is both temperature and pressure sensitive, and it is generally suppressed at higher temperatures and pressures. This happens due to temperature and pressure-induced changes in the electronic structure of the system. Even at low temperatures and normal pressure, a Jahn-Teller distortion does not occur for wide bandwidth systems like the rare earth nickelates, where Ni (Ni^{3+}) is Jahn-Teller active [22]. So, for a real material, the knowledge of the electronic structure is also needed to understand the origin of any structural distortion. In the next section, we discuss the electronic structure of $3d$ transition metal compounds.

1.3 Electronic structure of $3d$ Transition metal compounds

The electronic structure of $3d$ transition metal compounds can be described in terms of three essential parameters [23].

1. The on-site electron-electron Coulomb repulsion energy **U** within the transition metal $3d$ manifold.
2. The charge transfer energy $\mathbf{\Delta}$ to transfer an electron from a band like ligand(anionic) p state to an empty transition metal d orbital.
3. The transition metal $3d$ − ligand $2p$ hopping interaction strength $\mathbf{t_{pd}}$, which in turn determines the bandwidth **W** of the system.

1.3.1 On-site coulomb repulsion energy U and Hubbard model

Origin of the three parameters mentioned above is an effort to understand the ground state electronic structure of some transition metal compounds where band theory fails. The basic prediction of band theory is that, if there are even number of electrons per unit cell then the system could be either metal or insulator. But if there are an odd number of electrons per unit cell, then it must be a metal [24]. But this prediction fails in a number of cases, for example in CoO. CoO has a rock salt structure with one Co and one O atom in the unit cell. Co with an electronic configuration $3d^7 4s^2$ and O with $2s^2 2p^4$ results in an odd number(15) of electrons per unit cell. So according to band theory, it should be a metal, but experimentally it has been found to be an insulator [24, 25]. However the low temperature ground state structure of CoO is an antiferromagnetic(AFM) insulator. So, if we take the Co lattice and subdivide it into two magnetic sublattices so that one is with up-spin and the other one with down-spin, then the magnetic supercell is twice the chemical supercell and now there are even number of electrons [26]. Hence one can explain the low temperature AFM insulating state. But at sufficiently high temperatures above the Neel temperature the AFM ordering vanishes and the paramagnetic insulating state again has the chemical unit cell with odd number of electrons where band theory fails.

According to Mott [27–29], the reason of this failure is that, simple band theory do not takes into account the electron-electron Coulomb interactions. When we treat the electron-electron interaction quantum mechanically, the energy has a contribution from

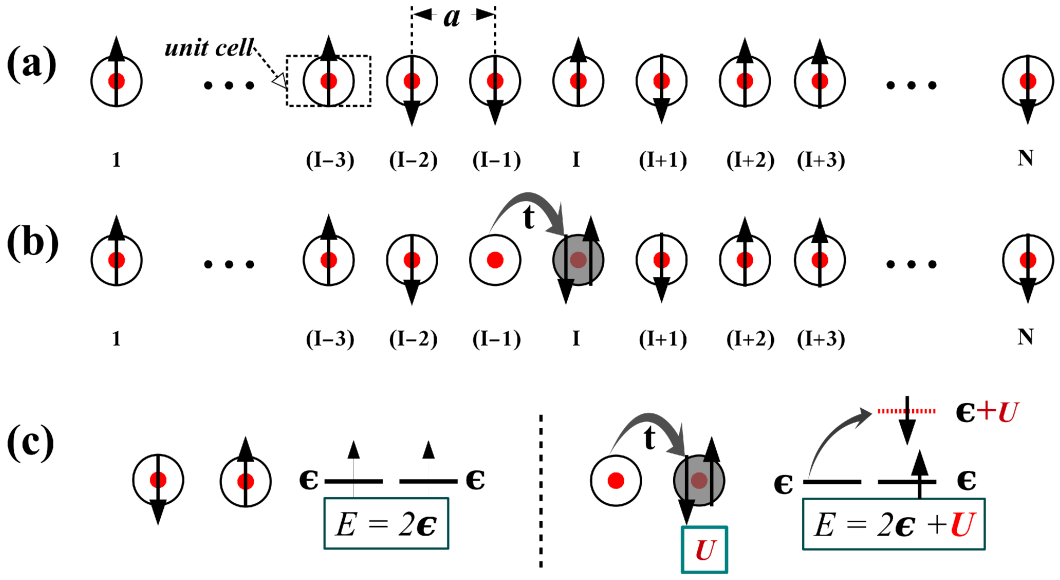

Figure 1.8: (a) A model for one-dimensional chain of atoms with a lattice constant a. There is a single orbital per atom that can be occupied by two electrons with opposite spins. No magnetic ordering of the electron spins are considered. (b) A non-interacting picture where electrons can hop from one site to other with a transition probability t. (c) Due to electron-electron correlation the gain from hopping(t) is compensated by the correlation energy **U** at the doubly occupied sites.

classical Coulomb energy, as well as quantum contributions such as an exchange(see chapter 2 for details). Together it is called electron-electron correlation, denoted by **U**. This can localize the electrons leading to an insulating ground state. A qualitative understanding of the importance of electron correlation follows from a simple model of a one-dimensional(1D) atomic chain, with a single electronic orbital per atom. As shown in Figure 1.8(a), we consider a single electron per atomic site without any spin correlation i.e. the spins of the electrons are random. Now if the electrons are non-interacting, then the down-spin electron at the (I-1)th site can easily hop to the Ith site having an up-spin electron with a transition probability t[see Figure 1.8(b)]. Due to such hopping, we have a single band with bandwidth $\mathbf{W} = 2zt$(where z is the number of nearest neighbors, $z = 2$ in 1D chain, $z = 4$ in square lattice, etc.) [30]. The band becomes full when two electrons, one with spin-up and the other with spin-down, occupy each site. But here single electron per site(unit cell) leads to a metallic state with a half-filled band[Figure 1.9(a)]. This is the non-interacting picture, but if we consider the electron-electron interaction, then the energy gain(t) due to hopping process as shown in Figure 1.8(b), will be compensated by on-site Coulomb correlation energy **U** at the doubly occupied Ith site[see Figure 1.8(c)]. According to Mott, this would split the single band in two bands. The lower band is formed from electrons that occupied an empty site(with energy ϵ) and the

upper one from electrons that occupies a site already taken by another electron(with energy $\epsilon + \mathbf{U}$)[see Figure 1.8(c)]. Now with one electron per site, the lower band would be fully occupied, and if there is any gap between the two bands the system would be an insulator.

Hubbard implemented the Mott physics in a simple model known as the Hubbard model [31, 32], which is given as,

$$H = -t \sum_{\langle ij \rangle \sigma} (c^{\dagger}_{i\sigma} c_{j\sigma} + H.C.) + \mathbf{U} \sum_{i} n_{i\uparrow} n_{i\downarrow} \tag{1.7}$$

Where $\langle ij \rangle$ indicates sum over i and j such that for each value of i, j is the nearest neighbor sites of the i^{th} site. $c^{\dagger}_{i\sigma} c_{j\sigma}$ indicates hopping of an electron with spin σ from the j^{th} site to the nearest neighbor i^{th} site. $n_{i\uparrow}$ and $n_{i\downarrow}$ gives the number of up-spin and down-spin electrons at the i^{th} site respectively.

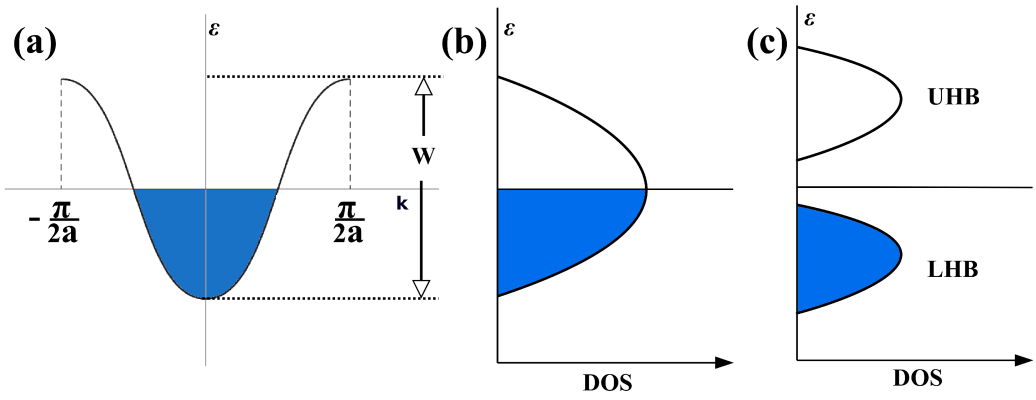

Figure 1.9: (a) A half filled band with band width **W** due to single electrons per site of a 1D chain of atoms. (b) The density of states corresponding to the half filled band. (c) Splitting of the half filled band into Upper and Lower Hubbard band as a result of electron-electron correlation.

For $\mathbf{U} = 0$, the model reduces to a simple nearest neighbor tight-binding model giving rise to a single band[Figure 1.9(a) and (b)]. The second term gives the electron-electron correlation between the up and down-spin electron at the i^{th} site. For a critical value of **U**, the half-filled band splits into two bands with a gap between them[see Figure 1.9(c)]. The fully occupied and unoccupied bands are called lower and upper Hubbard bands. Such a correlation driven insulating state is called a Mott insulator and the effective gap is $\sim (\mathbf{U} - W_{eff})$ called Mott-Hubbard gap which is controlled by the value of **U** and $W_{eff} = zt$, the effective d bandwidth.

1.3.2 Charge transfer energy Δ

The Mott-Hubbard picture of the electronic structure explains the insulating state of CuO, NiO as a result of gap opening due to coulomb correlation **U**. And the band gap value is determined by the strength of **U**. As **U** is an intra-atomic parameter, we expect that the band gap shall not vary significantly in the compounds containing the same transition metal atom. But it was observed that band gap strongly depends on the type of ligand in the compounds of late transition metals like Co, Ni, Cu [23,33]. For example, band gap decreases from 4.7 to 3.5 to 1.8 eV in $NiCl_2$, $NiBr_2$ and NiI_2 respectively [33]. This suggests that along with the transition metal d states, ligand p states also play an important role in determining the electronic structure.

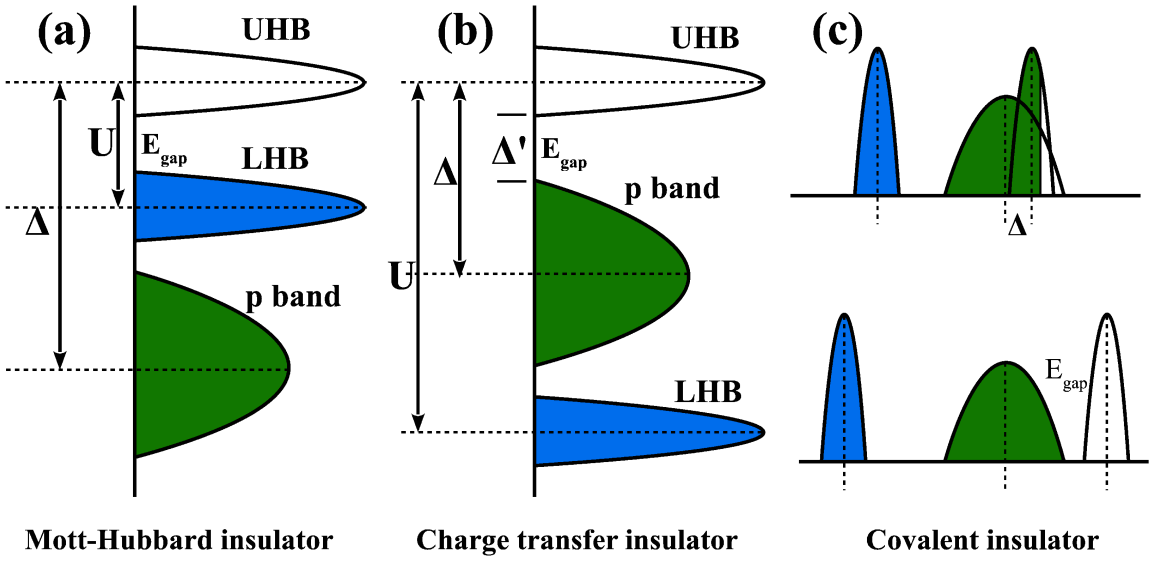

Figure 1.10: (a) Mott-Hubbard insulator for **U** < **Δ** where the gap is between two d bands. (b) Charge transfer insulator for **U** > **Δ** where the gap is between the ligand p band and the upper Hubbard band. (c) Expected band overlap and a metallic state in the -ve **Δ** region(upper panel) and opening of a gap due to strong $p-d$ hopping(lower panel)

According to Zaanen, Sawatzky, and Allen (ZSA) [34], for such transition metal compounds where strong hybridization effect of the d orbital and ligand p orbital is present, we need to consider two other relevant parameters. The charge transfer energy **Δ** to

transfer an electron from a band like ligand(anionic) p state to an empty transition metal d orbital and the transition metal $3d$ − ligand $2p$ hopping interaction strength $\mathbf{t_{pd}}$, which is mainly responsible in determining the transition metal d bandwidth. Now if we consider that the ligand p bandwidth is mainly due to $p-p$ hopping then, in the limit of $\mathbf{U} < \mathbf{\Delta}$, ligand p band lies below the lower Hubbard band and the electronic structure follows Mott-Hubbard picture[Figure 1.10(a)]. But in the limit $\mathbf{U} > \mathbf{\Delta}$, ligand p band lies in between the lower and upper Hubbard band[Figure 1.10(b)]. And if the system is insulating then, the gap is between the filed oxygen p band and empty upper Hubbard band. Such insulators are called Charge transfer insulators and the gap is controlled by the value of $\mathbf{\Delta}$. The reason for such nomenclature is that here charge transport is possible due to the lowest energy excitation that transfers an O p electron to the transition metal d orbital.

1.3.3 The ZSA phase diagram

Considering these three parameters Zaanen, Sawatzky, and Allen presented a phase diagram pointing out different metal and insulating regions for strongly correlated electron systems in the $\mathbf{U/t_{pd}} - \mathbf{\Delta}^{'}/\mathbf{t_{pd}}$ space. This is shown in Figure 1.11(a). $\mathbf{\Delta}^{'}$ is the effective charge transfer energy defined between the band edges as shown in Figure 1.10(b).

For, $\mathbf{U} < \mathbf{\Delta}$ we are in the Mott-Hubbard region[Figure 1.10(a)]. Now, $\mathbf{U} > W_{eff}$ ensures an insulating state which is the Mott-Hubbard insulator. $LaVO_3$, $LaTiO_3$, V_2O_3, Ti_2O_3 etc, are examples of such insulators [23]. But for $\mathbf{U} < W_{eff}$, the upper and lower Hubbard bands overlaps resulting in a metallic ground state. Such metals are called d band metals. TiO and VO are compounds belonging to this class [23].

On the other hand for $\mathbf{U} > \mathbf{\Delta}$, we are in the charge transfer region[Figure 1.10(b)]. If $\mathbf{\Delta}$ is greater than a critical value $\mathbf{\Delta}_C$ such that $\mathbf{\Delta}^{'}$ is positive then we get an insulating ground state, which is the charge transfer insulators. CuO is an example of charge transfer insulator [23]. But for $\mathbf{\Delta} < \mathbf{\Delta}^{'}$, O p band overlaps with the upper Hubbard band giving rise to a metallic state called p-type metal. CuS, NiSe, $LaNiO_3$ are examples of such metals [23].

Later, based on multiband Hubbard model calculations [23, 35, 36], it was shown that for negative values of $\mathbf{\Delta}^{'}$ we can still have an insulating state over a region for high values of $\mathbf{U}$. Such insulating state arises due to strong covalency effects between transition metal d and ligand p states and is termed as a covalent insulator. This is shown in the modified ZSA phase diagram[Figure 1.11(b)] between the p-type metal and charge transfer insulator regions. For negative values of $\mathbf{\Delta}^{'}$ system would be metallic without considering the $p-d$

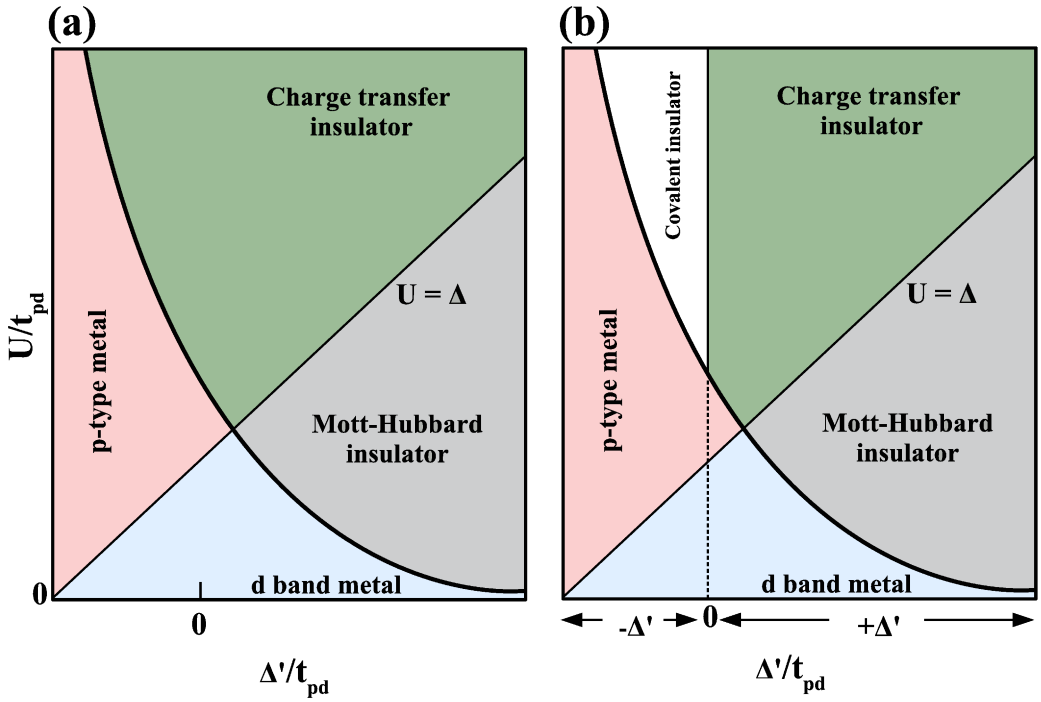

Figure 1.11: (a)The ZSA phase diagram (b) Modified ZSA phase diagram showing the covalent insulating region.

hybridization($\mathbf{t_{pd}}$) as a result of band overlap. This is shown in the upper panel of Figure 1.10(c). But a large value of $\mathbf{t_{pd}}$ mix the d and p states, pushing them energetically apart to form a nonzero band gap, similar to the case of bonding-antibonding splitting formed in molecular orbital theory [8][see lower panel of Figure 1.10(c)]. Increasing the formal valence of a transition metal ion has the primary effect of lowering $\mathbf{\Delta}$ and increasing $\mathbf{t_{pd}}$ that favors a covalent insulator state. The rare earth nickelates ($RNiO_3$) are the example of such compounds.

Now after knowing the details of the perovskite structure and basic parameters to describe the electronic structure of transition metal compounds, let us look into some example of structure-property correlation in rare earth nickelates.

1.4 Properties of Rare earth Nickelates

The rare earth nickelates($RNiO_3$) shows fascinating electronic and magnetic properties as a result of their complex electronic structure and flexibility of the perovskite structure to adopt internal and external changes [34, 37]. One of the interesting phenomena that we are going to discuss is the temperature driven metal to insulator transition. All

members of the $RNiO_3$ series(except $LaNiO_3$ that remains metallic at all temperatures) shows a sharp metal to insulator transition below a certain temperature(T_{MIT}). This can be observed as a sharp rise in the resistivity below T_{MIT} as shown in Figure 1.12(a) for $SmNiO_3$ thin films grown on $LaAlO_3$ substrate [1,38]. The high temperature state above T_{MIT} is metallic with an orthorhombic space group *Pbnm* and below T_{MIT} they become insulating/semiconducting [1]. The metal to insulator transition temperature for all the rare earth nickelates is shown in Figure 1.12(b). We can see that as we go from Pr to Lu, T_{MIT} gradually increases. At the same time, the evolution of the tolerance factor(α, along the x-axis) going from Pr to Lu, suggests that T_{MIT} and structure of the systems are correlated.

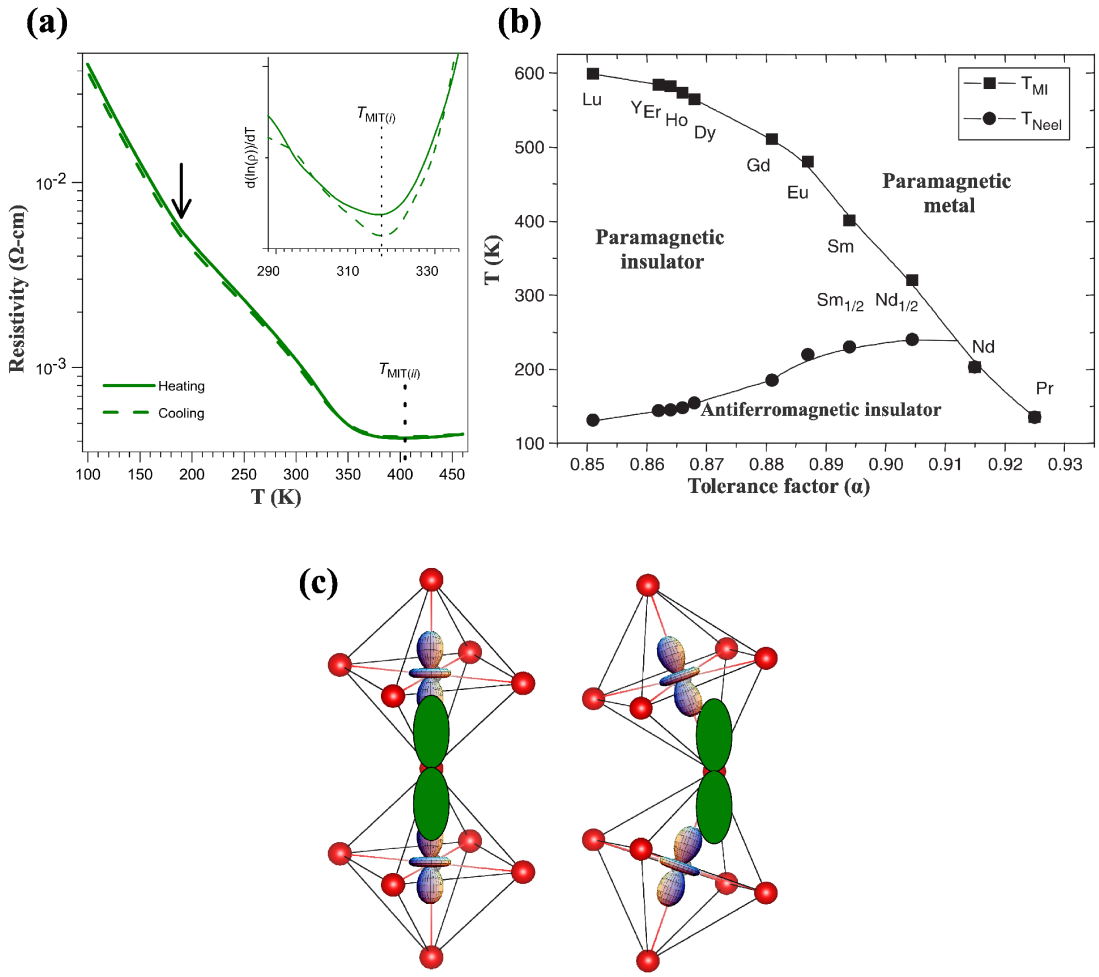

Figure 1.12: (a) Resistivity vs. Temperature plot showing the metal to insulator transition below $\sim$ 400 K in $SmNiO_3$ thin films(10 nm)[Figure taken from Ref. [38]] (b) Metal-insulator and magnetic transitions as a function of the tolerance factor α for the rare earth nickelates[Figure taken from Ref. [1]] (c) Straightening the Ni-O-Ni bond angle (by increasing rare earth-radius) increases the orbital overlap and stabilizes the metallic state.

The low temperature state of rare earth nickelates has been characterized as charge transfer insulators [23, 34, 39, 40], with the transition to a metallic state occurring due to the collapse of the charge transfer gap between the oxygen p valence band and Ni d conduction band[see Figure 1.10(b)]. As discussed before, crystal structure of $RNiO_3$ systems consist of corner shared NiO_6 octahedra with the rare earth atom(R) sitting inside the octahedral cavity at the A-site. The octahedra are tilted showing a $GdFeO_3$ type distortion with a deviation of the Ni-O-Ni bond-angle from 180^o. Now as we go from Pr to Lu the ionic radii gradually decrease due to an increase in the atomic number Z. As a result, the value of the tolerance factor given by Equation (1.8) decreases [40].

$$\alpha = \frac{(r_{_R} + r_{_O})}{\sqrt{2}(r_{_{Ni}} + r_{_O})} \tag{1.8}$$

This reduction in the tolerance factor is mainly accommodated by an increased buckling of the NiO_6 octahedral network [1, 40]. A larger compressibility of the RO_{12} unit compared to the NiO_6 unit results in a faster shrinking of the R-O distances compared to Ni-O distances. This results in an octahedral tilting with a decreased unit cell volume. As a result of increased buckling, the Ni-O-Ni bond angle deviates more and more from 180^o. As shown in Figure 1.12(c), this decreases the orbital overlap between the Ni d and O p states. As a result, the bandwidth of the conduction band and valence band decreases due to decrease in hopping strength $\mathbf{t_{pd}}$. This, in turn, increases the band gap of the system i.e. favors the insulating state over the metallic one. This explains the increasing $T_{_{MIT}}$ with decreased ionic radii of the R atom. For $PrNiO_3$, the average Ni-O-Ni bond angle is $\sim 158.5^o$ with a $T_{_{MIT}} \sim 135K$. Whereas for $LuNiO_3$, the average Ni-O-Ni bond angle reduces to $\sim 144.5^o$ increasing the $T_{_{MIT}}$ to 599K. It has been reported that $T_{_{MIT}}$ can be tuned continuously across this entire temperature range by mixing two different nickelates in the right proportion [1, 41]. For example, metal-insulator transition for $Nd_{0.45}Sm_{0.55}NiO_3$ takes place at room temperature.

Now along with the metal to insulator transition, the rare earth nickelates also shows a transition from a paramagnetic insulator to an anti-ferromagnetic insulator state at the temperature $T_{_{Neel}} \leq T_{_{MIT}}$. One of the proposed anti-ferromagnetic state is characterized by an ($\uparrow\uparrow\downarrow\downarrow$) order of the Ni moments along the three pseudocubic axis [42,43]. As shown in Figure 1.12(b), for R = Nd and Pr the $T_{_{Neel}}$ and $T_{_{MIT}}$ coincides, but as tolerance factor reduces further, the $T_{_{Neel}}$ and $T_{_{MIT}}$ separates from one another. This, suggests that an anti-ferromagnetic ordering of the Ni moments cannot be responsible for the insulating state [26] and can be ignored as a low-temperature phenomenon. The insulating state is a result of electron-electron correlation coupled with structural distortions [22, 44–46]. If

we consider a complete ionic picture of $RNiO_3(R^{3+}, Ni^{3+}, O_3^{2-})$, then $Ni^{3+}(d^7)$ in the low spin state($t_{2g}^6 e_g^1$) would be Jahn-Teller active due to orbital degeneracy in the e_g manifold and metallic due to a half-filled conduction band arising from the e_g states. Now the degeneracy can be removed via a Jahn-Teller distortion and may lead to an insulating state depending on the bandwidth of the system. So, for $RNiO_3$ we expect a Jahn-Teller distortion in the low temperature insulating state. Though structural analysis suggested such distortion for nickelates with small rare earth atoms, but such distortion was not observed for $NdNiO_3$ and $PrNiO_3$ [47] which are wide band width systems. For $NdNiO_3$ it was found that the insulating state is accompanied by a breathing mode distortion with two inequivalent NiO_6 octahedra having slightly different volume [48, 49].

1.4.1 Effect of pressure and strain

As described above, we see that there is a strong correlation between the Ni-O-Ni bond angle(θ) and the metal to insulator transition temperature T_{MIT}. Hence we can control the electronic structure and transition temperature by controlling the bond angle θ, and this can be done with external pressure or epitaxial strain.

External hydrostatic pressure reduces the unit cell volume and hence the Ni-O and R-O bond length decrease. In response to external pressure, the compressibility of the NiO_6 unit is much higher than the RO_{12} unit. This results in a faster shrinking of the Ni-O distances compared to R-O distances [50, 51]. A faster shrinking of the Ni-O bond lengths in-turn results in a straightening of the bond angle θ reducing the octahedral distortions and making the system more and more itinerant. This reduces T_{MIT} favoring a metallic phase [50–53]. For example, it has been reported that for $PrNiO_3$, the metal-insulator transition gets suppressed for pressures above 13-14 kbar [50, 53]. However the temperature dependence of the resistivity in the high pressure metallic phase shows non-Fermi liquid behavior [53].

Analogous to external pressure, thin films grown under compressive strain are also expected to reduce octahedral distortions and decrease the T_{MIT}. This has been observed in epitaxial films of $NdNiO_3$ grown under compressive strain [54–56]. Now, a reduction of T_{MIT} due to compressive strain simply suggests that T_{MIT} shall increase as a result of tensile strain. However experimental results show the opposite picture, instead of increasing, T_{MIT} also gets decreased under tensile strain. For example $NdNiO_3$ thin films grown on $NdGaO_3$($\sim 1.3\%$ tensile strain) shows a strong variation in the T_{MIT} as a function of film thickness. As shown in Figure 1.13, with increasing film thickness the strain is gradually relaxed and T_{MIT} approaches the bulk value $\sim$ 200 K [57, 58]. But in the ultra-thin limit

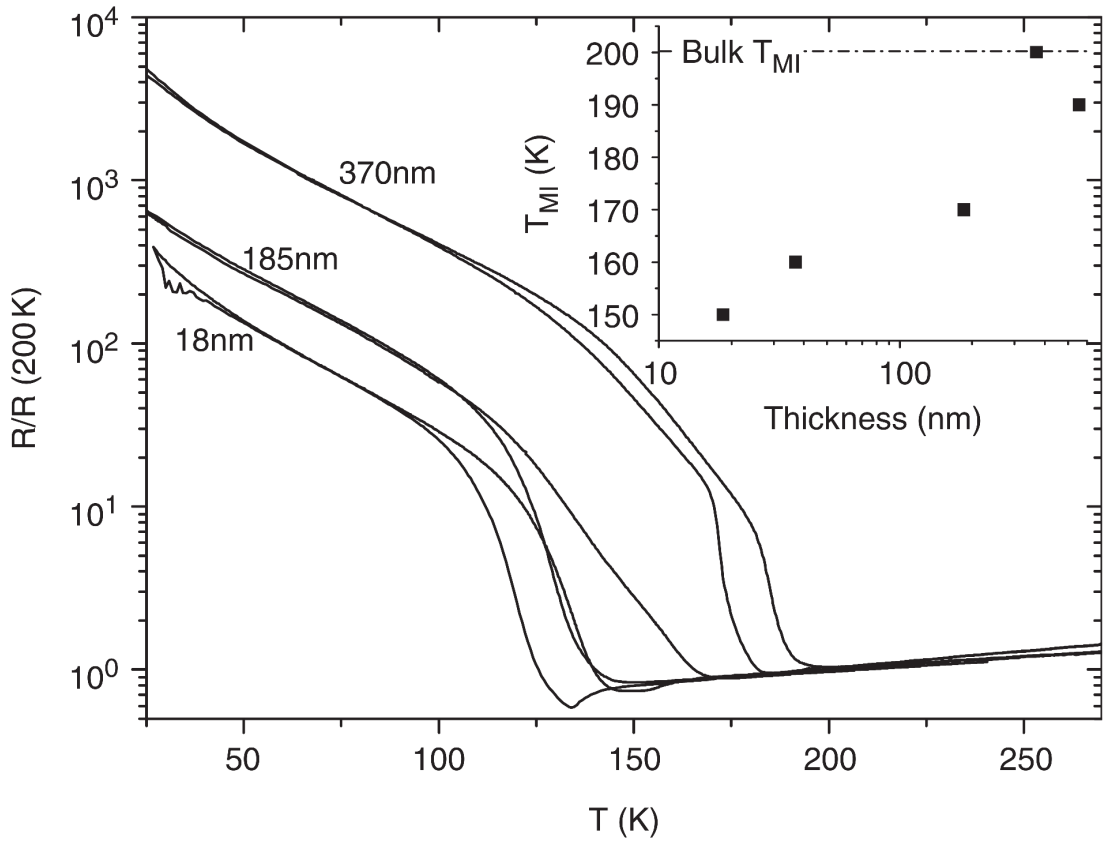

Figure 1.13: Normalized sheet resistance as a function of temperature for $NdNiO_3$ films of different thickness grown epitaxially on $NdGaO_3$ single crystal substrates (tensile lattice mismatch of 1.3%). Inset: evolution of T_{MIT}(here $T_{MIT} = T_{MI}$) as a function of film thickness. Epitaxial strain stabilizes the metallic phase and depresses the metal-insulator transition; as the strain is relaxed, the bulk behaviour is progressively recovered.[Figure taken from Ref. [1]]

where the effect of strain is maximum, we see a reduced $T_{MIT} \sim 150$ K. Such reduction of T_{MIT} can be explained by considering the tensile strain to be analogous to internal pressure. An increase in the size of the rare earth atom can be thought to producing internal pressure and increasing the R-O distance. This results in a straighter Ni-O-Ni bond angle θ. Similarly, a tensile strain also reduces octahedral distortions as a result of increasing R-O distances and hence reducing T_{MIT}. So, for the rare earth nickelates, we must remember that the fundamental NiO_6 structural units behave differently under internal and external changes.

The metal-insulator transition in the rare earth nickelates is coincident with a crystal distortion, where the insulating state is characterized by a two-sublattice symmetry breaking, with Ni on one sublattice having a decreased mean Ni - O bond length and the Ni on the other having an increased mean Ni - O bond length, defining a bond disproportionation/breathing mode distortion(BD) [44, 49, 59, 60]. This state is sometimes also referred to as "charge ordered(CO)" state. There is a debate in explaining the simultaneous oc-

currence of insulating phase with a bond disproportionation. D.I.Khomskii *et al.* [61] explains the insulating state in terms of charge disproportionation, where an electron is transferred from a Ni site to the nearest neighbor(n.n) Ni. This confirms an insulating state and leads to bond disproportionation as a result of dissimilar charges on two different Ni sites. On the other hand, there are claims [62,63] that there is actually no charge ordering on the Ni sites. All Ni atoms are equally occupied and there are holes on the oxygen network. The bond disproportionation is a result of asymmetric coupling of the oxygen holes with one of the Ni e_g electrons forming a singlet state. In the third chapter of this thesis using density functional theory(DFT) and model Hamiltonian approach [64], we show that occurrence of the insulating state with bond disproportionation in Neodymium nickelate($NdNiO_3$) is intimately related to a negative value of the effective charge transfer energy(a negative value of $\mathbf{\Delta'}$). BD occurs when the Ni d band just enters the oxygen p band and there are holes on the oxygen. For positive values of $\mathbf{\Delta'}$ system becomes metallic with absence of a BD. We also calculate the effective charge transfer energy $\mathbf{\Delta'}$ for all the rare earth nickelates. For R = Lu to Pr the values of $\mathbf{\Delta'}$ lie in the range of -0.41 to -0.27 eV indicating a situation where the Ni d band just enters the oxygen p band. As a result the ground state(GS) of the compounds are insulating with BD. For $LaNiO_3$, the value of $\mathbf{\Delta'}$ is $\sim$ -0.62 eV and the GS is metallic without any BD. So, from here conclude that a negative value of delta is necessary for BD to occur, however there is a critical value beyond which the itinerant limit is reached. There will be larger band overlap and system becomes metallic suppressing the MIT. Values of $\mathbf{\Delta'}$ in the range of -0.41 to -0.27 leads to an insulating GS with a small variation in the band gap values. In the insulating state, main role in controlling the band gap is played by the bandwidth($\mathbf{W}$). As we go from Lu to Pr the ionic radii of the rare earth atom increases and the bandwidth of the system also increases due to increased hybridization between the Ni d and O p states, this in turn drives the system more towards the itinerant limit and there shall be a systematic decrease in the metal to insulator transition temperature(T_{MIT}), in agreement with experimental observations as reported in earlier works [40, 65, 66]. From here we move to hybrid perovskites where at the A-site there is an organic molecule, which plays a complex role in determining the structure and hence electronic properties. So, in the next section we now discuss the general structural properties of a hybrid perovskite and how the ideas of structural distortions gets modified compared to the well known rules that are applicable in inorganic perovskites.

1.5 Octahedral tilting in Hybrid perovskites

In the previous section, we discussed the role of BO_6 octahedra as an important functional unit to control the electronic properties of perovskite nickelates. The B-O bond lengths and the B-O-B bond angles are strongly correlated with the electronic structure of the system. As discussed before, changes in the B-O-B bond angle occurs due to structural distortions that have been understood in terms of the Goldschmidt tolerance factor[see section 1.1]. The tolerance factor has emerged as an important tool which can be used to determine whether a system shows a tendency to tilt or not. Such a concept has existed for isolated atoms occupying the A-site and has been successful in explaining various experimental trends. But the tolerance factor approach becomes difficult to predict octahedral distortions when there is a molecule sitting at the A-site. Material systems consisting of organic and inorganic parts are called hybrid systems that offer an important opportunity to combine useful properties from these two chemical realms within a single molecular scale composite [67]. In hybrids, the organic molecules are generally sheltered inside the inorganic cage. In case of hybrid perovskites, an organic molecule sits at the A-site within the octahedral cavity. For example, Figure 1.14(a) shows a Methylammonium $(CH_3NH_3)^+$ or MA molecule sitting inside the inorganic cage formed by the B cation and X anions of a perovskite. The inorganic octahedral network is generally formed by the Group 14 elements like Ge, Sn, and Pb, sitting at the B-site together with a halogen Cl, Br or I as an anion. Hybrid perovskites with interesting chemical and structural properties [67–71] are becoming popular day by day, mainly for their use as a solar cell material.

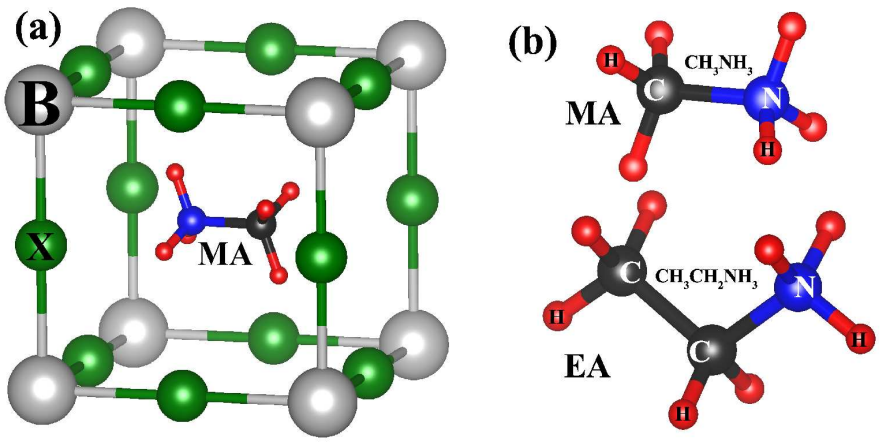

Figure 1.14: (a) A typical hybrid perovskite structure where a Methylammonium(MA) molecule is sitting at the A-site, inside the inorganic cage formed by B cation and anions. (b) A schematic representation of the structure of Methylammonium(MA)[upper panel] and Ethylammonium(EA)[lower panel] molecules.

Other organic molecules that can form hybrid perovskites are Formamidinium or FA, Ethylammonium or EA etc. The structure and components of the MA and EA molecules are shown in Figure 1.14(b) for clarity. Hence in contrast to inorganic perovskites where one had an isolated atom which could largely be approximated as a sphere, in the present case, one has an asymmetric cylindrical object occupying the A-site. Moreover, now there are hydrogen atoms associated with the molecule which can make hydrogen bonding with the anions. These additional factors make it difficult to predict the structural properties of such systems based on the concepts we have for inorganic perovskites.

Here we give a brief description of how the tolerance factor approach has been generalized for hybrid perovskites and the role of hydrogen bonding between the molecule and the anions in determining the structural distortions.

1.5.1 Generalized tolerance factor

The problem in determining the tolerance factor for such systems given by Equation (1.9), lies in estimating the ionic radii(r_{OM}) of the anisotropic organic molecules(OM). The problem of estimating effective ionic radii for the organic molecule has been addressed in the past. For example, a set of thermochemical radii for molecular anions was proposed by Kapustinskii and Yatsimirskii around 1940 [72]. In case of hybrid perovskites, the organic molecular cation makes hydrogen bonding with the anions leading to varying bond lengths, that makes it more difficult to define an ionic radii.

$$\alpha = \frac{(r_{OM} + r_X)}{\sqrt{2}(r_B + r_X)} \tag{1.9}$$

Recently G. Kieslich *et al.* have proposed a way [11] which involves calculating effective ionic radii of organic cations from the existing crystallographic data of hybrid perovskites. Depending on the level of anisotropy, the organic ions were considered either as a sphere or cylinder. For the case of organic cations, a sphere model considering the rotational degrees of freedom around the center of mass of the molecule was considered. With such considerations, the effective ionic radii were calculated using Equation (1.10).

$$r_{Aeff} = r_{mass} + r_{ion} \tag{1.10}$$

Where r_{mass} is the distance between the center of mass(CM) of the molecule and the atom that have the maximum distance from the center of mass, excluding the hydrogen atoms.

r_{ion} is the ionic radii of this atom. Using this in place of r_{OM} in Equation (1.9) allows one to calculate the tolerance factor for such hybrid systems.

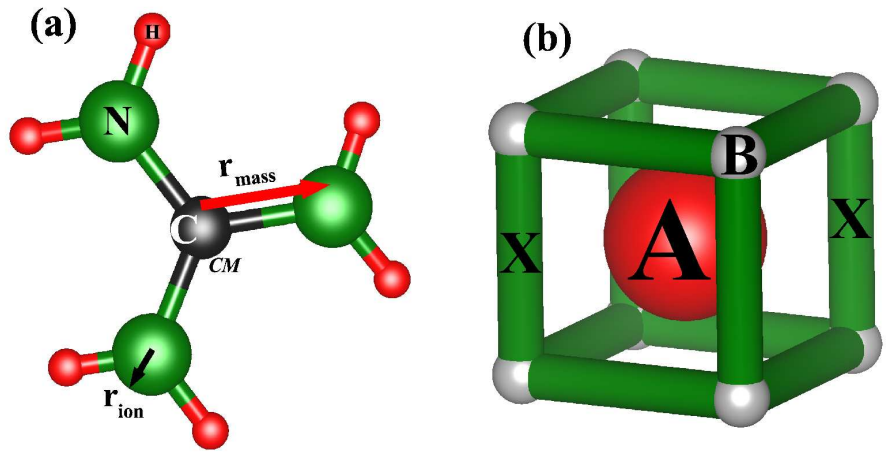

Figure 1.15: (a) Structure of the Guanidinium $[C(NH_2)_3]$ molecule with the center of mass(CM) at the C atom. r_{mass} and r_{ion} are also mentioned. (b) Schematic of the model considering the anions as rigid cylinders to calculate the tolerance factors of perovskites containing complex molecular anions like $HCOO^-$.

For example, as shown in Figure 1.15(a), in case of the Guanidinium $[C(NH_2)_3]^+$ cation they found a r_{mass} = r(C-N) = 132 pm and r_{ion} = r(N^{3-}) = 146 pm. Then Equation (1.10) gives a value of r_{Aeff} = 278 pm. Using this approach they calculated the effective radii for a set of organic molecules that can be used to estimate the tolerance factors for the corresponding perovskite systems. The effective ionic radii for some of the organic cations are given in Table 1.1.

Table 1.1: Effective ionic radii of molecular cations(taken from Ref. [11]). Ionic radii for the inorganic ions were used from Ref. [12]

	Organic cation	Effective ionic radii(r_{Aeff}) in pm
1	Ammonium $[NH_4]^+$	146
2	Hydroxylammonium $[H_3NOH]^+$	216
3	Methylammonium $[CH_3NH_3]^+$	217
4	Hydrazinium $[H_3N\text{-}NH_2]^+$	217
5	Azetidinium $[(CH_2)_3NH_2]^+$	250
6	Formamidinium $[NH_2(CH)NH_2]^+$	253
7	Imidazolium $[C_3N_2H_5\ ]^+$	258
8	Dimethylammonium $[(CH_3)_2NH_2]^+$	272
9	Ethylammonium $[(C_2H_5)NH_3]^+$	274
10	Guanidinium $[C(NH_2)_3]^+$	278
11	Tetramethylammonium $[(CH_3)_4N]^+$	292

For molecular anions such as $HCOO^-$, CN^-, the situation becomes more complicated due to their high anisotropy. For such a case they treated all molecular anions as rigid cylinders, with an effective radius r_{Aeff} and an effective height h_{Aeff}. These are shown as green cylinders(leveled as X) in Figure 1.15(b). The radius(r_{Aeff}) and the height(h_{Aeff}) of the cylinders were then evaluated using Equation (1.10). Using these concepts the general formula for calculating the tolerance factor of hybrid organic-inorganic systems is given by [11]:

$$\alpha = \frac{(r_{Aeff} + r_{Xeff})}{\sqrt{2}(r_B + 0.5h_{Xeff})} \tag{1.11}$$

Using this general formula they calculated the tolerance factor for a series of hybrid perovskites. The value for some of the important systems is given in Table 1.2.

Table 1.2: Tolerance factor of some important hybrid perovskite systems calculated using the generalized approach [11]). The effective ionic radii for the inorganic ions were taken from Ref. [12]

A-site Organic molecule	B-site cation	Anion(X)	Tolerance factor
Methylammonium	Pb	Cl	0.938
		Br	0.927
		I	0.912
	Sn	Cl	0.951
		Br	0.939
		I	0.922
Formamidinium	Pb	Cl	1.023
		Br	1.008
		I	0.987
	Sn	Cl	1.037
		Br	1.021
		I	0.998
Ethylammonium	Pb	Cl	1.072
		Br	1.055
		I	1.030
	Sn	Cl	1.087
		Br	1.069
		I	1.043

1.5.2 Role of Hydrogen bonding in octahedral tilting

Methylammonium lead iodide ($MAPbI_3$, MA = CH_3NH_3) is one of the well known and most studied members of the hybrid perovskite series. It has been shown both experimentally [73] as well as theoretically [74] that, structure and electronic properties of hybrid perovskites are strongly correlated. However the most important structural parameter to tune the electronic structure, the octahedral tilts usually occur in the low-temperature states. For example, $MAPbI_3$ undergoes a series of temperature dependent structural phase transition with an increased degree of octahedral tilting as the temperature decreases [75]. The high-temperature phase above 330 K is cubic without any octahedral tilts. As shown in Figure 1.16(a), the inorganic cage containing the MA molecule is a perfect cube with the Pb-I-Pb bond angles equal to 180^o. Below 330 K octahedral tilting occurs leading to a low symmetry tetragonal phase. The octahedral tilt pattern can be realized as originating from the high symmetry cubic state, due to rotation of the octahedra in an out of phase manner along one of the pseudocubic axis(z-axis/c-axis). This results in the in-plane(ab-plane) Pb-I-Pb bond angles to deviate from 180^o[see Figure 1.16(b)]. Below 160 K, with further symmetry lowering the system enters an orthorhombic phase due to octahedral rotations about all the pseudocubic directions and all Pb-I-Pb bond angles deviating from 180^o[Figure 1.16(c)].

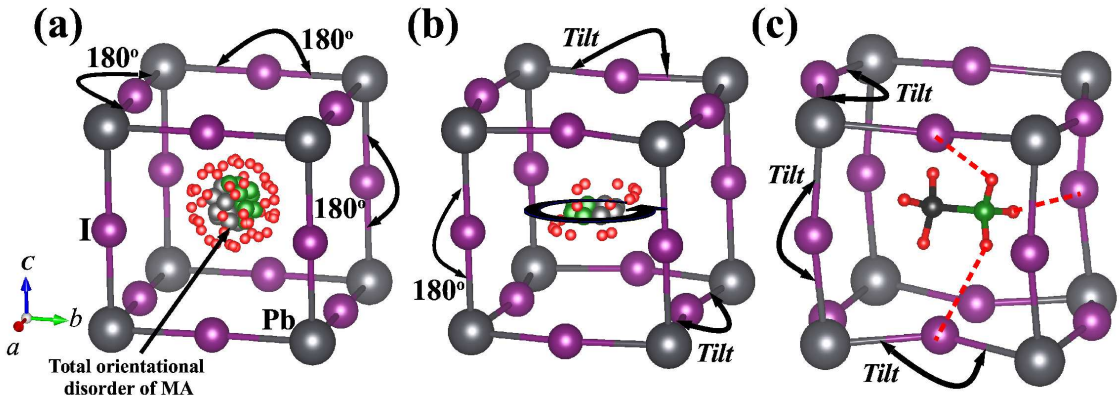

Figure 1.16: (a) Total orientational disorder of the MA molecule in the cubic phase without any octahedral tilts. The Pb-I-Pb bond angles along all the three cubic directions are 180^o (b) Below 330 K (MA)PbI_3 enters tetragonal phase with octahedral rotations about the c-direction, leading to the in-plane(ab-plane) Pb-I-Pb bond angles to deviate from 180^o and the molecule is four-fold orientationally disordered around the c-axis. (c) Deviation of all the Pb-I-Pb bond angles from 180^o in the orthorhombic phase below 160 K and ordering of the MA molecules.

Along with structural changes the dynamic state of the MA molecule also undergoes drastic changes . Missing X-ray diffraction pattern for the $(CH_3NH_3)^+$ group in the high temperature cubic phase already suggested static disorder or dynamic reorientation of the MA molecule. An electric dipole moment associated with the MA molecule makes it

possible to do dielectric measurements that can probe any dynamic motion associated with the molecule. Dielectric data [76] showed dynamic disorder of the MA molecule where the C-N axis is free to rotate about any direction. The disordered state of the molecule inside the inorganic cage is schematically shown in Figure 1.16(a). With decreasing temperature, the dynamic disorder also decreases. In the tetragonal phase the C-N axis of the molecule shows four-fold orientational disorder around the *c*-axis in the *ab*-plane[Figure 1.16(b)]. And in the orthorhombic phase ordering of the MA molecules takes place with a preferred orientation and stacking which again leads to formation of hydrogen bonding between the hydrogen atoms and the anions(I^-)[Figure 1.16(c)]. Previously it was shown that the hydrogen bonding plays an important role in determining the preferred orientation of the MA molecule [77]. The orientation of the molecule is such that, hydrogen bonding between the molecule and the anions is maximized. Recently, based on *ab-initio* density functional theory calculations [78], it has been shown that hydrogen bonding is also responsible for the octahedral tilts in the low temperature orthorhombic phase.

To show this they consider the low-temperature orthorhombic structure of $MAPbI_3$ and the inorganic perovskite series $APbI_3$, where A = K, Rb, Cs, and Fr. The low-temperature orthorhombic phase for each of the inorganic system shows a tilt pattern similar to $MAPbI_3$ as shown in Figure 1.17(a). For each system, they did two different calculations and calculated the total energy. In the first calculation, the structure was allowed to fully relax so that the ions can move to their equilibrium positions for a minimum energy configuration . The fully relaxed ground state(GS) structure for all systems were found to be distorted with octahedral tilting analogous to the experimental orthorhombic structure. In the second calculation they considered a high symmetry(HS) phase[see Figure 1.17(b)] for each systems where,

1. The unit cell dimension was exactly the same as the fully relaxed ground state(GS) structure.

2. Pb and I atoms were forcefully fixed at their ideal positions so that the PbI_6 octahedra become fixed and untilted.

3. The *A*-site cations were allowed to relax for their equilibrium position/configuration.

For the inorganic perovskites, the high symmetry phase considered in the calculations simply corresponds to the low temperature orthorhombic phase but without any octahedral tilts. For the $(MA)PbI_3$, it is a kind of hypothetical phase without any octahedral tilts, where the local coordinates of the MA cation were relaxed but with the same orientation and conformation found in the orthorhombic phase. After this, they quantify the energy

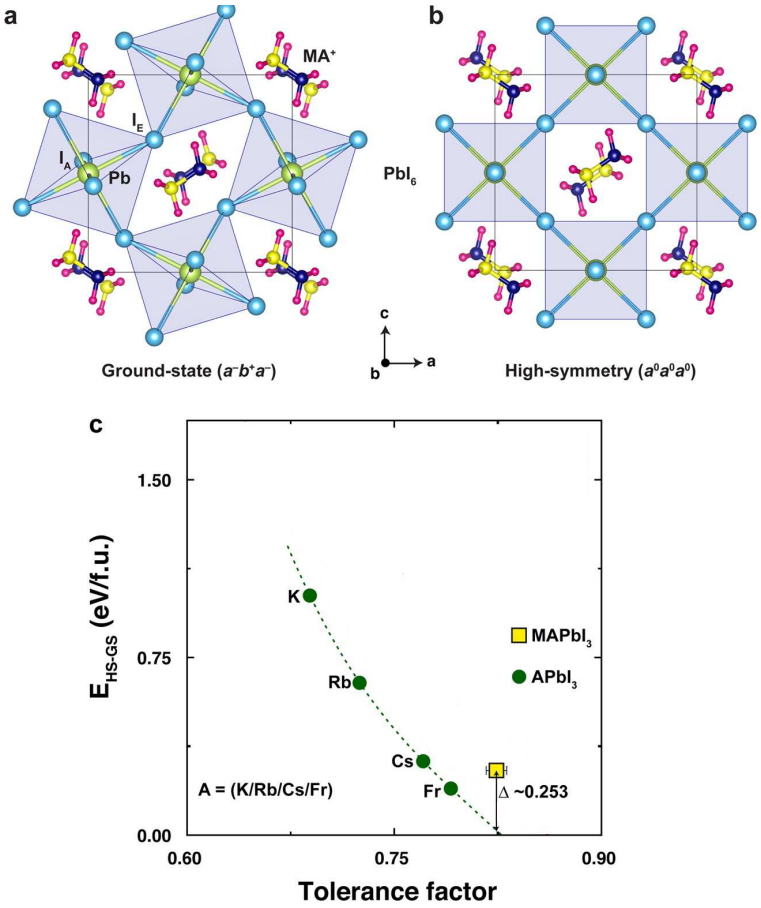

Figure 1.17: (a) The ground state (GS) and (b) high symmetry (HS) structures of orthorhombic $(MA)PbI_3$, composed of PbI_6 octahedra and MA molecules at the octahedral cavity. (c) The energy difference between the HS and the GS structures(E_{HS-GS}) as a function of the tolerance factor for the $APbI_3$ inorganic series (green circles) and $(MA)PbI_3$ (yellow square). The horizontal error bar in $(MA)PbI_3$ represent the difference in tolerance factor calculated using the sphere and cylinder methods(see section 1.5.1)[Figures are taken from Ref. [78]].

difference (E_{HS-GS}), between the fully relaxed ground state(GS) orthorhombic structure, and the high symmetry(HS) phase for each system. This energy difference gives a measure of the propensity of octahedral tilting. If E_{HS-GS} is positive then the system would have a ground state structure with octahedral tilts otherwise it would not like to tilt.

Along with this, the tolerance factor was also calculated for each of the systems to check for any mismatch in the ionic size and probable octahedral tilting due to steric effects. For this, a simple approach was followed [73]. They considered the effective ionic radii for each cation or anion as the radii of the sphere that contains 95% of the calculated electron density. For the MA^+ cation, both a sphere and a cylinder was considered to determine two effective radii that differ from each other by only 0.04 Å suggesting that this approach is reliable.

E_{HS-GS} for all the five systems as a function of the tolerance factor is shown in Figure 1.17(c). For the inorganic series $APbI_3$, as we go from K to Fr, the value of the tolerance factor increases due to an increase in the size of the *A*-site cation. On the other hand, the energy difference E_{HS-GS} between the non-tilted and tilted state decreases indicating a reduction in the octahedral tilting. This is in accordance with the general properties of a perovskite structure. The relation between E_{HS-GS} and tolerance factor for $APbI_3$ suggests that a hypothetical perovskite of the series $APbI_3$ with a tolerance factor of 0.83(extrapolation of the green curve in Figure 1.17(c) cuts x-axis at 0.83) would not like to tilt due the zero value of E_{HS-GS}. This perovskite of the $APbI_3$ series contains a hypothetical *A*-site cation with effective ionic radii same as determined for $MAPbI_3$ which also have a tolerance factor $\sim$ 0.83. But for $MAPbI_3$ we have a finite value of E_{HS-GS} $\sim$ 0.25, with a tilted ground state. Now the only extra mechanism that is present in $MAPbI_3$ compared to $APbI_3$ is the hydrogen bonding due to the presence of hydrogen atoms associated with the molecule. Based on this result they conclude that octahedral tilting in $MAPbI_3$ appears to be induced by hydrogen bonding and not by the size of the molecule.

In the fourth and fifth chapters of this thesis we study the role of the organic molecule in determining the properties of such materials taking the example of $(CH_3NH_3)PbBr_3$ [79]. The molecule CH_3NH_3 has two parts, the amine part(NH_3 group) and methyl part(CH_3 group). To have an idea of how the molecule interacts with the inorganic network, we mapped the *ab-initio* band structure onto a tight binding model. This helped us to switch off the covalent interactions between specific pair of atoms. Considering the optimized structure, we switched off the interactions between hydrogen and Br atoms. We see that the gain from covalency between methyl part and Br ions is almost an order of magnitude higher than the covalency gain from amine part. Due to the different nature of the two parts of the molecule it also acts as an electric dipole. Having understood the energetics governing the location of the molecule in the octahedral cavity as well as its interactions with the inorganic cage, we proceed to examine if the calculations could throw some light on the glassy dynamics that have been seen within the orthorhombic phase where the dipoles are believed to be frozen and ordered. Our analysis of small excursions of the molecule about its position in the optimized structure, and allowing the inorganic network to accommodate that change, suggest that the energy landscape is complex with multiple minimums which are close in energy. The differences in the structures are small with the molecule having different orientations. The presence of such close lying minima separated by large barriers are evidence for the observed glassy dynamics. The system could be quenched into either of these configurations which can additionally be accessed by thermal excitations.

The ordering of such microscopic dipoles in a material may or may not take place leading to ferroelectric properties. On the other hand there are materials which are at the brink of a ferroelectric transition, where the dipolar order is being suppressed by quantum fluctuations. Usual examples of ferroelectrics are d^0 materials i.e. those which have an empty d shell. This has been an empirical principle being used to roughly identify materials which would be ferroelectric. While not all d^0 materials are ferroelectric, it has been seen that several of them could be identified as incipient ferroelectrics, where there is no ferroelectric order down to low temperatures. TiO_2 is one such example. In such materials, a small perturbation could drive the system ferroelectric. In the sixth chapter of this thesis using *ab-initio* density functional theory calculations [80], we explore doping a Nb-Cr pair in TiO_2 as a route to drive it ferroelectric. Nb and Cr go into the 5+ and 3+ valence states and therefore behave like a dipole. Analogous to dilute magnetic semiconductors, where doping small concentrations of magnetic atoms in otherwise non-magnetic materials drives the system magnetic, here, the introduction of the dipole is shown to polarize regions in the vicinity of the dopant. Ferroelectricity is therefore found to be stabilized. While this mechanism is indeed found to work at low Nb-Cr doping, at higher doping concentrations a clustering of the dopant atoms is found to destroy long-range ferroelectric order. Finally in the seventh chapter we show how structural differences can lead to dissimilar ferroelectric properties considering two well known ferroelectric materials $BaTiO_3$ and $PbTiO_3$. Tetragonality in the ferroelectric structure of $BaTiO_3$ is smaller than $PbTiO_3$. Hence the off-center displacement of the Ti atom along the tetragonal axis is assisted by short-ranged repulsion forces that pushes the planer oxygen atoms in the opposite direction to that of the Ti atom. Where as due to a larger tetragonality in $PbTiO_3$, Ti displacement is dominated by the covalency gain between Ti atom and apical oxygen. So, in the next section we are going to discuss the general dielectric properties of ferroelectric materials and show how cation displacements within the octahedral units can lead to ferroelectric order in the system.

1.6 Ferroelectricity due to cation displacement

We have already discussed the importance of structural distortions like octahedral rotations and deformations in controlling the electronic structure of perovskite materials. In those cases, we mainly emphasized the role of A-site cation in controlling the octahedral tilts and distortion of the BX_6 octahedra as a result of the specific electronic configuration of the B cation. In such structural distortions, mainly the anions were displaced about the heavier cations which were fixed at particular lattice sites. However, distor-

tions due to the displacement of the cations can also lead to interesting properties in a perovskite system. The A-site cation, in general, does not have any direct contribution to the electronic properties and mainly results in steric effects. But the B-site cation could be responsible for magnetic properties of the material. Depending on the electronic configuration we could have a permanent magnetic moment of the B cation that can give rise to magnetic ordering. The B cation can also result in ferroelectric properties as a result of its displacement from the center of the octahedra. In this section, we are going to discuss the general properties of a ferroelectric material and the origin of ferroelectricity due to such cation displacements in perovskites.

1.6.1 Electric polarization and Dielectric response

Corresponding to the response of a material in the presence of an external electric field one may divide all materials into broadly two classes, conductors, and dielectrics. By response we mean the material getting polarized, i.e. the development of an electric field inside the material. Conductors contain a lot of free charges that are free to roam through the whole material. If there is an electric field inside such a material, the free charges redistribute in such a way to cancel the field so that the net field inside the material is zero. In the case of dielectrics, there are no free charges. All electronic charges are attached to atoms that build the material. Simply we can think that in the presence of an external electric field($\mathbf{E}_0$) the charges are unable to get detached from the atoms, but they are slightly displaced so that the positive and negative charge center of each atom gets separated to form a tiny dipole. And the material gets polarized when all the atomic dipoles point in the same direction. So, when we are speaking of polarization of a material, we are speaking of a macroscopic polarization [81] which is the average polarization over a large enough region consisting of many thousands of atoms. Because in the microscopic or atomic level there may be local polarization or local moments even in conductors due to charge separation but when we try to find the macroscopic polarization by averaging over a large enough region, we find that the moments are randomly oriented resulting in zero polarization. The Polarization of a dielectric material is measured with polarization vector $\mathbf{P}$ defined as,

$$\mathbf{P} = \textit{Electric dipole moment per unit volume.}$$

[This unit volume is large enough to accommodate many atoms and molecules.]

Dielectric materials can have different polarization mechanisms that can respond to an external electric field and result in polarization of the material. These are discussed below in brief:

1. **Electronic polarization:** If we consider any material simply as a collection of atoms then, with the application of an external electric field the atoms become polarized forming atomic dipoles. As shown in Figure 1.18(a), the electron cloud of each atom surrounding the nucleus become shifted by the field and the atom act as a dipole. This gives rise to electronic polarization. Solids formed as a result of van der Waals force, for example, solid Ar below 83.8 K are a collection of inert atoms where the electron cloud is tightly attached to their nuclei. In such case, the electronic polarization is quite small because the electron hardly shifts with respect to the nucleus. Whereas electronic polarization in covalent solids due to the valence electrons in the covalent bonds is much higher and significant. For example, in crystalline silicon, there are electrons shared with neighboring Si atoms in covalent bonds which are loosely bound to their parent atoms. When an electric field is applied, the negative charge distribution associated with these valence electrons becomes easily shifted with respect to the positive charges of the ionic Si cores and results in a large polarization.

2. **Ionic polarization:** This type of polarization occurs in ionic crystals such as NaCl, KCl etc. The ionic crystal is formed due to electrostatic interactions between ions located at well defined lattice sites. As an example, if we consider a one-dimensional(1D) NaCl crystal then as shown in the upper panel of Figure 1.18(b), it can be depicted as a chain of alternating Na^+ and Cl^- ions. Each pair of oppositely charged ions act as an electric dipole($\mathbf{p}$). In the absence of an external field, there is no net polarization because the dipole moments are lined up head to head and tail to tail canceling each other. The dipole $\mathbf{p}_+$ along the +ve x-axis cancels the dipole $\mathbf{p}_-$ along the -ve x-axis. Now if we apply an electric field along the +ve x-axis, then as shown in the lower panel of Figure 1.18(b), the Cl^- ions are pushed in the $-x$-direction and the Na^+ ions in the $+x$-direction about their equilibrium positions. In such a situation we have $\mathbf{p}_+ > \mathbf{p}_-$ and the net dipole moment is now no longer zero.

3. **Orientational/Dipolar polarization:** Some molecules possess a permanent dipole moments as a result of their ionic components. For example, the linear HCl molecule has a permanent dipole moment $\mathbf{p}$ from the Cl^- ion to the H^+ ion[Figure 1.18(c)]. In the liquid or gas phases, and in the absence of an electric field, they are

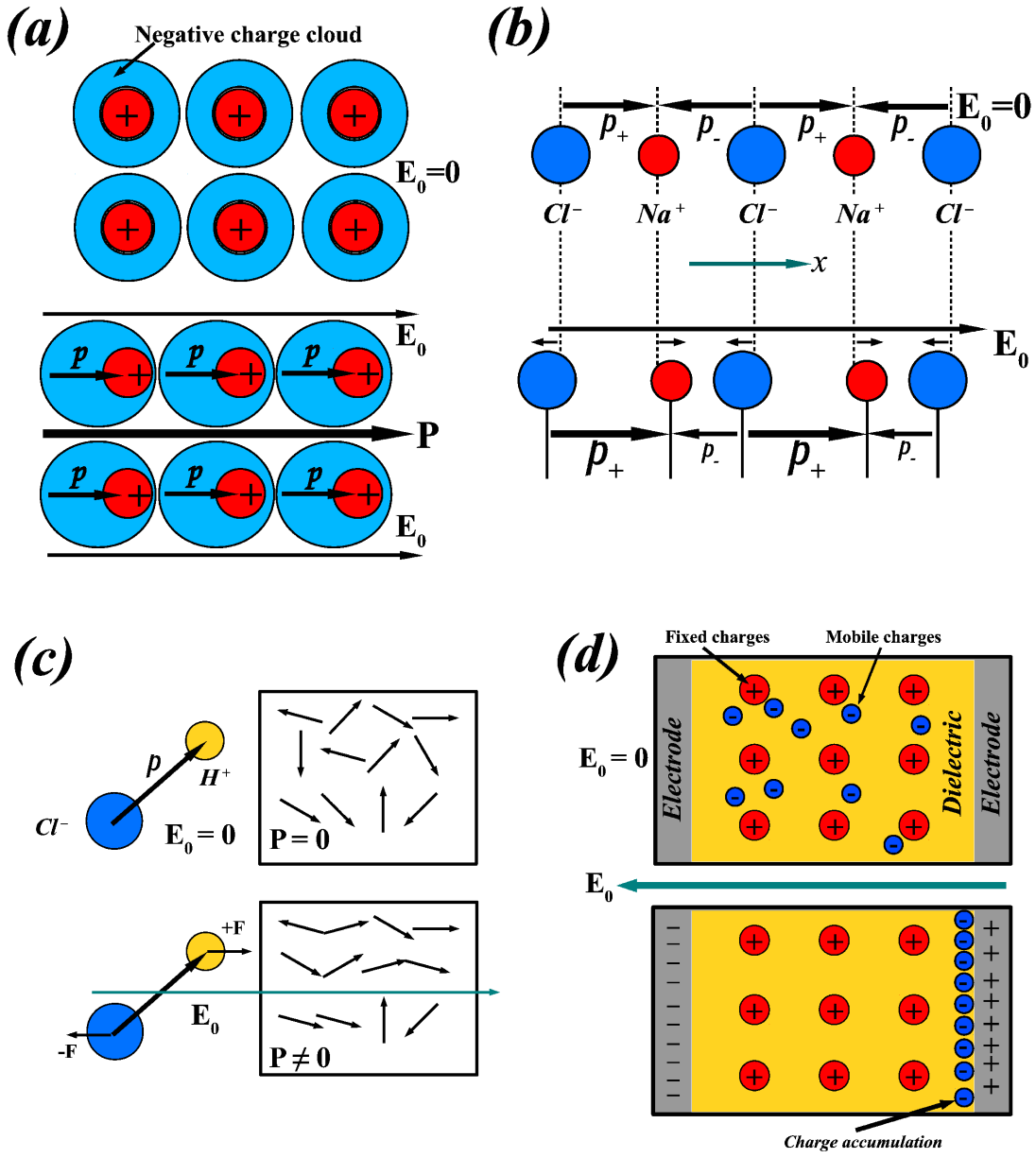

Figure 1.18: (a) The charge distribution of the valence electrons around the ion cores in a covalent solid, in absence and presence of an electric field. In the presence of an electric field, they are shifted with respect to the ion cores and act as a dipole. This gives overall polarization of the material. (b) A 1D NaCl chain. Without any external field, the positions of the ions are such that the dipoles along +ve and -ve x-direction cancels each other. But in the presence of an external field, the ions get shifted and there is a net dipole moment per unit cell. (c) The HCl molecule possesses a dipole moment **p** due to the H^+ and Cl^- ions. In the absence of any field, the dipoles are random due to thermal agitation. An external electric field produces a torque on the dipoles and tries to align them with the field direction. (d) A dielectric material between two electrodes with an equal number of positive ions and negative ions. The negative ions can move and with the application of an electric field, they accumulate at the interface near the positive electrode. There is a charge separation with a net polarization

randomly oriented as a result of thermal agitation[upper panel of Figure 1.18(c)]. Application of an external electric field **E** tries to align the dipoles of each individ-

ual molecule along the field direction and the material gets polarized[lower panel of Figure 1.18(c)].

4. **Interfacial polarization:** Interfacial polarization occurs whenever there is an accumulation of charge at an interface between two materials or between two regions within a material. The simplest example is interfacial polarization due to the accumulation of charges in the dielectric near one of the electrodes, as depicted in Figure 1.18(d).

The dielectric response in a simple sense is the dependence of the polarization or related /associated measurable quantities that can be directly measured from an experimental setup, with the electric field. It is an important tool for material characterization. We can get a lot of information both macroscopic as well as microscopic from this kind of measurements . The best way to see the dependence is by varying the electric field and see how polarization changes. The ultimate case would be to see the dependence with an *ac* electric field.

Dielectrics are used in capacitors, so let us start from here and know some general and basic macroscopic properties of a dielectric material. In a parallel plate capacitor, the charge stored on each plate($\pm$Q) is related to the potential difference(V) between the two plates as,

$$Q = CV \tag{1.12}$$

where, C is the capacitance of the capacitor. For a parallel plate capacitor,

$$C = \epsilon \frac{A}{d} \tag{1.13}$$

where, A = surface area of the plates, d = distance between the plates, ϵ = permittivity of the dielectric material between two plates. $\epsilon = \epsilon_0 \epsilon_r$, where, ϵ_0 is the permittivity of free space with a value of 8.85×10^{-12} F/m and ϵ_r is the relative dielectric permittivity or dielectric constant of the material. Now applying Gauss's law for a parallel plate capacitor gives,

$$|\mathbf{E}| = \epsilon \frac{V}{d} \tag{1.14}$$

where **E** is the total field inside the dielectric material. That means the material is now polarized and for most of the materials the polarization(**P**) becomes a linear function of the electric field **E** defined as [81],

$$\mathbf{P} = \chi \mathbf{E} \tag{1.15}$$

where χ is called the dielectric susceptibility and the materials that follow the above equation are called linear dielectrics. If a dielectric material is placed in an external electric field $\mathbf{E}_0$ then **P** cannot be computed from Equation (1.15) directly. So, we have to deal with a physically measurable quantity, **D**, the electric displacement field defined as,

$$\mathbf{D} = \epsilon \mathbf{E} = \epsilon_0 \mathbf{E} + \chi \mathbf{E} = \epsilon_0 \mathbf{E} + \mathbf{P} \tag{1.16}$$

For a parallel plate capacitor, $\mathbf{D} = Q/A$. Now, the above equations are for static electric field and with this, we do not get any information about the material properties. This is only possible if we observe the behavior of **P** in an *ac* field. Equation (1.15) is equally valid if **E** oscillates with a frequency $\omega(\omega = 2\pi f)$, given as [82],

$$\mathbf{P}(\omega) = \chi(\omega)\mathbf{E}(\omega) \tag{1.17}$$

One of the source of such oscillating electric field is the field in electromagnetic radiations, $\mathbf{E} = \mathbf{E}_0 cos(\omega t)$. The detail expression for Equation (1.17) can be derived by considering the polarization mechanism that is present in the material and how they behave under the oscillating electric field.

Complex analysis, by representing the oscillating electric field and polarization in term of exponential quantities gives an expression of $\chi(\omega)$ which is also complex with a real and imaginary part as,

$$\chi(\omega) = \tilde{\chi}(\omega) = \chi^{'}(\omega) - i\chi^{''}(\omega) \tag{1.18}$$

$\chi^{'}(\omega)$ defines the real component of $\mathbf{P}(\omega)$ in the equation, $\mathbf{P}(\omega) = \tilde{\chi}(\omega)\mathbf{E}_0 exp(i\omega t)$, where we consider the electric field at a particular point in space, i.e. in phase, with $\mathbf{E}(\omega) = Re[\mathbf{E}_0 exp(i\omega t)] = \mathbf{E}_0 cos(\omega t)$. So, $\chi^{'}(\omega)$ gives a measure of the oscillating polarization. $\chi^{''}(\omega)$ is often called the power dissipation factor. This arises due to the presence of damping terms in the equation of motion governing the evolution of the polarization

components under the oscillating field. In a broad sense, $\chi^{''}(\omega)$ indicates that the electric field has to do some work on the dielectric material to produce a net dipole moment density. Some energy is stored in the process of charge separation and is recoverable. Rest of the energy is used to overcome friction or resistance that opposes the development of dipole moment density or charge movement.

Frequency dependence of $\chi^{'}(\omega)$ and $\chi^{''}(\omega)$ gives important information about the polarization mechanism present in a dielectric material. Let us consider a system of N hydrogen atoms. We consider the nucleus to be fixed at lattice sites such that the only polarization mechanism present is electronic polarization due to the displacement of the single electron. If we consider an electric field applied along a particular direction then, we can model each atom as a 1D simple harmonic oscillator of mass m, charge q and force constant k, which can respond to an applied electric field with frequency ω. Solving the equation of motion for a forced and damped harmonic oscillator for such N oscillators gives a value for $\chi^{'}(\omega)$ and $\chi^{''}(\omega)$ as [83],

$$\chi^{'}(\omega) = \frac{Nq^2}{m}\left[\frac{(\omega_0^2 - \omega^2)}{(\omega_0^2 - \omega^2)^2 + \gamma^2\omega^2}\right] \tag{1.19}$$

$$\chi^{''}(\omega) = \frac{Nq^2}{m}\left[\frac{\gamma\omega}{(\omega_0^2 - \omega^2)^2 + \gamma^2\omega^2}\right] \tag{1.20}$$

where ω_0 is the natural frequency of oscillation of each of the oscillator and γ is the damping constant. A schematic plot of $\chi^{'}(\omega)$ and $\chi^{''}(\omega)$ as a function of the frequency, ω in the vicinity of the resonance frequency ω_0 is shown in Figure 1.19(a). As we go from left to right, $\chi^{'}(\omega)$ slowly increases with increasing frequency, this is called normal dispersion. As we reach the resonance frequency, $\chi^{'}(\omega)$ shows a sharp drop which signifies that the polarization mechanism gets inactive at larger frequencies as it is unable to follow the rapid switching of the polarizing field. This happens due to the damping and hence $\chi^{''}(\omega)$ shows a peak about the resonance frequency ω_0 indicating large energy dissipation as a result of large amplitude oscillation of the polarization elements. Here the broadening of $\chi^{''}(\omega)$ is due to the damping. More the damping more broad shall be the peak. Now frequency dependence of $\tilde{\chi}$ leads to a similar frequency dependence of the permittivity $\tilde{\epsilon}$ defined as,

$$\tilde{\epsilon}(\omega) = \epsilon_0 + \tilde{\chi}(\omega) = \epsilon^{'}(\omega) - i\epsilon^{''}(\omega) \tag{1.21}$$

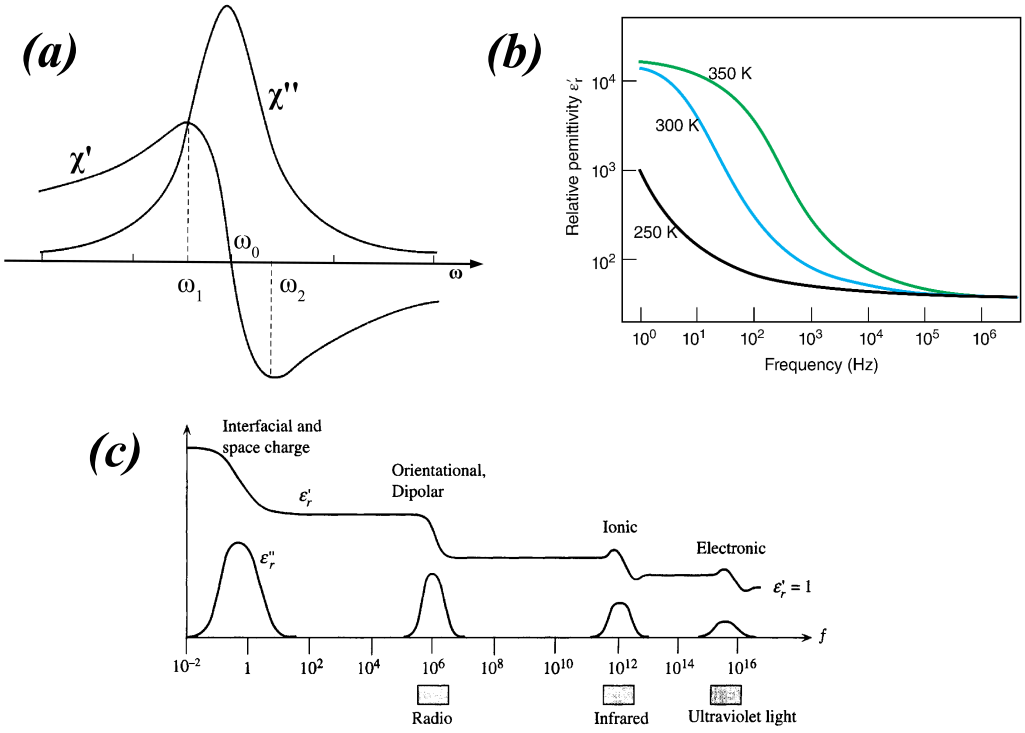

Figure 1.19: (a) A schematic representation of the frequency dependence of the real($\chi^{'}$) and imaginary($\chi^{''}$) part of dielectric susceptibility in the vicinity of the resonance frequency ω_0 (b) The temperature and frequency dependence of the relative permittivity, $\epsilon_r^{'}$, of $SrFe_{0.5}Ta_{0.5}O_3$ ceramics[Figure taken from Ref. [84]]. The logarithmic scales on each axis shall be noted. (c) The frequency dependence of the real($\epsilon_r^{'}$) and imaginary($\epsilon_r^{''}$) part of dielectric permittivity in the presence of interfacial, orientational, ionic, and electronic polarization mechanisms.[Figure taken from Ref. [85]]

The relative permittivity then becomes,

$$\tilde{\epsilon}_r(\omega) = \frac{\tilde{\epsilon}(\omega)}{\epsilon_0} = 1 + \frac{\tilde{\chi}(\omega)}{\epsilon_0} = \epsilon_r^{'}(\omega) - i\epsilon_r^{''}(\omega) \tag{1.22}$$

which gives,

$$\epsilon_r^{'}(\omega) = 1 + \frac{Nq^2}{m\epsilon_0}\left[\frac{(\omega_0^2 - \omega^2)}{(\omega_0^2 - \omega^2)^2 + \gamma^2\omega^2}\right] \tag{1.23}$$

and,

$$\epsilon_r^{''}(\omega) = \frac{Nq^2}{m\epsilon_0}\left[\frac{\gamma\omega}{(\omega_0^2 - \omega^2)^2 + \gamma^2\omega^2}\right] \tag{1.24}$$

In this regard we shall also define an important quantity often used in relation to the energy dissipation, called the dielectric loss factor or loss tangent and is defined as [85],

$$tan\delta = \frac{\epsilon_r^{''}}{\epsilon_r^{'}} \tag{1.25}$$

For material with no loss $\epsilon_r^{''} = 0$ and hence $tan\delta = 0$. The dispersion measurements are done in an isothermal way at a particular temperature. However, a variation of the quantities with temperature is also necessary and done, which can show the important signature of dielectric phase transition. The temperature has a similar effect on the polarization elements present in the system. The relative permittivity $\epsilon_r^{'}$ will tend to increase with temperature as polarizing elements become more mobile and they can easily respond to the oscillating field. The dependence of $\epsilon_r^{'}$ on temperature and measuring frequency of the dielectric ceramic material $SrFe_{0.5}Te_{0.5}O_3$ [84] is shown in Figure 1.19(b).

In real materials, there are many polarization mechanisms and depending on their response to the oscillating field, the dispersion of $\epsilon_r^{'}(\omega)$ and $\epsilon_r^{''}(\omega)$ can be very complicated. We can represent the general features of the frequency dependence of $\epsilon_r^{'}(\omega)$ and $\epsilon_r^{''}(\omega)$ as shown in Figure 1.19(c) [85]. Although the figure shows distinctive peaks in $\epsilon_r^{''}(\omega)$ and transition features in $\epsilon_r^{'}(\omega)$, in reality, these peaks and various features are broader. Moreover, the polarization effects depend on the crystal orientation. In the case of polycrystalline materials, various peaks in different directions overlap to exhibit a broadened overall peak [85]. Another interesting fact to note is the response frequency of different mechanisms. The resonance frequency for electronic polarization mechanism is higher than ionic, simply because in terms of oscillation electrons are much lighter than nuclei. Here we have an oscillation of electrons with respect to nuclei in an atom itself. Whereas in case of ionic polarization, oscillation of two different ions with respect to each other takes place. At low frequencies the space charge polarization occurs with more broader peaks because there can be a number of conduction mechanisms (different species of charge carriers and different carrier mobilities) for the charges to accumulate at interfaces, each having its own speed [85]. Orientational polarization, especially in many liquid dielectrics at room temperature, typically takes place at radio to microwave frequencies.

1.6.2 Ferroelectricity and its origin in perovskite $BaTiO_3$

Ordinary dielectric materials have a polarization in the presence of an external electric field only and get depolarized when the field is removed. But there are some dielectric materials that have a spontaneous polarization($\mathbf{P}_S$) i.e. they remain polarized even in the absence of any external electric field. The materials that show this property are called ferroelectrics. The distinguishing feature of ferroelectrics is that the spontaneous

polarization can be reversed by an applied electric field($\mathbf{E}_0$). The polarization($\mathbf{P}$) becomes a nonlinear function of the internal electric field $\mathbf{E}$. It is now dependent not only on the current electric field but also on its history, yielding a hysteresis loop. Ferroelectric effect was first observed in Rochelle salt (Potassium sodium tartrate a double salt with molecular formula $KNaC_4H_4O_6.4H_2O$) in 1917 by A.M. Nicolson and J.A. Anderson [86]. A few years later the physical properties of Rochelle salt were described in detail in a series of papers by J. Valasek around 1921 [87, 88]. However discovery of ferroelectricity in perovskite $BaTiO_3$ by Wul and Goldman (1945, 1946) [89] followed by other perovskites, such as $KNbO_3$ and $KTaO_3$(Matthias 1949), $LiNbO_3$ and $LiTaO_3$(Matthias and Remeika, 1949) and $PbTiO_3$(Shirane, Hoshino and Suzuki, 1950) [90], made it possible to investigate the microscopic origin of ferroelectricity in much simpler systems [91]. It is easy to understand that, in a ferroelectric material there are permanent dipole moments at the atomic level, which are correlated and points in the same direction even in absence of an external electric field. This gives rise to a spontaneous macroscopic polarization. In a crystalline material such permanent dipole moments shall develop within the structural unit or the unit cell. The correlation mechanism between the dipoles that makes them order is an important subject to study. But before that we shall understand how a permanent dipole can be generated in a crystalline material. Here we are going to to discuss how B-site cation displacement in perovskites can give rise to permanent dipole moment, taking the well known ferroelectric $BaTiO_3$ as an example.

The fundamental cause of ferroelectricity in oxide perovskites was originally attributed to the idea that a small B-site cation could 'rattle around' inside the BO_6 octahedra and off-center configurations can lead to stability of the structure [84, 92]. Considering a cubic unit cell for $BaTiO_3$, the Ti atom sits inside the center of a regular octahedron surrounded by six oxygen atoms[Figure 1.20(a)]. Now if we consider the system to be purely ionic, $BaTiO_3 \rightarrow Ba^{2+}Ti^{4+}O_2^{2-}$, then the Ti^{4+} ion would like to sit at the center of the octahedra for a maximum gain from electrostatic interactions. But as Ti^{4+} is a d^0 system, hence there is a significant covalent interaction possible between Ti and O atoms as a result of electron hopping. As a result, as shown in Figure 1.20(a), the Ti atom can move towards any one of the oxygen atoms to gain from an increased hopping interaction. Considering this facts W. P. Mason [92] *et al.* proposed a simple model for ferroelectricity in $BaTiO_3$ around 1948. In this model the small Ti^{4+} ion surrounded by six oxygen ions is depicted as being in an off-center six fold potential well minimum. Here, there is six potential minimum in the direction of the six oxygens which are displaced a distance δ from the center of the octahedra[see Figure 1.20(b)]. If the titanium nucleus is taken from a position such as 1 to position 2 directly across the unit cell, the form of the potential barrier may be as shown in Figure 1.20(c), in which ΔU represents the height of the

potential curve at the center with respect to that at the minimum. So under equilibrium condition the Ti^{4+} cations occupies any one of the minima via a displacement from the center.

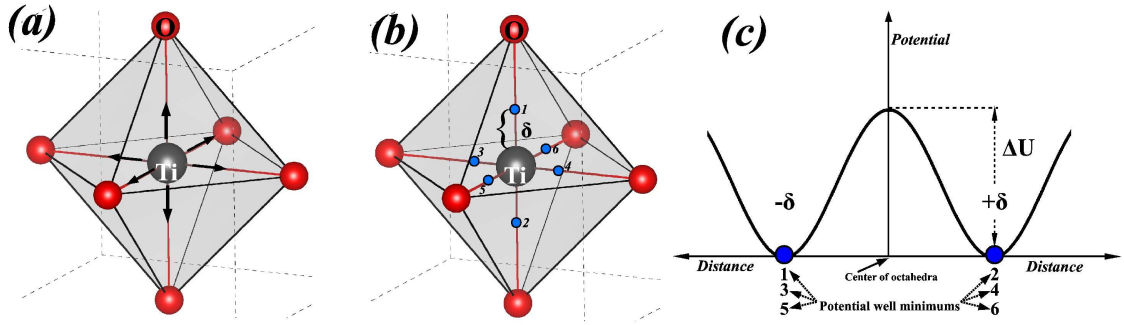

Figure 1.20: (a) Regular TiO_6 octahedra with the Ti atom surrounded by six oxygen atoms. Possible directions of movement of the Ti atom is shown by the arrows. (b) Location of six potential well minimums along the six Ti-O bonds at a distance δ from the center of the octahedra. (c) Shape of the potential barrier with height ΔU at the center of the octahedra during movement of the Ti ion from one minima to the other.

The displaced *B*-site cation creates an electric dipole within each octahedron. The direction of the dipole, or, equivalently, the position of the cation, could be switched from one off-center position to another under the influence of an external electric field. Above 120^o C, $BaTiO_3$ adopts the ideal cubic perovskite structure with lattice parameter, a = 3.97 Å [84] and behave like a normal paraelectric material. At this temperature the thermal energy becomes comparable to the barrier height ΔU, and without an applied field the dipoles are random due to thermal agitation. Below 120^o C an external electric field can make the cations to move towards a preferred direction which shall remain even after the removal of the field generating a spontaneous polarization, characteristic of a ferroelectric state. Such off-center displacement of the Ti atom $\sim$ 0.16 Å was measured with X-ray methods by Gordon Danielson [93]. However, there is also a cubic to tetragonal phase transition at 120^o C which was confirmed by X-Ray measurements for multicrystalline ceramic [94].

Below 120^o C the cubic cell contracts slightly along the a and b axes and expands slightly along the *c*-axis becoming tetragonal in shape[Figure 1.21(a)]. The change from cubic to tetragonal is accompanied by an off-center movement of the Ti^{4+} ions along the *c*-axis, and a slight change in octahedron dimensions so that two equatorial oxygen atoms move parallel to the +ve *c*-axis and in the opposite direction [Figure 1.21(b)]. The Ti-O bond lengths parallel to the *c*-axis now becomes, 2.2 and 1.8 Å respectively, while the equatorial bond lengths remain at 2 Å. This results in the formation of a dipole within each octahedron, with a net dipole moment $\sim$ 26 μCcm^{-2} [84], each pointing along the

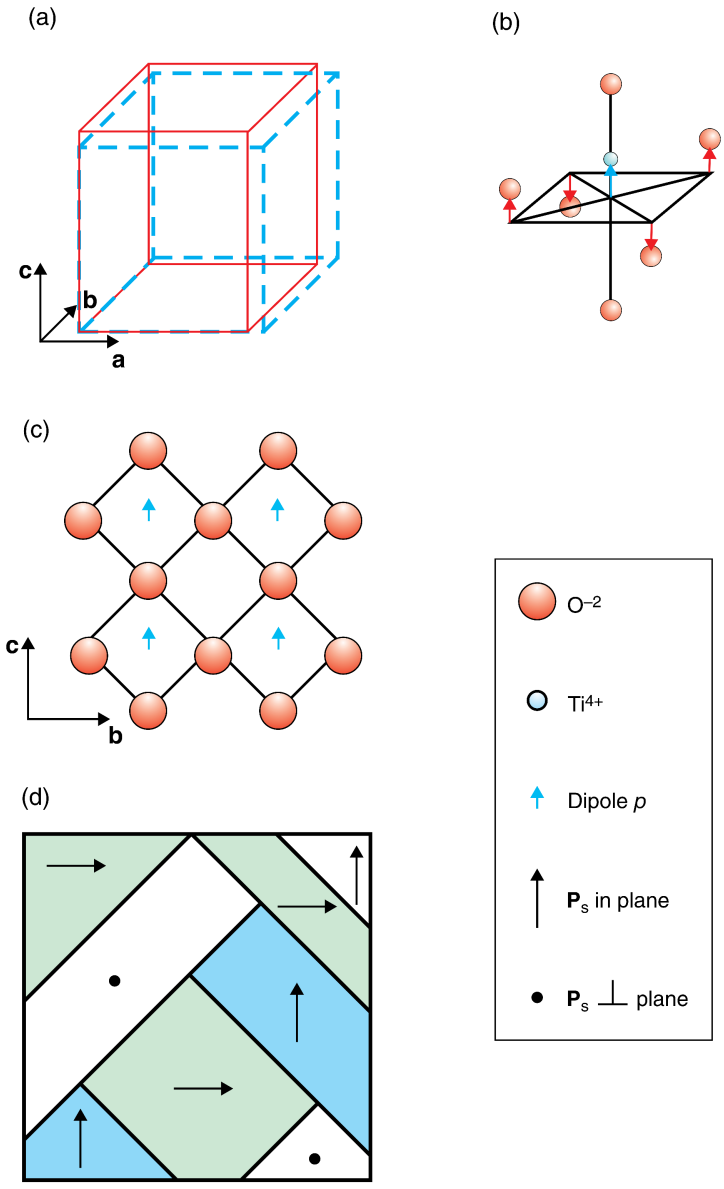

Figure 1.21: Tetragonal $BaTiO_3$: (a) The tetragonal unit cell compared to the cubic unit cell (dashed). Tetragonality is along the c-axis. (b) Displacements of the Ti and O atoms found in tetragonal $BaTiO_3$; (c) a schematic showing dipole array in tetragonal $BaTiO_3$; (d) schematic of a typical domain structure in a crystal slice. (All distortions are greatly exaggerated)[Figures are taken from Ref. [84]].

c-axis [Figure 1.21(c)]. So, now with a cubic to tetragonal phase transition, we have an easy axis of polarization(here c-axis) such that the ferroelectric distortion occurs in that direction and the material becomes spontaneously polarized. However the off-center Ti^{4+} position and the octahedral deformation can be changed with an electric field and hence the tetragonal phase of $BaTiO_3$ is ferroelectric [84] in nature. Now there is no preference as to which of the original cubic axes becomes the polar direction. It can happen along x, y or z-axis. On cooling a large crystal, any of these displacements is possible, and within

different regions of the crystal different orientations occur, leading to the formation of domains in which all the dipoles are aligned in a particular direction [Figure 1.21(d)]. The polarization directions in a domain are related to those in neighboring domains by the crystallography of the matrix [84].

1.6.3 Displacive phase transition and soft modes

All ferroelectric materials undergo a transition from a ferroelectric state to a paraelectric state on heating. This suggests that with heating either the microscopic dipole moments are now randomly oriented with each other to give an average polarization of zero or the microscopic dipole moments no longer exists to give a net polarization. The first case is known as an order-disorder phase transition. In the second case, the permanent dipole moments emerges below the transition temperature and becomes ordered to give rise to a spontaneous polarization. This is called a displacive phase transition. This type of phase transition is associated with a structural transition where the system undergoes a symmetry change. $BaTiO_3$ shows a displacive phase transition associated with a cubic to tetragonal distortion of the unit cell.

In the early 60's, the soft-mode concept was proposed to describe the mechanism of structural phase transitions related to ferroelectric materials. The predictions made by Cochran [95] that the phase transition in certain ferroelectrics might result from dynamical instability was a beginning. Any dynamic distortion (vibrational state) in a crystalline solid can be described in terms of its complete set of normal modes of vibration or phonons. When a solid experiences a transition from one crystal structure to another, the transition is often described essentially completely in terms of anomalous behavior of only a single such mode, characterized by its displacement eigenvector, frequency, and wavelength [96]. By a soft mode, it is meant that a normal vibrational mode (phonon) of the crystal which becomes unstable, so that it's normal frequency ω_s (at some particular wave vector $\mathbf{q}$ in the brillouin zone) tends to zero as $T \longrightarrow T_c$[Figure 1.22(a)].

This softening occurs as a result of anharmonic interactions in the crystal that cause a temperature renormalization of the phonon frequencies. Considering the anharmonicities the temperature dependence of the soft mode is then given as [97],

$$\omega^2 = \frac{|\omega_0^2|}{T_c}(T - T_c) \tag{1.26}$$

where, ω_0^2 is the negative harmonic value that we would calculate in the lattice dynamics calculation. The idea of the soft mode for displacive ferroelectric phase transitions is

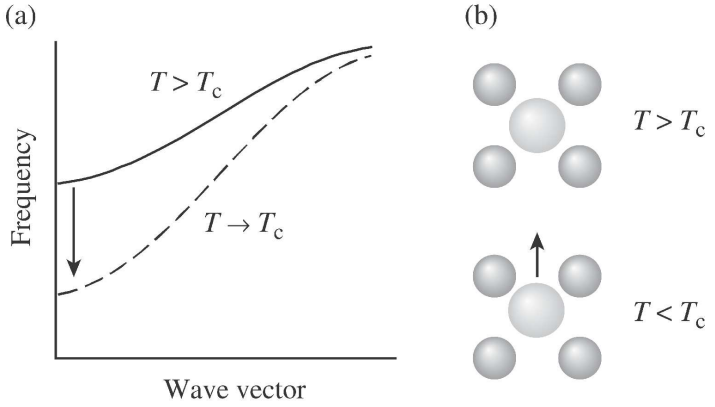

Figure 1.22: Schematic representations of ferroelectric soft mode behaviour: (a) behaviour of the phonon dispersion curves with temperature. (b) Atomic displacements. [Figures are taken from Ref. [97]]

implicit in the Lyddane-Sachs-Teller relation giving the relation between the low and high-frequency dielectric responses of the dielectric permittivity ϵ given as

$$\frac{\epsilon(\omega = 0)}{\epsilon(\omega = \infty)} = \frac{\omega_{LO}^2}{\omega_{TO}^2} \tag{1.27}$$

The point is that since the static dielectric constant $\epsilon(\omega = 0)$, diverges at the ferroelectric phase transition, then the above relation implies that ω_{TO}^2 tends to 0 at the same time. A particular phonon frequency going to zero indicates that the corresponding vibration (or the atomic positions) become "frozen" at this temperature and is no longer dynamical and produce a structure of another symmetry. This is schematically shown in Figure 1.22(b). It is to be noted that whereas in a second-order transition, the soft-mode frequency actually vanishes at the transition point, in a first-order transition the change of phase occurs before the frequency of the mode is able to go to zero [98]. Also softening occurs whenever we approach the transition temperature T_c for cooling or heating. This is expected because if the structural transition during cooling is due to the condensation of a soft-mode that exists above T_c then there must be some modes for the structure below T_c, instability or condensation of which gives rise to the phase transition as T_c is reached during the heating process. And there are as many soft modes below T_c as there are above T_c [98].

The structure of the new phase is uniquely determined by the eigenvector of the soft mode and the structure of the old phase. The eigenvector of a phonon mode is simply the array of atomic displacements relative to the lattice sites accompanying the excitation of that mode [96]. The vanishing of the normal mode frequency at T_c corresponds to a static imposition of this array of atomic displacements on the old structure[Figure 1.22(b)]. The

eigenvector of the soft mode $\mathbf{q}_c$ not only gives the displacement of the atoms within the unit cell relative to the lattice sites of the old phase to give a new structure, but it also determines the phase modulation of the displacement amplitude from one unit cell to the next through the same wave vector $\mathbf{q}_c$ (point to note is that $|\mathbf{q}| = 2\pi/\lambda$, where λ is the phonon wavelength).

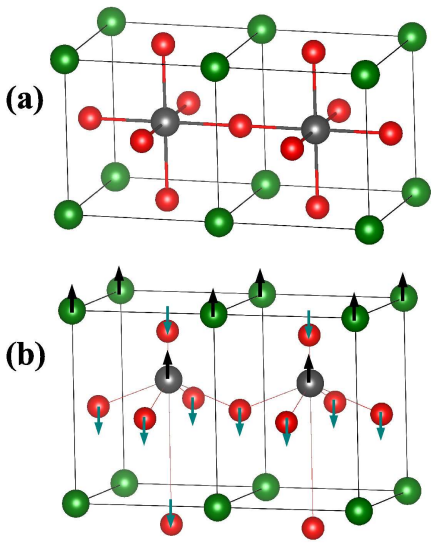

Figure 1.23: A typical structural distortion due to zone center phonon softening. For (a) $T > T_c$ and (b) $T < T_c$.

In the simplest case, such as the displacive ferroelectric phase transition, the array of displacements is identical for all unit cells, i.e. $\mathbf{q}_c = 0$. The phonon instability then occurs at the center of the Brillouin zone and there is no change in the number of atoms per unit cell in the phase transformation. For example, the non-ferroelectric cubic perovskite lattice as shown in Figure 1.23(a), is centrosymmetric(O_h^1). Displacement of the atoms as shown in Figure 1.23(b), removes the center of symmetry (C_{4v}) and imparts a dipole moment to the unit cell. The distortion in Figure 1.23(b), is just that carried by the lowest frequency transverse optic (infrared active) phonon [96].

Generally, however, the soft-mode eigenvector is more complicated and when $\mathbf{q}_c \neq 0$, both the magnitude and direction of $\mathbf{q}_c$ determine the size and shape of the new unit cell relative to the old. A number of crystals undergo phase transitions which involve softening of phonon mode at Brillouin zone boundaries. In these cases, the soft phonons can be either acoustic or optic modes[Figure 1.24(a)]. Because of mixing of eigenvectors, it is often the case that the distinction between them is not straightforward . One of the interesting results of a zone boundary soft mode phase transition is that the unit cell of the low-temperature phase is doubled in one or more directions. In some cases neighboring unit cells of the high-temperature state develop dipole moments, but as these

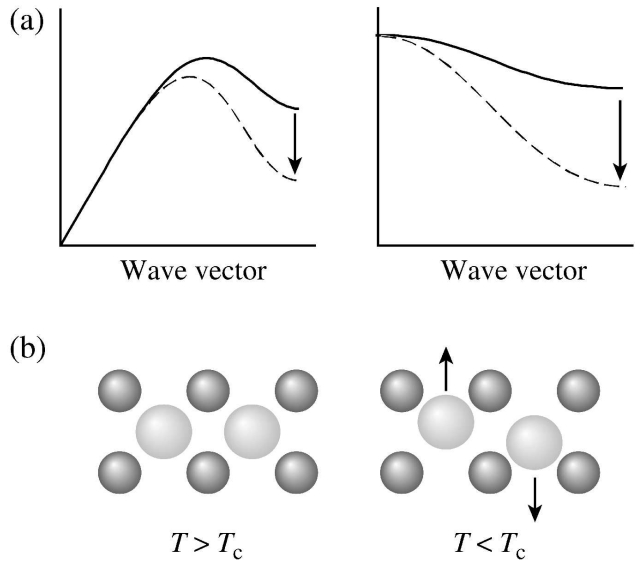

Figure 1.24: Schematic behaviour of (a) zone boundary acoustic and optic soft modes.(b) Atomic displacements showing doubling of the unit cell and canceling induced dipole moments. [Figures are taken from Ref. [97]]

are in opposite directions the unit cell at low temperature has no net moment[Figure 1.24(b)] [97]. The best example of a zone boundary phase transition is the cubic to tetragonal transition in the perovskite $SrTiO_3$ (transition temperature 110 K).

In this context we shall know that, whereas a ferroelectric phase transition is characterized by softening of a particular zone center phonon mode, in case of incipient ferroelectrics, the softening of a phonon mode occurs with a decrease in the temperature but never becomes completely soft down to lowest possible temperatures.

Bibliography

[1] G. Catalan, Phase Transitions **81**, 729 (2008).

[2] S. Middey, P. Mahadevan and D. D. Sarma, Phy. Rev. B **83**, 014416 (2011).

[3] J. M. Rondinelli, S. J. May and J. W. Freeland, MRS Bulletin **37**, 261 (2012).

[4] M. R. Filip, G. E. Eperon, H. J. Snaith and F. Giustino, Nat. Comm. **5**, 5757 (2014).

[5] J. Young and J. M. Rondinelli, J. Phys. Chem. Lett. **7**, 918 (2016).

[6] J. B. Torrance, P. Lacorre, A. I. Nazzal, E. J. Ansaldo and C. Niedermayer, Phy. Rev. B **45**, 8209 (1992).

[7] M. L. Medarde, J. Phys.: Condens. Matter **9**, 1679 (1997).

[8] S. Middey, J. Chakhalian, P. Mahadevan, J. W. Freeland, A. J. Millis and D.D. Sarma, Annu. Rev. Mater. Res. **46**, 305 (2016).

[9] J. M. Rondinelli, S. J. May, and J. W. Freeland, MRS Bull. **37**, 261 (2012).

[10] V. M. Goldschmidt, Naturwissenschaften **14**, 477 (1926).

[11] G. Kieslich, S. Sun, A. K. Cheetham, Chem. Sci. **5**, 4712 (2014).

[12] R. D. Shannon, Acta Crystallographica. A**32**, 751 (1976).

[13] J. Zhao, N. L. Ross and R. J. Angel, Phys Chem Minerals **31**, 299 (2004).

[14] R. Søndenå, S. Stølen, P. Ravindran, T. Grande, and N. L. Allan, Phys. Rev. B **75**, 184105 (2007).

[15] D.I. Khomskii, in Transition Metal Compounds (Cambridge University Press, Cambridge, (2014), pp. 25-36.

[16] H.H. Kung, Transition Metal Oxides: Surface Chemistry and Catalysis, Elsevier Science, NY, 1989.

[17] J. Varignon, M. N. Grisolia, J. Íñiguez, Agnès Barthélémy and Manuel Bibes, npj Quantum Materials **2**, 21 (2017).

[18] Patrick Fazekas, Atoms, Ions and Molecules. In: Lecture Notes On Electron Correlation And Magnetism. World Scientific, (1999), pp. 17-74.

[19] D. van der Marel and G. A. Sawatzky, Phys. Rev. B **37**, 10674 (1988).

[20] H. A. Jahn and E. Teller, Proc. R. Soc. London A**161**, 220 (1937).

[21] J.-S. Zhou, J.A. Alonso, J.T. Han, M.T. Fernández-Díaz,J.-G. Cheng, J.B. Goodenough, Journal of Fluorine Chemistry **132**, 1117 (2011).

[22] I. I. Mazin, D. I. Khomskii, R. Lengsdorf, J. A. Alonso, W. G. Marshall, R. M. Ibberson, A. Podlesnyak, M. J. Martínez-Lope, and M. M. Abd-Elmeguid, Phys. Rev. Lett. **98**, 176406 (2007).

[23] D. D. Sarma and S. R. Barman, Electronic Structure of Transition Metal Compounds. In: Spectroscopy of Mott Insulators and Correlated Metals. Springer Series in Solid-State Sciences, vol 119. Springer, Berlin, Heidelberg (1995).

[24] Patrick Fazekas, Mott Transition and Hubbard Model. In: Lecture Notes On Electron Correlation And Magnetism. World Scientific, (1999), pp. 147-197.

[25] D. Adler, Solid State Physics **21**, 1 (1969).

[26] J. C. Slater, Phys. Rev. **82**, 538 (1951).

[27] N. F. Mott, Proc. Phys. Soc. *A* **62**, 416 (1949).

[28] N. F. Mott, Philos. Mag. **6**, 287 (1961).

[29] N. F. Mott, Metal-Insulator Transitions, Taylor and Francis, London, (1974).

[30] D.I. Khomskii, in Transition Metal Compounds (Cambridge University Press, Cambridge, (2014), pp. 1-24.

[31] J. Hubbard, Proc. Roy. Soc. A **276**, 238 (1963).

[32] J. Hubbard, Proc. Roy. Soc. A **277**, 237 (1964).

[33] C. R. Ronda, G. J. Arends and C. Hass, Phys. Rev. B **35**, 4038 (1987).

[34] J. Zaanen, G.A. Sawatzky and J. W. Allen, Phys. Rev. Lett. **55**, 418 (1985).

[35] D. D. Sarma, J. Solid State Chem. **88**, 45 (1990).

[36] S. Nimkar, D. D. Sarma, H. R. Krishnamurthy, and S. Ramasesha, Phys. Rev. B **48**, 7355 (1993).

[37] M. Imada, A. Fujimori, and Y. Tokura, Rev. Mod. Phys. **70**, 1039 (1998).

[38] S. D. Ha, M. Otaki, R. Jaramillo, A. Podpirka, S. Ramanathan, J. of Solid State Chem. **190**, 233 (2012).

[39] J.B. Torrance, P. Lacorre, C. Asavaroengchai, and R.M. Metzger, Why are some oxides metallic, while most are insulating, Physica C **182**, 351 (1991).

[40] J.B. Torrance, P. Lacorre, A.I. Nazzal, E.J. Ansaldo, and C. Niedermayer, Phy. Rev. B **45**, 8209 (1992).

[41] G. Frand, O. Bohnke, P. Lacorre, J. Fourquet, A. Carre, B. Eid, J. Theobald, and A. Gire, J. Solid State Chem. **120**, 157 (1995).

[42] J. L. García-Muñoz, J. Rodríguez-Carvajal, and P. Lacorre, Europhys. Lett. **20**, 241 (1992).

[43] J. L. García-Muñoz, J. Rodríguez-Carvajal, and P. Lacorre, Phys. Rev. B **50**, 978 (1994).

[44] J. A. Alonso, J. L. García-Muñoz, M. T. Fernández-Díaz, M. A. G. Aranda, M. J. Martínez-Lope, and M. T. Casais, Phys. Rev. Lett. **82**, 3871 (1999).

[45] H. Park, A. J. Millis, and C. A. Marianetti, Phys. Rev. Lett. **109**, 156402 (2012).

[46] S. Johnston, A. Mukherjee, I. Elfimov, M. Berciu, and G. A. Sawatzky, Phys. Rev. Lett. **112**, 106404 (2014).

[47] J.-S. Zhou and J.B. Goodenough, Phys. Rev. B **69**, 153105 (2004).

[48] M. Zaghrioui, A. Bulou, P. Lacorre, and P. Laffez, Phys. Rev. B **64**, 081102 (2001).

[49] U. Staub, G.I. Meijer, F. Fauth, R. Allenspach, J.G. Bednorz, J. Karpinski, S.M. Kazakov, L. Paolasini, and F. d´acapito, Phys. Rev. Lett. **88**, 126402 (2002).

[50] P.C. Canfield, J.D. Thompson, S.W. Cheong, and L.W. Rupp, Phys. Rev. B **47**, 12357 (1993).

[51] M. Medarde, J. Mesot, P. Lacorre, S. Rosenkranz, P. Fischer, and K. Gobrecht, Phys. Rev. B **52**, 9248 (1995).

[52] X. Obradors, L.M. Paulius, M.B. Maple, J.B. Torrance, A.I. Nazzal, J. Fontcuberta, and X. Granados, Phys. Rev. B **47**, 12353 (1993).

[53] J.-S. Zhou, J.B. Goodenough, and B. Dabrowski, Phys. Rev. Lett. **94**, 226602 (2005).

[54] J.F. DeNatale and P.H. Kobrin, J. Mater. Res. **10**, 2992 (1995).

[55] G. Catalan, R. M. Bowman, and J. M. Gregg, Phys. Rev. B **62**, 7892 (2000).

[56] M.A. Novojilov, O.Yu. Gorbenko, I.E. Graboy, A.R. Kaul, H.W. Zandbergen, N.A. Babushkina, and L.M. Belova, Appl. Phys. Lett. **76**, 2041 (2000).

[57] G. Catalan, R.M. Bowman, and J.M. Gregg, J. Appl. Phys. **87**, 606 (2000).

[58] P. Goudeau, P. Laffez, A. Zaghrioui, E. Elkaim, and P. Ruello, Crys. Eng. **5**, 317 (2002).

[59] J. A. Alonso, M. J. Martínez-Lope, M. T. Casais, J. L. García-Muñoz, and M. T. Fernández-Díaz Phys. Rev. B **61**, 1756 (2000).

[60] J. A. Alonso , M. J. Martínez-Lope , M. T. Casais , M. A. G. Aranda, and M. T. Fernández-Díaz J. Am. Chem. Soc. **121**, 4754 (1999).

[61] I. I. Mazin, D. I. Khomskii, R. Lengsdorf, J. A. Alonso, W. G. Marshall, R. M. Ibberson, A. Podlesnyak, M. J. Martínez-Lope, and M. M. Abd-Elmeguid, Phys. Rev. Lett. 98, 176406 (2007).

[62] H. Park, A. J. Millis, and C. A. Marianetti, Phys. Rev. Lett. 109, 156402 (2012).

[63] S. Johnston, A. Mukherjee, I. Elfimov, M. Berciu, and G. A. Sawatzky, Phys. Rev. Lett. 112, 106404 (2014).

[64] S. Sarkar, B. Mandal, S. K. Pandey, P. Mahadevan, C. Franchini, A. J. Millis and D. D. Sarma, arXiv:1701.06819v1 (2017).

[65] M. L. Medarde, J. Phys. Condens. Matter 9, 1680 (1997).

[66] J. A. Alonso, M. J. Martínez-Lope, M. T. Casais, J. L. García-Muñoz, and M. T. Fernández-Díaz, Phys. Rev. B 61, 1756 (2000).

[67] D. B. Mitzi, J. Chem. Soc., Dalton Trans. 1 (2001).

[68] G. Hodes, Science **342**, 317 (2013).

[69] C. C. Stoumpos, C. D. Malliakas and M. G. Kanatzidis, Inorg. Chem. **52**, 9019 (2013).

[70] G. Xing, N. Mathews, S. Sun, S. S. Lim, Y. M. Lam, M. Grätzel, S. Mhaisalkar and T. C.Sum, Science **342**, 344 (2013).

[71] S. D. Stranks, G. E. Eperon, G. Grancini, C. Menelaou, M. J. P. Alcocer, T. Leijtens, L. M. Herz, A. Petrozza and H. J. Snaith, Science **342**, 341 (2013).

[72] A. F. Kapustinskii and Y. B. Yatsimirskii, Zhurnal Obshchei Khimii, **19**, 2191 (1949).

[73] M. R. Filip, G. E. Eperon, H. J. Snaith, F. Giustino, Nat. Commun. **5**, 5757 (2014).

[74] A. Amat, E. Mosconi, E. Ronca, C. Quarti, P. Umari, M. K. Nazeeruddin, M. Grätzel, F. De Angelis, Nano Lett. **14**, 3608 (2014).

[75] T. Baikie, Y. Fang, J. M. Kadro, M. Schreyer, F. Wei, S. G. Mhaisalkar, M. Graetzel, T. J. White, J. Mater. Chem. A **1**, 5628 (2013).

[76] A. Poglitsch and D. Weber, J. Chem. Phys. **87**, 6373 (1987).

[77] D. A. Egger and L. Kronik, J. Phys. Chem. Lett. **5**, 2728 (2014).

[78] J.-H. Lee, N. C. Bristowe, J. H. Lee, S.-H. Lee, P. D. Bristowe, A. K. Cheetham and H. M. Jang, Chem. Mater. **28**, 4259 (2016).

[79] S. Sarkar and P. Mahadevan, Phys. Rev. B **95**, 214118 (2017).

[80] N. V. P. Chaudhary, S. Sarkar , N. Sharma, A. K. Kundu, K. S. R. Menon, A. Das, P. Mahadevan and A. Venimadhav, Phys. Rev. B **96**, 024107 (2017).

[81] D. J. Griffiths, Introduction to electrodynamics, Pearson Prentice Hall, Third edition(2007), p 178-219.

[82] S. Kasap, P. Capper, Dielectric Response, in Springer handbook of electronic and photonic materials (Springer Science & Business Media, 2007).

[83] D. J. Griffiths, Introduction to electrodynamics, Pearson Prentice Hall, Third edition(2007), p 382-433.

[84] Richard J. D. Tilley, Dielectric Properties, in Perovskites, John Wiley & Sons, Ltd. (2016).

[85] S. O. Kasap, Principles of Electronic Materials and Devices, Third edition, McGraw-Hill, (2006).

[86] J. A. Anderson, Rep. Nat. Res. Council (April 1918).

[87] J. Valasek, Phys. Rev. **17**, 475 (1921).

[88] J. Valasek Phys. Rev. **19**, 478 (1922).

[89] B. Wul and J.M. Goldman, C.R. Acad. Sci. URSS **51** 21 (1946).

[90] G. Shirane, S. Hoshino, and K. Suzuki, J. phys. Soc. Japan **5**, 453 (1950).

[91] J. A. Gonzalo, B. Jimenez, Ferroelectricity: The Fundamentals Collection; Wiley-VCH: New York, 2005; Vol. 10.

[92] W. P. Mason and B. T. Matthias, Phys. Rev. **74**, 1622 (1948).

[93] G. C. Danielson, B. T. Matthias, and J. M. Richardson, Phys. Rev. **74**, 986 (1948).

[94] H.D. Megaw, Proc. Roy. Soc. **189** 261 (1947).

[95] W. Cochran, Phys. Rev. Lett. **3**, 412 (1959).

[96] P. A. Fleury, Annu. Rev. Mater. Sci. **6**, 157 (1976).

[97] M. T. Dove, Structure and Dynamics: An Atomic View of Materials, OUP Oxford, (2003).

[98] G. Venkataraman, Bull. Mater. Sci. **1**, 129 (1979).

Chapter 2

Theoretical Concepts

2.1 Introduction

Development of quantum mechanics at the beginning of twentieth century was one of the great scientific advancement to understand and predict material properties. Here the state of a system is described by a state function or a wave function ψ and all the measurable properties can be obtained by solving the Schrödinger equation. For example, in case of Hydrogen atom, the dynamics of the electron and its energy states(hence the electronic structure of Hydrogen atom) are described with great accuracy in agreement with experimental observations [1]. Knowing the electronic structure of any material system helps us to understand and predict its properties. Materials are basically collection of atoms, a system of nuclei and electrons, and the basic interaction between them is electrostatic. Nuclei are $\sim$ 1800 times heavier than the electrons and with some approximations can be treated as classical particles fixed at particular lattice sites. However, the electrons have to be treated quantum mechanically. Presence of more than one electron and the repulsive interaction between them make it a many-body problem, and solution of the many particle Schrödinger equation is a difficult task. Many powerful methods for an improved though approximate solution of the many particle Schrödinger equation have been developed. These can handle around 100 electrons but are computationally demanding. So, the exact many-body wave function $\psi(\mathbf{r_1}, \mathbf{r_2}, \cdots, \mathbf{r_N})(N =$ number of electrons in the system) remains inaccessible for most real systems. Hence we need some approximations to solve the many particle Schrödinger equation. This is generally done by reducing the many particle Schrödinger equation to some effective single particle equations and solving them. Density functional theory(DFT), as formulated by Kohn, Hohenberg, and Sham in the 1960's, is a smart way to solve the many particle Schrödinger equation that reduces the many-body problem to an effective single particle problem. This was done by considering the electron density $n(\mathbf{r})$ as a variable and expressing the energy of the system as a functional of the electron density, $E[n(\mathbf{r})]$. Determination of the ground state electron density $n_0(\mathbf{r})$ gives the ground state energy E_0, as well as the ground state wave function ψ_0 and hence the ground state electronic structure of any system. This is important because it is kind of solving the many particle Schrödinger equation by finding a function of just 3 variables, the electron density, rather than a complex function of $3N$ variables, the wave function.

We use DFT as implemented within the Vienna ab-initio simulation package (VASP) [2,3] to calculate the electronic structure and structural properties of the systems considered as a part of this thesis. DFT has become a standard tool for exploring material properties and understanding them at the atomic level. It has enhanced our scientific understanding of various physical problems from different areas of science. It also comes out to be very

useful in predicting material properties which are challenging to probe experimentally. For example, properties of materials at very high pressure would be difficult to explore experimentally due to instrumental limitations. DFT calculations can play an useful role in probing material properties at these extreme conditions, as shown in the work of Umemoto, Wentzcovitch, and Allen [4]. In this work they have studied the high pressure properties of bulk $MgSiO_3$, a silicate mineral that is important in planet formation.

In this chapter, we give a brief introduction of the density functional theory and its formulation as a density functional based approach. We also discuss some technical details to use DFT in computational physics. The electronic structure calculation of a periodic solid allows the description in terms of Bloch states [5]. These are delocalized/extended electronic states which are assigned a quantum number $\mathbf{k}$ for the crystal momentum, together with a band index n. A usual expansion involves basis states which are plane waves. This is widely used in electronic structure calculations but alternative representations are also available. The Wannier representation [6–8], which is essentially a real-space picture of localized orbitals, assigns as quantum numbers the lattice vector $\mathbf{R}$ of the unit cell where the orbital is localized, together with a band-like index n. Wannier functions can be a powerful tool in the study of the electronic and dielectric properties of materials and can provide an insightful picture of the nature of chemical bonding, otherwise missing from the band picture of extended orbitals [9]. We use the interface of VASP to WANNIER90 [10–12] to map the Bloch states onto Wannier functions, localized on the respective atoms via a unitary transformation. We do this to get a tight binding representation of the Hamiltonian in the basis of the maximally localized Wannier functions and calculate bonding energy of specific inter-atomic bonds. So, we also give a brief introduction of Wannier functions and its properties.

2.2 Formulation of Density functional theory

2.2.1 Many body Schrödinger equation and Born-Oppenheimer Approximation

In quantum mechanics the state of a system is described by a state function or wave function ψ, and all the measurable properties can be obtained by solving the Schrödinger equation. The time independent, non-relativistic Schrödinger equation $H\psi = E\psi$, is useful to calculate the electronic structure of atoms, molecules and solids. H is the Hamiltonian operator and ψ is a set of solutions, or eigenstates, of the Hamiltonian. Each solution, ψ_n , has an associated real eigenvalue, E_n, satisfying the eigenvalue equation.

The detailed structure of the Hamiltonian depends on the physical system under consideration. For simple systems the Schrödinger equation can be solved exactly. For example, in case of Hydrogen atom, a system of a single electron moving under the potential of a single proton $v(\mathbf{r})$, the time independent Schrödinger equation becomes:

$$\left[-\frac{\hbar^2}{2m}\nabla^2 + v(\mathbf{r})\right]\psi(\mathbf{r}) = \varepsilon\psi(\mathbf{r}) \tag{2.1}$$

where m is the mass of the electron and the wave function $\psi(\mathbf{r})$, is a function of a single electron coordinate $\mathbf{r}$. Solving this equation gives the electronic structure of the Hydrogen atom and the dynamics of the electron is defined by the time dependent Schrödinger equation $H\psi = i\hbar\frac{\partial\psi}{\partial t}$, which is not needed further for electronic structure calculations. For a solid material of our interest, the situation becomes complicated, where multiple electrons are interacting with multiple nuclei and among themselves. Such a many particle system is described by the many particle Schrödinger equation:

$$H\Psi(\mathbf{r}_i; \mathbf{R}_I) = E\Psi(\mathbf{r}_i; \mathbf{R}_I) \tag{2.2}$$

where the wave function Ψ is now a function of N electronic coordinates $\mathbf{r_i}$(i=1 to N) and M nuclear coordinates $\mathbf{R_I}$(I=1 to M). The Hamiltonian of the system is a sum of five terms which in atomic unit reads as:

$$H = -\frac{\hbar^2}{2m}\sum_i \nabla_i^2 + \frac{1}{2}\sum_{i\neq j}\frac{e^2}{|\mathbf{r}_i - \mathbf{r}_j|} - \frac{\hbar^2}{2M_I}\sum_I \nabla_I^2 + \frac{1}{2}\sum_{I\neq J}\frac{Z_I Z_J e^2}{|\mathbf{R}_I - \mathbf{R}_J|} - \sum_{i,I}\frac{Z_I e^2}{|\mathbf{R}_I - \mathbf{r}_i|} \tag{2.3}$$

where i , j refer to electrons and I , J refer to nuclei. Parameter e and m are the electronic charge and mass respectively. Z_I and M_I denote the nuclear charge and mass of the I^{th} nucleus respectively. This Hamiltonian can be written in a more compact form as:

$$H = T_e(\mathbf{r}) + V_{ee}(\mathbf{r}) + T_N(\mathbf{R}) + V_{NN}(\mathbf{R}) + V_{eN}(\mathbf{r}, \mathbf{R}) \tag{2.4}$$

where $\mathbf{R}$ is now indicating a set of nuclear coordinates, and $\mathbf{r}$ is the set of electronic coordinates. First two terms, $T_e(\mathbf{r})$ and $V_{ee}(\mathbf{r})$ represent the kinetic energy of the electrons and the electron-electron Coulomb repulsion respectively. The third and fourth terms, $T_N(\mathbf{R})$ and $V_{NN}(\mathbf{R})$ represent the kinetic energy of the nuclei and repulsive interaction between them respectively. The last term $V_{eN}(\mathbf{r}, \mathbf{R})$ represents the interaction between electrons and nuclei and couples the electronic and nuclear degrees of freedom. This term prevents

us from separating the total Hamiltonian into nuclear and electronic parts, which would make the problem a bit simpler and allow us to write the total wave function of the system as a product of nuclear and electronic terms, $\Psi(\mathbf{r};\mathbf{R}) = \Psi(\mathbf{r})\eta(\mathbf{R})$. The term $V_{eN}(\mathbf{r},\mathbf{R})$ is large and cannot be neglected. However, if we can assume that the nuclei are fixed and do not move then we can make the $\mathbf{R}$ dependence parametric and can split the problem into two separate parts. The separation of the nuclei and electrons into two separate mathematical problems is achieved using Born-Oppenheimer approximation(BOA) [13] or the Adiabatic approximation. The BOA rests on the fact that atomic nuclei are much heavier than electrons, each proton or neutron in a nucleus is ~ 1800 times massive than an electron. This means that electrons respond much more rapidly to changes in their surroundings than nuclei can. This allows us to say that the nuclei are nearly fixed with respect to electron motion and at any instant of time for a particular nuclear configuration the electrons are at their possible ground state.

Initially, $T_N(\mathbf{R})$ can be neglected since T_N is much smaller than T_e due to larger nuclear mass, and then for a fixed nuclear configuration $\{\mathbf{R}_a\}$ we have:

$$H^{ele}_{BOA} = T_e(\mathbf{r}) + V_{ee}(\mathbf{r}) + V_{NN}(\mathbf{R}) + V_{eN}(\mathbf{r},\mathbf{R}_a) \tag{2.5}$$

as the electronic Hamiltonian after BOA such that,

$$H^{ele}_{BOA}\Psi(\mathbf{r};\mathbf{R}_a) = E^{ele}\Psi(\mathbf{r};\mathbf{R}_a) \tag{2.6}$$

gives the electronic wave function $\Psi(\mathbf{r};\mathbf{R}_a)$ and energy $E^{ele}(\mathbf{R}_a)$, which now depends on $\mathbf{R}$ parametrically. Generally $V_{NN}(\mathbf{R})$ is neglected in Equation (2.5), since in this case $\mathbf{R}$ is just a parameter so that $V_{NN}(\mathbf{R})$ is just a constant and shifts the eigenvalues only by some constant amount. In that case we can write H^{ele}_{BOA} as,

$$H^{ele}_{BOA} = T_e(\mathbf{r}) + V_{ee}(\mathbf{r}) + V_{eN}(\mathbf{r},\mathbf{R}_a) \tag{2.7}$$

So, for any solid system the first step would be to solve Equation (2.7), that describes the electrons for fixed positions of the atomic nuclei. For a given set of electrons moving in the field of a set of nuclei, we get the lowest energy state or the ground state of the electrons. If we have M nuclei at positions $(\mathbf{R}_1,\mathbf{R}_2,\cdots,\mathbf{R}_M)$ then we can express the ground-state electronic energy, E^{ele}_0, as a function of the positions of these nuclei, $E^{ele}_0(\mathbf{R}_1,\mathbf{R}_2,\cdots,\mathbf{R}_M)$. This function is known as the adiabatic potential energy surface of the atoms. Once we

are able to calculate this potential energy surface we can know how does the energy of the material change as we move the atoms around [14].

But even after BOA the simplest possible electronic Hamiltonian[Equation (2.7)] for a fixed nuclear configuration $\{\mathbf{R}_a\}$, is not easy to solve. The term in the Hamiltonian defining the electron-electron interactions $V_{ee}(\mathbf{r})$, is the most critical one from the point of view of directly solving the equation. If this term was not there, that means for a non-interacting many electron system the equation reduces to a set of N independent single particle equations of the form,

$$h_i\varphi(\mathbf{r}_i) = \varepsilon\varphi(\mathbf{r}_i)[i = 1, 2, \cdots, N] \tag{2.8}$$

where N is the number of electrons in the system and h_i describes the kinetic and potential energies of the i^{th} electron. Solution of each such single particle equation gives the same set of single electron wave functions $\varphi_n(\mathbf{r})$ with energies ε_n. Then the ground state of the N electron system is simply expressed in terms of some simple or complex product of the N lowest energy wave functions $\varphi_1(\mathbf{r}_1)$, $\varphi_2(\mathbf{r}_2)$, ... ,$\varphi_N(\mathbf{r}_N)$ associated with the 1^{st}, 2^{nd}, ... ,N^{th} electron respectively. In band theory for periodic solid systems, the same approach is followed and the single electron states are called Bloch states [5]. But due to the presence of the electron-electron interaction term, individual electron wave function, $\varphi_i(\mathbf{r}_i)$, associated with the i^{th} electron, could not be found without simultaneously knowing the wave functions associated with all the other electrons in the system. This means, the Schrödinger equation is a many-body problem and we have to make some additional approximations to reduce it to an effective single particle problem. Various approaches were taken in this regard. Hartree-Fock (HF) and Density Functional theory (DFT) are two successful theories in which the two body interaction term is replaced by an effective single body potential. Next we are going to discuss the basic assumptions taken within these two approach to solve the electronic Hamiltonian after BOA[Equation (2.7)].

2.2.2 Hartree-Fock(HF) Theory : A wave function based approach

Hartree-Fock approach is an approximate way to solve the simplest form of the electronic Hamiltonian for an N electron system after BOA[Equation (2.7)]. We can write Equation (2.7) as a sum of two terms gives as:

$$H_{BOA}^{ele} = -\frac{\hbar^2}{2m}\sum_i \nabla_i^2 + \frac{1}{2}\sum_{i\neq j}\frac{e^2}{|\mathbf{r}_i - \mathbf{r}_j|} - \sum_{i,I}\frac{Z_I e^2}{|\mathbf{R}_I - \mathbf{r}_i|} \tag{2.9}$$

$$= \sum_i \left(-\frac{\hbar^2}{2m}\nabla_i^2 - \sum_I \frac{Z_I e^2}{|\mathbf{R}_I - \mathbf{r}_i|}\right) + \frac{1}{2}\sum_{i\neq j}\frac{e^2}{|\mathbf{r}_i - \mathbf{r}_j|} \tag{2.10}$$

$$= \sum_i (T_i + V_{ion}(\mathbf{r}_i)) + \frac{1}{2}\sum_{i\neq j}\frac{e^2}{|\mathbf{r}_i - \mathbf{r}_j|} \tag{2.11}$$

$$= \sum_i h_i + V_{ee}(\mathbf{r}) \tag{2.12}$$

Here the main objective is to calculate the full electron wave function corresponding to the ground state of the above Hamiltonian. Now, as the electrons are fermions, the N electron wave function must satisfy the Pauli exclusion principle that prohibits two electrons with the same spin at the same spatial position. Mathematically, the many electron wave function must be anti-symmetric with respect to position/spin exchange between two electrons.

Now if we consider a system of N non-interacting electrons, we can exclude the electron-electron interaction term $V_{ee}(\mathbf{r})$ and the problem reduces to solving N single particle equations of the form:

$$h\chi(\mathbf{x}) = \varepsilon\chi(\mathbf{x}) \tag{2.13}$$

Where, $h = T + V_{ion}(\mathbf{r})$, is the Hamiltonian for a single electron under the potential of ion cores $V_{ion}(\mathbf{r})$. The eigenfunctions χ, defined by this equation are called spin orbitals and $\mathbf{x}$ is the space-spin coordinate. $\mathbf{x} = \{\mathbf{r},\sigma\}$ defines the position as well as spin state(up or down) of any single electron. Solution of each such single particle equation gives the same set of single electron wave functions $\chi_n(\mathbf{x})(n = 1, 2, \cdots, N)$. The spin orbitals are ordered in a way so that the orbital with $n = 1$ has the lowest energy, the orbital with $n = 2$ has the next lowest possible energy, and so on. Then the ground state of the N electron system may be expressed as a simple product of the N lowest energy wave functions $\chi_1(\mathbf{x}_1)$, $\chi_2(\mathbf{x}_2)$, ... ,$\chi_N(\mathbf{x}_N)$ associated with the 1^{st}, 2^{nd}, ... ,N^{th} electron respectively. This approximation is called a Hartree product [15] and the energy of the ground state is the sum of the considered N spin orbital energies, $E_0 = \varepsilon_1 + \varepsilon_2 + \cdots + \varepsilon_N$. Along with its simplicity, the Hartree product has a serious drawback. It does not satisfy the antisymmetry principle. Fock in 1930 introduced a better approximation to the wave function by using a Slater determinant [16]. This is called Hartree-Fock approximation

[17]. In the Hartree-Fock approximation, the N-electron wave function is formed by expressing the overall wave function as the determinant of a matrix of single-electron wave functions so that it satisfies the antisymmetry principle.

$$\Psi_{HF}(\mathbf{x}_1, \mathbf{x}_2, \cdots \mathbf{x}_N) = \frac{1}{\sqrt{N!}} \begin{vmatrix} \chi_1(\mathbf{x}_1) & \chi_1(\mathbf{x}_2) & \cdots & \chi_1(\mathbf{x}_N) \\ \chi_2(\mathbf{x}_1) & \chi_2(\mathbf{x}_2) & \cdots & \chi_2(\mathbf{x}_N) \\ \vdots & \vdots & \ddots & \vdots \\ \chi_N(\mathbf{x}_1) & \chi_N(\mathbf{x}_2) & \cdots & \chi_N(\mathbf{x}_N) \end{vmatrix} \tag{2.14}$$

This has a lot of advantages over the simple Hartree product. It vanishes if two electrons have the same coordinates or if two of the one-electron wave functions are the same. It changes sign on coordinate exchange. This means that the Slater determinant satisfies Pauli exclusion principle. Also, it does not distinguish between electrons and we cannot say which electron is in which single particle state. This is consistent with the strange results of quantum mechanics for identical particles.

Now let us see how the electron-electron interaction term $V_{ee}(\mathbf{r})$ is approximated using Slater determinant states to reduce the many-body problem to an effective single particle problem. We start with the fact that Hartree-Fock wave functions will have the form of a Slater determinant which are normalized, and the electronic energy will be given by:

$$\begin{aligned} E_{HF}^{ele} = \langle \Psi_{HF} | H_{BOA}^{ele} | \Psi_{HF} \rangle &= \langle \Psi_{HF} | (\sum_i h_i) | \Psi_{HF} \rangle + \langle \Psi_{HF} | V_{ee}(\mathbf{r}) | \Psi_{HF} \rangle \\ &= \sum_i \varepsilon_i + \left\{ \sum_{ij} C_{ij} - \sum_{ij} J_{ij} \right\} \end{aligned} \tag{2.15}$$

After some rigorous mathematical steps which are not presented here, we can get the expressions for each of the terms in the above equation. ε_i is given as:

$$\varepsilon_i = \langle \chi_i | h | \chi_i \rangle = \int \chi_i^*(\mathbf{x}) \left[-\frac{\hbar^2}{2m} \bigtriangledown^2 + V_{ion}(\mathbf{r}) \right] \chi_i(\mathbf{x}) d\mathbf{x} \tag{2.16}$$

representing the energy of a non-interacting electron with spin orbital χ_i. C_{ij} and J_{ij} are called Coulomb integral and exchange integral respectively and are given by:

$$C_{ij} = \frac{e^2}{2} \int \int \chi_i^*(\mathbf{x}) \chi_j^*(\mathbf{x}') \frac{1}{|\mathbf{r} - \mathbf{r}'|} \chi_i(\mathbf{x}) \chi_j(\mathbf{x}') d\mathbf{x} d\mathbf{x}' \tag{2.17}$$

$$J_{ij} = \frac{e^2}{2} \int \int \chi_i^*(\mathbf{x}) \chi_j^*(\mathbf{x}') \frac{1}{|\mathbf{r} - \mathbf{r}'|} \chi_j(\mathbf{x}) \chi_i(\mathbf{x}') d\mathbf{x} d\mathbf{x}' \tag{2.18}$$

The exchange term given by Equation (2.18) is non zero only for like spins i.e. for $\sigma = \sigma'$.

Now for symmetric energy expressions, we can apply the variational theorem, which states that for any arbitrary Slater determinant state Ψ, the energy is always an upper bound to the true ground state energy of the system. Hence, we can obtain better approximate wave functions Ψ, by varying their parameters(spin orbitals χ) with the condition that the energy gets minimized. The electronic energy E_{HF}^{ele}, is now a functional of the spin orbitals, $E_{HF}^{ele}[\{\chi_i\}]$, and we can vary the spin orbitals for the lowest energy within a given functional space. The corresponding Slater determinant would be the closest to the true ground state wave function of the system. Hence, Hartree-Fock method determines the set of spin orbitals giving the lowest energy and gives us the best possible ground state Slater determinant state. We want to minimize the Hartree-Fock energy $E_{HF}^{ele}[\{\chi_i\}]$, with respect to changes in the spin orbitals $\chi_i \rightarrow \chi_i + \delta\chi_i$, such that the procedure leaves them orthonormal. This can be done by Lagrange's method of undetermined multipliers [18], where we introduce a functional $\mathcal{L}$ given as:

$$\mathcal{L}[\{\chi_i\}] = E_{HF}^{ele}[\{\chi_i\}] - \sum_j \varepsilon_j \int |\chi_j(\mathbf{x})|^2 d\mathbf{x} \tag{2.19}$$

where ε_j, are the undetermined Lagrange multipliers. Setting the first variation $\delta\mathcal{L} = 0$, and after some mathematical simplification, we obtain the Hartree-Fock equations defining the orbitals:

$$\begin{aligned}\left[-\frac{\hbar^2}{2m}\bigtriangledown^2 + V_{ion}(\mathbf{r})\right]\chi_i(\mathbf{x}) + \sum_{i\neq j}\left[\int |\chi_j(\mathbf{x}')|^2 \frac{e^2}{|\mathbf{r}-\mathbf{r}'|} d\mathbf{x}'\right]\chi_i(\mathbf{x}) \\ - \sum_{i\neq j}\left[\int |\chi_j^*(\mathbf{x}')\frac{e^2}{|\mathbf{r}-\mathbf{r}'|}\chi_i(\mathbf{x}')d\mathbf{x}'\right]\chi_j(\mathbf{x}) = \varepsilon_i\chi_i(\mathbf{x})\end{aligned} \tag{2.20}$$

where ε_i is the energy eigenvalue associated with spin orbital χ_i. The second term in the Equation (2.20) gives the Coulomb interaction between an electron with spin orbital χ_i, and the average charge distribution of the other electrons. This is called the Coulomb term. We can define a corresponding Coulomb operator $\widehat{C_j}$ as:

$$\widehat{C_j}(\mathbf{x}) = \int |\chi_j(\mathbf{x}')|^2 \frac{e^2}{|\mathbf{r}-\mathbf{r}'|} d\mathbf{x}' \tag{2.21}$$

giving the average local potential at point $\mathbf{r}$ due to the charge distribution of the electron in spin orbital χ_j. The third term in Equation (2.20) comes from the antisymmetry

requirement of the wave function and does not have a simple classical analogue. This is called the exchange term and we can define a corresponding exchange operator $\widehat{J_j}$ in terms of its action on an arbitrary spin orbital χ_i as:

$$\widehat{J_j}(\mathbf{x})\chi_i(\mathbf{x}) = \left[\int \chi_j^*(\mathbf{x}')\frac{e^2}{|\mathbf{r}-\mathbf{r}'|}\chi_i(\mathbf{x}')d\mathbf{x}'\right]\chi_j(\mathbf{x}) \tag{2.22}$$

And in terms of these Coulomb and exchange operators, we have the Hartree-Fock single particle equations as:

$$\left[-\frac{\hbar^2}{2m}\bigtriangledown^2 + V_{ion}(\mathbf{r}) + \sum_{j\neq i}\widehat{C_j}(\mathbf{x}) - \sum_{j\neq i}\widehat{J_j}(\mathbf{x})\right]\chi_i(\mathbf{x}) = \varepsilon_i\chi_i(\mathbf{x}) \tag{2.23}$$

We define,

$$V_H(\mathbf{x}) = \sum_{j\neq i}\widehat{C_j}(\mathbf{x}) - \sum_{j\neq i}\widehat{J_j}(\mathbf{x}) \tag{2.24}$$

as the Hartree potential, which is the average effective potential experienced by an electron due to the presence of remaining $(N-1)$ electrons making Hartree-Fock approximation a mean field approach.

Now we have to solve these single particle Hartree-Fock equations and obtain the N spin orbitals with lowest energies and then construct the ground state wave function as a Stater determinant of those N spin orbitals. And the total energy corresponding to the ground state would be the sum of the considered spin-orbital energies. To solve the single electron equations in a practical calculation, we need to expand the spin orbitals in a basis set. If the set of K number of functions $\phi_1(\mathbf{x}), \phi_2(\mathbf{x}), \cdots, \phi_K(\mathbf{x})$ defines the basis set, then we can approximate the spin orbitals as:

$$\chi_i(\mathbf{x}) = \sum_{j=1}^{K}\alpha_{ij}\phi_j(\mathbf{x}) \tag{2.25}$$

Hence we only need to find the expansion coefficients, α_{ij} , for $i = 1, \cdots, N$ and $j = 1, \cdots, K$ to fully define all the spin orbitals that are used in the HF method. Choosing a large basis set and functions that are initially similar to the real spin orbitals, improves the accuracy but with an increased computational cost. Now, to find the spin orbitals one needs to solve the single electron equations[Equation (2.23)] for which we need to know the Hartree potential V_H. But to define the Hartree potential(V_H), we must know

in turn, the individual spin orbitals associated with all the electrons. To break this loop, a Hartree-Fock calculation becomes an iterative procedure with the main steps as described below [14]:

Step 1 : Make an initial estimate of the spin orbitals [Equation (2.25)] by specifying the expansion coefficients, α_{ij}.

Step 2 : From the current estimate of the spin orbitals, define the Hartree potential V_H.

Step 3 : Using this Hartree potential V_H from step 2, solve the single electron Hartree-Fock equations for the spin orbitals.

Step 4 : If the spin orbitals found in step 3 are consistent with the orbitals used in step 2 satisfying some convergence criteria, then these are the final solutions to the Hartree-Fock problem. If not, then a new estimate or update for the spin orbitals must be made and we then return to step 2.

We are not going to discuss here the details of how to make an initial guess for spin orbitals, what shall be the convergence criteria and procedure to update the spin orbitals. But some basic problems associated with such wave function based approach needs to be discussed. One of the main problem is associated with the dimension of the wave function. Excluding the spin degrees of freedom, for a system of N electrons the total wave function is $3N$ dimensional. For example, the wave function for a nanocluster of 100 Pt atoms shall require more than 23,000 dimensions [14]. Accuracy of the calculation is another issue which depends on two main factors. (1) How accurately the electron-electron interaction is treated and (2) how accurately we represent the many electron Schrödinger wave function. Hartee-Fock method with Slater determinants includes exchange interaction, but this is not the only kind of electron correlation that we need to consider for good accuracy. Electrons repel each other according to Coulomb's law. Hartree-Fock replaces this instantaneous electron-electron repulsion with an average term where each electron feels the effect of an average electron charge cloud. This introduces an error in the wave function and the energy. Similarly, to accurately represent the true many electron Schrödinger wave function, we need infinitely large number of Slater determinants as basis set. But in Hartree-Fock theory we use a single Slater determinant state to represent the ground state, which is not a good approximation. The hypothetical energy of N electrons from a HF calculations using an infinitely large basis set, is known as the Hartree-Fock limit. This energy is not the same as the true ground state energy of the system and their difference is defined as the electron correlation energy. Hartree-Fock theory fails for systems where electron correlation is important. For example, Van der Waals systems where dispersion forces results from instantaneous electron-electron inter-

actions. Improvements can be made by considering Slater determinants that represents excited state along with the HF ground state. For example, configuration interaction (CI), coupled cluster (CC), Møller-Plesset perturbation theory (MP), quadratic configuration interaction (QCI) approach are among them.

2.2.3 Density Functional Theory : From wave function to electron density

The N electron wave function $\Psi(\mathbf{r}_1, \cdots, \mathbf{r}_N)$, is an abstract quantity that cannot be directly observed. The quantity that can be physically measured is the probability density $\Psi^*\Psi$. An equivalent quantity that can be physically measured in X-ray diffraction experiments is the electron density $n(\mathbf{r})$. The spin independent density of an N electron system is defined as,

$$n(\mathbf{r}_i) = N \int \Psi^*(\mathbf{r}_1, \cdots, \mathbf{r}_i, \cdots, \mathbf{r}_N)\Psi(\mathbf{r}_1, \cdots, \mathbf{r}_i, \cdots, \mathbf{r}_N) d\mathbf{r}_1 d\mathbf{r}_2 \cdot\cdot d\mathbf{r}_{(i-1)} d\mathbf{r}_{(i+1)} \cdot\cdot d\mathbf{r}_N \quad (2.26)$$

The electron density is a function of just 3 spatial variables and contains a large amount of information that is actually physically observable from the full wave function solution to the Schrödinger equation, which is a function of $3N$ coordinates. Like $\Psi(\mathbf{r}_1, \cdots, \mathbf{r}_N)$, $n(\mathbf{r})$ also vanishes at infinity and integrates out to the total number of particles, N in the system. If we are able to express the total energy E, of the electron system as a functional of the electron density $n(\mathbf{r})$, $E[n(\mathbf{r})]$, and apply variational method to determine the ground state electron density $n_0(\mathbf{r})$, corresponding to a minimum in $E[n(\mathbf{r})]$, then we can in-turn get all necessary information of the system including the ground state wave function Ψ_0. This is important because we can get the ground state solution for the electronic Hamiltonian[Equation (2.9)] by varying a function of 3 spatial variables for any electron system. A theory for electronic structure calculation based on the electron density $n(\mathbf{r})$, that was there since 1920 was the Thomas-Fermi(TF) theory [19,20]. Thomas-Fermi theory gives a rough approximation to the exact solution of the many-electron Schrödinger equation. This was quite useful for describing some qualitative trends like total energies of atoms, but in case of chemistry and materials science, which involve valence electrons, it was of almost no use. For example it did not lead to any chemical binding [21]. As stated by Walter Kohn in his Noble Lecture [21], it was the suggestion of the hypothesis, that a knowledge of the ground-state density of $n(\mathbf{r})$, for any electronic system (with

or without interactions) uniquely determines the system, became the starting point of modern density functional theory(DFT) as formulated by Kohn, Hohenberg, and Sham.

The entire field of density functional theory rests on two fundamental mathematical theorems proved by Hohenberg and Kohn [22] and the derivation of a set of equations by Kohn and Sham [23] in the mid 1960's.

Hohenberg Kohn Theorem 1 : The basic statement of the theorem is that, The ground state density $n_0(\mathbf{r})$ of a bound system of interacting electrons in some external potential $V_{ext}(\mathbf{r})$ determines this potential uniquely [21, 22].

Proof: Let $n(\mathbf{r})$, be the ground state density of N electrons in the external potential $V_{ext}(\mathbf{r})$, corresponding to the ground state wave function Ψ, and the energy E, of the Hamiltonian, $H = T_e + V_{ee} + V_{ext}$. T_e and V_{ee} are the kinetic and electron-electron interaction energy operators respectively[see Equations (2.3) and (2.4) for detail expression of T_e and V_{ee}]. Let us consider V'_{ext}, a different external potential, which also corresponds to the same ground state density $n(\mathbf{r})$. This will result in a different Hamiltonian H' and corresponding ground state wave functions Ψ' . Now,

$$\begin{aligned} E &= \langle\Psi|H|\Psi\rangle && (2.27)\\ &= \langle\Psi|T_e + V_{ee}|\Psi\rangle + \int n(\mathbf{r})V_{ext}(\mathbf{r})d^3r && (2.28)\end{aligned}$$

and

$$\begin{aligned} E' &= \langle\Psi'|H'|\Psi'\rangle && (2.29)\\ &= \langle\Psi'|T_e + V_{ee}|\Psi'\rangle + \int n(\mathbf{r})V'_{ext}(\mathbf{r})d^3r && (2.30)\end{aligned}$$

Since Ψ' is not the corresponding ground state of H,

$$\begin{aligned} E &= \langle\Psi|H|\Psi\rangle && (2.31)\\ &< \langle\Psi'|H|\Psi'\rangle = \langle\Psi'|H'|\Psi'\rangle + \langle\Psi'|[H - H']|\Psi'\rangle && (2.32)\\ &< E' + \int n(\mathbf{r})[V_{ext}(\mathbf{r}) - V'_{ext}(\mathbf{r})]d^3r && (2.33)\end{aligned}$$

Similarly,

$$E' < E + \int n(\mathbf{r})[V'_{ext}(\mathbf{r}) - V_{ext}(\mathbf{r})]d^3r \tag{2.34}$$

Adding both the above Equations (2.33) and (2.34) we get,

$$(E + E') < (E' + E) \tag{2.35}$$

This contradictory result proves the first theorem. Now as $V_{ext}(\mathbf{r})$ determines H, so another way to restate this result is that the ground state energy $E_0[n(\mathbf{r})]$ and wave function $\Psi_0[n(\mathbf{r})]$ from Schrödinger's equation are unique functional of the electron density $n(\mathbf{r})$. And the ground state electron density $n_0(\mathbf{r})$ in an external potential uniquely determines all properties, including the energy and wave function, of the ground state.

Hohenberg Kohn Theorem 2 : The second theorem states that, the ground state energy can be obtained variationally: The exact ground state energy corresponding to the full solution of the Schrödinger equation is the global minimum value of the functional $E[n(\mathbf{r})]$. And the electron density that minimizes the energy of the overall functional is the true ground state electron density. So, if $n_0(\mathbf{r})$ is the ground state electron density, then this implies that, for any density $n'(\mathbf{r})$, other than ground state density,

$$E[n'(\mathbf{r})] \geq E[n_0(\mathbf{r})] \tag{2.36}$$

Kohn-Sham Formulation :

For the Hamiltonian, $H = T_e + V_{ee} + V_{ext}$ of N interacting electrons in the external potential V_{ext}, the total energy functional can be written as,

$$E[n(\mathbf{r})] = F[n(\mathbf{r})] + \int n(\mathbf{r})V_{ext}(\mathbf{r})d^3r \tag{2.37}$$

where $F[n(\mathbf{r})] = T[n(\mathbf{r})] + E_{ee}[n(\mathbf{r})]$, is an unknown, but otherwise universal functional of the electron density $n(\mathbf{r})$ only. $F[n(\mathbf{r})]$ in the above equation represents the sum of kinetic energy and the electron-electron interaction energy and is called the Hohenberg-Kohn functional. The ground state energy can be obtained by minimizing this energy functional, subject to the constraint that the number of electrons N is conserved($\int n(\mathbf{r})d\mathbf{r} = N$), which leads to :

$$\frac{\delta}{\delta n(\mathbf{r})}\left[F[n(\mathbf{r})] + \int n(\mathbf{r})V_{ext}(\mathbf{r})d^3r - \mu_L\left(\int n(\mathbf{r})d^3r - N\right)\right] = 0 \tag{2.38}$$

with the Euler equation :

$$\mu_L = \frac{\delta F[n(\mathbf{r})]}{\delta n(\mathbf{r})} + V_{ext}(\mathbf{r}) \tag{2.39}$$

where, μ_L is the Lagrange multiplier associated with the constraint of constant N. The main problem is that, Hohenberg-Kohn theorems does not provide any actual form of the energy functional. Practically, this is being done with approximate forms. An approach to solve this problem was proposed by Kohn and Sham [23] and the idea was to replace the interacting N-electrons system by a hypothetical system of N non-interacting electrons whose ground state density coincides with that of the interacting system. The approach was to write the energy functional described in the Hohenberg-Kohn theorems in terms of the single electron wave functions, $\phi_i(\mathbf{r})$. Then the electron density $n(\mathbf{r})$ of N electron system can be written as,

$$n(\mathbf{r}) = 2\sum_{i=1}^{N}\phi_i^{\star}(\mathbf{r})\phi_i(\mathbf{r}) \tag{2.40}$$

The factor of 2 comes because we are treating the problem without spin degrees of freedom and each orbital ϕ_i, can be occupied by two electrons with opposite spins. The total wave function Ψ_{KS}, for this type of system is exactly given by a Slater determinant of single particle orbitals $\phi_i(\mathbf{r}_i)$. Then the functional $F[n(\mathbf{r})]$ can be expressed as a sum of three terms as:

$$F[n(\mathbf{r})] = T_0[n(\mathbf{r})] + E_H[n(\mathbf{r})] + E_{XC}[n(\mathbf{r})] \tag{2.41}$$

where,

$$T_0[n(\mathbf{r})] \;=\; \sum_i \langle\phi_i| - \frac{\hbar^2}{2m}\nabla^2|\phi_i\rangle \tag{2.42}$$

$$E_H[n(\mathbf{r})] = \frac{e^2}{2}\int\int n(\mathbf{r})\frac{1}{|\mathbf{r}-\mathbf{r}'|}n(\mathbf{r}')d^3rd^3r' \tag{2.43}$$

$$= \frac{e^2}{2}\sum_{i,j}\langle\phi_i\phi_j|\frac{1}{|\mathbf{r}-\mathbf{r}'|}|\phi_i\phi_j\rangle \tag{2.44}$$

$T_0[n(\mathbf{r})]$ is the kinetic energy of a non-interacting electron gas of density $n(\mathbf{r})$ and $E_H[n(\mathbf{r})]$ is the classical electron-electron interaction energy(Hartree energy) of the electrons. $E_{XC}[n(\mathbf{r})]$ is the exchange-correlation energy, which contains the difference between the exact and non-interacting kinetic energies and also the non-classical contributions of the electron-electron interactions such as exchange energy. This is expressed as:

$$E_{XC}[n(\mathbf{r})] = T[n(\mathbf{r})] - T_0[n(\mathbf{r})] + E_{ee}[n(\mathbf{r})] - E_H[n(\mathbf{r})] \tag{2.45}$$

Minimization of the total energy functional from the Kohn-Sham formulation, by applying variational principle[Equation (2.38)] leads to the self consistent Kohn-Sham equations given as:

$$[-\frac{\hbar^2}{2m}\nabla^2 + V_{ext}(\mathbf{r}) + V_H(\mathbf{r}) + V_{XC}(\mathbf{r})]\phi_i(\mathbf{r}) = \epsilon_i\phi_i(\mathbf{r}) \tag{2.46}$$

For the electrons under the potential of nuclei, $V_{ext}(\mathbf{r})$ corresponds to the $V_{ion}(\mathbf{r})$ like in the Hartree-Fock single particle equations [Equation (2.23)]. $V_H(\mathbf{r})$ is the classical part of the Hartree potential given as,

$$V_H(\mathbf{r}) = \frac{\delta E_H[n(\mathbf{r})]}{\delta n(\mathbf{r})} \tag{2.47}$$

$$= e^2\int\frac{n(\mathbf{r}')}{|\mathbf{r}-\mathbf{r}'|}d^3r' \tag{2.48}$$

This potential describes the Coulomb repulsion between the electron in any one of the Kohn-Sham orbital and the total electron density defined by all electrons in the system. So, a part of V_H involves a coulomb interaction between the electron and itself. The self-interaction is not physical, and the correction for this is also considered in the unknown exchange-correlation potential V_{XC} given as,

$$V_{XC}(\mathbf{r}) = \frac{\delta E_{XC}[n(\mathbf{r})]}{\delta n(\mathbf{r})} \tag{2.49}$$

One crucial point to remember is that, the ground state density obtained by solving the Kohn-Sham equations for an alternative non-interacting Kohn-Sham system, is the same as the exact ground state density. But the single particle wave functions ϕ_i are solely mathematical functions with no physical meaning associated to them. To get the single particle wave functions ϕ_i, we need to solve the Kohn-Sham equations[Equation (2.46)]. Now to solve the Kohn-Sham equations(forgetting for now that the function V_{XC} is unknown) we need to know the Hartree potential. And to define the Hartree potential we need to know the electron density which in-turn requires all the single electron wave functions ϕ_i. So, again to break this loop, and calculate the ground state density the problem is usually treated in an iterative way with the following steps [14] :

Step 1 : Define an initial, trial electron density, $n(r)$.

Step 2 : Solve the Kohn-Sham equations defined using the trial electron density to find the single-particle wave functions, ϕ_i.

Step 3 : Calculate the electron density defined by the Kohn-Sham single-particle wave functions from Step 2, $n_{KS}(\mathbf{r}) = 2\sum_i \phi_i^\star(\mathbf{r})\phi_i(\mathbf{r})$.

Step 4 : Compare the calculated electron density, $n_{KS}(\mathbf{r})$, with the electron density used in solving the Kohn-Sham equations, $n(\mathbf{r})$. If the two densities are consistent and satisfy some convergence criteria, then this is the ground state electron density and we get the ground state energy. If the two densities are different, $n(\mathbf{r})$ must be updated in some way. Once this is done, the process begins again from step 2.

In the above discussion of solving the Kohn-Sham equations, we ignored one important fact that the form of the function V_{XC} was not known. To define the mathematical problem(Kohn-Sham equations) properly, we need to know the form of the exchange-correlation potential $V_{XC}(\mathbf{r})$. For this, approximate forms of $V_{XC}(\mathbf{r})$ are used. In the next section we give a brief overview of some of the form of $E_{XC}[n(\mathbf{r})]$ most widely used in DFT calculations that leads to $V_{XC}(\mathbf{r})$.

2.2.4 Approximations for the exchange - correlation Energy $\mathbf{E_{XC}[n(r)]}$

Here we try to give a brief and general picture of how these approximations are done. For details we refer to the main articles that has been mentioned in the text. If Ψ is the ground state wave function of the electronic Hamiltonian[Equation (2.9)] for the N electron system, then the expectation value for the electron-electron interaction V_{ee} is given as,

$$\langle \Psi | V_{ee} | \Psi \rangle = \frac{e^2}{2} \int \int \frac{P(\mathbf{r}, \mathbf{r}')}{|\mathbf{r} - \mathbf{r}'|} d^3r d^3r' \tag{2.50}$$

Where, $P(\mathbf{r}, \mathbf{r}')$ is the pair-density giving the probability of simultaneously finding an electron at the point $\mathbf{r}$ within volume element d^3r, and another electron at $\mathbf{r}'$ in volume element d^3r'. For non-interacting electrons there is no correlation and the probability of finding a pair of electrons at the points $\mathbf{r}$ and $\mathbf{r}'$ is simply the product of the densities at the respective points as,

$$P^{claccical}(\mathbf{r}, \mathbf{r}') \quad = \quad n(\mathbf{r}) n(\mathbf{r}') \tag{2.51}$$

leading to the classical Hartree energy E_H[Equation (2.43)]. But quantum mechanical effect of exchange and correlation interactions reduce the classical value of the electron density at $\mathbf{r}$ due to the presence of the second electron at $\mathbf{r}'$. Therefore each electron creates a depletion, or hole, of electron density around itself as a direct consequence of exchange-correlation effects. Taking account of the hole, the pair-density can be written as,

$$P^{QM}(\mathbf{r}, \mathbf{r}') \quad = \quad n(\mathbf{r}) n(\mathbf{r}') + n(\mathbf{r}) n_{_{XC}}(\mathbf{r}, \mathbf{r}') \tag{2.52}$$

$n_{_{XC}}(\mathbf{r}, \mathbf{r}')$ is called the exchange-correlation hole density, taking into account the quantum mechanical effects. The exchange-correlation energy functional, $E_{XC}[n(\mathbf{r})]$, can be defined as [24],

$$E_{XC}[n(\mathbf{r})] = \int n(\mathbf{r})\varepsilon_{XC}(\mathbf{r})d^3r \tag{2.53}$$

where,

$$\varepsilon_{XC}(\mathbf{r}) = \frac{e^2}{2}\int \frac{n_{XC}(\mathbf{r},\mathbf{r}')}{|\mathbf{r}-\mathbf{r}'|}d^3r' \tag{2.54}$$

is the exchange-correlation energy per particle. The exchange-correlation potential(V_{XC}), then follows from Equation (2.49). The functionals can be characterized by the way in which the density surrounding each electron is sampled in order to construct $\varepsilon_{XC}(\mathbf{r})$.

Local Density Approximation(LDA) :

Local density approximation(LDA) can be called the mother of all approximations proposed by Hohenberg and Kohn in their original DFT paper [22]. The LDA approximates the true exchange-correlation energy of a system at each point in space, by the exchange-correlation energy of a homogeneous electron gas(HEG) of the same density observed at that point. The homogeneous electron gas is the only system for which the form of the exchange-correlation energy is known precisely. LDA only uses the local density, and the exchange-correlation energy functional is written as,

$$E_{XC}^{LDA}[n(\mathbf{r})] = \int n(\mathbf{r})\varepsilon_{XC}^{HEG}(\mathbf{r})d^3r \tag{2.55}$$

where $\varepsilon_{XC}^{HEG}(\mathbf{r})$, is the exchange-correlation energy density corresponding to a homogeneous electron gas of density $n(\mathbf{r})$. $\varepsilon_{XC}^{HEG}(\mathbf{r})$ can be separated into exchange and correlation parts as,

$$\varepsilon_{XC}^{HEG}(\mathbf{r}) = \varepsilon_{X}^{HEG}(\mathbf{r}) + \varepsilon_{C}^{HEG}(\mathbf{r}). \tag{2.56}$$

This exchange part $\varepsilon_{X}^{HEG}(\mathbf{r})$ was derived analytically by Dirac and is known for a homogeneous electron gas [25]. However, the analytic expressions for ε_{C}^{HEG} in case of the homogeneous electron gas is only known in two limits of high [26,27] and low [28] electron densities.

Generalized Gradient Approximation (GGA) :

LDA is the simplest approximation that is not appropriate for real systems where the electron density is not uniform due to formation of spatially directed bonds. So, the next approximation is the generalized gradient approximation (GGA). To consider the spatial

variation in the electron density, the exchange-correlation energy density is expressed in terms of both the local electron density as well as the gradient of the electron density. To represent this fact, we can express the exchange-correlation functional under GGA approximation as,

$$E_{XC}^{GGA}[n(\mathbf{r})] = \int n(\mathbf{r})\varepsilon_{XC}^{HEG}[n(\mathbf{r}), |\nabla n(\mathbf{r})|]d^3r \tag{2.57}$$

Most important work in developing GGA functional was initiated by Perdew and co-workers [29]. Now the information of the gradient of the electron density can be included in various ways leading to large number distinct GGA functionals. Some of the most popular forms are Perdew and Wang (PW91) [30], Becke-Lee-Yang-Par (B-LYP) [31] and Perdew, Burke and Enzerhof (PBE) [32] functionals.

Meta-Generalized Gradient Approximation(MGGA) :

The next type of approximations that follows after GGA is the meta-generalized gradient approximation(MGGA). MGGA functionals include information from $n(\mathbf{r})$, $\nabla n(\mathbf{r})$ and $\nabla^2 n(\mathbf{r})$. The kinetic energy density corresponding to the Kohn-Sham orbitals,

$$\tau(\mathbf{r}) = \frac{1}{2}\sum_{i=1}^{N} |\nabla \phi_i(\mathbf{r})|^2 \tag{2.58}$$

is equivalent to the Laplacian of the electron density, and thus may be used in meta-GGA functionals instead of $\nabla^2 n(\mathbf{r})$. The Tao-Perdew-Staroverov-Scuseria (TPSS) functional [33] is an example of meta-GGA functional.

Hybrid Functionals :

Hybrid functionals include contributions from the exact exchange(Hartree-Fock) energy with a GGA functional having a general form,

$$E_{XC}^{Hybrid} = \alpha(E_X^{HF} - E_X^{GGA}) + E_{XC}^{GGA} \tag{2.59}$$

where E_X^{HF} is the Hartree-Fock exchange energy expression as given in Equation 2.18 with Kohn-Sham orbitals used in place of spin orbitals. One of the feature of this quantity is that it is non-local. To evaluate it at a particular point of the configuration space the value of ϕ_i must be known at all points. The coefficient, α, determines the amount of exact-exchange mixing which is fitted semi-empirically. HSE functionals [34] named after J. Heyd, G. E. Scuseria, and M. Ernzerhof is one such example. These functionals are expected to be more accurate while studying the strongly correlated electron systems

due to their large self-interaction correction but are computationally expensive due to the non-local nature.

2.3 Numerical Approximations for DFT Calculations

Using DFT we are trying to calculate the electronic structure of a collection of atoms. DFT basically defines a mathematical problem for any such physical system with an approximate form of the exchange-correlation functional. The mathematical problem is to solve a set of mathematical equations(Kohn-Sham equations) in an iterative manner to get the ground state electron density. The problem cannot be solved analytically but numerically with a series of numerical approximations. For example integrations are done considering a finite number of grid points, infinite sums are truncated to finite ones. Due to such approximations errors may enter. In this regard, a well converged solution is the one which is very close to the exact solution of the mathematical problem defined by DFT. Here we make a brief discussion on such numerical approximations.

2.3.1 Plane Wave Basis and Energy cutoff :

To numerically solve the Kohn-Sham equations we first need a proper basis set to expand the single particle orbitals and represent them with the expansion coefficients. Here we are interested in the electronic structure of crystalline materials with periodic arrangements of atoms. The entire crystal can be generated from a periodic repetition of a basic unit called the unit cell defined by three unit vectors, $\mathbf{a}_1$, $\mathbf{a}_2$, $\mathbf{a}_3$. The single particle electronic states for the non-interacting electrons in periodic system are called Bloch states [5] with the form :

$$\phi_{\mathbf{k}}(\mathbf{r}) = e^{i\mathbf{k}\cdot\mathbf{r}} u_{\mathbf{k}}(\mathbf{r}) \tag{2.60}$$

where, $u_{\mathbf{k}}(\mathbf{r})$ is periodic in space with periodicity of the crystal, i.e. $u_{\mathbf{k}}(\mathbf{r} + n_1\mathbf{a}_1 + n_2\mathbf{a}_2 + n_3\mathbf{a}_3) = u_{\mathbf{k}}(\mathbf{r})$ for any integer values of n_1, n_2, n_3. So, Bloch states are basically plane waves modified by a periodic function $u_{\mathbf{k}}(\mathbf{r})$. Periodicity of $u_{\mathbf{k}}(\mathbf{r})$ allows it to be expanded in terms of plane waves as,

$$u_{\mathbf{k}}(\mathbf{r}) = \sum_{\mathbf{G}} C_{\mathbf{G}} e^{i\mathbf{G}\cdot\mathbf{r}} \tag{2.61}$$

where, $\mathbf{G} = m_1\mathbf{b}_1 + m_2\mathbf{b}_2 + m_3\mathbf{b}_3$, is a reciprocal lattice vector defined in terms of reciprocal space unit vectors $\mathbf{b}_1$, $\mathbf{b}_2$, $\mathbf{b}_3$(which can be expressed in terms of real space unit vectors $\mathbf{a}_1$, $\mathbf{a}_2$, $\mathbf{a}_3$ using the standard definition) for any integer values of m_1, m_2, m_3. So, now the Bloch states are given as,

$$\phi_{\mathbf{k}}(\mathbf{r}) = \sum_{\mathbf{G}} C_{\mathbf{G}+\mathbf{k}} e^{i(\mathbf{G}+\mathbf{k})\cdot\mathbf{r}} \tag{2.62}$$

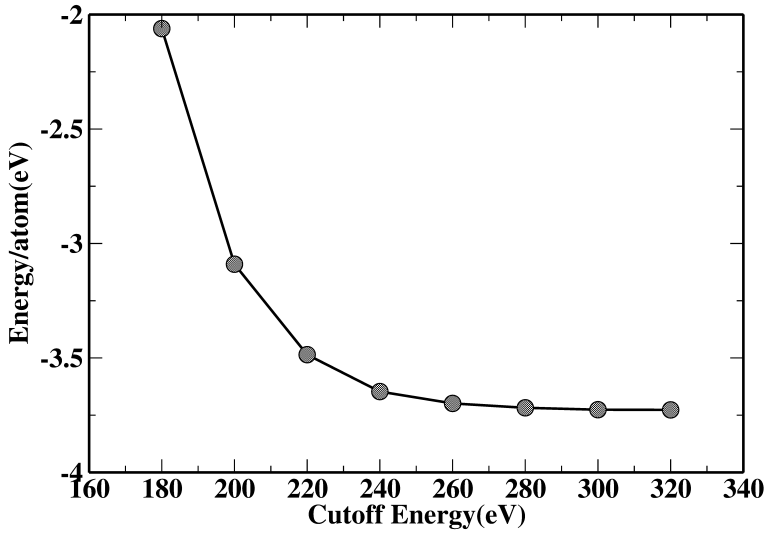

Figure 2.1: Total energy per atom of fcc Cu using a 10×10×10 k-points grid as a function of the cutoff energy E_{cut}

This is an infinite sum of plane waves with kinetic energies $E = \frac{\hbar^2}{2m}|\mathbf{k}+\mathbf{G}|^2$. For a periodic system, such states are reasonable to choose as the single electron orbitals ϕ_i, in the Kohn-Sham equations and we can use plane waves as the basis set to expand the Kohn-Sham orbitals. This is why such DFT calculations are sometimes referred to as plane wave calculations. The problem is that Equation (2.62) involves a summation over an infinite number of possible values of $\mathbf{G}$. For practical calculations we need to truncate this infinite sum to a finite one. For this we consider a cutoff energy defined as,

$$E_{cut} = \frac{\hbar^2}{2m} G_{cut}^2 \tag{2.63}$$

so that, the plane waves with kinetic energy lower than the cutoff energy are included in the basis. The error introduced in this approximation can be minimized by increasing E_{cut} till the total energy of the system converges showing no significant variation with any further change in E_{cut}.

Figure 2.1 shows the convergence of the total energy per atom(using DFT as implemented in VASP) of fcc Cu as a function of E_{cut}. GGA was considered for the exchange-correlation functional. A 10×10×10 Monkhorst-Pack k-mesh was used for performing the k-space integrations(This is discussed in details in the next section). We can see from Figure 2.1 that, changing value of E_{cut} from 300 to 320 eV, the total energy change per atom is less than 1 meV. Hence we can use $E_{cut} = 300eV$ for the above calculation for a well converged result.

2.3.2 Performing K-Space Integrations :

In any practical DFT calculation, a large amount of time is spent in evaluating k-space integrals in the Brillouin zone with the form [14],

$$g = \frac{V_{cell}}{(2\pi)^3} \int_{BZ} g(\mathbf{k}) d\mathbf{k} \tag{2.64}$$

Where V_{cell}, is the volume of the unit cell of the crystal. Numerically integrals are evaluated by evaluating the value of the function $g(\mathbf{k})$, at some finite set of k-points within the Brillouin zone and summing them with proper weight. Such method give more and more accurate results as we increase the number of k-points and the numerical method may converge to the exact result of the integral.

The question is how to choose the k-points to evaluate such integrals efficiently. The most widely used method of considering equally spaced points in the Brillouin zone was developed by Monkhorst and Pack [35]. For example, for a cubic or almost cubic unit cell the reciprocal unit cell is also cubic and we can consider same number of k-points along each k-space unit vector $\mathbf{b}_i$. If N number of k-points are considered along each direction then the calculation is leveled as $N \times N \times N$ k-points calculation. To test the convergence, the way is to increase the value of N till there is no significant variation in the total energy with any further change in N. Figure 2.2 shows the convergence of the total energy(using DFT as implemented in VASP) of fcc Cu as a function of N. GGA was considered for exchange-correlation functional with a converged E_{cut} value of 300 eV.

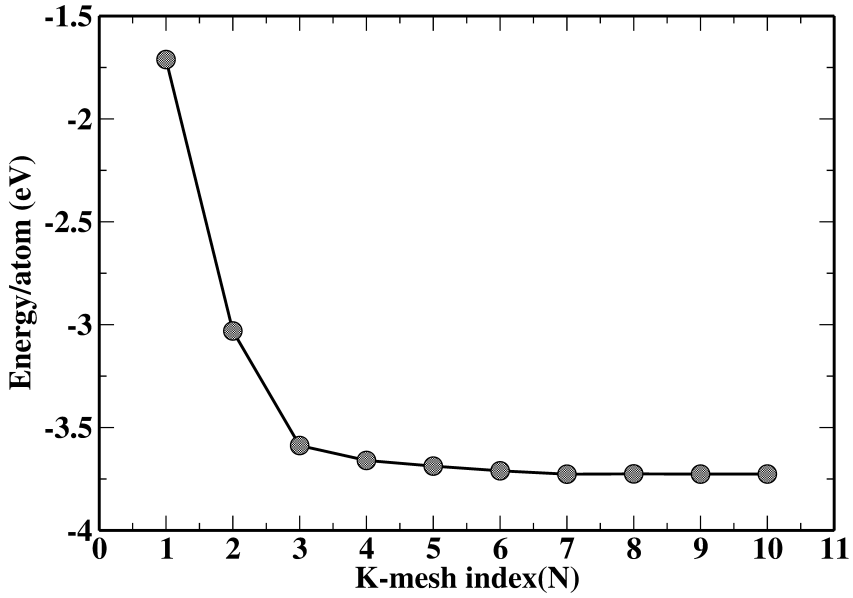

Figure 2.2: Total energy per atom for fcc Cu as a function of N implying a $N \times N \times N$ k-points calculation

Changing the value of N from 7 to 8, the total energy change per atom is less than 1 meV. Hence we can use $7 \times 7 \times 7$ or $8 \times 8 \times 8$ k-points grid in the above calculation for a well converged result.

2.3.3 Frozen core approximation and Pseudopotential :

In any real material the electrons of the atoms that are chemically important are the valence electrons because they take part in bonding. The core electrons that are tightly attached to the nucleus remain more or less inert. Also the kinetic energy of the core electrons are much higher than the valence electrons and their wave function are highly oscillating on short length scale. As a result we need large energy cutoff value for a plane wave basis set to represent them. So, if we are able to approximate the properties of the core electrons then we can reduce the computation cost by reducing the number of plane waves in the basis set.

The popular approach to treat the core electrons is to use pseudopotentials. A pseudopotential replaces the electron density from the core electrons with a smoothed density chosen to match various important physical and mathematical properties of the true ion core. This is the frozen core approximation. In this approximation, if $|\psi^c\rangle$ and $|\psi^v\rangle$ represent the quantum states for core electrons and the valence electrons respectively then

one can construct smooth valence states $|\phi^v\rangle$ orthogonal to $|\psi^c\rangle$ as [36],

$$|\phi^v\rangle = |\psi^v\rangle + \sum_c \alpha_c \psi^c(\mathbf{r}) \tag{2.65}$$

where α_c can be determined from the orthogonality condition $\alpha_c = \langle\psi^c|\phi^v\rangle$. The pseudo wave functions satisfies the modified Schrödinger equation:

$$\left[H + \sum_c (\epsilon^v - \epsilon^c)|\psi^c\rangle\langle\psi^c|\right]|\phi^v\rangle \;=\; \epsilon^v|\phi^v\rangle \tag{2.66}$$

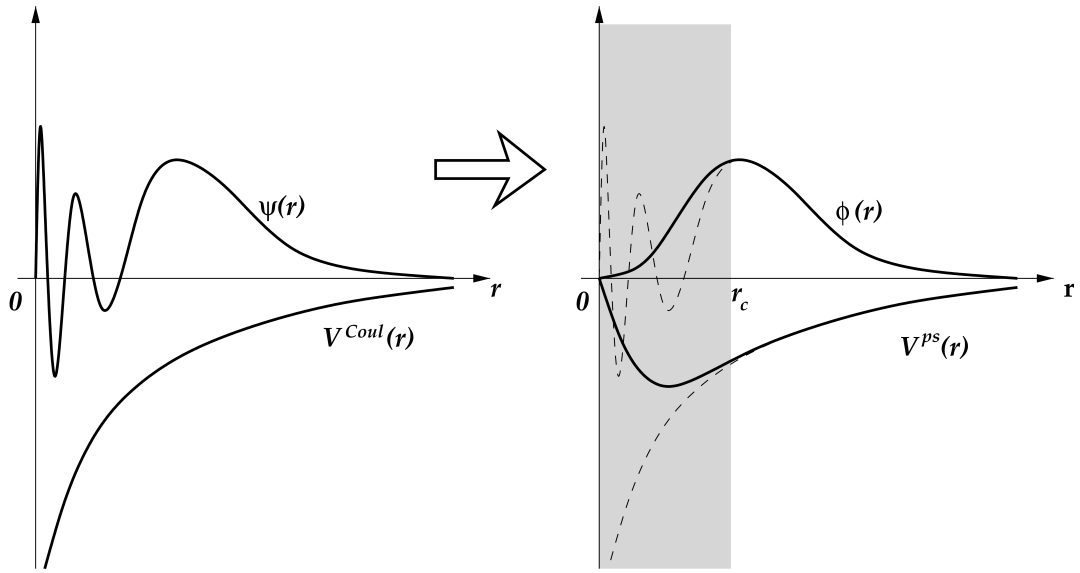

Figure 2.3: Schematic diagram of the Pseudopotential $V^{PS}(r)$ and pseudo-wavefunction $\phi(r)$. The left figure shows valence wave function $\psi(r)$ and Coulomb potential $V^{Coul}(r)$. In the right figure, r_c represents the cutoff radius beyond which the wave function and the potential are not affected.(Taken from, Atomic and Electronic Structure of Solids, E. Kaxiras, Cambridge University Press [37])

So, we can construct a Pseudo-Hamiltonian,

$$H^{PH} = \left[H + \sum_c (\epsilon^v - \epsilon^c)|\psi^c\rangle\langle\psi^c|\right] \tag{2.67}$$

with the same eigenvalues as the original Hamiltonian H, but with a smoother wave function. The corresponding potential,

$$V^{PP} = V + \sum_c (\epsilon^v - \epsilon^c)|\psi^c\rangle\langle\psi^c| \tag{2.68}$$

is called pseudo-potential, where V is the nuclear potential in H. The second term is a correction term and repulsive in nature as $\epsilon^v > \epsilon^c$, indicating that the valence electrons experience a net repulsive force due to the core electrons. Figure 2.3 schematically illustrates the pseudo-potential approach. Beyond the core region i.e. above a cutoff radius, r_c, pseudo-wavefunctions and pseudopotentials are identical to the all electron wave functions and potential respectively, while in the core region (within r_c), a weaker potential will be experienced by this new set of valence states.

In DFT calculations any pseudopotential for an atom define a minimum cutoff energy that should be used. Pseudopotentials requiring high cutoff energies are said to be hard, while pseudopotentials with low cutoff energies are called soft, which are computationally efficient. There are also ultrasoft pseudopotential(USPP) [38] that require very low cutoff energy.

2.3.4 Projector Augmented Wave(PAW) method :

One disadvantage of using USPPs is that the construction of the pseudopotential for each atom requires a number of empirical parameters to be specified. Current DFT codes typically only include USPPs that have been carefully developed and tested, but they do in some cases include multiple USPPs with varying degrees of softness for some elements [14]. Another frozen core approach that avoids some of the disadvantages of USPPs is the projector augmented-wave(PAW) method originally introduced by Blöchl [39] and later adapted for plane-wave calculations by Kresse and Joubert [40]. In such approximation, an all electron wave function is constructed, with which all integrals are calculated as a combination of smooth functions extending throughout space and contribution from the localized muffin tin orbitals [41, 42]. Hence the total wave function in this case is a combination of valence state wave functions $\tilde{\psi}_i^v(\mathbf{r})$ and a linear transformation function relating the all-electron valence functions $\psi_j^v(\mathbf{r})$ to $\tilde{\psi}_i^v(\mathbf{r})$ which is given as,

$$\psi_j^v(\mathbf{r}) = \tilde{\psi}_j^v(\mathbf{r}) + \sum_i (|\phi_i\rangle - |\tilde{\phi}_i\rangle)\langle\tilde{p}_i|\tilde{\phi}_i\rangle \tag{2.69}$$

In the above equation, index i is for the atomic site $\mathbf{R}$, $|\tilde{p_i}\rangle$ are the projector functions for localized pseudo partial wave which satisfy the orthogonality condition, $\langle\tilde{p_i}|\tilde{\phi_j}\rangle = \delta_{i,j}$. Within this formalism, the all electron charge density can be derived from Equation (2.69) as,

$$n(\mathbf{r}) = \tilde{n}(\mathbf{r}) + n^1(\mathbf{r}) - \tilde{n}^1(\mathbf{r}), \tag{2.70}$$

where,

$$\tilde{n}(\mathbf{r}) = \sum_i f_i |\tilde{\psi_i}(\mathbf{r})|^2 \tag{2.71}$$

$$n^1(\mathbf{r}) = \sum_i f_i \sum_{j,k} \langle\tilde{\psi_i}|\tilde{p_j}\rangle \phi_j(\mathbf{r})\phi_k(\mathbf{r})\langle\tilde{p_k}|\tilde{\psi_i}\rangle \tag{2.72}$$

$$\tilde{n}^1(\mathbf{r}) = \sum_i f_i \sum_{j,k} \langle\tilde{\psi_i}|\tilde{p_j}\rangle \tilde{\phi}_j(\mathbf{r})\tilde{\phi}_k(\mathbf{r})\langle\tilde{p_k}|\tilde{\psi_i}\rangle \tag{2.73}$$

In the above expressions, f_i's represent the occupancies of the eigenstates $\tilde{\psi_i}$, $\tilde{n}(\mathbf{r})$ is the pseudo-charge density and is evaluated from the pseudo-wavefunctions with plane wave basis. $n^1(\mathbf{r})$ and $\tilde{n}^1(\mathbf{r})$ are the on-site charge densities localized within the augmented sphere around each atom. Total energy of the system when calculated from these charge densities can also be divided into three parts.

2.4 Introduction to Wannier Functions

After electronic structure calculation for a periodic solid, the state of the system is described in terms of band states/Bloch states [5]. These are delocalized/extended electronic states which are assigned a quantum number $\mathbf{k}$ for the crystal momentum, together with a band index n. This is widely used in electronic structure calculations but alternate representations are also available. The Wannier representation [6–8], which is essentially a real-space picture of localized orbitals, assigns as quantum numbers, the lattice vector $\mathbf{R}$ of the unit cell where the orbital is localized, together with a band-like index n. Wannier functions can be a powerful tool in the study of the electronic and dielectric properties of materials and can provide an insightful picture of the nature of chemical bonding, otherwise missing from the band picture of extended orbitals [9].

We start with the fact that, single electronic states for the non-interacting electrons in periodic system are called Bloch states [5] with the form :

$$\Phi_{n\mathbf{k}}(\mathbf{r}) = e^{i\mathbf{k}\cdot\mathbf{r}} u_{n\mathbf{k}}(\mathbf{r}) \tag{2.74}$$

n is the band index, $u_{n\mathbf{k}}(\mathbf{r})$ is periodic in space with periodicity of the crystal, i.e. $u_{n\mathbf{k}}(\mathbf{r}+\mathbf{R}) = u_{n\mathbf{k}}(\mathbf{r})$ for any lattice vector $\mathbf{R} = n_1\mathbf{a}_1 + n_2\mathbf{a}_2 + n_3\mathbf{a}_3$. Here we do not know the exact form of $\Phi_{n\mathbf{k}}(\mathbf{r})$ due to the unknown function $u_{n\mathbf{k}}(\mathbf{r})$. Now in a Tight binding approximation the crystal is described as collection of weakly interacting atoms so that there is negligible overlap of the valence electrons. Hence the atomic description is not completely irrelevant. Then we can express $\Phi_{n\mathbf{k}}(\mathbf{r})$ in terms of the atomic wave functions $\psi_n(\mathbf{r})$, which are solutions of the atomic Hamiltonian$[H_{at}\psi_n(\mathbf{r}) = \varepsilon_n\psi_n(\mathbf{r})]$ as linear combination of atomic orbitals located at the lattice points $\mathbf{R}$:

$$\Phi_{n\mathbf{k}}(\mathbf{r}) = \sum_{\mathbf{R}} e^{i\mathbf{k}\cdot\mathbf{R}} \psi_n(\mathbf{r}-\mathbf{R}) \tag{2.75}$$

$\psi_n(\mathbf{r}-\mathbf{R})$ is the n^{th} atomic orbital at lattice point $\mathbf{R}$. Such expansion satisfy the Bloch condition.

$$\begin{aligned}
\Phi_{n\mathbf{k}}(\mathbf{r}+\mathbf{R}) &= \sum_{\mathbf{R}'} e^{i\mathbf{k}\cdot\mathbf{R}'} \psi_n(\mathbf{r}+\mathbf{R}-\mathbf{R}') && (2.76)\\
&= e^{i\mathbf{k}\cdot\mathbf{R}} [\sum_{\mathbf{R}'} e^{i\mathbf{k}\cdot(\mathbf{R}'-\mathbf{R})} \psi_n(\mathbf{r}-(\mathbf{R}'-\mathbf{R})] && (2.77)\\
&= e^{i\mathbf{k}\cdot\mathbf{R}} \Phi_{n\mathbf{k}}(\mathbf{r}) && (2.78)
\end{aligned}$$

The energy bands that we get in this way show almost no dispersion with $\mathbf{k}$ due to the crude way of approximating the atomic orbitals as basis. The solution is to introduce functions $\phi_n(\mathbf{r})$ that are not necessarily atomic orbitals but can be derived from a linear combination of atomic orbitals as,

$$\phi_n(\mathbf{r}) = \sum_m b_m \psi_m(\mathbf{r}) \tag{2.79}$$

Where different type of combinations give rise to different type of such functions. In terms of these functions the Bloch states are represented as,

$$\Phi_{n\mathbf{k}}(\mathbf{r}) = \sum_{\mathbf{R}} e^{i\mathbf{k}\cdot\mathbf{R}}\phi_n(\mathbf{r}-\mathbf{R}) \tag{2.80}$$

This functions are called Wannier functions, which are the Fourier coefficients of the inversion formula and are expressed in terms of the Bloch states $\Phi_{m\mathbf{k}}$ as,

$$\phi_n(\mathbf{r}-\mathbf{R}) = \frac{V}{(2\pi)^3}\int_{BZ}\left[\sum_m U^{\mathbf{k}}_{mn}\Phi_{m\mathbf{k}}(\mathbf{r})\right]e^{-i\mathbf{k}\cdot\mathbf{R}}d\mathbf{k}, \tag{2.81}$$

Such Wannier functions can be defined for any band. Unlike atomic functions $\psi_n(\mathbf{r})$, the Wannier functions $\phi_n(\mathbf{r}-\mathbf{R})$ at different lattice site and with different band index are orthogonal. The Wannier functions $\phi_n(\mathbf{r}-\mathbf{R})$ for all n and $\mathbf{R}$ form a complete orthogonal set to describe the Bloch states. They offer an alternative localized basis set for exact description of the independent electron levels.

In the Equation (2.81), V is volume of the unit cell and integration is over the whole Brillouin zone. $U^{\mathbf{k}}$ is the unitary matrix which is used to mix the Bloch states at each $\mathbf{k}$ point in the Brillouin zone of the crystal and is not a unique one. The varying spatial extensions of the Wannier functions depend upon the choice of $U^{\mathbf{k}}$ in the above expression. This non-uniqueness of $U^{\mathbf{k}}$ arise from the fact that orbitals represented by Bloch states belong to a set of bands that are separated by energy gaps from each other but have degeneracies within themselves and thus at each $\mathbf{k}$ point there will be many unitary transformations possible within themselves. This makes uses of Wannier functions unsuitable in the case of real problems. A procedure to eliminate this arbitrariness was proposed by Marzari and Vanderbilt [11]. In this method, iteratively redefined transformations would lead to uniquely defined set of maximally-localized Wannier functions (MLWFs). This approach can be applied to a variety of problems starting from an isolated system to a periodic solid. For the entanglement band problem, this approach was extended by Souza *et al.* [12].

Bibliography

[1] D. J. Griffiths, Introduction to Quantum Mechanics, 2nd Ed. Prentice Hall, 2005.

[2] G. Kresse and J. Hafner, Phys. Rev. B **47**, 558 (1993) ; G. Kresse and J. Hafner, Phys. Rev. B **49**, 14251 (1994); G. Kresse and J. Furthmüller, Phys. Rev. B **54**, 11169 (1996).

[3] G. Kresse and J. Furthmüller, Comput. Mater. Sci., **6**, 15 (1996).

[4] K. Umemoto, R. M. Wentzcovitch, and P. B. Allen, Science **311**, 983 (2006).

[5] F. Blöch, Z. Physik **52**, 555 (1928).

[6] G. H. Wannier, Physical Review **52**, 191 (1937).

[7] W. Kohn, Physical Review **115**, 809 (1959).

[8] J. des Cloizeaux, Physical Review **129**, 554 (1963).

[9] N. Marzari, A. A. Mostofi, J. R. Yates, I. Souza, and D. Vanderbilt, Rev. Mod. Phys. **84**, 1419 (2012).

[10] A. A. Mostofi, J. R. Yates, Y.-S. Lee, I. Souza, D. Vanderbilt, and N. Marzari, Comput. Phys. Comm. **178**, 685 (2008).

[11] N. Marzari and D. Vanderbilt, Phys. Rev. B **56**, 12847 (1997).

[12] I. Souza, N. Marzari and D. Vanderbilt, Phys. Rev. B **65**, 035109 (2001).

[13] M. Born and J. R. Oppenheimer, Zur Quantentheorie der Molekeln, Ann. Physik 84, 457(1927).

[14] D. S. Sholl and J. A. Steckel, Density Functional Theory : A Practical Introduction (Wiley-Interscience) (2009).

[15] D. R. Hartree, The wave mechanics of an atom with non-Coulombic central field: Parts I, II, III. Proc. Cambridge Phil. Soc. 24, 89, 111, 426(1928).

[16] J. C. Slater, Phys. Rev. **34**, 1293 (1929).

[17] V. Fock, Naherungsmethode zur Losung des quanten-mechanischen Mehrkorper-probleme, Z. Phys. 61, 126(1930).

[18] G. Arfken, Mathematical Methods for Physicists. 3rd Edition, Academic Press, NY (1985).

[19] L. H. Thomas, Proc. Cambridge Philos. Soc. **23**, 542 (1927).

[20] E. Fermi, Atti Accad. Naz. Lincei, Cl. Sci. Fis. Mat. Nat. Rend. **6**, 602 (1927).

[21] W. Kohn, Rev. Mod. Phys. **71**, 1253 (1999).

[22] P. Hohenberg and W. Kohn, Phys. Rev. **136**, B864 (1964).

[23] W. Kohn and L. J. Sham, Phys. Rev. **140**, A1133 (1965).

[24] J. P. Perdew, K. Burke, and Y. Wang, Phys. Rev. B **54**, 16533 (1996).

[25] P. A. M. Dirac, Proc. Cambridge Phil. Roy. Soc. **26**, 376 (1930).

[26] M. Gell-Mann and K. A. Brueckner, Phys. Rev. **106**, 364 (1957).

[27] W. J. Carr and A. A. Maradudin, Phys. Rev. **133**, A371 (1964).

[28] E. Wigner, Phys. Rev. **46**, 1002 (1934).

[29] J. P. Perdew, Phys. Rev. Lett. **55**, 2370 (1985).

[30] J. P. Perdew and Y. Wang, Phys. Rev. B **45**, 13244 (1992).

[31] A. D. Becke, Phys. Rev. A **38**, 3098 (1988); C. Lee, W. Yang, R. G. Parr, Phys Rev. B **37**, 785 (1988); A. D. Becke, J. Chem. Phys. **96** 2155 (1992).

[32] J. P. Perdew, K. Burke, and M. Ernzerhof, Phys. Rev. Lett. **77**, 3865 (1996).

[33] J. Tao, J. P. Perdew, V. N. Staroverov, and G. E. Scuseria, Phys. Rev. Lett. **91**, 146401 (2003).

[34] J. Heyd, G. E. Scuseria, and M. Ernzerhof, J. Chem. Phys. **118**, 8207 (2003).

[35] Hendrik J. Monkhorst and James D. Pack, Phys. Rev. B **13**, 5188 (1976).

[36] James C. Phillips and Leonard Kleinman, Phys. Rev. **116**, 287 (1959).

[37] E. Kaxiras, Atomic and Electronic Structure of Solids, Cambridge University Press, UK,(2003).

[38] D. Vanderbilt, Phys. Rev. B. **41**, 8412 (1990).

[39] P.E. Blöchl, Phys. Rev. B **50**, 17953 (1994).

[40] G. Kresse, and J. Joubert, Phys. Rev. B textbf59, 1758 (1999).

[41] O. K. Andersen and R. V. Kasowski, Phys. Rev. B **4**, 1064 (1971).

[42] O. K. Andersen, 1971, Computational Methods in Band Theory, p. 178, edited by P. M. Marcus, J. F. Janak and A. R. Williams (Plenum Press).

Chapter 3

The driving force for charge ordering in rare earth nickelates

3.1 Introduction

Although the $3d$ transition metal oxides have been studied since the 1950's, improved growth and characterization techniques as well as new theoretical approaches have continued to yield new insights [1–5]. The rare earth perovskite nickelates are of particular current interest. These materials exhibit metal-insulator transitions for all members of the family $RENiO_3$ (where RE denotes a rare earth ion), with the exception of RE = La [6, 7]. The metal-insulator transition is coincident with a crystal distortion in which the mean Ni-O bond length alternates between two inequivalent Ni sites, defining a bond disproportionation [8–11]. This state is sometimes also referred to as "charge ordered". The presence of the rare earth atom in the perovskite lattice has always been understood as controlling the structural distortions. An atom with a smaller ionic radius leads to a smaller volume of the unit cell. However, this would also imply shorter Ni-O bond lengths. This shortening of the bond lengths has the effect of increasing the Coulomb repulsion between electrons on Ni and those on oxygen. The NiO_6 octahedra rotate leading to longer Ni-O bond lengths. This results in Ni-O-Ni angles which deviate from 180^o, with the smaller RE ion resulting in larger deviations of the Ni-O-Ni angle. The bandwidth of the Ni d states is controlled by the effective hopping interaction strength, which depends on the Ni-O-Ni angle. Initially, the metal-insulator transition in the nickelates was understood as being driven by the modified bandwidth arising from the rotation of the NiO_6 octahedra [12]. However, later analysis of the structure revealed a breathing mode distortion associated with the NiO_6 octahedra. One Ni atom had an expanded NiO_6 octahedron associated with it, while the other had a contracted NiO_6 octahedron associated with it [8]. While there was no significant charge difference between the two Ni sites, the associated Ni-O bond lengths led to one of the Ni atoms with longer Ni-O bond lengths ($\sim$ 2 Å) being labeled Ni^{2+}, while the other with shorter Ni-O bond lengths ($\sim$ 1.9 Å) was labeled Ni^{4+}. A similar finding has emerged in the context of other charge ordered nickelates [8–11].

While the rare earth perovskite nickelates exhibit bond disproportionation, the rare earth perovskite cobaltates formed with the neighboring transition metal atom Co in the same oxidation state exhibit no such ordering. An important parameter that controls the electronic structure for the late transition metal oxides is the charge transfer energy(Δ), given by the energy required to transfer an electron from the oxygen p levels to the transition metal d levels. The charge transfer energy decreases as one goes across the $3d$ transition metal series from Ti to Cu [13] and it is natural to associate the change in charge transfer energy with the propensity to bond disproportionation.

Formal valence considerations assign the d^7 configuration to the Ni in the $RENiO_3$ perovskites. However, if the charge transfer energy is strongly negative, the electronic configuration is more appropriately represented as $d^8\bar{L}$ (with the $\bar{L}$ denoting a hole on the ligand). The importance of an effectively negative charge transfer energy in this family of compounds was first pointed out by Barman *et al.* [14] while discussing the insulating ground state of $NdNiO_3$ in contrast to the metallic one of $LaNiO_3$. Mizokawa *et al.* [15] carried out model Hamiltonian calculations for a multiband Hubbard model and could capture the bond disproportionation at a negative value of the charge transfer energy when they included a breathing mode distortion of the NiO_6 octahedra. This suggests that the combination of lattice distortions and a negative charge transfer energy drove the charge ordering. Mazin and coworkers [16] argued that the charge ordering was an alternative to Jahn-Teller distortions, and part of the energy lowering associated with the disproportionation came from the energy gain from Hund's intra-atomic exchange interactions, which favor a high-spin d^8 state. Building on the Mizokawa picture, Park, Millis and Marianetti [17] presented density functional plus dynamical mean field calculations that explained the disproportionation in terms of a site-selective Mott transition occurring in a situation in which the charge transfer energy was very negative, and Johnson and collaborators later considered the same physics in a model system perspective [18]. On the other hand, Peil and Georges [19] argued that an appropriate low energy description of the physics was in terms of a Hubbard model with a vanishing or negative U; in this effective low energy picture, the bond-disproportionated state is indeed characterized by charge order.

In this paper, we take a new approach to this issue by examining in more detail the connection between bond disproportionation and the charge transfer energy. Introducing a potential on the Ni d states, we are able to vary the charge transfer energy and examine the ensuing changes in the structure as well as the electronic structure within an *ab-initio* framework in contrast to all model Hamiltonian approaches in the past. We find that the onset of charge ordering is characterized by the point at which the Ni d band enters the oxygen p band, defining the effective negative charge transfer energy(Δ_{eff}) [20, 21]. This destabilizes the RE-oxygen network which is otherwise ionic, driving the charge ordering.

3.2 Methodology

The electronic structure of $NdNiO_3$ was calculated within a projected augmented wave [22] implementation of density functional theory within the Vienna ab-initio simulation package (VASP) [23, 24] code. The experimental lattice parameters were taken [25]. The

magnetic structure (both T-AFM [26, 27], non-collinear E′-AFM [28] and FM) was imposed and the electronic structure was calculated within the Dudarev implementation [29] of GGA+U with a U of 4 eV on the Ni sites. The generalized gradient approximation(GGA) [30] was used for the exchange correlation functional. A Monkhorst-Pack [31] k-points grid of 4×6×2 was used for calculating the electronic structure of the magnetic supercell. While the lattice parameters were kept fixed at the experimental values, the internal positions were optimized to find the minimum energy configuration so that the forces were less than 10^{-3} eV/Å. The general features of the structure are similar when we assume ferromagnetic order. Consequently, the rest of the analysis in terms of microscopic model has been carried out for the ferromagnetic unit cell which is smaller. A k-point mesh of 6×4×6 and an energy cutoff of 500 eV was used for the plane waves considered in the basis. Spheres of radii 1 Å are constructed around each atom for the calculation of the density of states and magnetic moment and within the spheres centered on the Ni ions a *d*-symmetry potential of constant radial part is introduced. The structure is then optimized to find the structural and magnetic parameters in the presence of the potential and the charge transfer energy is quantified by using maximally localized Wannier function methods [32–34] to map the *ab-initio* band structure onto a tight binding model using the VASP to Wannier90 interface [35]. The Bloch states are mapped onto Wannier functions, localized on the respective atoms via a unitary transformation. The angular parts are given by the relevant spherical harmonics. Once the transformation matrices are determined, one has a tight binding representation of the Hamiltonian in the basis of the maximally localized Wannier functions. The results are used to construct a schematic diagram of the electronic structure.

For the thin film calculations, we consider putting layers of $NdNiO_3$ on the $NdGaO_3$ substrate along the *c*-direction. The supercells used in the calculation were further considered to be symmetric about the middle NdO layer to cancel any net polarization in the system. There were five NdO and six GaO_2 layers in the $NdGaO_3$ substrate. However, in $NdGaO_3$ Nd and Ga are in 3+ oxidation state and O is in 2- oxidation state. So, the NdO layer in the substrate has a net +ve charge whereas the GaO_2 layer has a net -ve charge, making the system inevitably doped. To cancel this intrinsic doping we took a new approach and replaced $NdGaO_3$ with $SrTiO_3$ where both SrO and TiO_2 layers are neutral, keeping the lattice parameters and position of the atoms same as $NdGaO_3$. A 14 Å vacuum was considered to take care of any inter-layer interactions. A k-mesh grid of $2 \times 4 \times 1$ was used to perform the k space integrations along with an energy cutoff of 400 eV. Internal coordinates were relaxed for a minimum energy configuration till the forces on the atoms were less than 10^{-3} eV/Å.

3.3 Results and Discussion

There are two candidate orderings which have been proposed for the magnetic structure of the magnetic nickelates. The first corresponds to an up-up-down-down ordering of the spins on the Ni along the three pseudo cubic directions and has been referred to as T-AFM type magnetic structure [26, 27]. There are variants that differ slightly in the stacking of these chains and differ slightly in the total energy [27]. The other structure corresponds to a non-collinear one in which the neighboring spins have equal magnitude but are rotated by 90^o [28]. We have used both of these structures to initialize our calculations; we find that both cases relax to the same magnetic configuration. The fully relaxed structure contains NiO_6 octahedra of short mean bond length ($\sim$ 1.90 Å) and NiO_6 octahedra of longer mean bond length ($\sim$ 2.0 Å). The Ni sites with short-bond octahedra have a zero magnetic moment, while the Ni sites with long-bond octahedra have a magnetic moment of 1.50 μ_B (Ni^{2+}). A similar difference of moment was found experimentally and was initially interpreted as a Ni charge disproportionation [8]. However, examining the density of states associated with each of the Ni sites (Figure 3.1), we find that the t_{2g} states on both Ni sites are completely filled, while the mean occupancy of the e_g states on both sites is ~ 2. On the long-bond Ni site(Ni^{2+}), the majority spin e_g channel is found deep inside the valence band and is fully occupied, while the minority spin e_g channel is empty, with a very small admixture of O p implying a Ni d^8 configuration. On the short-bond Ni sites(Ni^{4+}) the high-lying e_g states are found at $\sim$ 1-2 eV in the conduction band and have significant O p admixture; these are antibonding states; the corresponding bonding states are located deep inside the valence band. The significant O p admixture suggests that one should associate an electronic configuration of $d^8\bar{L}^2$ as previously suggested [15,17,18]. As discussed by Park *et al.* [17] the spin splitting of these states is very small (zero in the present calculation).

The almost ubiquitous charge ordering among the rare-earth nickelates suggests that it should be associated with some aspect of the electronic structure. Among the undoped transition metal oxides with the same chemical formula and same oxidation state, it is only the nickelates which exhibit charge ordering. As the transition metal d levels get increasingly stabilized with respect to the oxygen p levels as one move across the $3d$ transition metal series [13], we went on to examine if it was the charge transfer energy which was responsible for this unusual behaviour. Having established that the DFT+U calculations correctly reproduce the basic physics of $NdNiO_3$, we analyze the consequences of varying the charge transfer energy. We introduced a constant potential on the Ni d states and varied the charge transfer energy Δ in steps. Structural optimization of the atomic positions was carried out to examine the implications of the modifications

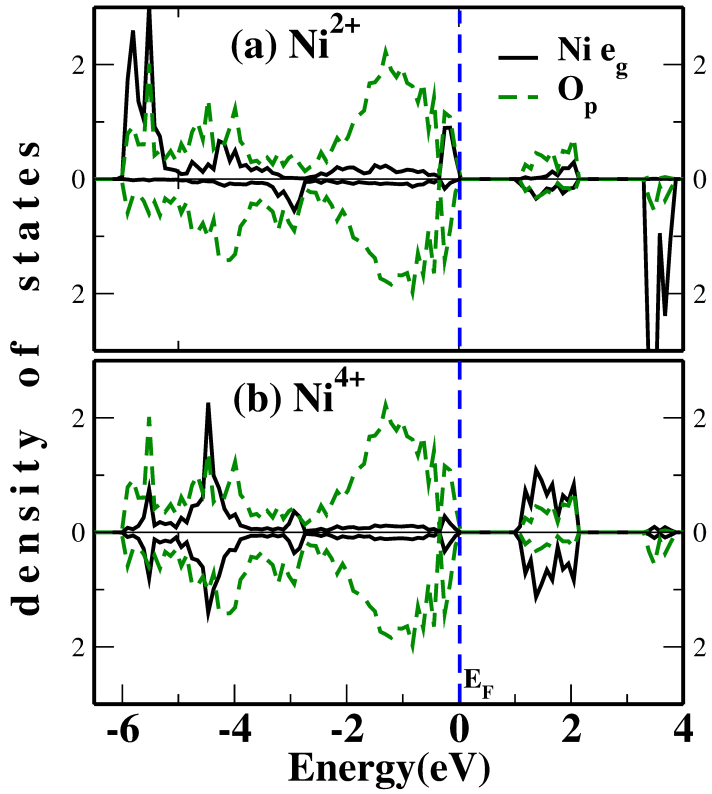

Figure 3.1: The spin resolved (upper and lower panel) Ni e_g and O p contributions to the density of states for (a) Ni^{2+}, (b) Ni^{4+} sites in $NdNiO_3$ considering the T-type antiferromagnetic structure and U = 4 eV on Ni.

of Δ on the structure. For convenience in the analysis and interpretation, we consider a ferromagnetic ground state (which can also be stabilized in the DFT+U method, although it is not the true ground state). In the ferromagnetic state the inequivalent Ni sites have respectively a large and a small moment, but in contrast to the T-type antiferromagnetic state the smaller moment, while much less than the larger one, is not zero. In order to quantify the changes in the charge transfer energy that was introduced, we carried out a mapping of the electronic structure onto a tight binding model which includes Ni d and O p states in the basis(see the methodology section for the method). Maximally localized Wannier functions are used for the radial part of the wavefunction. As the presence of magnetic order can move the Ni d levels with respect to their positions in the absence of it, leading to a double counting of the effects of the exchange interactions, we use the nonmagnetic calculation to define the value of Δ for each calculation where the potential at the Ni site has been varied. The on-site energies of the Ni d and O p levels extracted from the mapping were used to calculate the value of Δ for each case as the energy difference between the O p levels and Ni e_g levels. In order to show the quality of the fit, we show a comparison of the *ab-initio* band structure and the fitted band structure in Figure 3.2 for one of the Δ values, $\Delta = 0.81$ eV. We vary the potential acting on the Ni,

and for each value of the potential determine the magnetic moments, at each Ni site, the amplitude of the bond disproportionation, and the charge transfer energy Δ as defined from the Wannier mapping.

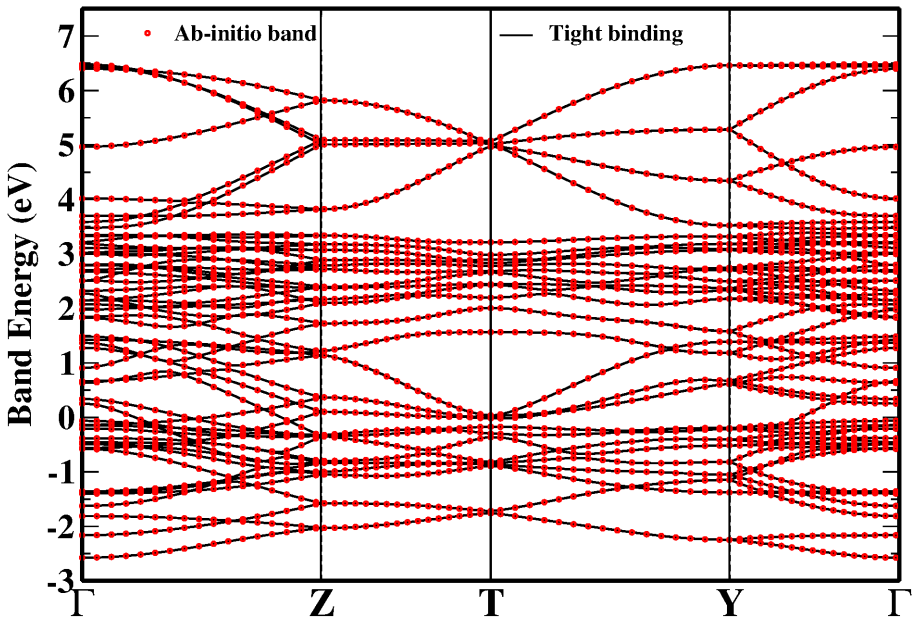

Figure 3.2: A comparison of the *ab-initio* band structure and the tight binding fit for nonmagnetic $NdNiO_3$ at a $\Delta = 0.81$ eV

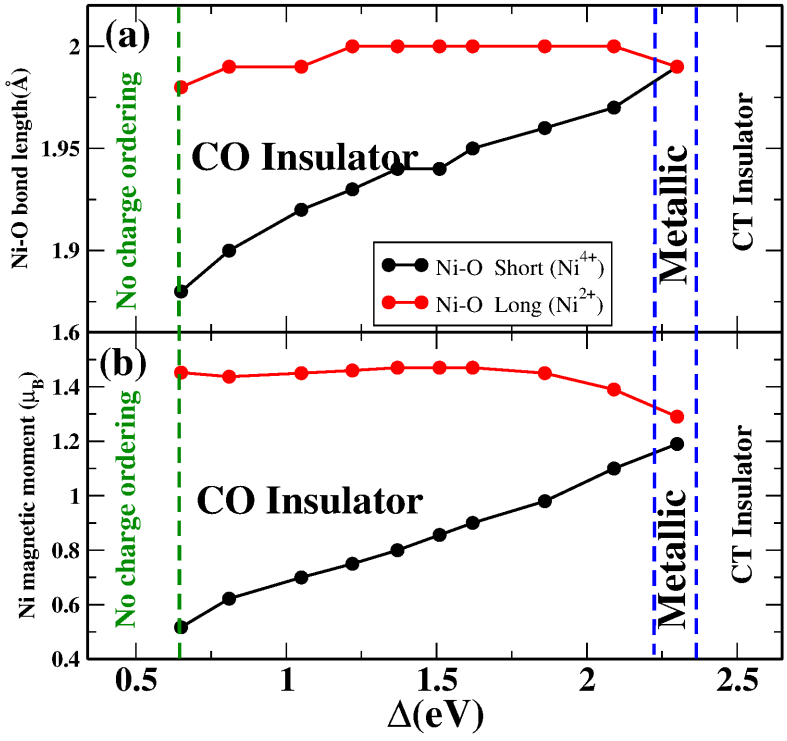

Figure 3.3: Variation in the (a) Ni-O bond lengths and (b) Magnetic moments on the Ni sites with Δ for ferromagnetic $NdNiO_3$ with U = 4 eV.

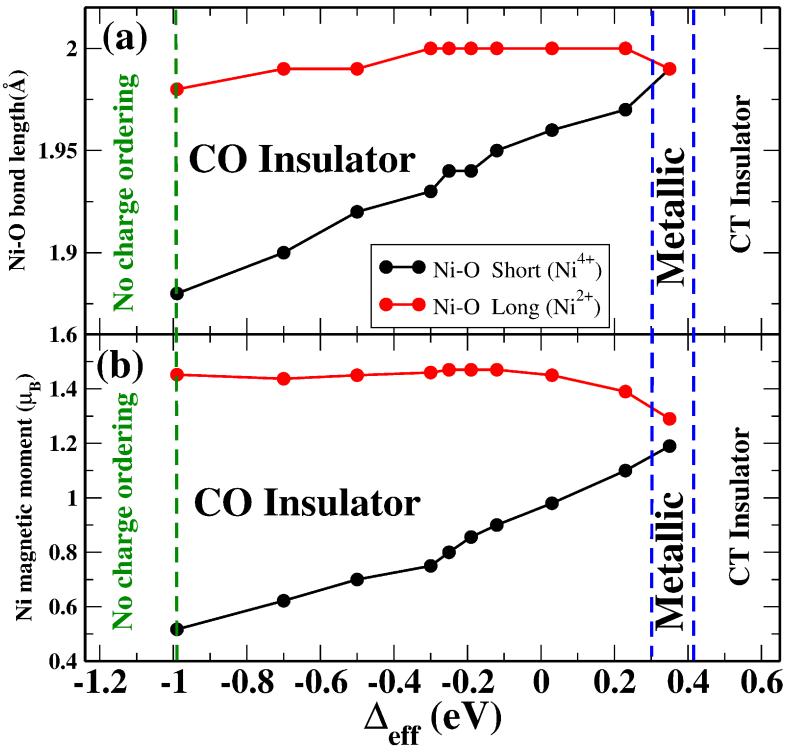

Figure 3.4: Variation in the (a) Ni-O bond lengths and (b) Magnetic moments on the Ni sites with Δ_{eff} for ferromagnetic $NdNiO_3$ with U = 4 eV.

Because the charge transfer energy is a monotonic function of the on-site potential, we plot the magnetic moments and mean octahedral bond lengths against charge transfer energy Δ in Figure 3.3. As Δ is increased from the value ~ 0.65 eV, Figure 3.3(a) shows that the mean bond length of the short-bond octahedra increases(from a value of ~ 1.88 Å), while the mean bond length of the long-bond octahedra changes only slightly. For charge transfer energies greater than about 2 eV the difference between the two mean octahedral bond lengths becomes negligible and they are order of 2.00 Å for both the Ni sites when $\Delta = 2.3$ eV. In contrast to the result for the T-type antiferromagnetic configuration where the Ni^{4+} sites had a zero magnetic moment associated with them, in the ferromagnetic configuration we find that the Ni^{4+} sites have a finite magnetic moment associated with them. Figure 3.3(b) shows a similar increase in the magnetic moment of the short-bond site(from 0.52 μ_B) as the charge transfer energy is increased, with the difference in moments between sites becoming negligible for $\Delta \gtrsim 2.30$ eV. In this region, the values for both the Ni atoms are ~ 1.20 μ_B.

Having established that the charge transfer energy controls the disproportionation physics, we now consider in more detail the mechanism. In order to understand the point at which we had the onset of charge ordering, we calculated the bandwidth of the oxygen p band. This was done by switching off the p-d interactions and calculating the width of the

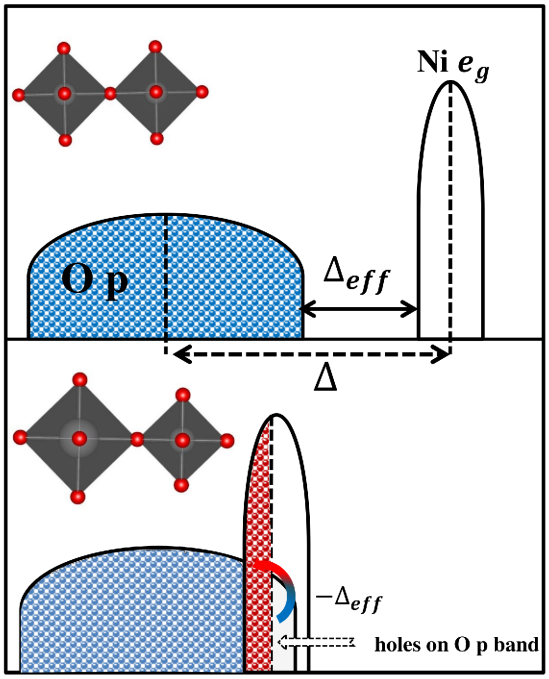

Figure 3.5: Schematic indicating the definitions Δ and Δ_{eff} used in the text. While a positive Δ_{eff} has uniform NiO_6 octahedra, a negative Δ_{eff} leads to transfer of holes to the oxygen p bands and occurrence of a breathing distortion of the NiO_6 octahedra.

oxygen p band. The depth of the oxygen p levels inside the oxygen p band(W_p), is used to determine an effective charge transfer energy, Δ_{eff} given as $\Delta - W_p$(The definition of Δ and Δ_{eff} in a comparative manner is shown schematically in Figure 3.5). The mean octahedral bond lengths and magnetic moments of Ni^{2+} and Ni^{4+} against the effective charge transfer energy Δ_{eff} are plotted in Figure 3.4. For the value of $\Delta_{eff} \sim 0.3$ eV we see no bond disproportionation with both the Ni atoms having equal mean Ni-O bond lengths and the system becomes metallic. There is a small difference in the magnetic moments associated with the two Ni atoms, and this could be an effect of the LDA+U method we use that try to localize the electrons. Below the value of 0.3 eV, we see the occurrence of bond disproportionation with two different Ni atoms having different Ni-O bond lengths and magnetic moments. Also, the system becomes insulating as a result of the charge ordering(CO) which is shown in Figure 3.4. Hence the onset of charge ordering seems to be associated with the point at which the holes begin to occupy the oxygen p band, factoring in a finite width of the transition metal d band. This is the reason we find a narrow sliver of charge-ordered insulating state even for $\Delta_{eff} > 0$, before becoming metallic. For larger finite Δ_{eff} the system is a charge transfer(CT) insulator as indicated in Figure 3.4. At a qualitative level this can be understood as follows. In contrast to the transition metal-oxygen network which is very covalent, the rare earth-

oxygen network is very ionic. With the holes moving onto the oxygens, this ionic network is destabilized. Beyond a critical number of holes, one finds that the structure distorts, driving the charge ordering instability. We find that the disproportionation disappears when the charge transfer energy becomes large enough that the p-band becomes filled, as shown schematically in the upper panel of Figure 3.5. This supports the view [17] that the disproportionation arises from a preferential hybridization of the ligand holes with one of the Ni states.

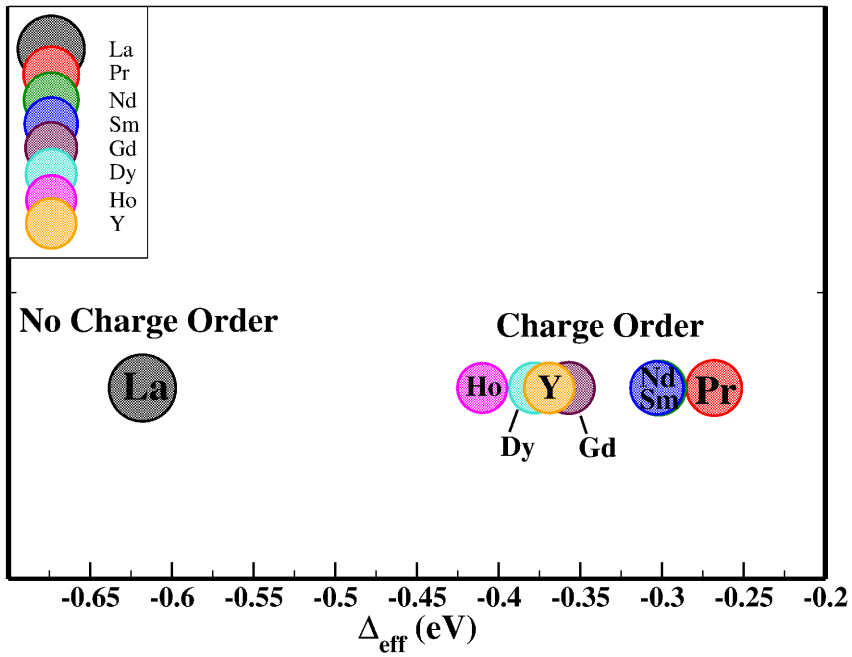

Figure 3.6: Δ_{eff} calculated for all the rare earth nickelates with U = 2 eV on Ni sites.

We then examine the implications of the phase diagram in the context of all the rare earth nickelates. For this, we have calculated the effective charge transfer energy Δ_{eff} for all the rare earth nickelates[Figure 3.6]. A U of 2 eV was found to give the correct antiferromagnetic state as the ground state for $NdNiO_3$. We therefore performed the calculation for all the nickelates using a U of 2 eV on the Ni site. For RE = Ho to Pr, the values lie in the range of -0.41 to -0.27 eV indicating a situation where the Ni d band enters the oxygen p band and there are holes on the oxygens. As a result, the ground state(GS) of the compounds are insulating with bond disproportionation. For $LaNiO_3$, the value of Δ_{eff} is $\sim$ -0.62 eV and the GS is metallic without any bond disproportionation. So, from here we can conclude that a negative value of delta is necessary for bond disproportionation to occur, however, there is a critical value beyond which the itinerant limit is reached. There will be larger band overlap and system becomes metallic suppressing the MIT. Values of Δ_{eff} in the range of -0.41 to -0.27 eV leads to an insulating GS with a small variation in the band gap values. In the insulating state, the

main role in controlling the band gap is played by the bandwidth(W). As we go from Lu to Pr the ionic radii of the rare earth atom increases and the bandwidth of the system also increases due to increased hybridization between the Ni d and O p states, this in turn drives the system more towards the itinerant limit and there shall be a systematic decrease in the metal to insulator transition temperature(T_{MIT}), in agreement with experimental observations as reported in earlier works [12, 36, 37].

Is there a critical length scale for charge ordering? :

D. Meyers *et al.* [38] have found that charge ordering seems to vanish in the limit of 15 unit cells for films of $NdNiO_3$ grown on $NdGaO_3$. In order to examine this aspect, we have calculated the electronic structure of the films at the bulk as well as the few monolayers limit.

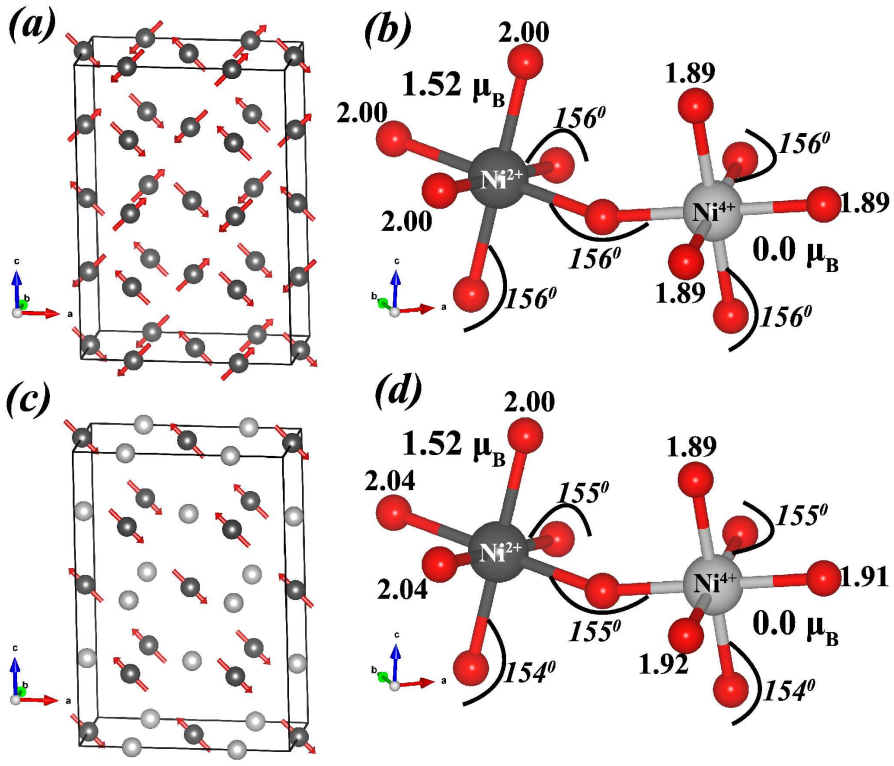

Figure 3.7: (a) The E′ type non-collinear antiferromagnetic ordering of the Ni moments. (b) Ni-O bond lengths and Ni-O-Ni bond angles of Ni^{2+} and Ni^{4+} along the three pseudo cubic directions for non-strained $NdNiO_3$. (c) Effective collinear type antiferromagnetic ordering of the Ni^{2+} moments in the optimized structures of both strained and non-strained $NdNiO_3$. (d) Ni-O bond lengths and Ni-O-Ni bond angles of Ni^{2+} and Ni^{4+} along the three pseudo cubic directions for strained $NdNiO_3$.

We first looked at the bulk limit which was appropriately strained to mimic the $NdGaO_3$ substrate. For this we have used the in-plane (ab-plane) lattice parameters of $NdGaO_3$(a

= 5.43 and $b = 5.50$Å) and experimentally reported c value of 7.60Å. This is equivalent to applying a tensile strain of 1.4%. A E′ type non-collinear antiferromagnetic ordering was imposed on the Ni sites[Figure 3.7(a)]. The converged solution shows a breathing mode distortion of the NiO_6 octahedra with two inequivalent Ni atoms[Figure 3.7(d)] having large and short Ni-O bond lengths. The Ni atom with larger Ni-O bonds(Ni^{2+}) has a magnetic moment $\sim 1.52\mu_B$, whereas the magnetic moment associated with the Ni atom having shorter Ni-O bonds(Ni^{4+}) was found to be zero. This results in an effective collinear type antiferromagnetic ordering of the Ni moments as shown in Figure 3.7(c). However, due to the effect of strain, we do not see a pure breathing mode distortion in the system that we observe in the non-strained case[Figure 3.7(b)]. For each NiO_6 octahedra the in-plane bond lengths become larger compared to the out of plane bond lengths. The in-plane Ni-O-Ni bond angles are found to be 155^o whereas the out of plane bond angle is 154^o. This is also in contrast to the non-strained case where the Ni-O-Ni bond angles are equal to 156^o along all the three pseudo cubic directions. So, application of strain $\sim$ 1.4% is not enough to destabilize the charge ordered insulating ground state.

Next, to examine if there is any thickness dependence of the charge ordering, we consider thin films of $NdNiO_3$ grown on $SrTiO_3$ substrate but with the lattice parameters of $NdGaO_3$(see the methodology section for details). For the thin film calculation, we again consider the E′ type non-collinear magnetic ordering on the Ni atoms as well as ferromagnetic ordering for a comparison purpose. For thin film calculations, the antiferromagnetic state comes out to be the ground state and is insulating in nature. This is in contrast to the bulk calculations where we get ferromagnetic as the ground state. Hence only the antiferromagnetic solutions were considered for the further analysis of structural and magnetic properties which are described below as a function of increasing layer thickness.

2 monolayer case: The 2 monolayer case is equivalent to depositing one formula unit of $NdNiO_3$ on the substrate. This consists of a single NdO layer and a NiO_2 layer[Figure 3.8(a)]. This makes the thin film to be NiO_2 terminated. Due to this, the Ni atoms in the single NiO_2 layer do not have a complete octahedral coordination. A non-collinear type antiferromagnetic ordering was considered on the Ni atoms as shown in Figure 3.8(d). The structural analysis of the optimized structure shows all the Ni atoms to be identical having an equivalent environment. The Ni-O bonds of all NiO_5 polyhedra are found to be identical with a Ni moment $\sim 1.2\ \mu_B$[Figure 3.8(b)]. Hence there is no charge ordering in the system. The two in-plane Ni-O-Ni bond angles are found to be $\sim 164^o$ and 172^o. These are larger and close to 180^o compared to the bulk values as a result of incomplete coordination of the Ni atoms.

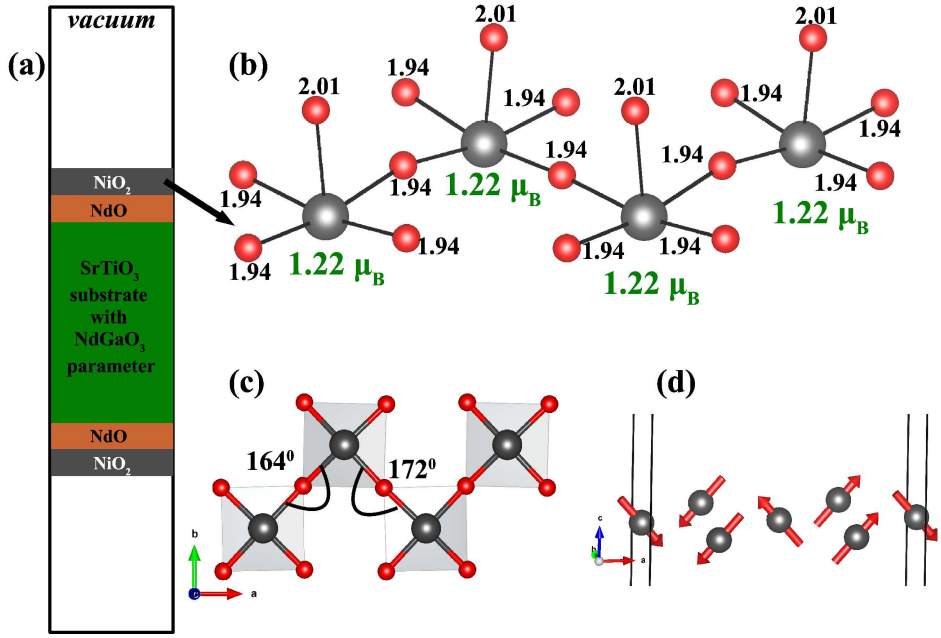

Figure 3.8: 2 monolayer case : (a) Schematic showing the two monolayers of $NdNiO_3$ on $NdGaO_3$ substrate. (b) Ni-O bond lengths and (c) the in-plane(*ab*-plane) Ni-O-Ni bond angles after structural optimization. The magnetic moments associated with each of the Ni atoms are also mentioned. (d) Non-collinear type antiferromagnetic ordering of the Ni moments in the single NiO_2 layer.

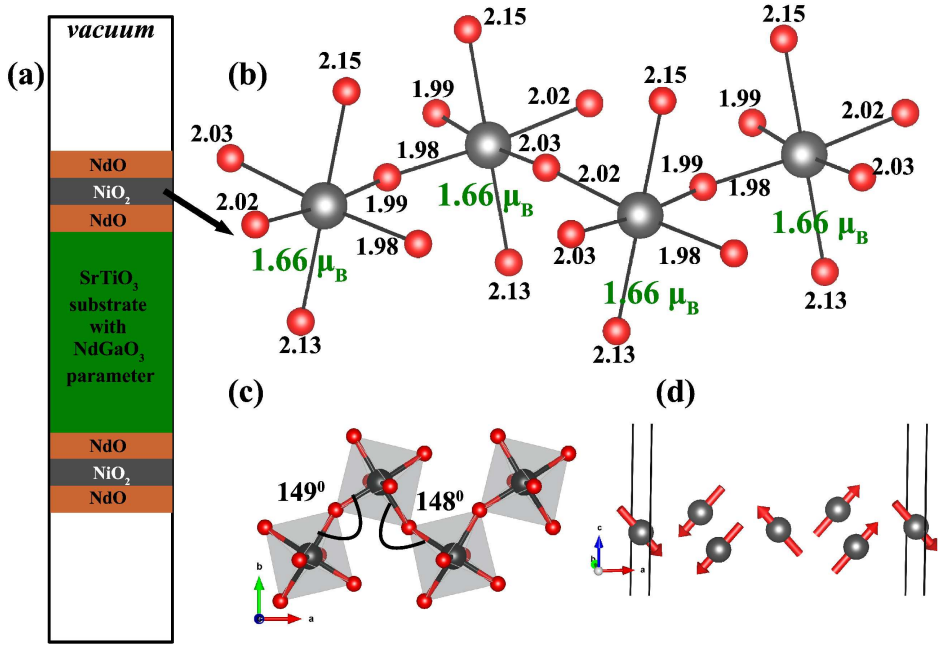

Figure 3.9: 3 monolayer case : (a) Schematic showing the three monolayers of $NdNiO_3$ on $NdGaO_3$ substrate. (b) Ni-O bond lengths and (c) the in-plane(*ab*-plane) Ni-O-Ni bond angles after structural optimization. The magnetic moments associated with each of the Ni atoms are also mentioned. (d) Non-collinear type antiferromagnetic ordering of the Ni moments in the single NiO_2 layer.

3 monolayer case: As shown in Figure 3.9(a), the 3 monolayer $NdNiO_3$ thin films are produced by adding another NdO layer on top of the NiO_2 layer. This NdO termination makes the coordination of the Ni atoms in the NiO_2 layer complete and now they have octahedral coordination. The same magnetic ordering identical to the 2 monolayer case was considered on the Ni sites[Figure 3.9(d)]. The Ni-O bond lengths in the optimized structure are shown in Figure 3.9(b). Again we see that the Ni-O bond lengths of all the NiO_6 octahedra are identical with an associated magnetic moment of 1.66 μ_B. There is no signature of charge ordering. However now, due to full octahedral coordination, the Ni moment values are close to the bulk values($\sim$ 1.5 μ_B). Also, the Ni-O-Ni bond angles are $\sim 150^o$, close to the bulk values.

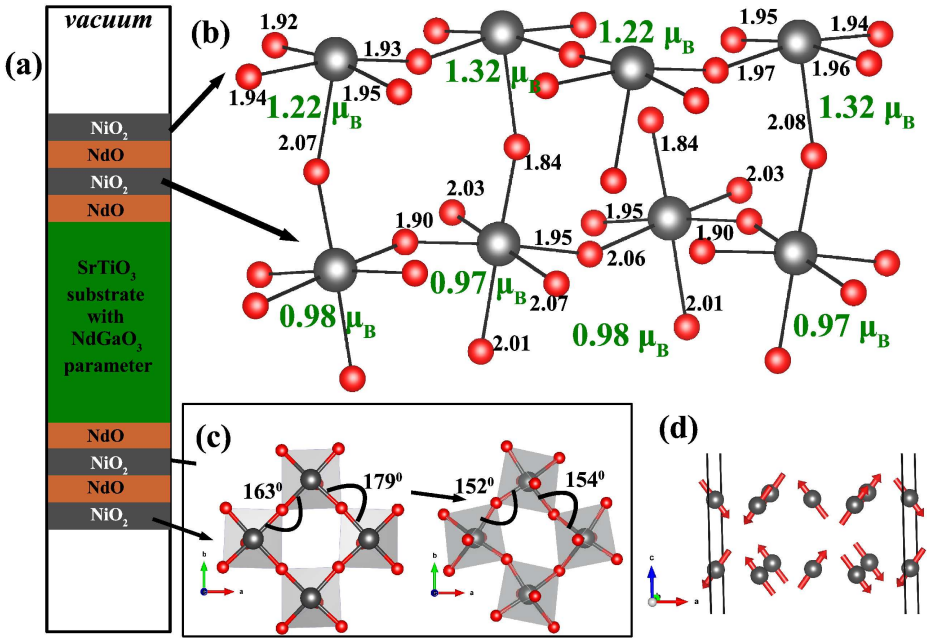

Figure 3.10: 4 monolayer case : (a) Schematic showing the four monolayers of $NdNiO_3$ on $NdGaO_3$ substrate. (b) Ni-O bond lengths and (c) the in-plane(ab-plane) Ni-O-Ni bond angles in the two NiO_2 layers after structural optimization. The magnetic moments associated with each of the Ni atoms are also mentioned. (d) Non-collinear type antiferromagnetic ordering of the Ni moments in the two NiO_2 layers.

4 monolayer case: Now we have two layers of NdO and two layers of NiO_2[Figure 3.10(a)]. This again makes the thin film to be NiO_2 terminated with the top NiO_2 layer having an incomplete coordination of oxygen atoms. The non-collinear antiferromagnetic ordering imposed on the two Ni layers is shown in Figure 3.10(d). After structural optimization, all the Ni atoms in the first NiO_2 layer having full octahedral coordination shows identical Ni-O bonds and a magnetic moment $\sim$ 0.98 μ_B. The Ni atoms on the topmost layer shows small variation in the Ni-O bonds as well as Ni moments between two Ni sites[Figure 3.10(b)]. However the variations are too small and we again have a

non-charge ordered solution. The in-plane Ni-O-Ni bond angles in the first NiO_2 layer are found to be $\sim 152^o$ and 154^o close to the bulk values, whereas the values for the top-most NiO_2 layer are found to be $\sim 163^o$ and 172^o, again due to an incomplete octahedral coordination. The out of plane bond angle is $\sim 159^o$.

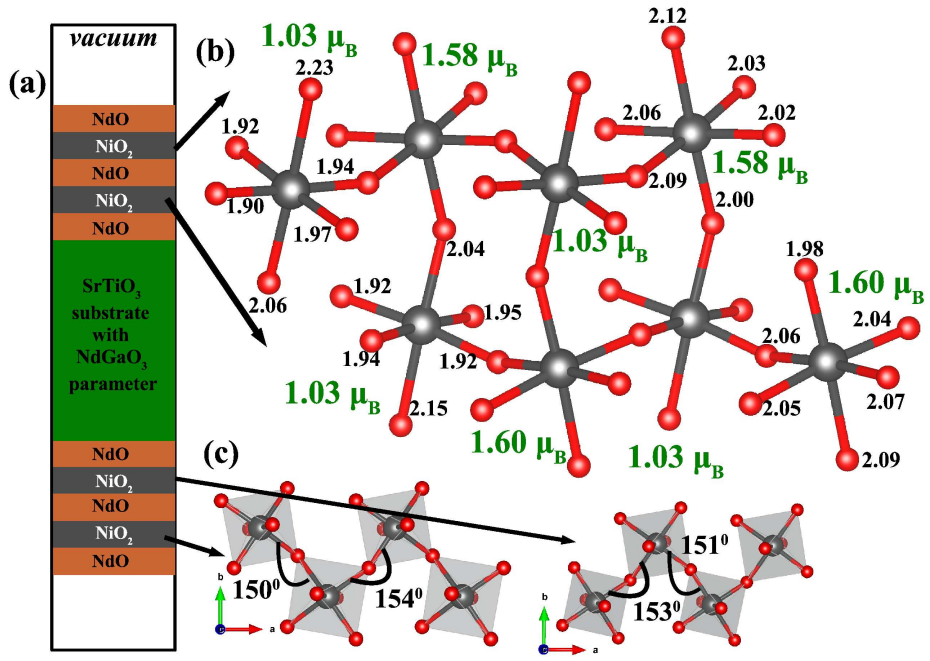

Figure 3.11: 5 monolayer case : (a) Schematic showing the five monolayers of $NdNiO_3$ on $NdGaO_3$ substrate. (b) Ni-O bond lengths and (c) the in-plane(*ab*-plane) Ni-O-Ni bond angles in the two NiO_2 layers after structural optimization. The magnetic moments associated with each of the Ni atoms are also mentioned.

5 monolayer case: The ordering of the NdO and NiO_2 layers for the 5 monolayer case is shown in Fig. 3.11(a). Again with NdO termination, now we have two NiO_2 layers where the Ni atoms have a complete octahedral environment. The magnetic ordering imposed on the Ni atoms is similar to what has been shown in Figure 3.10(d). Now we can see a breathing mode type distortion in the system with two distinct Ni atoms having different in-plane Ni-O bond lengths[Figure 3.11(b)]. The Ni atoms having a shorter in-plane Ni-O bond length $\sim$ 1.9 Å shows a smaller magnetic moment $\sim$ 1.0 μ_B, whereas the Ni atoms having an in-plane bond lengths $\sim$ 2.0 Å have an magnetic moment value of $\sim$ 1.60 μ_B. However, the observed bond disproportionation is not equivalent to the bulk case and the charge ordering is incomplete. The in-plane Ni-O-Ni bond angles in both the NiO_2 layers are now close to the bulk values showing some small asymmetries[Figure 3.11(c)]. The out of plane bond angle is $\sim 154^o$.

6 monolayer case: The layer configuration for the 6 monolayer case is shown in Figure 3.12(a). Now again the film is NiO_2 terminated which have incomplete octahedral

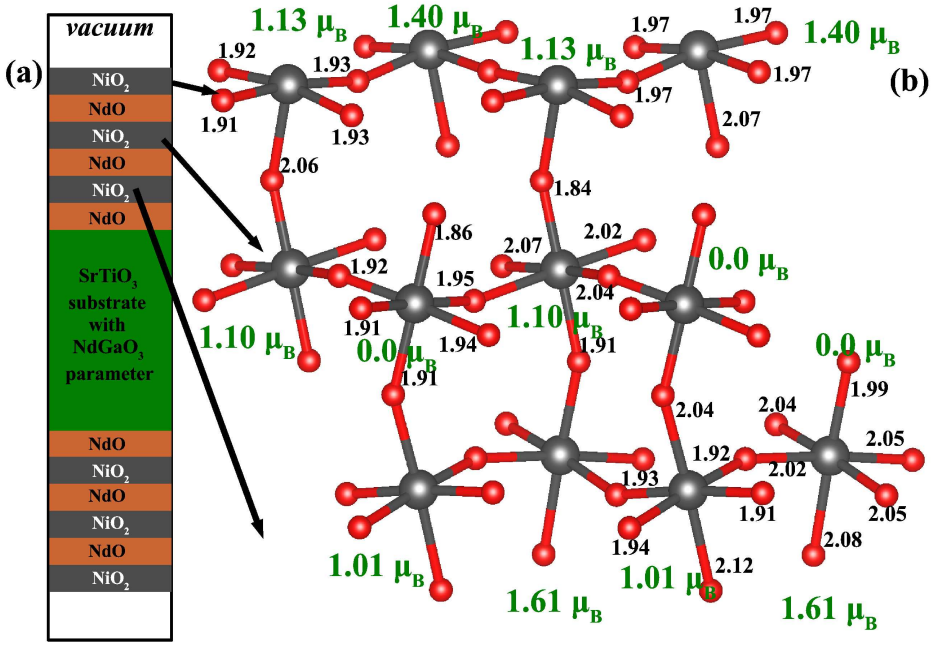

Figure 3.12: 6 monolayer case : (a) Schematic showing the six monolayers of $NdNiO_3$ on $NdGaO_3$ substrate. (b) Ni-O bond lengths in the three NiO_2 layers after structural optimization. The magnetic moments associated with each of the Ni atoms are also mentioned.

coordination. The imposed magnetic ordering on the Ni atoms are equivalent to the magnetic moments of the first three Ni layers as shown in Figure 3.7(a). As shown in Figure 3.12(b), now the Ni atoms in the first and the third layer shows incomplete charge ordering similar to the 5 monolayer case, whereas the Ni atoms in the middle layer, sandwiched between the other two NiO_2 layers shows a charge ordering similar to the bulk case with two Ni atoms having zero magnetic moment. However, we do not observe any breathing mode distortion comparable to the bulk calculations and the charge ordering is still incomplete. The Ni-O-Ni bond angles in the middle NiO_2 layer is $\sim 150^o$ and 152^o, whereas for the top most NiO_2 layer with incomplete octahedral coordination they are $\sim 163^o$ and 171^o respectively. The out of plane bond angles alternate between $\sim 152^o$ and 157^o respectively.

3.4 Conclusion

The origin of charge ordering in the rare earth nickelates has been examined within first principle electronic structure calculations for the case of $NdNiO_3$. The charge transfer energy between the oxygen p and the transition metal d states has been systematically varied. The onset of charge ordering is found to be associated with the point when

holes are located on the oxygen p band and is shown to take place beyond a critical concentration. Although among the bulk rare earth nickelates the charge ordering seems almost ubiquitous, as the size is reduced, one finds that there is a critical length scale below which one has incomplete charge order/ no charge order consistent with the experimental result.

Bibliography

[1] M. K. Wu, J. R. Ashburn, C. J. Torng, P. H. Hor, R. L. Meng, L. Gao, Z. J. Huang, Y. Q. Wang, and C. W. Chu Phys. Rev. Lett. **58**, 908 (1987).

[2] R. von Helmolt, J. Wecker, B. Holzapfel, L. Schultz, and K. Samwer Phys. Rev. Lett. **71**, 2331 (1993).

[3] A. Asamitsu, Y. Moritomo, Y. Tomioka, T. Arima, and Y. Tokura Nature **373**, 407 (1995).

[4] J. Liu, M. Kargarian, M. Kareev, B. Gray, P. J. Ryan, A. Cruz, N. Tahir, Y. Chuang, J. Guo, J. M. Rondinelli, J. W. Freeland, G. A. Fiete, and J. Chakhalian Nat. Comm. **4**, 2714 (2013).

[5] J. Y. Zhang, H. Kim, E. Mikheev, A. J. Hauser, and S. Stemmer Sci. Rep. **6**, 23652 (2016).

[6] G. Catalan, Phase Transitions **81**, 729 (2008).

[7] S. Middey, J. Chakhalian, P. Mahadevan, J. W. Freeland, A. J. Millis, and D.D. Sarma, Annu. Rev. Mater. Res. **46**, 305 (2016).

[8] J. A. Alonso, J. L. García-Muñoz, M. T. Fernández-Díaz, M. A. G. Aranda, M. J. Martínez-Lope, and M. T. Casais Phys. Rev. Lett. **82**, 3871 (1999).

[9] J. A. Alonso, M. J. Martínez-Lope, M. T. Casais, J. L. García-Muñoz, and M. T. Fernández-Díaz Phys. Rev. B **61**, 1756 (2000).

[10] J. A. Alonso , M. J. Martínez-Lope , M. T. Casais , M. A. G. Aranda, and M. T. Fernández-Díaz J. Am. Chem. Soc. **121**, 4754 (1999).

[11] U. Staub, G. I. Meijer, F. Fauth, R. Allenspach, J. G. Bednorz, J. Karpinski, S. M. Kazakov, L. Paolasini, and F. d'Acapito Phys. Rev. Lett. **88**, 126402 (2002).

[12] J. B. Torrance, P. Lacorre, A. I. Nazzal, E. J. Ansaldo, and C. Niedermayer, Phys. Rev. B **45**, 8209 (1992).

[13] P. Mahadevan, N. Shanthi, and D. D. Sarma Phys. Rev. B **54**, 11199 (1997).

[14] S.R. Barman, A. Chainani and D.D. Sarma, Phys. Rev. B **49**, 8475 (1994).

[15] T. Mizokawa, D. I. Khomskii, and G. A. Sawatzky Phys. Rev. B **61**, 11263 (2000).

[16] I. I. Mazin, D. I. Khomskii, R. Lengsdorf, J. A. Alonso, W. G. Marshall, R. M. Ibberson, A. Podlesnyak, M. J. Martínez-Lope, and M. M. Abd-Elmeguid Phys. Rev. Lett. **98**, 176406 (2007).

[17] H. Park, A. J. Millis, and C. A. Marianetti Phys. Rev. Lett. **109**, 156402 (2012).

[18] S. Johnston, A. Mukherjee, I. Elfimov, M. Berciu, and G. A. Sawatzky Phys. Rev. Lett. **112**, 106404 (2014).

[19] A. Subedi, O. E. Peil, A. Georges, Phys. Rev. B **91**, 075128 (2015).

[20] D. D. Sarma, J. Solid State Chem. **88**, 45 (1990).

[21] S. Nimkar, D. D. Sarma, H. R. Krishnamurthy and S. Ramasesha, Phys. Rev. B **48**, 7355 (1993).

[22] (a) P. E. Blöchl, Phys. Rev. B **50**, 17953 (1994). (b) G. Kresse, and D. Joubert, Phys. Rev. B **59**, 1758 (1999).

[23] (a) G. Kresse and J. Hafner, Phys. Rev. B **47**, 558 (1993). (b) G. Kresse and J. Hafner, Phys. Rev. B **49**, 14251 (1994). (c) G. Kresse and J. Furthmüller, Phys. Rev. B **54**, 11169 (1996).

[24] G. Kresse and J. Furthmüller, Comput. Mater. Sci., **6**, 15 (1996).

[25] J. L. García-Muñoz, M. A. G. Aranda, J. A. Alonso, and M. J. Martínez-Lope, Phys. Rev. B **79**, 134432 (2009).

[26] J. L. García-Muñoz, J. Rodríguez-Carvajal, and P. Lacorre Phys. Rev. B **50**, 978 (1994).

[27] F. Y. Bruno, K. Z. Rushchanskii, S. Valencia, Y. Dumont, C. Carrétéro, E. Jacquet, R. Abrudan, S. Blügel, M. Ležaić, M. Bibes, and A. Barthélémy, Phys. Rev. B **88**, 195108 (2013).

[28] D. Meyers, J. Liu, J. W. Freeland, S. Middey, M. Kareev, J. Kwon, J. M. Zuo, Yi-De Chuang, J. W. Kim, P. J. Ryan, J. Chakhalian, Sci. Rep. **6**, 27934 (2016).

[29] S. L. Dudarev, G. A. Botton, S. Y. Savrasov, C. J. Humphreys and A. P. Sutton, Phys. Rev. B **57**, 1505 (1998).

[30] (a) J. P. Perdew, K. Burke and M. Ernzerhof, Phys. Rev. Lett. **77**, 3865 (1996). (b) J. P. Perdew, K. Burke and M. Ernzerhof, Phys. Rev. Lett. **77**, 3865 (1996).

[31] Hendrik J. Monkhorst and James D. Pack, Phys. Rev. B **13**, 5188 (1976).

[32] A. A. Mostofi, J. R. Yates, Y.-S. Lee, I. Souza, D. Vanderbilt, and N. Marzari, Comput. Phys. Commun. **178**, 685 (2008).

[33] N. Marzari and D. Vanderbilt, Phys. Rev. B **56**, 12847 (1997).

[34] I. Souza, N. Marzari and D. Vanderbilt, Phys. Rev. B **65**, 035109 (2001).

[35] C. Franchini, R. Kovacik, M. Marsman, S. Sathyanarayana Murthy, J. He, C. Ederer and G. Kresse, J. Phys. Cond. Mat **24**, 235602 (2012).

[36] M. L. Medarde, J. Phys. Condens. Matter **9**, 1680 (1997).

[37] J. A. Alonso, M. J. Martínez-Lope, M. T. Casais, J. L. García-Muñoz, and M. T. Fernández-Díaz, Phys. Rev. B **61**, 1756 (2000).

[38] D. Meyers, J. Liu, J. W. Freeland, S. Middey, M. Kareev, J. M. Zuo, Yi-De Chuang, J. -W. Kim, P. J. Ryan, and J. Chakhalian, arXiv:1505.07451v4 (2015).

Chapter 4

Role of the A-site cation in determining the properties of Hybrid Perovskite $CH_3NH_3PbBr_3$

4.1 Introduction

There is a strong correlation between the structure and the property of a material [1–5]. Tunability in the property of such materials has been achieved by varying parameters which induce changes in the structure. Considering the well studied perovskite oxides given by the formula ABO_3 where the A-site is usually occupied by a rare earth atom or an alkali metal atom and the B-site is a transition metal atom, one finds that a change in the size of the atom occupying the A-site results in changes in the electronic structure. The system could be either insulating or metallic, with changes being induced in the temperature at which the metal to insulator transition happens [6–8]. The changes emerge from structural changes [1–8] which involve a rotation of the BO_6 octahedra leading to deviations of the B-O-B angle from 180° expected in an ideal cubic perovskite. Assuming an almost rigid BO_6 octahedron, the size of the A cation controls the volume of the unit cell. A smaller size of the A cation results in a reduction of the cell volume. This results in shorter B-O distances, which would then lead to an increase in the Coulomb repulsion between electrons on B and those on O. To compensate for this increased Coulomb repulsion, the BO_6 octahedra tilt resulting in longer B-O bonds as well as B-O-B angles that deviate from 180°. Largely steric effects have been believed to be responsible for the octahedral tilts in inorganic perovskites. Most of the perovskites are not good light absorbers due to their band gap value deviating from the required range. Mitzi *et al.* used perovskites with halides, ammonium cations and Sn^{2+} in optoelectronic devices, which formed the basis for the development of perovskites for solar cells [9, 10].

Recently a new class of hybrid organic-inorganic perovskite based semiconductors are drawing significant attention, specially for their use as solar cell material. Low cost and fast preparation techniques in laboratory environment [11], high charge carrier mobilities and large diffusion lengths [11–15] makes them an efficient and promising solar cell material, showing conversion efficiency over 20% [16]. In the hybrid perovskites, the A-site is occupied by an organic molecule. Hence in contrast to earlier where one had a spherical atom, in the present case one has a cylindrical object occupying the A-site. This would then imply that only specific orientations would be favored by the molecule. Moreover now there are hydrogen atoms associated with the molecule which are involved in bonding with the anions. Considering the most extensively studied member of these series, $CH_3NH_3PbI_3$($MAPbI_3$), it was shown that replacing MA with an ion which had the same ionic radii led to the octahedral tilts vanishing [17]. This led them to the conclusion that it was the hydrogen bonding with the anions that led to the octahedral tilts found in the experimental structure. So, here the interaction between the molecule and the inor-

ganic cage also plays an important role in determining the overall structural and hence electronic properties of the system.

While the role of the cation at the *A*-site have been long recognized as playing an important role in the structure of the hybrid perovskites, recent experiments on $MAPbI_3$ have brought forth another unusual aspect. Temperature dependent studies of the relative permittivity have found a strong frequency dependence even in the orthorhombic phase [18]. This is surprising as the molecular dipoles are believed to be ordered in the orthorhombic phase of the hybrid perovskites [19, 20]. This rules out any relaxation due to free rotation of the dipoles which may be found in the high temperature tetragonal and cubic phases. Further, symmetry analysis allow for a three-fold rotation of the molecule about its molecular axis in the orthorhombic phase. However, the barriers associated with these rotations have been found to be greater than 70 meV when the inorganic network was kept rigid [21]. Hence the origin of the observed dipolar relaxations which are suggestive of glassy dynamics in the low temperature orthorhombic phase are puzzling. There have been suggestions of the presence of static disorder, associated with a partial reorientation of the C-N axis in analogy to plastic crystals that have been offered [22]. Older experiments on $MAPbBr_3$ [23] and $MASnBr_3$ [24] also suggest similar behavior.

In this chapter, we examine the total energy landscape of $MAPbBr_3$ using first principle electronic structure calculations. Earlier studies have shown that the interaction between the molecule and the inorganic cage is via hydrogen bonding. A dominant contribution to the energy lowering during the structural optimization has the hydrogen atoms attached to the nitrogen end of the molecule (H_N) coming closer to some of the Br atoms of the inorganic cage. The Br atoms respond by coming closer to the hydrogen atoms. This results in the octahedral distortions that one encounters, which unlike in inorganic perovskites result in larger distortions of some angles over others. The decrease of H_N-Br bond lengths are suggestive of strong covalent interactions between the H_N and Br atoms. However, a microscopic analysis carried out in terms of mapping onto a tight-binding Hamiltonian reveals that a significant component of the interaction emerges from electrostatic interactions. Further analysis reveals that one has a complex energy landscape with deep valleys and large barriers emerging from competing interactions. There is no implicit relation suggesting that shorter H_N-Br bond lengths would determine the favored orientation of the molecule. This leads to the presence of two minima whose energy differ by just 5 meV, but correspond to different orientations of the molecule in the *ac*-plane as well as different tilt angles. This barrier was found while rotating the molecular C-N axis in steps in the *ac*-plane and then relaxing the whole system. The barrier height between the two minima is of the order of 30 meV per formula unit which is lower than that required for

the twisting motions about the C-N axis in the orthorhombic phase with rigid inorganic network reported in a previous DFT study [21]. The presence of deep valleys with similar energies, suggests that the system could be quenched in either of these configurations, in addition to the configurations being accessible by thermal excitations.

The ordering of the molecular dipoles in the *ac*-plane has neighboring dipoles at an angle of ~ 130 degrees with respect to each other. This results in a net dipole moment within the plane. These dipoles could be stacked in a ferroelectric arrangement or an antiferroelectric arrangement in the *b*-direction. We explore both these configurations and find that they are energetically degenerate. So, this comprises another source of orientational disorder in the structure. Both these can explain the glassy dynamics that have been seen in the orthorhombic phase.

4.2 Methodology

The electronic structure of the systems were calculated using a projected augmented wave (PAW) [25] implementation of density functional theory within Vienna ab-initio simulation package (VASP) [26, 27]. The generalized gradient approximation(GGA) [28] was used for the exchange-correlation functional. Inclusion of the non-local, weak van der Waals(vdW) interactions are necessary to correctly predict the structural properties. A GGA+vdW density functional theory calculation has been found to give a good estimation of the lattice parameters and structural properties [29, 30]. Dispersive interactions are responsible for a significant contraction of the unit cell, correcting the overestimation in general done by GGA. It also gives a band gap close to the experimental values for Pb based compounds which is striking compared to normal semiconductors for which we need to consider hybrid functionals. This happens due to cancellation of errors [31]. However, it cannot accurately describe the band dispersions. Inclusion of the spin-orbit coupling(SOC) slightly changes the Pb$-X$(where X is halide atom) bond lengths but strongly underestimates the band gap and SOC-GW is needed for accurate description of the electronic structure [30, 31]. Still DFT calculations are useful for determination of structural properties and sufficient for comparison of electronic properties of homologous systems [32]. DFT-D2 method of Grimme [33] was considered to introduce dispersive interactions within the system. A gamma centered Monkhorst-Pack k-mesh of $8\times6\times8$ was used to perform the k-space integrations. In addition to this, an energy cutoff of 400 eV was used for the kinetic energy of the plane waves included in the basis. The orthorhombic unit cell [34] was used though both the lattice parameters and the internal positions were optimized till the forces on the atoms were less than 10^{-3} eV/Å to find

the minimum energy structure. This structure has a space group symmetry *Pnma* and is non-polar. This phase is an intermediate phase that was referred to as phase IV, different from the phase that was reported previously by Poglitsch and Weber [20] having a space group $Pna2_1$ which is polar in nature. Also dielectric measurements [23] show a peak in the dielectric constant while entering this orthorhombic phase and have been interpreted as suggestive of a ferroelectric nature. The optimized lattice parameters were found to be 7.87, 11.69, 8.46 Å $\sim$ 1% smaller on average than the experimental values. The average Pb-Br bond lengths are reduced by 0.7% and average Pb-Br-Pb bond angles are reduced by 2.5% in the optimized structure compared to the experimental structure. In the rest of the text we refer to this structure as the optimized structure. All results described in the text are with the optimized lattice parameters unless specified otherwise. *Ab-initio* band structure was mapped on to a tight binding model using an interface of VASP to WANNIER90 [35–37]. A basis consisting of Pb s and p, Br p, C p and H s states were used. The Bloch states are mapped onto Wannier functions, localized on the respective atoms via a unitary transformation. The angular parts are given by the relevant spherical harmonics. Once the transformation matrices are determined, one has a tight binding representation of the Hamiltonian in the basis of the maximally localized Wannier functions.

4.3 Results and Discussion

As pointed out in the Introduction, there is a strong coupling between the structure and the properties in these perovskites. While the molecule at the *A*-site does not contribute to any of the states several eV on either side of the Fermi energy, through modifications in the structure, it determines the electronic structure. We therefore examine all these aspects.

4.3.1 How does the molecule sit inside the inorganic cage?

In an inorganic perovskite, the atom at the *A*-site can be treated as a spherical entity and so there is no preferred orientation. There could however be a displacement of the atom from the center of the cage. However, here, the molecule at the *A*-site can be regarded as a cylindrical object. We need to explore different orientations and determine the favored orientation. This analysis would help us understand the microscopic energetics involved in determining the structure.

The orientation of the molecule

In order to understand the microscopic considerations that determine the favored orientation of the molecule, we start by considering the idealized orthorhombic cell without any octahedral tilts. This is shown in Figure 4.1(a). As seen along the *b*-axis, the octahedral cavity in which the molecule sits is a rectangle. If the C-N axis of the molecule is kept in the *ac*-plane, the two configurations/orientations along which the molecule has maximum freedom are the diagonals of the rectangle. In other configurations the distance between the molecule and the inorganic cage as well as the space for the molecule are less. This leads to Coulomb repulsions between the electrons on different atoms dictating the energetics, resulting in configurations higher in energy by almost 30 meV per formula unit(fu) as the molecule is rotated in the *ac*-plane. The optimized structure has the octahedral tilts which are in Glazer's notation [38] given by $a^-b^+a^-$. This results in the rectangular cavity being transformed into a rhombus-shaped cavity[see Figure 4.1(b)]. One now has two inequivalent diagonals along which the molecule can lie. Steric effects again determine the favored orientation to be along the long diagonal, as the N-Br bond lengths are significantly reduced to 3 Å as against 3.38 Å when the molecule was forcefully oriented along the short diagonal. The latter configuration is lower in energy by 540 meV per formula unit [39].

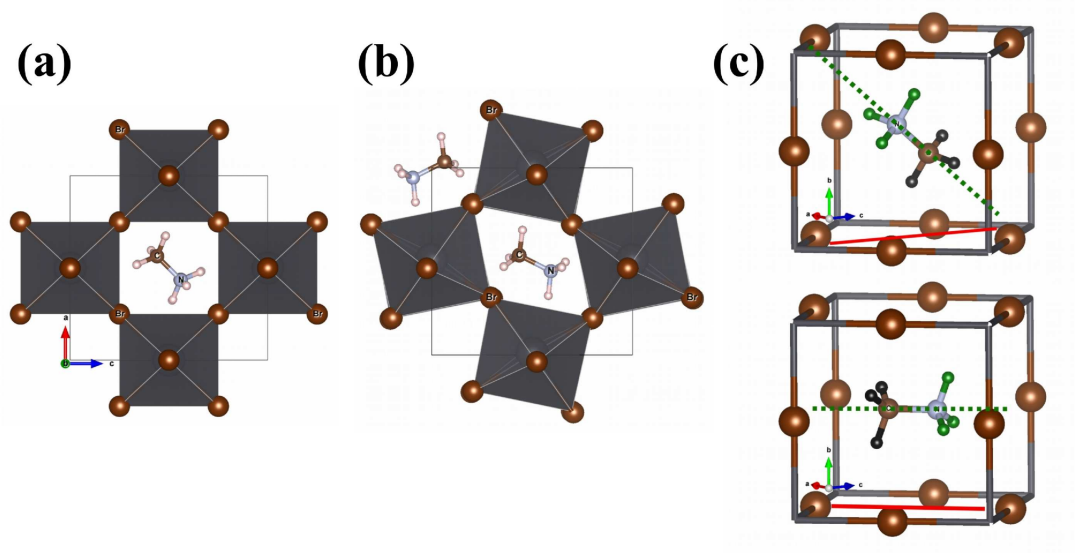

Figure 4.1: Bird's eye view in the *ac*-plane of (a)orthorhombic unit cell of $MAPbBr_3$ without any octahedral tilts, (b) experimental orthorhombic cell. (c) Top: An alternate orientation of the molecule along a body diagonal of the cavity shown by the dotted line was considered, its projection on the *ac*-plane is shown by solid line. Bottom: Orientation in the optimized structure.

If steric effect were the dominant energetics dictating the orientation of the molecule in the cage, an alternate configuration which should be favored is one in which the molecule lies along the body diagonal of the cavity as there would be space for the molecule to spread out. This is shown in the top panel of Figure 4.1(c). For comparison the location/orientation of the molecule inside the cavity for the optimized structure is shown in the lower panel of Figure 4.1(c).

Placing the molecule in the *ac*-plane as in the optimized structure, one finds results in an in-phase rotation of the octahedra in the *b*-direction so that no atoms of the cage come too close to the molecule. This is the reason for the $a^-b^+a^-$ tilt pattern that one has in this case. Changing the orientation of the molecule to that shown in the upper panel of Figure 4.1(c) allows for a tilt pattern in which the rotations in the *b*-direction are out of phase i.e. $a^-b^-a^-$[See section 1 of Appendix A]. This is also higher in energy by 160 meV/fu over the optimized structure which has the molecule in the *ac*-plane. These results suggests that the orientation of the molecule controls the octahedral tilts but there are other considerations apart from steric effects which determine the orientation of the molecule in the octahedral cavity. A detailed description to determine the favored orientation of the molecule is given in section 2 of Appendix A and can work as a guiding steps to determine the GS structure for any other system with a different organic molecule.

Does the molecule sit at the center of the inorganic cage?

The organic molecule comprises of two different atoms with different electronegativities which are connected to hydrogens. This sets up a dipole in each octahedral unit of the cell. Placing the molecule in the undistorted orthorhombic structure as shown in Figure 4.1(a), one finds that the molecule does not sit with its center coinciding with the geometric center of the cell. It however moves to one part of the cage with the consideration being that shorter bonds are made between the hydrogen atoms attached to the nitrogen atom(H_N) and the Br atoms[Figure 4.2(b)]. The question that follows is how do these dipoles order. This has been a controversial topic in the literature [40]. In the *ac*-plane the nearest-neighbor dipoles makes an angle of $\sim 130^o$ in the ground state structure(See section 3 of Appendix A for a schematic view). This arrangement is a result of the correlation between the favored orientation of the molecule and octahedral tilts. The next question we asked was how do the dipole moments along the cavity in the *b*-direction orient themselves. We could have a ferroelectric arrangement, where the dipole moments align or an antiferroelectric arrangement of the dipole moments(See section 3 of Appendix A for a schematic view). The former arrangement has the methyl/ammonium groups of the molecule vertically stacked. Consequently, the separation between groups

of the same type is the least in this arrangement. In a simplified picture we can think of the CH_3 group as a cation i.e. $(CH_3)^+$ while the NH_3 group is thought of as an anion $(NH_3)^-$. In this simplified picture, the separation between fragments with the same charge is the least in the ferroelectric type of stacking. This should increase the Coulomb interactions. Considering the ferroelectric and the antiferroelectric orientations of the dipole, one found that the antiferroelectric configuration was lower in energy by 120 meV/fu. In these calculations we allowed only the molecule to relax. However, when we allowed the inorganic cage to relax with the ferroelectric stacking, one arrived at a structure with lower symmetry (monoclinic) which was energetically degenerate with the antiferroelectric one (the optimized structure).

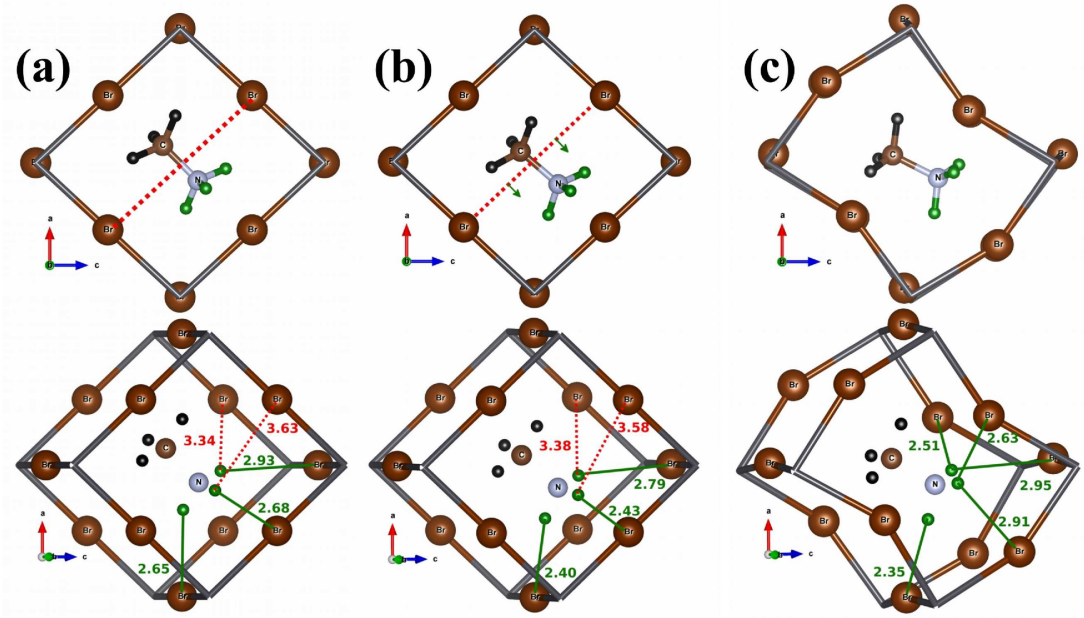

Figure 4.2: (a)Position of the molecule at the center of the ideal cavity(upper panel) and corresponding H-Br bonds(lower panel). (b) Movement of the molecule from the center of the cage shown by dotted line(upper panel) and increased hydrogen bonding after the movement(lower panel) compared to the ideal case shown in Figure 2(a). (c) Distorted cavity due to octahedral tilts(upper panel) and corresponding hydrogen bondings(lower panel). The hydrogen atoms in the NH_3 and CH_3 group are indicated by light(green) and dark(black) circles respectively. Distance between H atoms of NH_3 and Br atoms less than 3.0 Å are shown by solid green lines. The numbers denote the corresponding distances in Angstroms.

4.3.2 How does the molecule interact with the inorganic cage?

The movement of the NH_3 end of the molecule away from the center suggests that the molecule interacts with the inorganic cage through the hydrogens. Although hydrogen is known to form multicenter bonds [41], it is not clear what is the nature of the bond

here. In order to examine this aspect and understand the microscopic considerations that led to the shorter H_N-Br bonds, we mapped the *ab-initio* band structure onto a tight binding model(see the methodology section for the method). Maximally localized Wannier functions are used for the radial part of the wave function. As we have the complete Hamiltonian here, we can switch off interactions associated with parts. This analysis was done for three situations shown in Figs. 4.2(a)-4.2(c) which we now call case1, case2, case3 respectively. In case1, we have considered an orthorhombic unit cell with no octahedral tilts. The molecule is at the center on the octahedral cavity. In case2, again there are no octahedral tilts but the molecule was allowed to relax. It was found to move towards one part of the cage making shorter H_N-Br bonds. In case3, the whole system was relaxed and we arrive at the optimized crystal structure which is found to have octahedral tilts as well as displacement of the molecule. The superposition of the *ab-initio* and tight binding bands for case3 is shown in Figure 4.3(a)(others are given in section 4 of Appendix A).

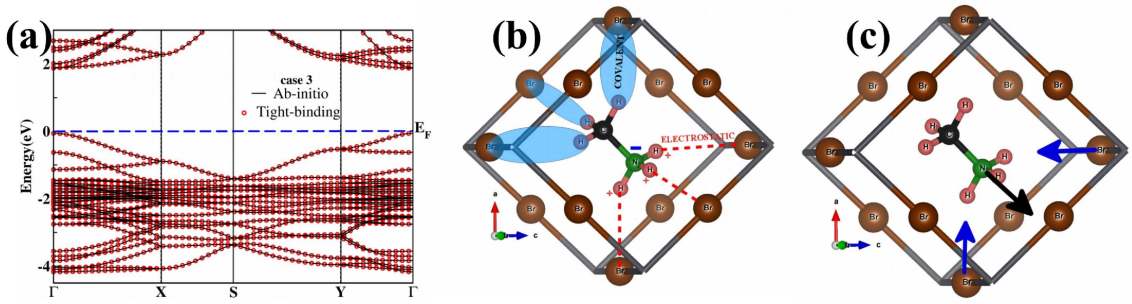

Figure 4.3: (a) The tight-binding(circles) and *ab-initio*(solid line) band structure of optimized $MAPbBr_3$ for case3. (b) Schematic showing how the molecule interacts with the inorganic cage. There is stronger covalent interaction between the methyl group and Br atoms whereas it is largely electrostatic in nature between amine group and Br atoms. (c) As a result of this asymmetric interaction the molecule move towards one direction and Br atoms may also be displaced towards the molecule, giving rise to octahedral tilts.

In each case we have a good description of the *ab-initio* band structure in terms of the tight-binding model. This allows us to discuss the role of the electronic structure on the observed structural changes. Since we have the tight binding Hamiltonian in each case, this allows us to switch off a particular set of hopping interactions to determine the energy gain via covalency from the considered hopping channel. The most surprising result that we find (Table 4.1) is that the gain from covalency between H_C-Br is almost an order of magnitude higher than the energy gain from covalency between H_N-Br. This result is similar for all the three cases tabulated in Table 4.1. This suggests that the driving force for H_N moving towards Br is not increased covalent interactions but is most probably electrostatic in nature. This is shown schematically in Figure 4.3(b).

Table 4.1: Quantitative analysis of the covalent interaction between hydrogen and Br atoms

	Energy per fu in meV		
Interactions	case1	case2	case3
H-Br ALL	0.0	0.0	0.0
H_N-Br OFF	63.0	98.0	108.0
H_C-Br OFF	518.0	525.0	495.0

As N is more electronegative than C, one finds that electrons from the hydrogen atoms attached to it are transferred to the nitrogen atom. This leaves the hydrogen atoms with a net positive charge. They in turn get attracted to the negatively charged Br atoms and hence the H_N-Br bond lengths become shorter. This explains the very small covalent component of the H_N-Br interactions, despite the fact that the structural optimization results in shorter H_N-Br bond lengths. The lowering of energy of the system by forming shorter H_N-Br bonds has the amine end of the molecule moving towards the inorganic cage as a result of an attractive Coulomb interaction. The Br atoms of the cage are also displaced from their edge centered positions in the idealized perovskite lattice shown in Figure 4.3(c) towards H_N atoms. As a result the Pb-Br-Pb angles deviate from 180^o. This is the reason why hydrogen bonding is responsible for driving the octahedral tilts.

Examining the spatial distributions of the wave functions, we find that the basis functions associated with the NH_3 part of the molecule turn out to be $s-p$ hybrids as shown in Figure 4.4(a). The spread of the wave function is small and is given in Table 4.2. A similar analysis of the basis functions associated with the hydrogens attached to the CH_3 end of the molecule reveal that the basis functions are $s-p$ hybrids with weight on two of the hydrogen atoms as well as on C. This is shown in Figure 4.4(b). In comparison with the basis functions associated with the hydrogens attached to the NH_3 end of the molecule, here, we find that the spreads are at least double for two of the basis functions. However the spread for one of the basis functions of the hydrogen atom[shown in Figure 4.4(c)] is found to be anomalously high, almost four times larger compared to the other two.

Table 4.2: Spread of the wannier functions of the hydrogens attached to N and C atoms in the optimized structure

Hydrogens attached to	Spread in $Å^2$		
H_N	0.58	0.60	0.62
H_C	4.08	1.28	1.29

A clue for the larger spreads can be found when one examines the interaction strengths. These are specified in Figure 4.4 for the cases where the matrix elements (MEs) are significant . The interaction strengths of the basis functions localized on the NH_3 end of the molecule are found to be smaller than those which are localized on the CH_3 end, indicat-

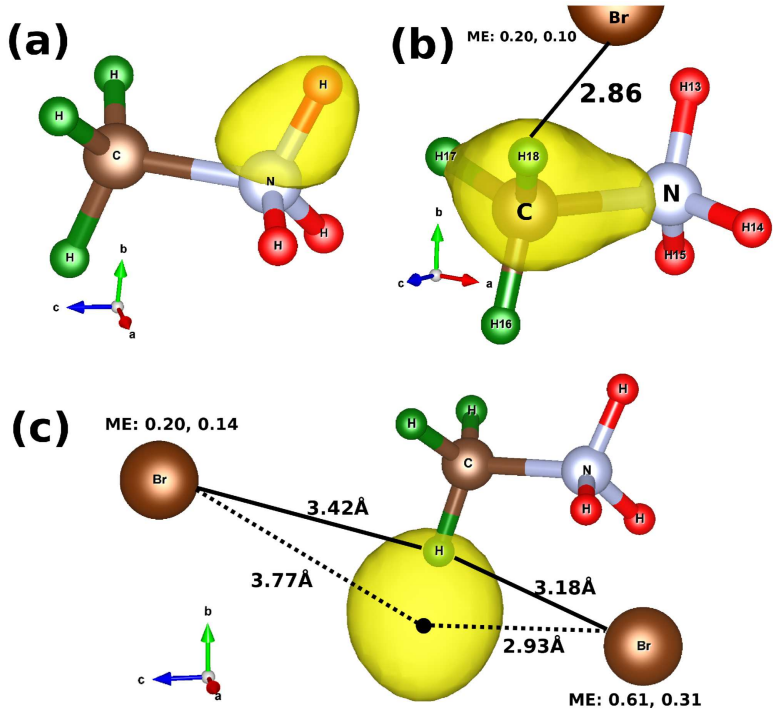

Figure 4.4: (a) The spatial distribution of the Wannier functions(WFs) of the hydrogens attached to the N atom (b) The spatial distribution of the two hydrogen WFs attached to the C atom with smaller spread and (c) having the largest spread with the Wannier center(shown by black dot) moving away from the C-H bond. The matrix elements(MEs) corresponding to the interactions of these basis functions with Br are also specified. An isosurface value equal to half the maximum value was used to make these plots.

ing larger covalency in the later case. The most surprising result is for the interactions of the basis function shown in Figure 4.4(c). Here one finds that the basis function has its center shifted away from the C-H bond. This shift allows it to interact strongly with two of the Br atoms. This suggests the formation of a multicenter bond by hydrogen with C as well as the two Br atoms which have been shown.

4.3.3 Implications on physical properties

Having understood the energetics governing the location of the molecule in the octahedral cavity as well as its interactions with the inorganic cage, we proceed to examine if the calculations could throw some light on the glassy dynamics that have been seen within the orthorhombic phase.

The molecular dipoles are believed to be frozen in their position in the low temperature structure [19, 20] with earlier works suggesting that the barriers for rotation(rotation/tumbling motion) of the molecule are large. Theoretical calculations shows that for twisting motions about the C-N axis, the barriers are $\sim$ 100 meV [21] when the

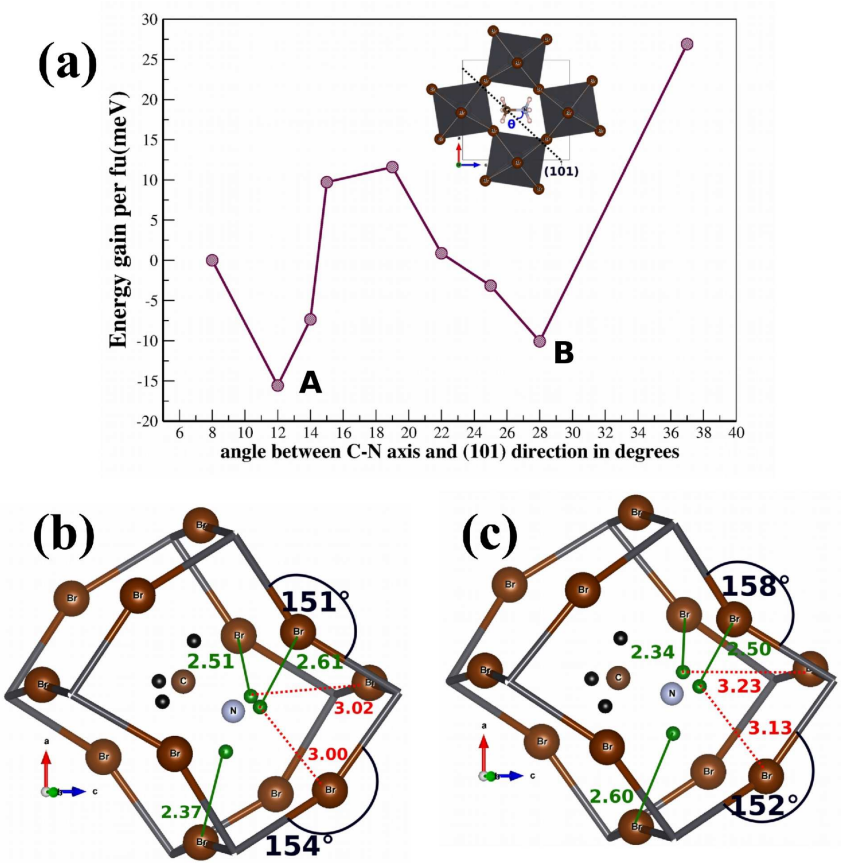

Figure 4.5: (a) The change in the energy as a function of the rotation(in ac-plane) angle of the molecule. The angle θ is shown in the inset. The optimized structure for the two minimum energy configurations where C-N axis makes an angle (b) $\sim 12^o$ (configuration A) and (c)$\sim 28^o$ (configuration B) with the (101) direction

inorganic network was kept rigid. Our analysis of small excursions of the molecule about its position in the optimized structure suggest that the energy landscape is complex. One cannot consider the rotations of the molecule alone, keeping the inorganic cage rigid. The cage has to be allowed to relax during the rotations of the molecule. Hence allowing for small rotations of the molecule in the ac-plane we find there is another minimum whose energy is just 9 meV/fu higher. This energy difference is very sensitive to the volume of the unit cell. Using the experimental lattice parameters, the difference is found to be 5 meV/fu as shown in Figure 4.5(a). The optimized structures for configuration A(ground state structure) and configuration B(the second minimum) are shown in Figs. 4.5(b) and 4.5(c). The differences in these two structures are small with the Pb-Br-Pb angles changing from 151^o and 154^o to 158^o and 152^o accompanied by deviations in the H_N-Br bond lengths from 2.37, 2.51, 2.61 Å to 2.60, 2.34, 2.50 Å. The presence of such close lying

minima separated by large barriers are evidence for the observed glassy dynamics. The system could be quenched into either of these configurations which can additionally be accessed by thermal excitations.

An additional source of orientational disorder emerges from the fact that the dipoles stacked in the *b*-direction have the same energy for a ferroelectric arrangement as well as an antiferroelectric arrangement. One should point out here that one allowed the inorganic cage to relax when we considered these two orientations of the dipoles. Configurations with a ferroelectric stacking of the dipoles along *b*-direction, without allowing the inorganic cage to relax, are found to be higher in energy than the antiferroelectric configuration by about 120 meV/fu, which was mentioned previously. The energy landscapes with deep valleys separated by high barriers is reminiscent of what one usually finds in glassy systems and could explain the glassy dynamics that have been seen in experiments.

4.4 Conclusions

The origin of the glassy dynamics that have been seen in the orthorhombic phase of hybrid perovskites has been studied considering (MA)$PbBr_3$ as an example. A complex energy landscape is found with deep valleys and high barriers for molecular rotations within the *ac*-plane. Additionally the stacking of dipoles in the *b*-direction is found to be energetically degenerate for a ferroelectric as well as an antiferroelectric arrangement again with higher energies for intermediate orientations. These results could explain the observed glassy dynamics found in the low temperature structure where the dipoles are expected to be frozen in certain orientations.

Bibliography

[1] G. Catalan, Phase Transitions **81**, 729 (2008).

[2] S. Middey, P. Mahadevan and D. D. Sarma, Phy. Rev. B **83**, 014416 (2011).

[3] J. M. Rondinelli, S. J. May and J. W. Freeland, MRS Bulletin **37**, 261 (2012).

[4] M. R. Filip, G. E. Eperon, H. J. Snaith and F. Giustino, Nat. Comm. **5**, 5757 (2014).

[5] J. Young and J. M. Rondinelli, J. Phys. Chem. Lett. **7**, 918 (2016).

[6] J. B. Torrance, P. Lacorre, A. I. Nazzal, E. J. Ansaldo and C. Niedermayer, Phy. Rev. B **45**, 8209 (1992).

[7] M. L. Medarde, J. Phys.: Condens. Matter **9**, 1679 (1997).

[8] S. Middey, J. Chakhalian, P. Mahadevan, J. W. Freeland, A. J. Millis and D.D. Sarma, Annu. Rev. Mater. Res. **46**, 305 (2016).

[9] D. B. Mitzi , C. A. Feild , W. T. A. Harrison , A. M. Guloy , Nature **369** , 467 (1994).

[10] D. B. Mitzi , S. Wang , C. A. Feild , C. A. Chess , A. M. Guloy , Science **267** , 1473 (1995).

[11] G. Hodes, Science **342**, 317 (2013).

[12] D. B. Mitzi, J. Chem. Soc., Dalton Trans. 1 (2001).

[13] C. C. Stoumpos, C. D. Malliakas and M. G. Kanatzidis, Inorg. Chem. **52**, 9019 (2013).

[14] G. Xing, N. Mathews, S. Sun, S. S. Lim, Y. M. Lam, M. Grätzel, S. Mhaisalkar and T. C.Sum, Science **342**, 344 (2013).

[15] S. D. Stranks, G. E. Eperon, G. Grancini, C. Menelaou, M. J. P. Alcocer, T. Leijtens, L. M. Herz, A. Petrozza and H. J. Snaith, Science **342**, 341 (2013).

[16] NREL Efficiency Chart at:
$https://www.nrel.gov/pv/assets/images/efficiency-chart.png$

[17] J.-H. Lee, N. C. Bristowe, J. H. Lee, S.-H. Lee, P. D. Bristowe, A. K. Cheetham and H. M. Jang, Chem. Mater. **28**, 4259 (2016).

[18] D. H. Fabini, T. Hogan, H. A. Evans, C. C. Stoumpos, M. G. Kanatzidis and R. Seshadri, J. Phys. Chem. Lett. **7**, 376 (2016).

[19] N. Onoda-Yamamuro, T. Matsuo, H. Suga, J. Phys. Chem. Solids. **51**, 1383 (1990).

[20] A. Poglitsch, D. Weber, J. Chem. Phys. **87**, 6373 (1987).

[21] J.-H. Lee, N. C. Bristowe, P. D. Bristowe, A. K. Cheetham, Chem. Commun. **51**, 6434 (2015).

[22] J. Even, M. Carignano and C. Katan, Nanoscale **8**, 6222 (2016).

[23] N. Onoda-Yamamuro, T. Matsuo, H. Suga, J. Phys. Chem. Solids. **53**, 935 (1992).

[24] N. Onoda-Yamamuro, T. Matsuo, H. Suga, J. Chem. Thermodyn. **23**, 987 (1991).

[25] P. E. Blöchl, Phys. Rev. B **50**, 17953 (1994); G. Kresse, and D. Joubert, Phys. Rev. B **59**, 1758 (1999).

[26] G. Kresse and J. Hafner, Phys. Rev. B **47**, 558 (1993) ; G. Kresse and J. Hafner, Phys. Rev. B **49**, 14251 (1994); G. Kresse and J. Furthmüller, Phys. Rev. B **54**, 11169 (1996).

[27] G. Kresse and J. Furthmüller, Comput. Mater. Sci., **6**, 15 (1996).

[28] J. P. Perdew, K. Burke and M. Ernzerhof, Phys. Rev. Lett. **77**, 3865 (1996); J. P. Perdew, K. Burke and M. Ernzerhof, Phys. Rev. Lett. **77**, 3865 (1996);

[29] D. A. Egger and L. Kronin, J. Phys. Chem. Lett. **5(15)**, 2728 (2014).

[30] Y. Wang, T. Gould, J. F. Dobson, H. M. Zhang, H. G. Yang, X. D. Yao and H. J. Zhao, Phys. Chem. Chem. Phys. **16**, 1424 (2014).

[31] P. Umari, E. Mosconi, F. De Angelis, Sci. Rep. **4**, 4467 (2014).

[32] J. S. Manser, J. A. Christians and P. V. Kamat, Chem. Rev. **116**, 12956 (2016).

[33] S. Grimme, J. Comput. Chem. **27**, 1787 (2006).

[34] H. Mashiyama, Y. Kawamura and Y. Kubota, J. Korean Phys. Soc. **51**, 850 (2007).

[35] A. A. Mostofi, J. R. Yates, Y.-S. Lee, I. Souza, D. Vanderbilt, and N. Marzari, Comput. Phys. Comm. **178**, 685 (2008).

[36] N. Marzari and D. Vanderbilt, Phys. Rev. B **56**, 12847 (1997).

[37] I. Souza, N. Marzari and D. Vanderbilt, Phys. Rev. B **65**, 035109 (2001).

[38] A. M. Glazer, Acta Crystallogr. A **31**, 756 (1975).

[39] After forcefully orientating the C-N axis of the molecule along the short diagonal of the rhombus shaped cavity, no ionic relaxation was done. This was found to be higher in energy by 540 meV/fu compared to the optimised structure.

[40] G. Sharada, P. Mahale, B. P. Kore, S. Mukherjee, M. S. Pavan, C. De, S. Ghara, A. Sundaresan, A. Pandey, T. N. G. Row and D. D. Sarma, J. Phys. Chem. Lett. **7**, 2412 (2016) and references therein.

[41] A. Janotti and C. G. Van de Walle, Nat. Mater. **6**, 44 (2007).

Chapter 5

Hybrid Perovskites under pressure: Revisiting some structural chemistry concepts

5.1 Introduction

The thrust for moving away from a dependence of energy on fossil fuels has led to growing attention on other sources, solar energy being one of the options. An important element of any process harnessing solar energy and converting it to an electric current involves using the incident photons to create electron-hole pairs across a band gap. These charge carriers then have to be physically separated before they recombine [1]. In this process a current is generated. An obvious route to increase this current is to have more electron-hole pairs. As the solar spectrum shows a maximum intensity(i.e. more photons) within the visible region between 1.7 and 3.2 eV, tuning the band gap of the solar cell material within this energy window is desired for maximum absorption of the solar energy. Though a number of semiconductors have their band gaps within this energy range, not all of them can be used in solar cells due to some constraints, the primary one being the presence of defects. Along with a desired band gap and the possibility of band gap tuning, we need large diffusion lengths and lifetime for the charge carriers, so that they can be easily separated before the recombination takes place. The presence of defects hampers this. High mobility of the charge carriers are also desired for swift transport and minimal loss.

Recently a new class of perovskite materials have been found to be attractive for use in solar cells. These are called hybrid perovskites where the A-site is occupied by an organic molecule. Due to high charge carrier mobilities, large diffusion lengths and carrier lifetime [2–6] , low cost and fast preparation techniques in laboratory environment [2], and a conversion efficiency of over 20% [7], they have become the subject of intense research activity. An advantage of this type of perovskite materials that emerges is the multiple number of ways that one can control the band gap. Theoretical calculations show that the electronic structure of inorganic/hybrid lead halide perovskites [$(A/\mathrm{OM})\mathrm{Pb}X_3$, A = inorganic atom, OM = organic molecule, X = halide atom] have contributions from the s, p states of Pb and p states of the anion X. The valence band maximum is found to emerge from the interactions between the Pb s and X p states and has dominantly X p character. The conduction band minimum has Pb p character. This immediately suggests that by tuning the strength of the Pb s - X p interaction, one can change the band gap of these materials. A route to achieve this is by structural modifications. Though the atom/molecule at the A-site has no electronic states several eV about the Fermi energy, it can still control the structural properties and hence have an indirect effect on the electronic structure and therefore the band gap. It has been well known that the size of the atom/molecule at the A-site of the perovskite lattice plays an important role in determining the size of the unit cell that results in a change of the Pb-X bond lengths and Pb-X-Pb bond angles. These two have different effects on the band gap of the system. A

smaller size of the A-site cation results in a reduction of the cell volume. This results in shorter Pb-X distances, which would then lead to an increase in the Coulomb repulsion between electrons on Pb and those on X. To compensate for this increased Coulomb repulsion, the PbX_6 octahedra tilt resulting in Pb-X-Pb angles that deviate from 180° as well as small elongations of the Pb-X bond lengths. A shorter Pb-X bond length increases the splitting between the bonding and anti-bonding states. The valence band is pushed up in energy and this decreases the separation between the valence band maximum(VBM) and conduction band minimum(CBM), resulting in a reduction of the band gap. On the other hand deviation of the Pb-X-Pb angle from 180° decreases the bandwidth of the valence band as a result of reduced connectivity of the PbX_6 units. This increases the separation between VBM and CBM resulting in an increased band gap. These results suggest opposite tendencies of the modifications in the electronic structure when the cation at the A-site is replaced by a smaller atom. The natural question that follows is, which effect dominates. Our calculations with the inorganic perovskite $CsPbBr_3$ in the orthorhombic phase shows that the changes in the Pb-Br bond lengths dictate the changes in the band gap of the system. One finds a systematic increase in the band gap with increase in the volume of the unit cell. The band gap tuning is also possible by other means. For example, the band gap and optical properties of (A/OM)PbX_3 can be easily tuned in the entire visible region of the electromagnetic spectrum by anion exchange [8,9]. Replacing Pb with Sn in the general composition (MA)$Sn_xPb_{(1-x)}X_3$ has also been reported to control the band gap [10,11]. These are similar to band gap changes seen in binary semiconductors by changing the cation or the anion.

The situation becomes more complex in the case of hybrid perovskites. In contrast to inorganic perovskites where the A-site is occupied by an spherical atom, in the present case one has an organic molecule which is asymmetric in shape. In addition to this, now there are hydrogen atoms associated with the molecule that are involved in hydrogen bonding with the halide ions. *Ab-initio* calculations with $CH_3NH_3PbI_3$($MAPbI_3$) shows that replacing MA with an ion which had the same ionic radii led to the octahedral tilts of the Pb-I network vanishing [12]. This led them to the conclusion that it was hydrogen bonding with the anions that led to the octahedral tilts found in the low temperature experimental structure. So here, hydrogen bonding along with steric effect plays an important role in the structural distortions. Also due to the asymmetry of the molecule, certain orientations are preferred over others. A change in orientation of the molecule leads to a change in structural distortions giving rise to a complex potential energy landscape [13,14]. Hence changing the organic molecule in the hybrid perovskites can be an effective way to tune the band gap of the system. But compared to inorganic systems, here a systematic study of the effect of changing the organic molecule is not straight forward.

Several factors have to be considered while replacing the organic molecule. The molecule within the octahedral cavity does not stay at the center of the inorganic cage but moves towards one end to maximize hydrogen bonding. Such movements of the molecule along with its asymmetry lead to anisotropic changes in the structural distortions. The ground state(GS) orientation and conformation of the molecule also needs to be determined to obtain the GS structure of the system. Otherwise the optimized structure may lead to different tilt systems for different molecular orientations than what is observed in experiment. Due to these factors, no systematic trends in the band gap have been found as a function of the organic molecule [15]. Unless one isolates the different factors, the conclusions are also clouded, leading to an ambiguity in the role of the organic molecule at the *A*-site. The paper by Aman *et al.* [16] suggests that larger cations are expected to have reduced band gaps due to decreased octahedral tilting. In contrast, Safdari *et al.* [17], find an increase in the band gap as the *A*-site cation is changed from MA to EA to PA.

Our calculations with $MAPbBr_3$ in the orthorhombic phase shows that changes in the volume lead to change in the movement as well as rotation of the molecule. The structural changes are such that the steric effects result in larger variations of the out of plane bond lengths compared to the in-plane bond lengths, but negligible changes in some of the Pb-Br-Pb bond angles, with a decrease in the volume of the unit cell. This leads to very small band gap changes arising from variations in bond angles. However an expansion of the unit cell volume results in band gap changes arising from variations in both the bond lengths as well as the bond angles. Armed with this understanding, we replaced MA by EA($CH_3CH_2NH_3$) within the octahedral cavity. Taking into consideration the proper orientation, conformation of the molecule and optimizing the unit cell volume, we found that the band gap increased with a dominant effect emerging from an increased Pb-Br bond lengths.

5.2 Methodology

The electronic structure of the systems were calculated using a projected augmented wave (PAW) [18] implementation of density functional theory within Vienna *ab-initio* simulation package (VASP) [19, 20]. The generalized gradient approximation(GGA) [21] was used for the exchange-correlation functional. Inclusion of the non-local, weak van der Waals(vdW) interactions are necessary to correctly predict the structural properties. A GGA+vdW density functional theory calculation has been found to give a good estimation of the lattice parameters and structural properties [22, 23]. Dispersive interactions are

responsible for a significant contraction of the unit cell, correcting the overestimation in general done by GGA. It also gives a band gap close to the experimental values for Pb based compounds which is striking compared to normal semiconductors for which we need to consider hybrid functionals. This happens due to cancellation of errors [24]. However, it cannot accurately describe the band dispersions. Inclusion of the spin orbit coupling(SOC) slightly changes the Pb-X bond lengths but strongly underestimates the band gap and SOC-GW is needed for accurate description of the electronic structure [23, 24]. Still DFT calculations are useful for determination of structural properties and sufficient for comparison of electronic properties of homologous systems [25]. DFT-D2 method of Grimme [26] was considered to introduce dispersive interactions within the system. Gamma centered Monkhorst-Pack k-mesh of 8×6×8 was used to perform the k-space integrations. In addition to this, an energy cutoff of 600 eV was used for the kinetic energy of the plane waves included in the basis. The orthorhombic unit cell [27] was used for all the calculations and the internal positions were optimized till the forces on the atoms were less than 10^{-4} eV/Å to find the minimum energy structure. This structure has a space group symmetry *Pnma* and is non-polar. For a band gap comparison between $MAPbBr_3$ and $EAPbBr_3$ the lattice parameters were optimized. For $MAPbBr_3$, the optimized lattice parameters are found to be 7.97, 11.83, and 8.56 Å, very close to the experimental values of 7.98, 11.84, and 8.56 Å respectively. For $EAPbBr_3$, the optimized lattice parameters are found to be 8.11, 12.04, and 8.71 Å. Here we considered the long C-N bond (2.44 Å) as the axis of the molecule. In order to find the positions of the atoms, the orientation and stacking of the EA molecule were chosen so as to maximize hydrogen bonding and minimize steric effects. The long C-N bond of the EA molecule was chosen to lie along the (101) direction(*ac*-plane), similar to what one had for the MA case. The stacking of the molecules in the *b*-direction was chosen with the C end of the lower molecule sitting below the N end of the upper molecule. The structure was then relaxed in several steps to optimize the volume of the unit cell. The stacking of the molecules and orientation in the optimized structure is shown in the inset of Figure 5.5(c). Several other configurations were considered for the EA molecule. These were found to be local minima with higher energies. An orthorhombic unit cell [28] of $CsPbBr_3$ was used for the calculations.

5.3 Results and Discussion

We first consider the effect of changes in the volume of the unit cell on the band gap of the system. To examine this we have considered the experimental low temperature

structure for $CH_3NH_3PbBr_3$($MAPbBr_3$) which is orthorhombic. The internal positions were relaxed so that the ions took their minimum energy configuration in the lattice. The two in-plane(*ac*-plane) Pb-Br-Pb bond angles were found to be $\sim 153^o$ while the out of plane Pb-Br-Pb angle was found to be larger and equal to $\sim 167^o$ in the optimized unit cell. In order to vary the volume, we carried out a uniform expansion and compression of the unit cell in steps up to a variation of 6% about its experimental volume. All angular distortions were kept constant, and the change in the band gap as a function of the volume was calculated.

This is shown in Figure 5.1(a) where the band gap variations are shown with respect to the value for the 0% case. The variations in the band gap are found to be monotonic, with the band gap increasing with an increase in volume.

In order to understand the reason for this trend in the band gap as the volume is varied, it is useful to examine the expected changes in the electronic structure. This is shown schematically in panel (c) of Figure 5.1. The Pb *s* states which are deep inside the valence band interact with the anion *p* states forming bonding and antibonding states. The antibonding states determine the position and character of the valence band maximum. The Pb *p* states make up the conduction band minimum. A change in the volume results in an elongation of the Pb-Br bond length. As the hopping interactions strengths for an electron from Pb *s* to Br *p* levels scale with distance as $1/r^2$ [29], the elongation is expected to decrease the hopping strengths. This results in a reduction in the bonding-antibonding separation, resulting in the valence band maximum getting pushed deeper into the valence band. This leads to the observed increase in the band gap with volume.

In the calculations examining the volume increase, the angular distortions of the $PbBr_6$ octahedra were kept fixed and their effect on the band gap increase was not examined. We have therefore considered the orthorhombic unit cell at the experimental volume and placed the Pb and Br atoms at their ideal positions in this unit cell. This leads to a high symmetry orthorhombic cell without any octahedral tilts. All three Pb-Br-Pb bond angles along the three pseudo cubic axis are 180^o. We then introduce angular distortions in this high symmetry structure in steps in a controlled manner. We rotate the PbX_6 octahedras about the pseudo cubic (101) direction in a cooperative way such that they are out of phase along the pseudo cubic axes in the *ac*-plane and in phase along the pseudo cubic *b*-direction. This introduces a, $a^-b^+a^-$ tilt pattern [30] consistent with the dominant $GdFeO_3$ distortions found for $MAPbBr_3$. In four steps we increase the angular distortions while the volume of the unit cell is kept fixed. In each case we calculate the band gap. The change in the band gap as a function of the Pb-Br-Pb angle is shown

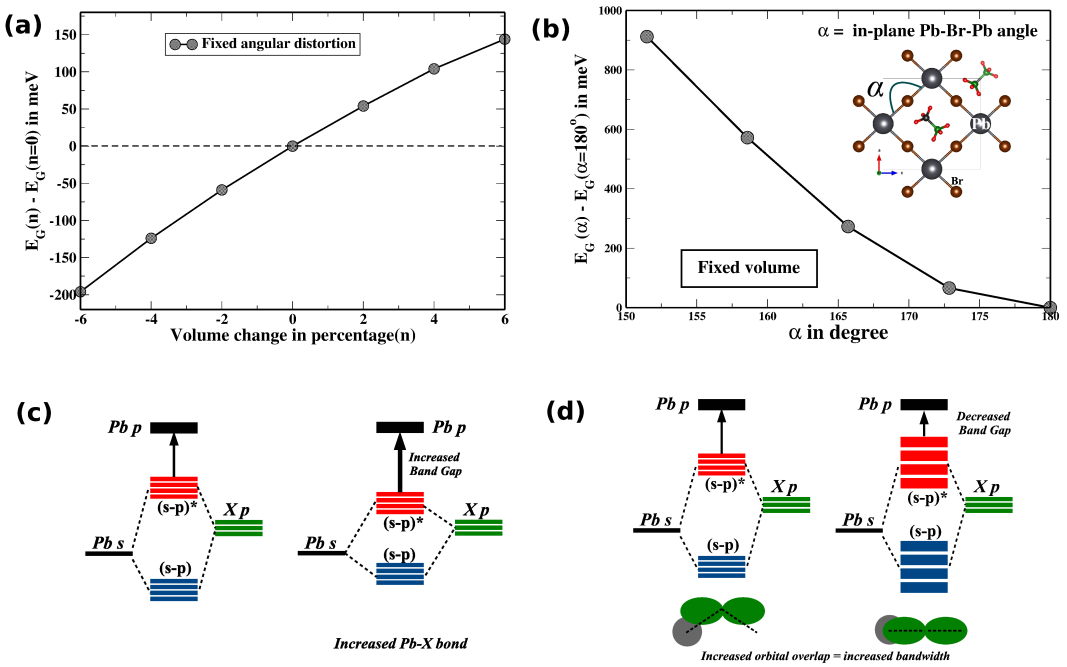

Figure 5.1: (a) Band gap variation as a function of uniform volume change about the experimental volume and with a fixed angular distortion of the optimized structure. (b) Variation in the band gap as function of angular distortion with fixed unit cell volume. (c) Increased band gap due to an decreased bonding-antibonding splitting as a result of increased Pb-X bond length. (d) Decreased band gap due to an increased bandwidth as a result of decreased angular distortion.

in Figure 5.1(b). We find that as the $PbBr_6$ octahedra rotate and the Pb-Br-Pb angle deviates from 180^o, the band gap of the system is found to increase.

Again we used the schematic representation of the electronic structure shown in Figure 5.1(d) to understand the expected changes with the angular distortions. the deviation of the Pb-Br-Pb angle from 180^o results in reduced connectivity of the octahedral networks. This leads to a reduced bandwidth associated with both the bonding and antibonding states as the angle deviates from 180^o. This leads to an increase in the band gap and explains the trends seen in Figure 5.1(b).

The calculations presented in Figure 5.1 had some constraints associated with them. In reality, however, when one replaces an atom at the A-site with an atom with a larger ionic radius, one has an increase in the volume of the unit cell. As a result there is an increase in the Pb-Br bond length, as well as a decrease in angular distortions of the Pb-Br-Pb network. As one saw earlier, the former effect would result in an increase in the band gap while the latter effect would result in a decrease. This immediately raises the question of which effect is expected to dominate and dictate the changes one expects when an atom

of smaller ionic radius at the A-site is replaced by an atom with a larger ionic radius. In order to examine this aspect, we considered the inorganic perovskite $CsPbBr_3$.

The experimental low temperature orthorhombic unit cell was considered. This was then subject to uniform expansion and compression of 4% with respect to the experimental volume. The atomic positions were relaxed at each volume and we show a representative $PbBr_6$ octahedra in each of the three cases in Figure 5.2.

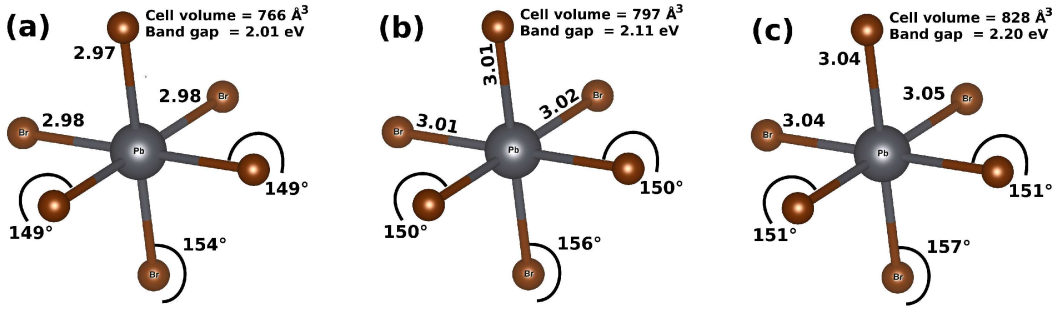

Figure 5.2: Pb-Br bond lengths and Pb-Br-Pb bond angles along the three pseudocubic directions in the optimized structures of $CsPbBr_3$ for (a) 4% volume compression (b) experimental volume and (c) 4% volume expansion.

The octahedron for the 4% compressed case is shown in Figure 5.2(a). One finds that the in-plane(ab-plane) Pb-Br-Pb angles are found to be 149^o while the out of plane angles are found to be larger and equal to 154^o. These angles have to be compared with those for the optimized experimental unit cell shown in Figure 5.2(b) where the in-plane angles are 150^o while the out of plane angles are 156^o. There are also changes in the Pb-Br bond lengths in the compressed structure. They are found to be reduced with respect to the experimental unit cell. Consequent to these structural changes one also finds a decrease in the band gap. These results suggest that it is the bond length changes which dominate and determine the change in the band gap.

Examining the case of expansion of the unit cell volume, the geometry of one octahedron for the 4% expansion case is shown in Figure 5.2(c). Here one finds an increase in the in-plane bond angles with respect to the experimental unit cell of 151^o from 150^o as well as an increase of the out of plane bond angles from 156^o to 157^o. The bond length increase is much larger and this is what determines the band gap change that one finds of ~ 0.09 eV.

The ideas of how the octahedra responds when a perovskite of the form ABX_3 is subject to a volume change have conventionally been described in terms of the compressibility of the AX_{12} units versus the BX_6 units [31]. These ideas translate into whether the

volume changes reflect in larger changes in the bond lengths or in the bond angles. Hence depending on the relative compressibilities, one could have either the band gap increasing or decreasing. This brought us to the question, what happens when one has a molecule at the *A*-site. Would one of the two effects dominate and therefore provide a universal trend in the case of the hybrid perovskites.

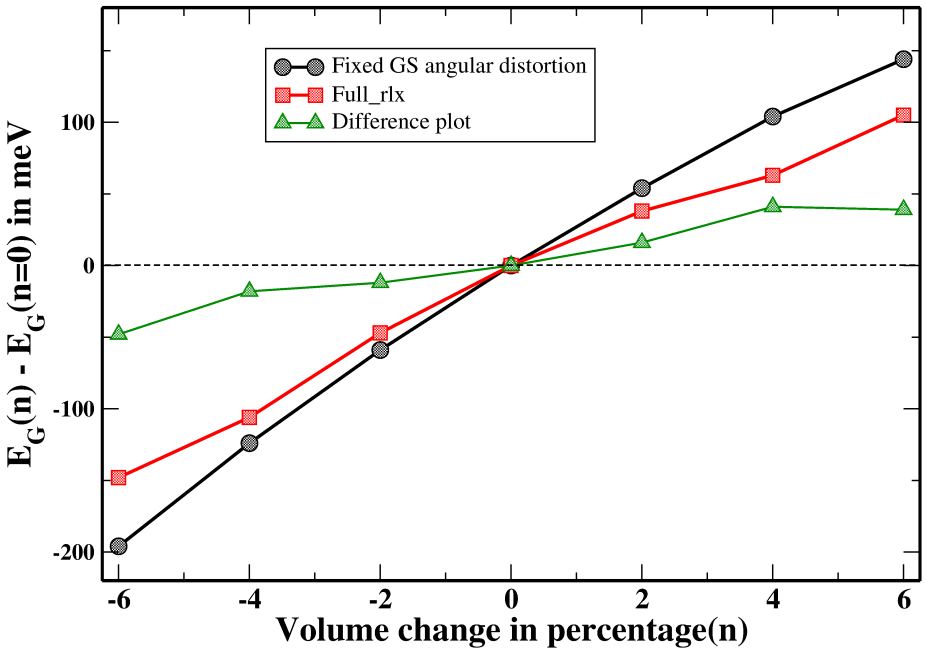

Figure 5.3: Band gap variation in $MAPbBr_3$. *Circle* : Band gap variation as a function of uniform volume change about the experimental volume and with a fixed angular distortion of the optimized structure. *Square* : Band gap variation as a function of uniform volume change about the experimental volume and with an allowed structural optimization. *Triangle* : Difference plot.

In order to understand the role of *A*-site compressibility versus *B*-site compressibility, we consider the case of $MAPbBr_3$. A theoretical scheme allows us to disentangle the contributions from each of these parts by considering limiting cases. We took the optimized ground state experimental structure and considered uniform expansion and contraction of the unit cell volume about the experimental volume keeping the angular distortion fixed. For each case we calculate the band gap of the systems. This has been plotted with respect to the value determined for the experimental volume (n = 0)[see Figure 5.3(circles)]. Next at each volume we have optimized the internal positions of the ions to their minimum energy position(Full relax structures), This induces additional angular distortions compared to the structures where angular distortions were kept fixed. The band gap was calculated for each case and has been plotted with respect to the value determined for the experimental volume (n = 0)[see Figure 5.3(squares)]. The band gap at each volume without any change in the angular distortion, is indeed found to be larger. This is expected because, as we have discussed earlier, change in angular distortion op-

poses the change in bond lengths. However the enhancements are found to be quite small where volume changes are 1-2 % of the experimental volume. This suggests that in this regime one can clearly say that bond length changes dictate the band gap change.

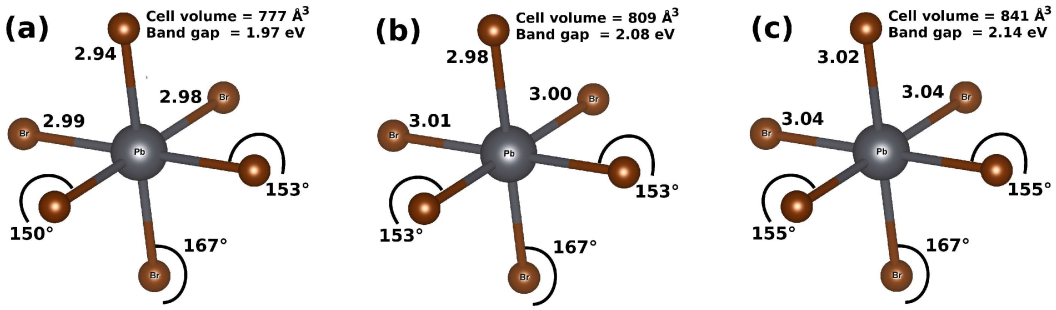

Figure 5.4: Pb-Br bond lengths and Pb-Br-Pb bond angles along the three pseudocubic directions in the optimized structures of $MAPbBr_3$ for (a) 4% volume compression (b) experimental volume and (c) 4% volume expansion.

To quantify this further, we examine the $PbBr_6$ octahedra in a few cases. These are shown in Figure 5.4 and correspond to the optimized structures at 4% compression, experimental volume as well as the 4% expanded case. The Pb-Br bond lengths as well as the Pb-Br-Pb angles have been indicated in each case. Considering the unit cell corresponding to the uniformly compressed $PbBr_6$ octahedra, one finds changes in both the in-plane and out of plane bond lengths. Changes in the out of plane bond lengths are larger compared to the in-plane ones. The in-plane bond angles are also found to change asymmetrically, with no variation seen in one of the in-plane Pb-Br-Pb bond angle. The out of plane bond angles also don't show any variation. Due to volume compression, the effect of the molecular asymmetry becomes significant resulting a change in only one of the bond angles. This accounts for the small changes in band gap found for the compressed structures arising from variations in the Pb-Br-Pb angles. One can therefore infer that steric effects associated with the interactions of the molecule with the inorganic cage dictate the bond angles and bond lengths, leading to smaller variations in the bond angles for the compressed unit cells. Hence for compressed systems, bond length changes dominantly determine the observed band gap variations.

The results of the expanded unit cell are however different. There is larger freedom for the molecule to move around. Variations of the bond lengths are similar for in-plane as well as out of plane ones. The in-plane bond angles are also found to change modestly and symmetrically. However, similar to the compressed systems, here also the out of plane bond angles hardly change. Hence all bond lengths and most of the bond angles contribute to the band gap variations found for the expanded case.

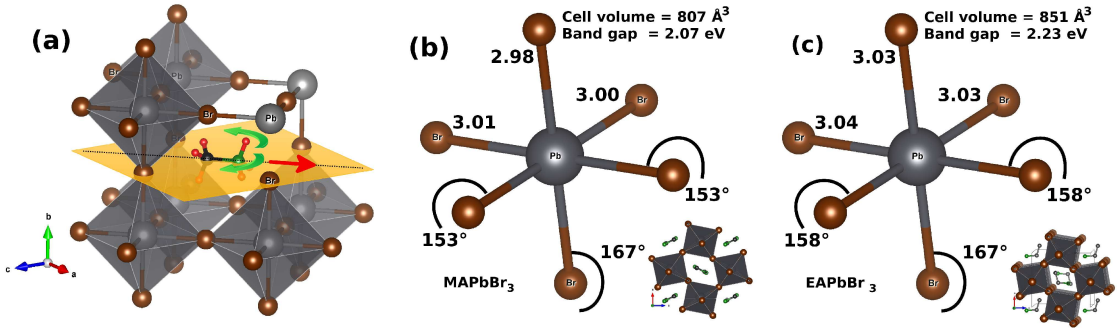

Figure 5.5: (a) Position of the MA molecule inside the octahedral cavity and its translational, orientational degrees of freedom in the *ac*-plane. Pb-Br bond lengths and Pb-Br-Pb bond angles along the three pseudocubic directions in the optimized structures with optimized volume of (a) $MAPbBr_3$ and (b) $EAPbBr_3$. Insets: Conformation of the MA and EA molecules.

One interesting result that is common, both in case of volume expansion and contraction, is that the out of plane Pb-Br-Pb bond angles remains invariant. This can be understood by considering the position of the molecule inside the octahedral cavity. As shown in Figure 5.5(a), the MA molecule inside the octahedral cavity lies in the *ac*-plane and has translational degrees of freedom within the plane and small orientational degrees of freedom about its axis [14]. The Br atoms that are part of the out of plane Pb-Br-Pb angles lie in the same plane of the molecule and strongly interact with it. With a change in the unit cell volume, the molecule readjust its position and orientation in the *ac*-plane in such a manner that the positions of the apical Br atoms remain unchanged resulting in no variation of the out of plane Pb-Br-Pb angles. The Br atoms that take part in the in-plane bond angles do not lie in the same plane of the molecule and change its position with volume change leading to deviation of the bond angles as expected.

Having understood the microscopic considerations that go into determining the band gap, we wanted to check the effect of putting a larger molecule at the *A*-site. For this we replaced MA by EA = $CH_3CH_2NH_3$. EA is a larger molecule than MA and is more asymmetric having a triangular shape with two Carbon atoms(See the inset of Figure 5.5(c), the molecule is in the octahedral cavity). For $EAPbBr_3$ no experimental data exists for the three dimensional compound in the perovskite structure. So, we use our understandings of the microscopic interactions leading to the ground state structure from $MAPbBr_3$, and predict the favored structure for $EAPbBr_3$(See the methodology section for a detail description). For the purpose of comparison, the volume of $MAPbBr_3$ was also optimized. The structure, volume and band gap of volume optimized $MAPbBr_3$ and $EAPbBr_3$ are shown in Figs. 5.5(b) and 5.5(c) respectively. Stacking of the molecules are shown the insets. There is a 5.5% increase in volume going from MA to EA, as a result the

Pb-Br bond lengths are found to increase. Here also the EA molecule has translational degree of freedom in the *ac*-plane. As a result of this the out of plane Pb-Br-Pb bond angles along the *b*-direction remain almost unchanged. The in-plane bond angles increase from 153^o to 155^o as result of the larger size of the EA molecule and this has an opposite effect on the band gap change. The band gap increases by 160 meV going from MA to EA and the dominant contribution is from the Pb-Br bond length changes.

5.4 Conclusions

In any perovskite system(ABX_3) the change in the unit cell volume due to a change in the size of the *A*-site cation results in a change in the *B*-*X* bond lengths as well as *B*-*X*-*B* bond angles. These are the main structural parameters that directly control the electronic structure of the system. For instance replacing the cation at the *A*-site with a larger atom results in an increase in the *B*-*X* bond length as well as *B*-*X*-*B* bond angles. An increase in the bond length is found to decrease the band gap while an increase in the bond angle results in an decreased band gap. Whether the change in bond lengths or the bond angles control band gap changes depends entirely on the relative compressibilities of the BX_6 and AX_{12} polyhedra. Our calculations suggests that, for hybrid lead halide perovskites the changes in the Pb$-X$ bond lengths plays the dominant role in determining the changes in the electronic structure, especially when one is compressing the unit cell. In this limit standard concepts of structural changes discussed in the context of inorganic perovskites are no longer valid. Steric effects of the molecule with the inorganic cage dictate the structural changes leading to bond angles changes being small. In the expanded unit cell limit, however both effects contribute.

Bibliography

[1] F. Liu, W. Wang, L. Wang, G. Yang, Nanomaterials and Energy **2**, 3 (2012).

[2] G. Hodes, Science **342**, 317 (2013).

[3] D. B. Mitzi, J. Chem. Soc., Dalton Trans. 1 (2001).

[4] C. C. Stoumpos, C. D. Malliakas and M. G. Kanatzidis, Inorg. Chem. **52**, 9019 (2013).

[5] G. Xing, N. Mathews, S. Sun, S. S. Lim, Y. M. Lam, M. Grätzel, S. Mhaisalkar and T. C.Sum, Science **342**, 344 (2013).

[6] S. D. Stranks, G. E. Eperon, G. Grancini, C. Menelaou, M. J. P. Alcocer, T. Leijtens, L. M. Herz, A. Petrozza and H. J. Snaith, Science **342**, 341 (2013).

[7] NREL Efficiency Chart at:
$https://www.nrel.gov/pv/assets/images/efficiency-chart.png$

[8] D. Cui, Z. Yang, D. Yang, X. Ren, Y. Liu, Q. Wei, H. Fan, J. Zeng, S. F. Liu, J. Phys. Chem. C **120**, 42 (2016).

[9] S. A. Kulkarni, T. Baikie, P. P. Boix, N. Yantara, N. Mathews, S. Mhaisalkar, J. Mater. Chem. A **2**, 9221 (2014).

[10] F. Hao, C. C. Stoumpos, D. H. Cao, R. P. H. Chang, M. G. Kanatzidis, Nat. Photonics **8**, 489 (2014).

[11] B. Lee, C. C. Stoumpos, N. Zhou, F. Hao, C. Malliakas, C.-Y. Yeh, T. J. Marks, M. G. Kanatzidis, R. P. H. Chang, J. Am. Chem. Soc. **136**, 15379 (2014).

[12] J.-H. Lee, N. C. Bristowe, J. H. Lee, S.-H. Lee, P. D. Bristowe, A. K. Cheetham and H. M. Jang, Chem. Mater. **28**, 4259 (2016).

[13] J. S. Bechtel, R. Seshadri and A. Van der Ven, J. Phys. Chem. C **120**, 12403 (2016).

[14] Sagar Sarkar and Priya Mahadevan, Phys. Rev. B **95**, 214118 (2017).

[15] D. Yang, J. Lv, X. Zhao, Q. Xu, Y. Fu, Y. Zhan, A. Zunger and L. Zhang, Chem. Mater **29**, 524 (2017).

[16] A. Amat, E. Mosconi, E. Ronca, C. Quarti, Paolo Umari, Md. K. Nazeeruddin, M. Grätzel, and F. D. Angelis, Nano Lett. **14**, 3608 (2014).

[17] M. Safdari, A. Fischer, B. Xu, L. Kloo and J. M. Gardner, J. Mater. Chem. A, **3**, 9201 (2015).

[18] P. E. Blöchl, Phys. Rev. B **50**, 17953 (1994); G. Kresse, and D. Joubert, Phys. Rev. B **59**, 1758 (1999).

[19] G. Kresse and J. Hafner, Phys. Rev. B **47**, 558 (1993) ; G. Kresse and J. Hafner, Phys. Rev. B **49**, 14251 (1994); G. Kresse and J. Furthmüller, Phys. Rev. B **54**, 11169 (1996).

[20] G. Kresse and J. Furthmüller, Comput. Mater. Sci., **6**, 15 (1996).

[21] J. P. Perdew, K. Burke and M. Ernzerhof, Phys. Rev. Lett. **77**, 3865 (1996); J. P. Perdew, K. Burke and M. Ernzerhof, Phys. Rev. Lett. **77**, 3865 (1996);

[22] D. A. Egger and L. Kronin, J. Phys. Chem. Lett. **5(15)**, 2728 (2014).

[23] Y. Wang, T. Gould, J. F. Dobson, H. M. Zhang, H. G. Yang, X. D. Yao and H. J. Zhao, Phys. Chem. Chem. Phys. **16**, 1424 (2014).

[24] P. Umari, E. Mosconi, F. De Angelis, Sci. Rep. **4**, 4467 (2014).

[25] J. S. Manser, J. A. Christians and P. V. Kamat, Chem. Rev. **116**, 12956 (2016).

[26] S. Grimme, J. Comput. Chem. **27**, 1787 (2006).

[27] H. Mashiyama, Y. Kawamura and Y. Kubota, J. Korean Phys. Soc. **51**, 850 (2007).

[28] M. Rodová, J. Brožek, K. Knížek and K. Nitsch, J. Therm. Anal. Cal. **71**, 667 (2003).

[29] W. A. Harrison, Electronic Structure and Properties of Solids (Freeman, San Francisco, 1980).

[30] A. M. Glazer, Acta Crystallogr. A31, 756 (1975).

[31] J. Zhao, N. L. Ross and R. J. Angel, Phys Chem Minerals **31**, 299 (2004).

Chapter 6

Doping a dipole into an incipient ferroelectric: A route to stabilizing ferroelectricity

6.1 Introduction

The well known ferroelectric materials $BaTiO_3$, $PbTiO_3$ with an empty d shell, belong to the perovskite family and exhibit ferroelectric properties below a certain temperature due to a displacive phase transition [1]. Such a phase transition leads to a displacement of the atoms which results in the development of a net dipole moment in the unit cell. These displacements have been understood in terms of the softening of a particular phonon mode with temperature. The frequency of that mode decreases as the temperature decreases, becoming soft at the transition temperature resulting in a change in the crystal structure. The eigenvector corresponding to the soft-mode determines the structure below the transition temperature. Some members of the perovskite family, for example $SrTiO_3$, $KTaO_3$ have a soft polar mode that shows a decrease in the frequency with decreasing temperature but never becomes completely soft even at the lowest attainable temperature. These materials are called quantum paraelectrics or incipient ferroelectrics. Suppression of the ferroelectric phase transition has been explained by the presence of quantum fluctuations [2, 3], which play an important role as there are several competing structures with very small energy differences at low temperatures [3]. Associated with the polar mode, the temperature(T) dependence of the dielectric constant(ε) also shows anomalous behavior. Compared to ferroelectric materials there is no peak feature in the ε(T) vs T plot. ε slowly increases with a decreasing temperature and as T$\rightarrow$ 0 K, it remains constant with a large value of $\sim$ 100 [2, 4, 5]. This is also in contrast with normal dielectrics like oxides, alkali halides having a smaller value of ε between 5 and 10, and which decreases with a decreasing temperature [5]. Incipient ferroelectrics are in a critical state in between the ferroelectric and paraelectric state and are interesting from both a physics and an applications point of view.

Small external perturbations have been found to be able to destroy this state and drive the system ferroelectric [6]. For example a small amount of strain on $SrTiO_3$ can drive the system ferroelectric at low temperatures [7, 8]. There is also a report of room temperature ferroelectricity in $SrTiO_3$ by applying strain [9]. Another way to stabilize the ferroelectric phase is to introduce impurities in the system. A-site, B-site and simultaneous A-site and B-site substitution in $SrTiO_3$ has been studied. Small amount of Ca doping at the Sr site drives the system ferroelectric [10, 11]. B-site substitution have smaller effects, but substitution of two ions with different valency at the B-site, such as in $SrTi_{(1-x)}(Mg_{1/3}Nb_{2/3})_xO_3$ show a relaxor behaviour [12] where we observe a broad peak in the dielectric permittivity(ε') as a function of temperature. The peak temperature(T_m) shifts towards higher values with an increase in the measuring frequency leading to a frequency dispersion. However no ferroelectric hysteresis was observed at low tempera-

tures below T_m characterizing it as a glass like relaxor phase. For simultaneous A and B-site substitution, such as in $[SrTi]_{(1-x)}[PbMg_{1/3}Nb_{2/3}]_xO_3$ [12, 13], a relaxor behaviour with ferroelectric properties at low temperatures can be observed depending on the doping concentrations. Li doping at the K-site in $KTaO_3$ also shows relaxor behaviour [14]. Relaxor behaviour in doped incipient ferroelectrics is associated with the presence of polar/ferroelectric nanodomains in the system [15,16]. Formation of such polar nanodomains are due to the presence of dipolar defects that polarizes the surrounding region depending on the correlation length of the host material. The dipolar interactions here can lead to long-range ferroelectric order or to a glass-like relaxor state depending on several factors, such as concentration of the defects, polarizability of the host lattice, temperature etc.

Another example of an incipient ferroelectric apart from the perovskites, is TiO_2 in the rutile phase. The unit cell is tetragonal with a c/a ratio of $\sim$0.64. Ti and O atoms form chains of edge sharing TiO_6 octahedra running parallel to the c-direction. These chains are corner shared with each other in the ab-plane. Phonon dispersions show softening of the polar A_{2u} mode with decreasing temperature, but never becomes completely soft [17, 18]. Associated with the soft-mode, the dielectric constant measurements also shows the signature of an incipient ferroelectric [19]. There are recent reports from first principle electronic structure calculations, showing ferroelectricity in strained TiO_2 [20–22]. Previously co-doping of Nb(as donor) and In, Al, Ga(as acceptor) was reported to give rise to high dielectric permittivity with minimal loss as a result of localization of the doped charge carriers within the defect cluster [23]. Dielectric measurements of the (Nb+In) co-doped samples showed both high temperature and low temperature dielectric relaxation with a frequency dispersion in the dielectric permittivity as a function of temperature. The high temperature dielectric relaxation above 450 K was attributed to Maxwell-Wagner interfacial polarization, whereas the low temperature dielectric relaxation below 50 K was attributed to the freezing of the pinned electrons within the defect clusters. This low temperature dielectric relaxation can also be the signature of a relaxor state with the formation of polar nanodomains as a result of co-doping. However such a possibility was not explored here.

In this chapter, we report *ab-initio* density functional theory based calculations to explore the effect of co-doping Nb(as donor) and Cr(as acceptor) in rutile TiO_2. Structural analysis shows polar distortions in the TiO_6 octahedra in the vicinity of the dopants. Nb going in to the system as Nb^{5+} carries an effective positive charge, whereas Cr going as Cr^{3+} has an effective negative charge. Doping such an charged complex is equivalent to doping an electric dipole. It is found that, here the dipolar electric field associated with the doped pair is the perturbation to drive the polar distortions. Doping a donor-

acceptor pair is different from doping individual atoms or co-doping neutral pairs. We have examined individual dopants, co-dopants which cannot act as a dipole and hence no polar distortion in the the TiO_6 octahedra was found. Also correlation in the direction of the polar distortions in each TiO_6 octahedra, suggests formation of polar regions around the doped dipoles. This mechanism also works when we dope Nb-In indicating that, co-doping charged pairs can develop polar regions surrounding them in TiO_2. Now, the doping concentration and the degree of ordering of the doped dipoles decide if the system would be ferroelectric or glass-like. Our calculations considers a perfectly ordered distribution of the doped dipoles leading to a ferroelectric state with high value of polarization. Experimental results however shows a ferroelectric behaviour for lower doping concentrations $\leq 5\%$ with a maximum value of ~ 300 $\mu C/m^2$ for 1% doping [24]. No ferroelectric properties was found for a 10% doped sample. Our calculations shows a polarization value of ~ 3400 $\mu C/m^2$ for 2.5% doping which increases to ~ 8400 $\mu C/m^2$ for a doping concentration of 5%. The calculated values are of the order of magnitude higher compared to the experimentally reported values due to the initial condition of perfect ordering of the doped dipoles. This suggests an increase in the polarization value with increasing doping. However with increasing doping, the probability of clustering of the doped dipoles also increases. We found within our calculation that clustering favors for a doing concentration of 10% and has the effect of decreasing the polarization of the system to 500 $\mu C/m^2$ which would otherwise be negligible in real systems.

6.2 Methodology

The electronic structure of the systems were calculated using a projected augmented wave (PAW) [25] implementation of density functional theory within Vienna ab-initio simulation package (VASP) [26] [27]. The generalized gradient approximation(GGA) [28] was used for the exchange-correlation functional. Depending on the unit cell dimensions a Monkhorst-Pack k-mesh [29] of 4×4×4, 4×4×2 and 2×2×4 were used for the 72, 120 and 216 atom systems respectively. The supercells were generated from the experimental tetragonal unit cell of rutile TiO_2 [30]. The lattice constants were kept fixed at the experimental values, but the internal coordinates were relaxed for a minimum energy configuration. The internal positions were optimized till the forces on the atoms were less than 10^{-3} eV/Å. In addition to this, an energy cutoff of 400 eV was used for the kinetic energy of the plane waves included in the basis. Polarization of the systems were calculated using the Berry Phase Technique [31, 32] within VASP.

6.3 Results and Discussion

We started with the experimental rutile structure of TiO_2 with the experimental lattice parameters a = b = 4.59Å and c = 2.96Å. The volume of the unit cell was kept fixed and the ionic positions were relaxed to get the minimum energy configuration. As shown in Figure 6.1(a), the relaxed structure do not show any ferroelectric(FE) distortions, where the Ti atoms are sitting at the center of the TiO_6 octahedra. Now there was no ferroelectric distortions in the experimental structure also and to check if we are stuck into some local minima during the structural optimization process, we introduced a small ferroelectric distortion in the experimental unit cell. The Ti atom at the center of the unit cell was displaced towards one of the six O atoms surrounding it. Now the relaxed structure showed ferroelectric distortions in the unit cell, with off-centering of the Ti atoms along one of the Ti-O bond as shown in Figure 6.1(b). Interestingly both the paraelectric and ferroelectric structure as shown in Figure 6.1(a) and 6.1(b) respectively, were found to be energetically degenerate. This is in agreement with the fact that, rutile TiO_2 is an incipient ferroelectric, where quantum fluctuations prevent the ferroelectric distortions to occur at low temperatures [3].

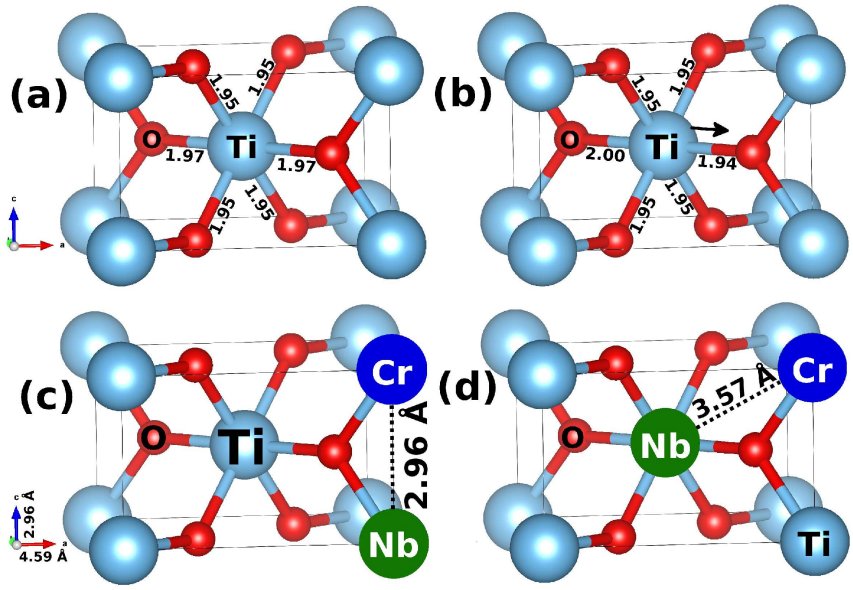

Figure 6.1: Upper panel : Tetragonal unit cell of TiO_2. (a) No ferroelectric distortion or off-centering of the Ti atom in the relaxed experimental unit cell. (b) Off-centering of the Ti atom in the relaxed unit cell with an initial ferroelectric distortion. Lower panel : Two possible doping configuration among many others where Nb, Cr replaces (c) two nearest neighbor Ti atoms in the first case, and (d) two next nearest neighbor Ti atoms in the second case.

Next we proceed to see if co-doping Nb-Cr can remove this degeneracy between the two competing structures. For this we first considered a 120 atom supercell of TiO_2 with 40

Ti atoms and replaced two of them with one Cr and one Nb atom. This corresponds to a doping concentration of 5%. We considered various possible ways of doping the Nb-Cr pair in the supercell. The most favored configuration was found to be the one where the separation between the doped pairs was minimum with a value of 2.96Å. As shown in Figure 6.1(c), this involves replacing two Ti atoms along the c-direction which are nearest neighbors. This configuration was energetically favored by 40 meV over the next suitable configuration, where the Nb and Cr was separated by 3.57Å, replacing two next nearest neighbor Ti atoms shown in Figure 6.1(d).

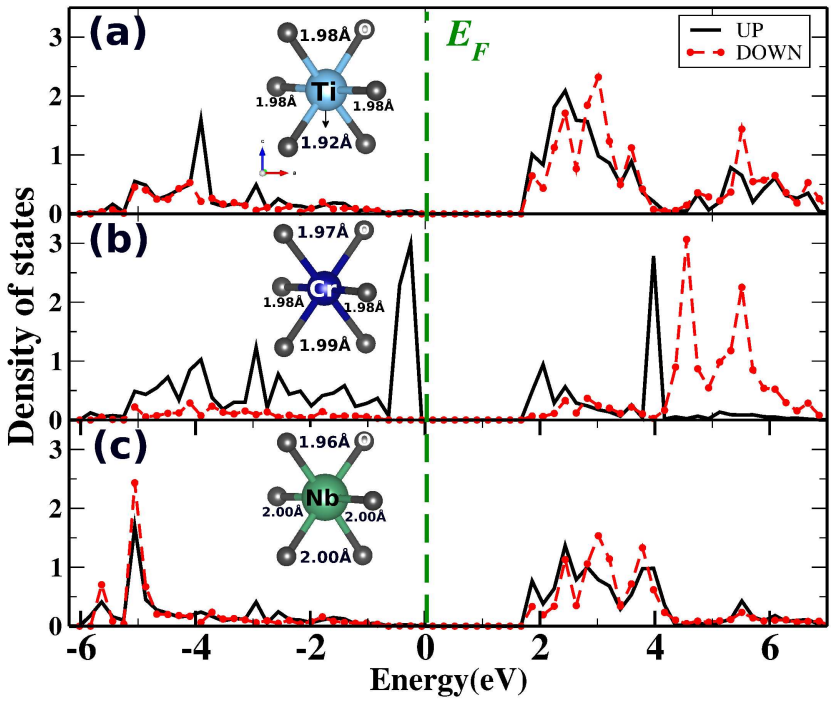

Figure 6.2: The calculated up (solid line) and down (dashed line) spin projected (a) Ti d, (b) Cr d, and (c) Nb d partial density of states at 5% of doping. The Ti atom which is just above the Cr atom is the one for which the density of states is shown. The transition metal(TM)-oxygen bond lengths of the (TM)O_6 octahedra are shown in the insets.

Analysis of the electronic structure helps us to understand the origin of such energy lowering for a nearest neighbor doping configuration. Atom projected partial density of states shows that, Ti with a d^0 electron configuration is in a 4+ oxidation state[Figure 6.2(a)]. Cr has a $d^3(Cr^{3+})$ electron configuration[Figure 6.2(b)]. An associated magnetic moment of 2.90 μ_B also suggests the 3+ oxidation state of Cr. Nb with a d^0 electron configuration[Figure 6.2(c)] is in Nb^{5+} state. So in contrast to isovalent substitution, here Nb carries an effective positive charge whereas Cr has an effective negative charge. The atoms in such a charged complex attract each other via coulomb interaction and can gain in energy when comes closer. This is the reason why a separation of 2.96Å is

energetically favorable than 3.57Å. Also the doped atoms do not contribute any states at the Fermi level and leaves the system insulating. Structural analysis shows off-centering of the Ti atoms in the TiO_6 octahedra in the vicinity of the doped atoms[inset of Figure 6.2(a)]. Off-centering of the Cr and Nb atoms in the c-direction was also observed[insets of Figs. 6.2(b)-6.2(c)]. Total energy of this structure is lower by $\sim$ 10 meV per formula unit over the structure where no off-centering of the transition metal(TM) atoms were allowed, suggesting that such co-doping stabilizes the ferroelectric structure tilting the energy balance in these incipient ferroelectrics.

The question that followed immediately was whether co-doping was essential or we could dope either Cr or Nb in the system and the effect would be similar. This is important because there are possibilities for both Cr and Nb to induce polar distortions in the system individually. Cr with a d^3 electron configuration is a band insulator and not J-T active. But it may distort and gain in energy by second order Jahn-Teller effects [33] which could lead to polar distortions being stabilized. This in-turn may trigger polar distortions in the TiO_6 octahedra. To address this we took the same supercell of TiO_2 and replaced one Ti with a Mn atom which corresponds to a doping concentration of 2.50%. Mn^{4+} with a d^3 electron configuration is a stable valence state for Mn and we expect an isovalent substitution with charge neutrality maintained. Analysis of the partial density of states[Figure 6.3(a)] along with a magnetic moment of 3.05 μ_B shows that Mn has a d^3 electron configuration and leads to an insulating state as expected. Though the system comes out to be insulating, no off-centering of the Ti atoms as well as Mn atom was observed in the relaxed structure[inset of Figure 6.3(a)]. Calculations were also done for 5% doping in a similar manner by replacing two nearest neighbor Ti atoms with Mn along the c-direction. This also gives similar result as described above without any polar distortions in the system. Not every band insulator distorts leading to an off-centering of transition metal atoms, and these observations are consistent with that. So doping Mn alone doesn't stabilize the ferroelectric state.

Now the other doped atom Nb has a large ionic radii compared to Ti. So doping Nb is analogous to applying internal strain in the system which may again trigger polar distortions of Ti in TiO_6 octahedra. To check this we do a similar analysis by doping a large Zr at the Ti-site. Zr is chosen as we have no associated charge doping for Zr^{4+}. Atom projected partial density of state [Figure 6.3(b)] along with a zero magnetic moment shows an isovalent substitution of the Zr atom with a d^0 electron configuration. Zr^{4+} also has a large ionic radii and induces internal strain. Though the system comes out to be an insulator, the structural analysis shows no off-centring in the TiO_6 as well as ZrO_6 octahedra [inset of Figure 6.3(b)]. Increasing the doping concentration from 2.5 to 5%

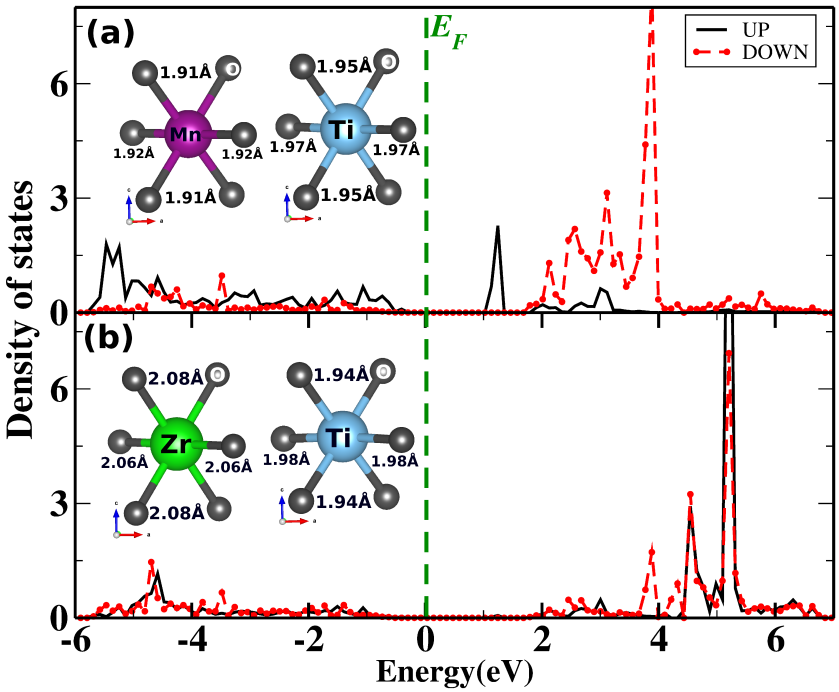

Figure 6.3: The calculated up (solid line) and down (dashed line) spin projected (a) Mn *d* and (b) Zr *d* partial density of states at 2.5% of doping. The transition metal-oxygen bond lengths of the (TM)O_6 octahedra are shown in the insets.

was also not able to induce any polar distortions. So doping only an atom with large ionic radii and applying internal strain is not enough to induce ferroelectricity in TiO_2.

There is something more that happens when we dope two different atoms(Nb-Cr pair) compared to doping the same type of atoms in the system. For Nb-Cr co-doping the Ti-Cr bond length along the *c*-direction is 2.90Å, whereas Ti-Nb bond length is 3.04Å. As shown in Figure 6.4(a), there is a deliberate breaking of inversion symmetry in the *c*-direction for Nb-Cr doping, which is not possible when we dope the same type of atoms (Mn or Zr) in the system. To check the role of the symmetry breaking, we doped Zr-Mn pair in the system similar to Nb-Cr doping.

As shown in Figure 6.4(a), the Ti-Mn bond length along the *c*-direction is found to be 2.90Å and Ti-Zr bond length is 3.04Å. Though doping of the Zr-Mn pair broke inversion symmetry in the *c*-direction, the relaxed structure showed no off-centering of either Ti, Mn or Zr atoms[Figure 6.4(b)]. So, inversion symmetry breaking may be an essential but not the sufficient condition to induce polar distortions in the system. Nb-Cr co-doping is different from Zr-Mn doping where both Zr and Mn goes as Zr^{4+} and Mn^{4+}. Nb going as Nb^{5+} and Cr going as Cr^{3+} ensures an effective positive/negative charge for Nb and Cr respectively. Such a charged complex has an electric dipole associated with it[Figure

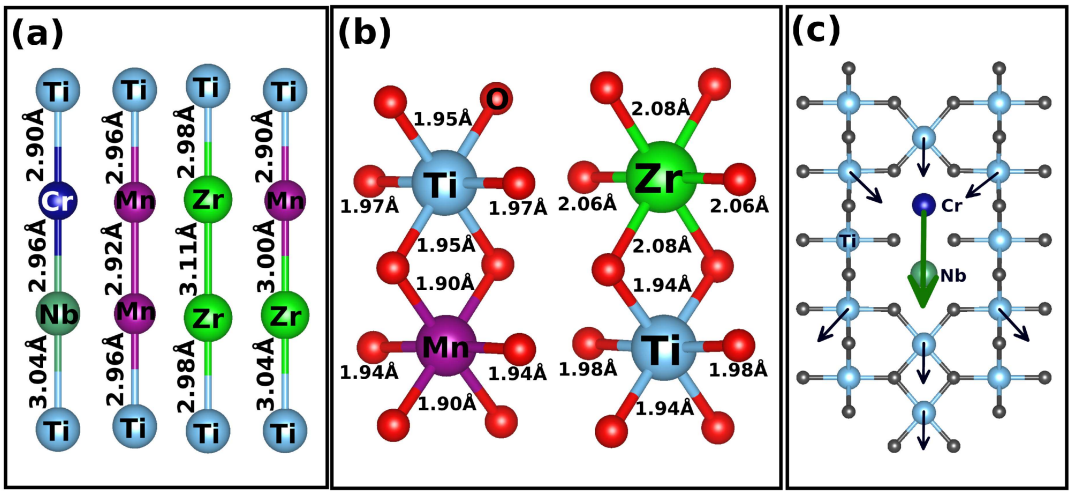

Figure 6.4: (a) Ti-dopant distances for different doping cases. For Nb-Cr co-doping there is a deliberate breaking of inversion symmetry with different Cr-Ti and Nb-Ti distances along c-axis. Whereas when we dope only Mn or Zr in the system, there is no inversion symmetry breaking. However for Zr-Mn co-doping there is similar inversion symmetry breaking like Nb-Cr co-doping. (b) For 5% Zr-Mn co-doping, instead of inversion symmetry breaking no off-centering of the metal atoms in the (TM)O_6 octahedra was observed. Zr-O, Mn-O and Ti-O bond lengths are shown. (c) Schematic representation of the doped Nb-Cr pair acting as a dipole and the polarization in the nearby TiO_6 octahedra.

6.4(c)]. Structural analysis shows that, the dipolar field associated with the Nb-Cr pair polarizes the neighboring TiO_6 octahedra. The off-centering in the surrounding TiO_6 octahedras has a dominant component in the same direction as the doped dipole. As shown in Figure 6.4(c), this indicates formation of small polar regions surrounding the charged complex. Formation of such polar regions in incipient ferroelectrics are reported to give rise to relaxor behaviour in the dielectric measurement data [15,16]. Compared to a normal ferroelectric that shows a sharp peak at the ferroelectric transition temperature, a relaxor shows a broad peak in the dielectric permittivity(ε') as a function of temperature. The peak temperature(T_m) also shifts towards higher values with an increase in the measuring frequency leading to a frequency dispersion. The low temperature state below T_m of a relaxor can be either ferroelectric or glass like depending of the doping concentration and degree of dipolar ordering. Low temperature pyrocurrent measurements of the Nb-Cr co-doped TiO_2 confirm the ferroelectric nature of the samples for a low doping concentrations [24]. Spontaneous polarization measurements showed a maximum value of $\sim 300\ \mu C/m^2$ for 1% doping and was observed for doping concentrations $\leq 5\%$. A doping concentration of 10% showed no ferroelectric behaviour at any temperature.

To address this we calculated the polarization of the co-doped samples using berry phase method. A doping concentration of 2.77% gives a polarization value of $\sim 3400\mu C/m^2$. This increases to $\sim 8400\ \mu C/m^2$ for a concentration of 5%. The calculated polarization

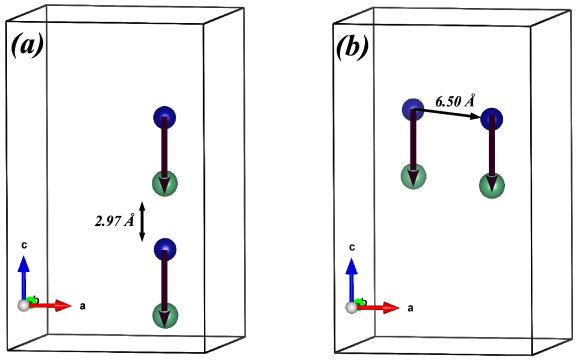

Figure 6.5: Doping of two Nb-Cr pair for 10% doping with two situations. (a) Clustering and (b) non-clustering of the two doped dipoles. For the non-clustering case, the two doped dipoles are separated by a distance of $\sim$ 6.50 Å.

values are an order of magnitude higher compared to the experimental values due to perfect ordering of the doped dipoles considered in our calculations. This in-turn suggests an enhanced polarization value with increasing doping concentration. But with an increasing doping concentration, the probability of clustering also increases. For a 10% doping concentration we introduce a pair of (Nb-Cr) units in the supercell considering both clustered and non-clustered geometries of the doped pairs. A typical situation of clustering and non-clustering of the doped atoms are shown in Figs. 6.5(a) and (b) respectively. The clustered state was found to be the ground state over the non-clustered state(by an energy of 62 meV) where the two doped (Nb-Cr) units were far apart[see Figure 6.5(b)]. The calculated polarization for the clustering case was found to have reduced significantly to 500 μC/m^2, although one expects a negligible polarization value in the real material.

6.4 Conclusions

In summary, quantum paraelectricity is a manifestation of the competition of quantum fluctuations with the long-range dipolar ordering. External perturbations such as strain or pressure have been shown to induce long-range dipolar order in these systems. Considering the example of TiO_2 which is known to be a quantum paraelectric, first principle electronic structure calculations suggest that doping by either Nb or Cr has no effect on the quantum paraelectric state. However co-doping with a donor-acceptor pair as shown in this case (Nb-Cr pair) stabilizes the ferroelectric state. The Nb-Cr defect pair polarizes the environment, pushing the subtle energy balance towards the ferroelectric state. The phenomenon is reminiscent to dilute magnetic semiconductor where doping of a magnetic atom polarizes the charge carriers. This method of dipole doping induced ferroelectricity

can be advantageous in designing new ferroelectrics and multiferroics. It is however restricted to the low doping regime as at higher concentrations one finds clustering and the loss of polarization.

Bibliography

[1] M. E. Lines and A. M. Glass, Principles and Applications of Ferroelectrics and Related Materials(Clarendon, Oxford, 1977).

[2] K. A. Müller, H. Burkard, Phys. Rev. B **19**, 3593 (1979).

[3] W. Zhong, D. Vanderbilt, Phys. Rev. B **53**, 5047 (1996).

[4] R. Viana, P. Lunkenheimer, J. Hemberger, R. Böhmer, A. Loidl, Phys. Rev. B **50**, 601 (1994).

[5] V. V. Lemanov, A. V. Sotnikov, E. P. Smirnova, M. Weihnacht, R. Kunze, Solid State Commun. **110**, 611 (1999).

[6] J. H. Barrett, Phys. Rev. **86**, 118 (1952).

[7] W.J. Burke and R.J. Pressley, Solid State Commun. **9**, 191 (1971).

[8] H. Uwe and T. Sakudo, Phys. Rev. B **13**, 271 (1976).

[9] J. H. Haeni, P. Irvin, W. Chang, R. Uecker, P. Reiche, Y. L. Li, S. Choudhury, W. Tian, M. E. Hawley, B. Craigo et al., Nature **430**, 758 (2004).

[10] J. G. Bednorz and K. A. Müller, Phys. Rev. Lett. **52**, 2289 (1984).

[11] T. Mitsui and W. B. Westphal, Phys. Rev. **124**, 1354 (1961).

[12] V. V. Lemanov, Defects and Surface-Induced Effects in Advanced Perovskites, Eds. G. Borstel et al. (Kluwer Academic Publishers, Dordrecht, 2000), pp. 329-340.

[13] V. V. Lemanov, A. V. Sotnikov, E. P. Smirnova, M. Weihnacht, O. Hässler, Fiz. Tverd. Tela (St. Petersburg) **41**, 1091 (1999).

[14] J. Toulouse, B.E. Vugmeister, and R. Pattnaik, Phys. Rev. Lett. **73**, 3467 (1994).

[15] G. A. Samara, Solid State Physics **56**, 239 (2001).

[16] G. A. Samara, J. Phys.: Condens. Matter **15**, R367 (2003).

[17] J. G. Traylor, H. G. Smith, R. M. Nicklow, and M. K. Wilkinson, Phys. Rev. B **3**, 3457 (1971).

[18] F. Gervais and W. Kress, Phys. Rev. B **28**, 2962 (1983).

[19] R. A. Parker, Phys. Rev. **124**, 1719 (1961).

[20] Y. Liu, L. Ni, Z. Ren, G. Xu, C. Song, and G. Han, J. Phys.: Condens. Matter **21**, 275901 (2009).

[21] P. D. Mitev, K. Hermansson, B. Montanari, and K. Refson, Phys. Rev. B **81**, 134303 (2010).

[22] N. Li-Hong, L. Yong, R. Zhao-Hui, S. Chen-Lu, and H. Gao-Rong, Chin. Phys. B **20**, 106102 (2011).

[23] W. Hu, Y. Liu, R. L. Withers, T. J. Frankcombe, L. Norén, A. Snashall, M. Kitchin, P. Smith, B. Gong, H. Chen et al., Nat. Mater. **12**, 821 (2013).

[24] N. V. P. Chaudhary, S. Sarkar, N. Sharma, A. K. Kundu, K. S. R. Menon, A. Das, P. Mahadevan and A. Venimadhav, Phys. Rev. B **96**, 024107 (2017).

[25] P. E. Blöchl, Phys. Rev. B **50**, 17953 (1994); G. Kresse, and D. Joubert, Phys. Rev. B **59**, 1758 (1999).

[26] G. Kresse and J. Hafner, Phys. Rev. B **47**, 558 (1993) ; G. Kresse and J. Hafner, Phys. Rev. B **49**, 14251 (1994); G. Kresse and J. Furthmüller, Phys. Rev. B **54**, 11169 (1996).

[27] G. Kresse and J. Furthmüller, Comput. Mater. Sci., **6**, 15 (1996).

[28] J. P. Perdew, K. Burke and M. Ernzerhof, Phys. Rev. Lett. **77**, 3865 (1996); J. P. Perdew, K. Burke and M. Ernzerhof, Phys. Rev. Lett. **77**, 3865 (1996).

[29] Hendrik J. Monkhorst and James D. Pack, Phys. Rev. B **13**, 5188 (1976).

[30] W. H. Baur and A. A. Khan, Acta Cryst. **B27**, 2133 (1971).

[31] R. D. King-Smith and D. Vanderbilt, Phys. Rev. B **47**, 1651 (1993).

[32] R. Resta, Rev. Mod. Phys. **66**, 899 (1994).

[33] S. Bhattacharjee, E. Bousquet, and P. Ghosez, Phys. Rev. Lett. **102**, 117602 (2009).

Chapter 7

Mechanism for Ferroelectricity in $PbTiO_3$ and comparison with $BaTiO_3$.

7.1 Introduction

Ferroelectricity is a property of certain materials in which they possess a spontaneous electric polarization that can be reversed by the application of an external electric field. Ferroelectricity was discovered around 1920 in Rochelle salt by Valasek [1, 2]. However the discovery of ferroelectricity in $BaTiO_3$ by Wul and Goldman (1945, 1946) shifted the attention of the researchers to investigate the origin of ferroelectricity in a much simpler structure, the perovskite structure. Instead of the structural simplicity, a complete understanding of the microscopic origin of ferroelectricity in the perovskite oxides is still missing. Considering a fully ionic model it was shown that the origin of ferroelectricity in $BaTiO_3$ is a result of the competition between short-range and long-range Coulomb forces [3–5]. The short-ranged Coulomb interactions favor the cubic paraelectric phase whereas long-range electrostatic forces favor the ferroelectric(polar) state. Later using *ab-initio* calculations it was shown that the covalent interactions between the Ti d and O p states were essential for the ferroelectric distortions to occur [4, 6]. Recently it was shown that ferroelectricity survives in $BaTiO_3$ even in the presence of oxygen vacancies(charge carriers) [7]. Ferroelectric distortions were found to survive up to a critical concentration of 0.1 electrons per unit cell [8]. This further raised the question about the role of the long-range interactions in stabilizing ferroelectricity and it has been shown that only the short-range portion of the screened Coulomb interactions play a role in ferroelectric distortions, with an interaction range of the order of the lattice constant in the case of $BaTiO_3$.

The combined role of covalency and short-range repulsive forces resulting in the polar distortions in $BaTiO_3$ has been examined in details [9]. Considering structural distortions found in the experimental unit cell of $BaTiO_3$, it was shown within *ab-initio* calculations, that the dominant distortion in tetragonal $BaTiO_3$ is aided by short-range repulsive forces. The displacement of the Ti atom towards one of the apical oxygens gives an energy gain from the increased hopping between Ti and oxygen. However, this is expected to be destabilized by the increased repulsion between the electrons on Ti and oxygen. Total energy as a function of Ti displacement towards one of the apical oxygens in the ideal perovskite structure shows no minimum. However movement of the planar oxygens in the direction opposite to the Ti atoms decreases the repulsion between the electrons on the planar oxygens and Ti, as well as that with the apical oxygens, thereby aiding the observed ferroelectric distortions.

Like $BaTiO_3$, $PbTiO_3$ is also a classic example of a ferroelectric material with a perovskite structure. The oxides $BaTiO_3$ and $PbTiO_3$ have similar cohesive properties and

unit cell volume [4] but show very different ferroelectric behavior. Both are paraelectric (non-polar) at high temperatures and have a simple cubic perovskite structure. $BaTiO_3$ undergoes three ferroelectric phase transitions, cubic to tetragonal (at 393 K), tetragonal to orthorhombic (at 278 K) and orthorhombic to rhombohedral (at 183 K), whereas $PbTiO_3$ has only one, cubic to tetragonal at 766 K. The ferroelectric distortions involve small displacements of the cations relative to the anions, leading to a net dipole moment per unit volume. The displacements in the tetragonal ferroelectric phase of both the compounds are different in nature and are also larger in $PbTiO_3$ [10]. Moreover, in the tetragonal ferroelectric phase $PbTiO_3$ has a large tetragonal c/a strain (6%) than $BaTiO_3$ (1%). Interestingly the ferroelectric distortions in the tetragonal phase of $PbTiO_3$ are different from that of $BaTiO_3$. The apical oxygen atoms move in the same direction of the Ti atom displacement. This further raises the question about the role of the short-range forces in $PbTiO_3$. Our calculations show that due to structural difference and additional tetragonality the energy gain due to increased covalency is sufficient to drive a polar distortion in the unit cell.

7.2 Methodology

The electronic structure of the systems were calculated using a projected augmented wave (PAW) [11] implementation of density functional theory within Vienna ab-initio simulation package (VASP) [12] [13]. The generalized gradient approximation(GGA) [14] was used for the exchange-correlation functional. Experimental tetragonal unit cell of $BaTiO_3$ [15] with lattice parameters a = 3.99Å, c = 4.04Å and $PbTiO_3$ [16] with lattice parameters a = 3.90Å, c = 4.13Å was used. The lattice constants were kept fixed at the experimental values, but the internal coordinates were relaxed for a minimum energy configuration where required. The internal positions were optimized till the forces on the atoms were less than 10^{-4} eV/Å. A Monkhorst-Pack k-mesh of $8 \times 8 \times 8$ was used to perform the k space integrations. In addition to this, an energy cutoff of 600 eV was used for the kinetic energy of the plane waves included in the basis.

7.3 Results and Discussion

We start by giving a brief review of the results we previously have for $BaTiO_3$ [9]. At the high temperature, barium titanate ($BaTiO_3$) has a cubic non-polar structure. Ba atoms are at the corner positions of the cube, Ti atoms are at base center and O atoms

are at face-centered positions. These are the ideal positions for which the positive and negative charge centers coincide and we do not have any dipole moments per unit cell. The low temperature structure [15] considered for $BaTiO_3$ is the tetragonal structure with ferroelectric distortions. The atoms are shifted from their ideal positions in such a way that now there is a net dipole moment developed in the unit cell, as a result of positive and negative charge center separation. The ferroelectric displacements of the atoms from their ideal position are shown in Figure 7.1(a).

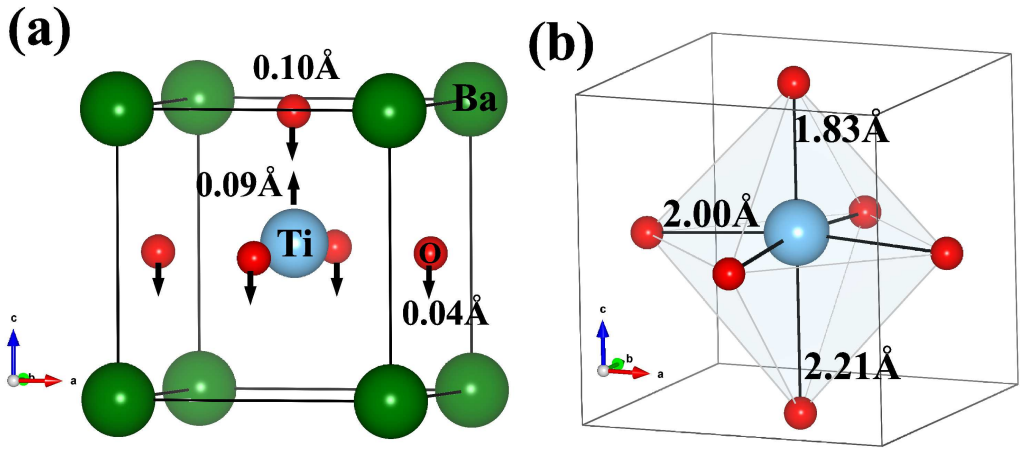

Figure 7.1: Experimental tetragonal unit cell of $BaTiO_3$. (a) Displacement of atoms from their ideal positions (b) unequal Ti-O bond lengths due to ferroelectric distortions.

Analysis of the experimental structure shows three possible microscopic interactions that can control the energetics.

1. Energy gain from hopping due to a shorter Ti-O bond length(1.83Å) as shown in Figure 7.1(b).

2. Energy gain from long-range Coulomb interactions arising due to the non-vanishing dipole moments in the unit cell as a result of displacement of the atoms from their ideal positions[Figure 7.1(a)].

3. Energy loss from short-range Coulomb repulsion as some of the atoms are coming closer to each other.

Considering the dipolar interaction to be weak, the first question that comes is whether the gain in band energy(increased hopping) from a shorter Ti-O bond along the *c*-axis, [Figure 7.1(b)] stabilizes the ferroelectric state. To verify this a model calculation was performed. The ideal paraelectric structure was taken where the atoms sit at their ideal

positions in the tetragonal unit cell. Ba atoms at the corner of the unit cell, Ti atoms are at base center and O atoms are at face-centered positions. Then the Ti atom was moved in steps of 0.005Å from the center of the unit cell towards one of the apical oxygen while all other atoms were sitting at their ideal positions [inset of Figure 7.2(a)]. Similarly, one of the apical oxygen was moved towards the Ti atom while the position of all the other atoms was kept fixed[inset of Figure 7.2(b)]. In each case, the total energy of the system was calculated and has been plotted as a function of displacement as shown in Figure 7.2.

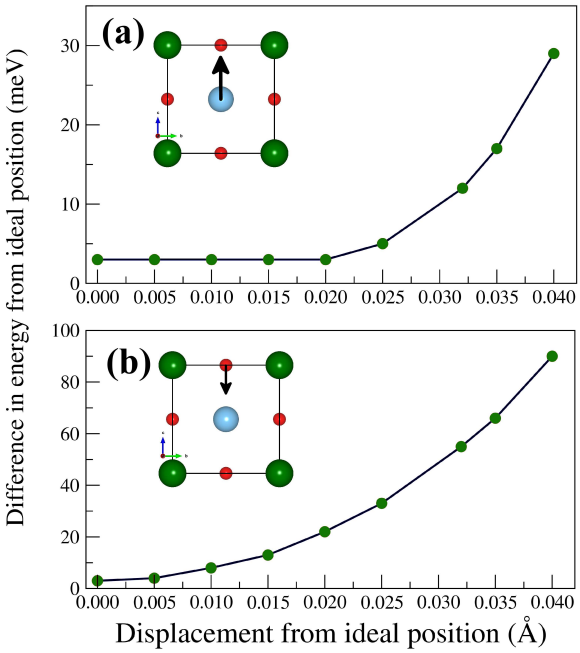

Figure 7.2: Total energy variation with (a) Ti displacement and (b) Apical-O displacement from their ideal position in the ideal perovskite structure. Figures plotted with the data taken from Ref. [9]

With a displacement of the atoms from their ideal positions, we expect a gain in energy due to an increased covalency between the Ti and apical oxygen as the distance between them is decreasing. But as shown in Figure 7.2, no such energy lowering was observed. There is also no minimum in the energy vs. displacement data in either case. This suggested that the band energy gain alone was not enough to stabilize the ferroelectric structure. Some additional interactions have to be considered. The only aspect that was missing in the above study is the role of the planar oxygens. Displacement of the planar oxygens in a direction opposite to that of the Ti displacement[Figure 7.1(a)] was not entirely clear.

In order to examine that, the Hartree energy of the system was measured as a function of the displacement of the Ti and apical oxygen, similar to the total energy calculation. This is shown in Figs. 7.3(a) and (b) respectively. In both cases, we see a sharp increase in the

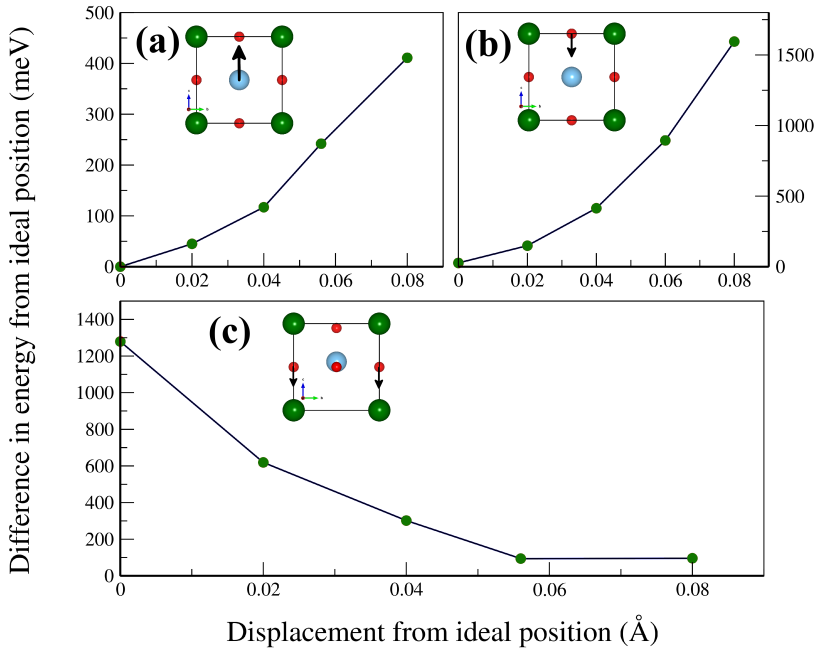

Figure 7.3: Hartree energy variation with (a) Ti displacement and (b) apical oxygen displacement from their ideal positions in the ideal perovskite structure. (c) Displacement of planar oxygens from their ideal face-centered positions in the experimental structure of $BaTiO_3$. The displacements are along the c-axis and away from the Ti atom. Figures plotted with the data taken from Ref. [9]

Hartree energy from the very beginning as the atoms are moved from their ideal positions. This increase in Hartree energy is expected because, as the atoms come closer, repulsion between the electrons on Ti and O increases as a result of charge cloud overlapping. Next, the role of the planer oxygens was examined. In this case, all the atoms were considered at their experimental positions except the planar oxygens, which were kept at the ideal positions(face-center position of the unit cell). In this case, it was found that as the planar oxygens moved away from the Ti atom[inset of Figure 7.3(c)], the Hartree contribution to the total energy decreased[Figure 7.3(c)]. The larger change in Hartree energy associated with oxygen displacements is due to the fact that, oxygen p orbitals are much more extended in space. One of the interesting observation in the above calculations is that, the change in energy associated with the Ti displacement of 0.08 Å towards apical oxygens is 0.41 eV, while that for apical oxygen is 1.57 eV for the same displacement[Figs. 7.3(a) and (b)]. This indicates that a substantial portion of the Coulomb repulsion is between the electrons on the apical oxygens and the planar oxygens, as a result of their extended wave functions. So the conclusion was that the movement of the planar oxygens opposite to the Ti provides a part of the energy reduction required to allow the Ti atom and the apical oxygen to move towards each other. So this is how short-ranged Coulomb interactions can be said to stabilize ferroelectricity.

After this, in this work, we started examining the role of covalency and Coulomb repulsions in driving the ferroelectric distortions in $PbTiO_3$. In case of $PbTiO_3$ the only chemical difference that we have with respect to $BaTiO_3$ is that Pb in the 2+ oxidation state has a lone pair $6s$ electron associated with it, $Pb^{2+} \rightarrow [Xe]4f^{14}5d^{10}6s^2$. This also needs an investigation to see if the lone pair has any role for the difference in the properties of $BaTiO_3$ and $PbTiO_3$. At high temperatures lead titanate ($PbTiO_3$) also has a cubic non-polar structure with the atoms sitting in their ideal positions. Pb atoms are at the corner positions of the cube, Ti atoms are at base center positions and O atoms are at face-centered positions. The low-temperature structure of $PbTiO_3$ is tetragonal and ferroelectric. The atoms are not in their ideal positions. So there is a net dipole moment in the unit cell. The experimental tetragonal structure and the ferroelectric displacement of the atoms are shown in Figure 7.4(a).

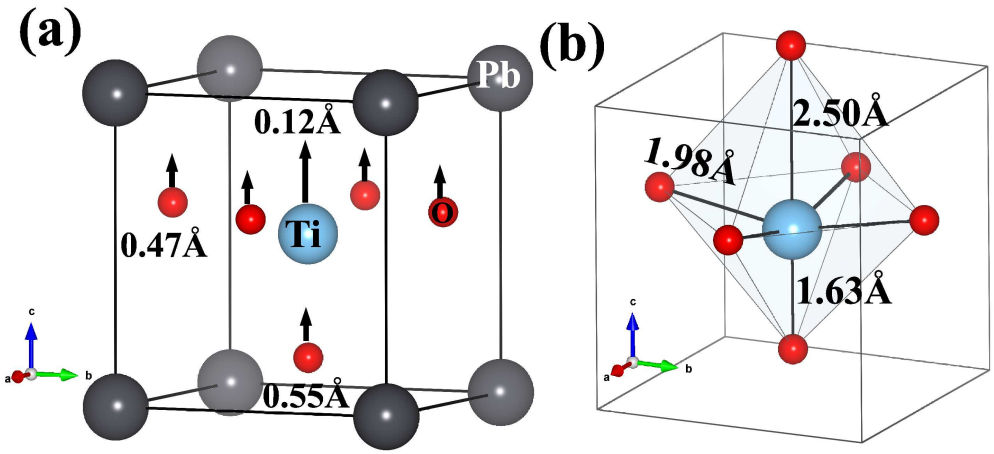

Figure 7.4: Experimental tetragonal unit cell of $PbTiO_3$. (a) Displacement of atoms from their ideal positions (b) unequal Ti-O bond lengths due to ferroelectric distortions.

In Contrast to $BaTiO_3$, here all the atoms have shifted from their ideal position in the same direction(+ve c-direction) and are also larger. Here also we start by asking the same question. If the band energy gain (increased covalency) due to the shorter Ti-O bond[Figure 7.4(b)] is able to stabilize the ferroelectric state. To investigate that we considered the ideal para-electric structure and similarly moved the Ti atom towards one of the apical oxygen [inset of Figure 7.5(a)], and one of the apical oxygen towards the Ti atom [inset of Figure 7.5(b)]. During such displacements, all other atoms stayed at their ideal positions. The variation in the total energy as a function of the displacement of the atoms is shown in Figs. 7.5(a) and (b) respectively.

Now in contrast to $BaTiO_3$, we see a prominent energy minimum associated with the Ti atom displacement at ~ 0.14Å from the center of the unit cell[Figure 7.5(a)]. This suggests a favored off-center position of the Ti atom as a result of increased covalency

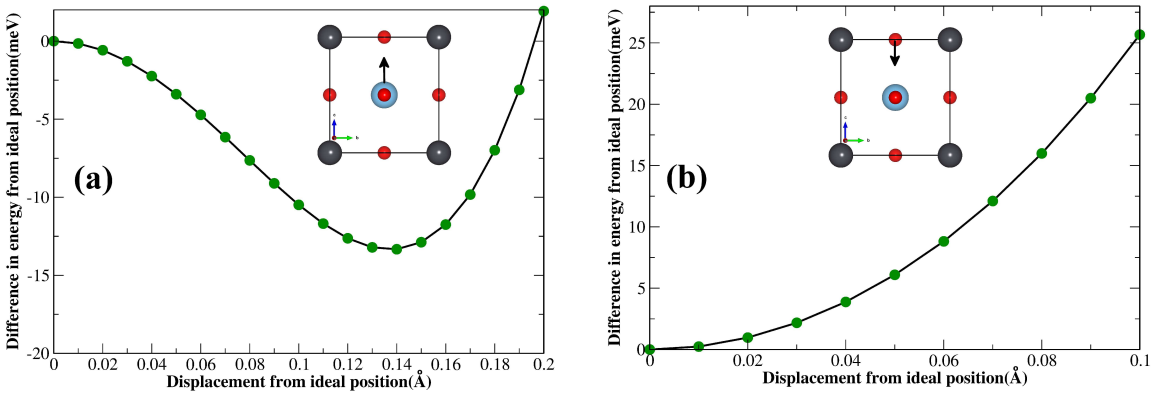

Figure 7.5: Total energy variation with (a) Ti displacement and (b) Apical-O displacement from their ideal position in the ideal perovskite structure.

which was missing in case of $BaTiO_3$. The apical oxygen displacement, however, shows no energy gain probably due to its repulsive interactions with the planer oxygens similar to the case of $BaTiO_3$. To check this further the Hartree energy was also measured as a function of the displacement of the atoms and has been shown in Figure 7.6.

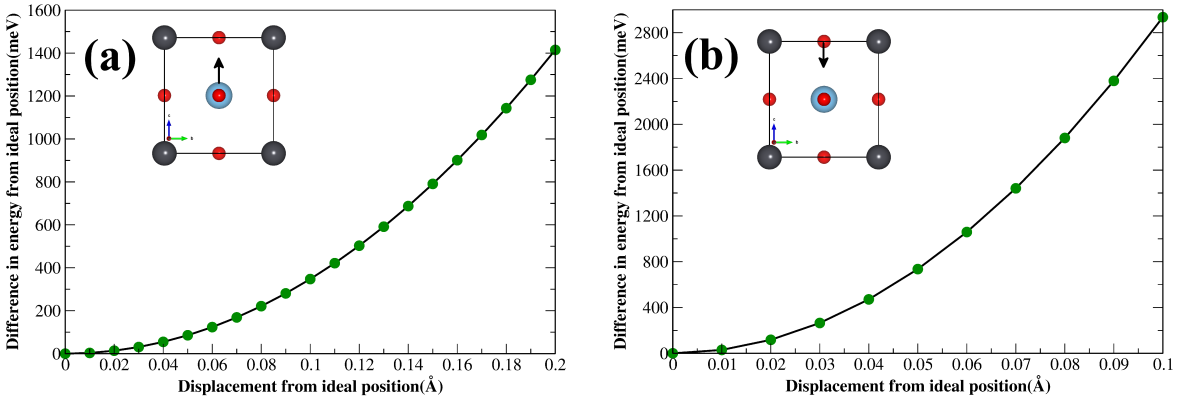

Figure 7.6: Hartree energy variation with (a) Ti displacement and (b) apical oxygen displacement from their ideal positions in the ideal perovskite structure.

Hartree energy increases as expected as a result of increased coulomb repulsion between the electron clouds. Here also we see a larger increase in the Hartree energy associated with apical oxygen displacement compared to Ti atom, indicating the repulsive interaction between the apical and planer oxygens. This is the reason that we do not see any minimum in the total energy plot when the apical oxygen was displaced towards the Ti atom. The energy loss due to increased Coulomb repulsion dominates over the gain from covalency.

So, the main difference between $BaTiO_3$ and $PbTiO_3$ is that in case of $PbTiO_3$ total energy as a function of Ti displacement from its ideal position shows an energy minimum which was absent in case of $BaTiO_3$. Considering the chemical and structural differences,

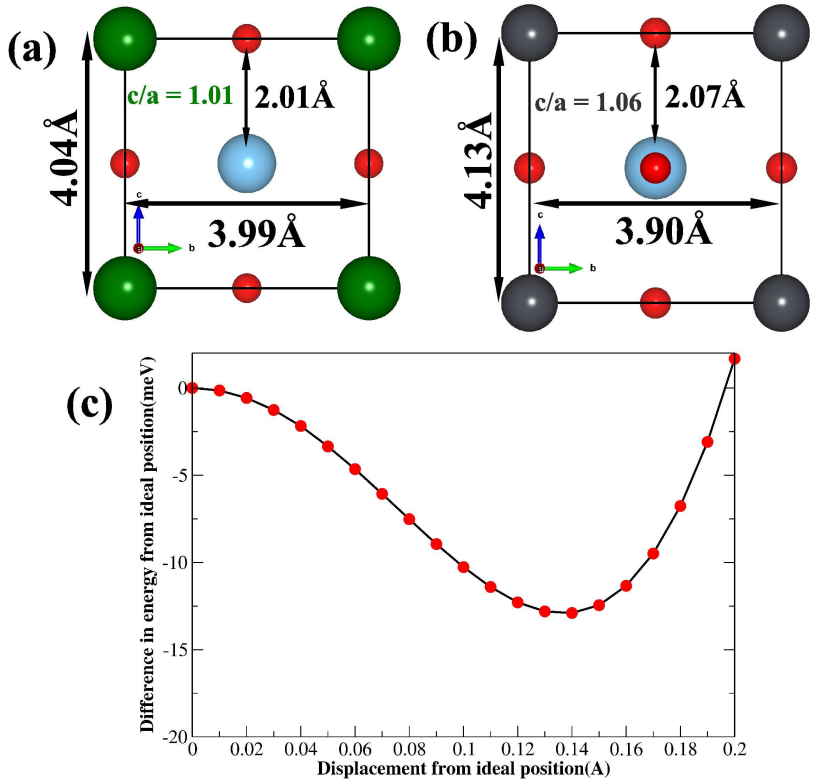

Figure 7.7: Unit cell dimension and tetragonality of the (a) $BaTiO_3$ and (b) $PbTiO_3$ unit cell with the atoms sitting in their ideal positions. (c) Total energy variation with Ti displacement towards apical oxygen in $BaTiO_3$ with the experimental lattice parameters of $PbTiO_3$.

there can be two possible reasons for the energy minimum. (1) The structural difference: Tetragonal distortion is large in $PbTiO_3$ than $BaTiO_3$[Figs. 7.7(a) and (b)]. The c/a ratio in $PbTiO_3$ is 1.06, larger compared to $BaTiO_3$ where it is an order of 1.01. (2) The lone pair effect of the Pb 6s states which was mentioned at the beginning. To examine these aspects, we took the ideal paraelectric structure of $PbTiO_3$ and replace Pb with Ba. This is equivalent to considering $BaTiO_3$ with the same tetragonality of the $PbTiO_3$ unit cell. Then we calculated the total energy as a function of Ti displacement from its ideal position towards one of the apical oxygen. The result is shown in Figure 7.7(c). We see exactly the same description as was seen for the case of $PbTiO_3$. We get an energy minimum of $\sim$ 0.14Å. So we see that the additional tetragonal distortion rather than the lone pair effect is responsible for the ferroelectric behavior in $PbTiO_3$. In $PbTiO_3$ there is more spacing along the c-direction compared to $BaTiO_3$. As shown in Figs. 7.7(a) and (b), the distance between the Ti atom and apical oxygen in the ideal paraelectric structure of $PbTiO_3$ is $\sim$ 2.07 Å, larger compared to $BaTiO_3$, where it is $\sim$ 2.01 Å. As a result, the energy gain due to increased hopping is greater than energy loss due to Coulomb repulsion

between the Ti and apical oxygen in $PbTiO_3$. However, we need further investigation to see if the lone pair plays any crucial role for this large tetragonality in $PbTiO_3$.

7.4 Conclusions

Cation displacements in perovskite titanates give rise to long-range ferroelectric order. In case of the well-known ferroelectrics, $BaTiO_3$ and $PbTiO_3$ the cation displacements are similar in nature but are aided by different microscopic interactions due to their structural differences. In case of $BaTiO_3$ the short-range and long-range Coulomb forces play a crucial role to stabilize the ferroelectric state. The displacement of the Ti atom towards one of the apical oxygens is aided by movement of the planar oxygens in the direction opposite to the Ti atom that decreases the repulsion between the electrons on the planar oxygens and Ti, as well as that with the apical oxygens. In contrast $PbTiO_3$ has a large tetragonal c/a strain (6%) than $BaTiO_3$(1%), and our calculations show that the band energy gain from cation displacement is enough to stabilize the ferroelectric distortion. However, the lone pair $6s$ electrons associated with Pb may play a crucial role for a larger tetragonality of $PbTiO_3$ that needs further investigation.

Bibliography

[1] J. Valasek, Phys. Rev. **17**, 475 (1921).

[2] J. Valasek Phys. Rev. **19**, 478 (1922).

[3] W. Cochran, Adv. Phys. **9**, 387(1960).

[4] R. E. Cohen, Nature **358**, 136 (1992).

[5] W. Zhong, D. Vanderbilt, and K. M. Rabe, Phys. Rev. B **52**, 6301 (1995).

[6] R. E. Cohen, H. Krakauer, Phys. Rev. B **42**, 6417 (1990).

[7] T. Kolodiazhnyi, M. Tachibana, H. Kawaji, J. Hwang, and E. T. -Muromachi, Phys. Rev. Lett. **104**, 147602 (2010).

[8] Y. Wang, X. Liu, J. D. Burton, S. S. Jaswal, and E. Y. Tsymbal, Phys. Rev. Lett. **109**, 247601 (2012).

[9] Abhinav Kumar, *Understanding complex ordering in transition metal oxides*, Thesis submitted in WBUT (2012).

[10] J. Harada, R. Peninsky, B.C. Frazer, Acta crystallogr. **A26**, 608 (1970).

[11] P. E. Blöchl, Phys. Rev. B **50**, 17953 (1994); G. Kresse, and D. Joubert, Phys. Rev. B **59**, 1758 (1999).

[12] G. Kresse and J. Hafner, Phys. Rev. B **47**, 558 (1993) ; G. Kresse and J. Hafner, Phys. Rev. B **49**, 14251 (1994); G. Kresse and J. Furthmüller, Phys. Rev. B **54**, 11169 (1996).

[13] G. Kresse and J. Furthmüller, Comput. Mater. Sci., **6**, 15 (1996).

[14] J. P. Perdew, K. Burke and M. Ernzerhof, Phys. Rev. Lett. **77**, 3865 (1996); J. P. Perdew, K. Burke and M. Ernzerhof, Phys. Rev. Lett. **77**, 3865 (1996);

[15] G. H. Kwei, A. C. Lawson, S. J. L. Billinge, and S. W. Cheong, J. Phys. Chem. **97**, 2368 (1993).

[16] J. Joseph, T. M. Vimala, V. Sivasubramanian, V. R. K. Murthy, J. Mat. Sci. **35**, 1571 (2000).

Chapter 8

Summary and Conclusions

There is a strong correlation between the structure and the property of a material. Tunability in the property has been achieved by varying parameters which induce changes in the structure. Considering the well studied perovskite oxides given by the formula ABO_3 where the A-site is usually occupied by a rare earth atom or an alkali metal atom and the B-site is a transition metal atom, one finds that a change in the size of the atom occupying the A-site results in changes in the electronic structure. The system could be either insulating or metallic, with changes being induced in the temperature at which the metal to insulator transition happens. As pointed out earlier, the changes emerge from structural changes induced by a number of parameters.

In the third chapter of this thesis, we have studied the structure-property relations in inorganic perovskites taking the example of the rare earth nickelates, and show how the size of the rare earth atom control the electronic properties via modulation in the structure. The rare earth nickelates exhibit metal-insulator transitions(MIT) for all members of the family $RNiO_3$ (where R denotes a rare earth ion), with the exception of R = La. The metal-insulator transition is coincident with a crystal distortion, where the insulating state is characterized by a two-sublattice symmetry breaking, with Ni on one sublattice having a decreased mean Ni-O bond length and the Ni on the other having an increased mean Ni-O bond length, defining a bond disproportionation/breathing mode distortion(BD). This state is sometimes also referred to as "charge-ordered(CO)" state. According to Zaanen, Sawatzky, Allen(ZSA), the electronic structure of $3d$ transition metal compounds are described by three parameters. The coulomb correlation strength within the transition metal $3d$ manifold(U), transition metal d bandwidth(W) and Δ, given by the energy required to transfer an electron from the oxygen p levels to the transition metal d levels. Δ plays an important role in the late transition metal oxides. In this work using density functional theory(DFT) and model Hamiltonian approach, we show that occurrence of the insulating state with bond disproportionation in Neodymium nickelate($NdNiO_3$) is intimately related to a negative value of the effective charge transfer energy(a negative value of Δ_{eff}). The breathing mode distortion occurs when the Ni d band enters the oxygen p band and there are holes on the oxygen. For positive values of Δ_{eff} system becomes metallic with the absence of a breathing mode distortion. Along with this, we calculate the Δ_{eff} for all the rare earth nickelates. For R = Lu to Pr the values lie in the range of -0.41 to -0.27 eV indicating a situation where the Ni d band just enters the oxygen p band. As a result, the ground state(GS) of the compounds are insulating with bond disproportionation. For $LaNiO_3$, the value of Δ_{eff} is $\sim$ -0.62 eV and the GS is metallic without any bond disproportionation. So, from here we can conclude that a negative value of delta is necessary for bond disproportionation to occur, however, there is a critical value beyond which the itinerant limit is reached. There will be larger band

overlap and system becomes metallic suppressing the MIT. We also show that, although among the bulk rare earth nickelates the charge ordering seems almost ubiquitous, as the size is reduced, one finds that there is a critical length scale below which one has incomplete charge order/ no charge order consistent with the experimental result.

In the fourth chapter, we investigate the properties of hybrid perovskites where at the A-site there is an organic molecule, which plays a complex role in determining the structure and hence electronic properties. In contrast to earlier where one had a spherical atom, in the present case, one has a cylindrical object occupying the A-site. The presence of a molecule at the A-site of a hybrid perovskite leads to unusual behavior compared to its inorganic counterpart. Considering the case of $(CH_3NH_3)PbBr_3$, we find that it is both the size of the molecule as well as its orientation in the cage formed by the Pb and Br atoms which determine the favored structure. At the microscopic level, the basic energetics which comes into play are steric effects as well as hydrogen bonding. While the molecule is asymmetrically placed in the cuboctahedral cavity, a mapping of the $ab-initio$ band structure to a tight-binding model reveals that the movement of the amine end(NH_3) of the molecule towards the Br atoms is driven primarily by electrostatic considerations. While the hydrogen bonding is responsible for driving the octahedral tilts, the energy lowering considerations do not follow a simple prescription of minimizing H-Br bond lengths. The presence of several competing energetics results in a complex low-energy landscape with deep valleys and high barriers between them which could explain the glassy dynamics seen even at low temperatures in the orthorhombic structure where the dipoles are believed to be frozen.

In the fifth chapter, we investigate the effect of replacing the organic molecule at the A-site of a hybrid perovskite system. In any perovskite system(ABX_3) the change in the unit cell volume due to a change in the size of the A-site cation results in a change in the B-X bond lengths as well as B-X-B bond angles. These are the main structural parameters that directly control the electronic structure of the system. For instance, replacing the cation at the A-site with a larger atom results in an increase in the B-X bond length as well as B-X-B bond angles. An increase in the bond length is found to decrease the band gap while an increase in the bond angle results in a decreased band gap. Whether the change in bond lengths or the bond angles control band gap changes depends entirely on the relative compressibilities of the BX_6 and AX_{12} polyhedra. Our calculations suggest that for hybrid lead halide perovskites the changes in the Pb-X bond lengths plays the dominant role in determining the changes in the electronic structure, especially when one is compressing the unit cell. In this limit standard concepts of structural changes discussed in the context of inorganic perovskites are no longer valid. Steric effects of the

molecule with the inorganic cage dictate the structural changes leading to bond angles changes being small. In the expanded unit cell limit, however, both effects contribute.

In the sixth chapter, we have studied the effect of doping a dipole into an incipient ferroelectric material. In a ferroelectric material, microscopic dipole moments are formed due to cation displacements from their ideal positions in the paraelectric structure. The ordering of such microscopic dipoles in a material may or may not take place leading to ferroelectric properties. On the other hand, there are materials which are on the brink of a ferroelectric transition, where the dipolar order is being suppressed by quantum fluctuations. Usual examples of ferroelectrics are d^0 materials i.e. those which have an empty d shell. This has been an empirical principle being used to roughly identify materials which would be ferroelectric. While not all d^0 materials are ferroelectric, it has been seen that several of them could be identified as incipient ferroelectrics, where there is no ferroelectric order down to low temperatures. TiO_2 is one such example. In such materials, a small perturbation could drive the system ferroelectric. In this work using ab-initio density functional theory calculations, we explore doping a Nb-Cr pair in TiO_2 as a route to drive it ferroelectric. Nb and Cr go into the 5+ and 3+ valence states and therefore behave like a dipole. Analogous to dilute magnetic semiconductors, where doping small concentrations of magnetic atoms in otherwise non-magnetic materials drives the system magnetic, here, the introduction of the dipole is shown to polarize regions in the vicinity of the dopant. Ferroelectricity is therefore found to be stabilized. While this mechanism is indeed found to work at low concentration Nb-Cr doping, at higher doping concentrations a clustering of the dopant atoms is found to destroy long-range ferroelectric order.

Finally, in chapter seven we show how structural differences can lead to dissimilar ferroelectric properties considering two well known ferroelectric materials $BaTiO_3$ and $PbTiO_3$. Tetragonality in the ferroelectric structure of $BaTiO_3$ is smaller than $PbTiO_3$. Hence the off-center displacement of the Ti atom along the tetragonal axis is assisted by short ranged repulsion forces that push the planer oxygen atoms in the opposite direction to that of the Ti atom. Whereas due to a larger tetragonality in $PbTiO_3$, Ti displacement is dominated by the covalency gain between Ti atom and apical oxygen.

Appendix A

A.1 $a^-b^-c^-$ octahedral tilt pattern

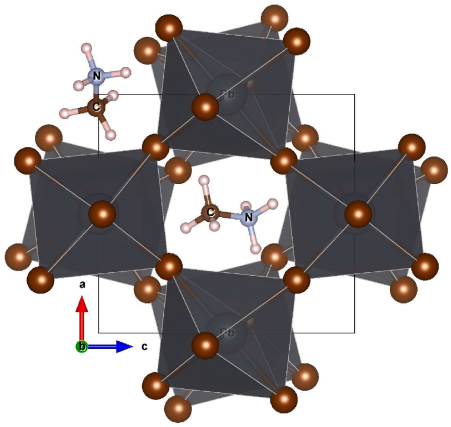

Figure A.1: $a^-b^-c^-$ octahedral tilt pattern viewed along the *b*-axis when the system was relaxed with a molecular orientation along the body diagonal of the cavity as shown in the upper panel of Figure 4.1(c) of chapter 4.

A.2 Finding the favored orientation of the molecule inside the cavity

Apart from steric effects, hydrogen bonding between the molecule and the Br ions also play an important role in determining the ground state orientation inside the ideal octahedral cavity. In order to probe how important hydrogen bonding was for the orientation that the molecule adopted, we again consider the two configurations/orientations of the molecule shown in Figure 4.1(c) of chapter 4. The first direction of orientation is perpendicular to one of the four faces of the cavity parallel to the *b*-axis shown by the shaded area in Figure A.2(a). The second direction is along one of the large body diagonals of the cavity,

and the corresponding anion plane is shown by a dotted area in Figure A.2(a). Indeed maximizing hydrogen bonding would involve short bonds made between hydrogen and the Br atoms. The molecule was oriented along both these direction in the ideal structure and only the molecule was allowed to relax and gain energy from hydrogen bonding.

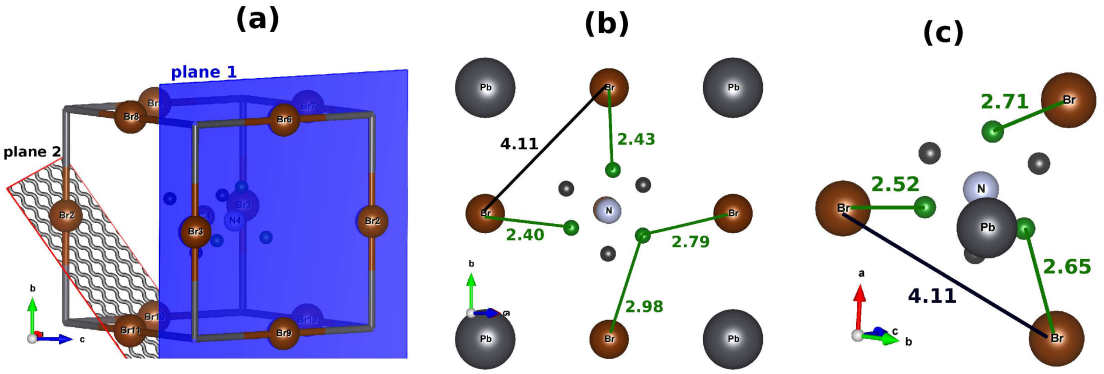

Figure A.2: (a) Two anionic planes corresponding to the two possible orientations of the molecule and the relevant H_N-Br distances after the molecule was relaxed are shown for orientation of the molecule towards (b) plane 1 and (c) plane 2. The hydrogen bonds less than 3Å are shown with solid green lines.

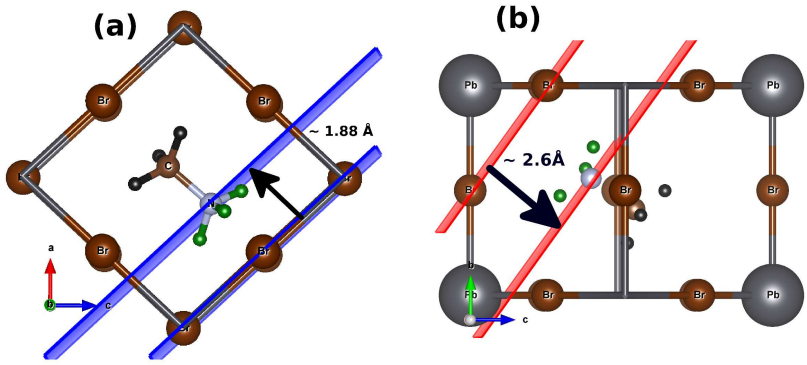

Figure A.3: (a) Distance between the amine part(nitrogen atom) of the molecule and the corresponding anion plane after the molecule was relaxed with an orientation towards (a) plane 1 and (b) plane 2.

In both the cases the amine part of the molecule was found to move towards the Br planes. Shorter H_N-Br distances were found in the first case[Figure A.2(b)] where the molecule was able to move closer to the anion plane[Figure A.3(a)]. For the second case, the close proximity of the Pb atoms prevented the molecule to come too close to the anion plane[Figure A.3(b)] resulting in a weaker hydrogen bonding with the anions[Figure A.2(c)]. Hence the former orientation that has shorter H-Br distance was found to be favored by 32 meV per formula unit over the other. These results help us conclude that while the orientation of the molecule controls the octahedral rotations, the favored orientation is determined by other additional factors such as steric effects, interaction

between the molecule and the inorganic cage as was mentioned in the main text of chapter 4. For performing a DFT calculation with a new molecule at the A-site and see the changes that it can induce in the electronic structure, the first task would be to get the ground state structure of the system. But the problem is that we cannot put the molecule inside the cavity in any arbitrary orientation. Due to the complex potential energy landscape the calculation may get stuck in some local minima. To reach the ground state structure the ground state orientation of the molecule needs to be determined. We can perform the following steps to determine that:

1. Take the inorganic network where we want to put the molecule and switch off the octahedral tilts.
2. Take the molecule and orient it in such a way that the amine part faces the anionic planes.
3. Select the anionic plane/orientation in the undistorted cavity that gives the maximum H-bonding when only the molecule is relaxed. Relaxing the whole system from this configuration gives the ground state structure.

A.3 Conformation of the molecule

There is a dipole moment associated with the molecule due to different electronegativities of the C and N atoms. The two possible stacking of the dipoles along the b-axis is shown in Figure A.4(a) and the arrangement in the ac-plane is shown in Figure A.4(b).

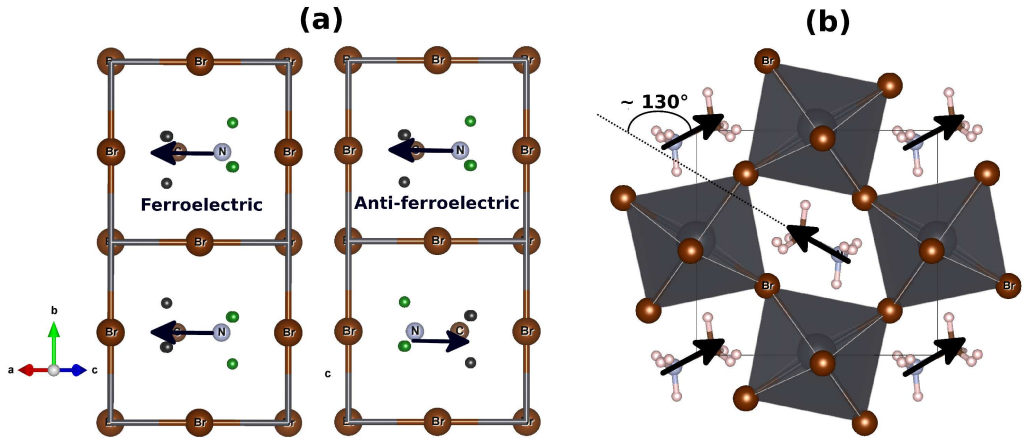

Figure A.4: (a) Ferroelectric and antiferroelectric stacking of the molecular dipoles along the b-axis. (b) Orthogonal arrangement of the dipoles in the ac-plane

A.4 Fitting of Tight binding and Ab-initio band structure

The superposition of the *ab-initio* and tight binding bands for case1 and case2(refer to section 3 of chapter 4) are shown in Figure A.5(a) and A.5(b)respectively.

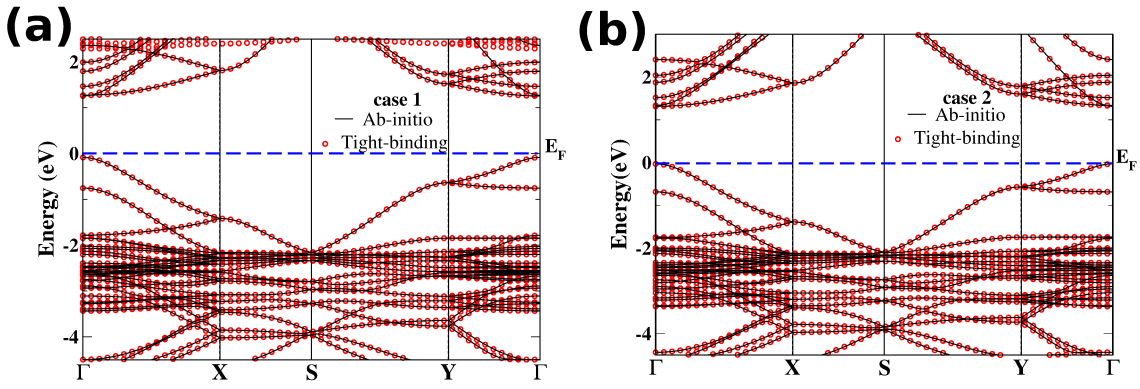

Figure A.5: The fitting of tight-binding and ab-initio band structure for (a) case1, where the molecule is at the center of the cavity without any octahedral tilts. (b) case2, where the molecule is allowed to move for maximum hydrogen bonding.